Theoretical Studies on
Brown Dwarfs and Extrasolar Planets

Dissertation
zur Erlangung des Doktorgrades

des Department Physik
der Universität Hamburg

verfasst von

René Heller

aus

Hoyerswerda

Hamburg, den 09. Juli 2010

Contents

List of Figures

List of Symbols

~	Proportional			
$\approx$	Approximately			
$\equiv$	Is equivalent to			
$\triangleq$	Is equal to by definition			
$:=$	Is defined by			
$=:$	Defines			
$\lceil x \rceil$	x is rounded up to the next natural number			
∞	Infinity			
$\ln(a)$	$\log_e(a)$			
$\log(a)$	$\log_{10}(a)$			
π	Ratio of a circle's circumference to its diameter			

$$\pi = 4 \cdot \sum_{n=0}^{\infty} \frac{(-1)^n}{2n+1} \approx 3.14159$$

c	Speed of light	c	$\triangleq$	$299{,}792{,}458\,\mathrm{m\,s^{-1}}$
G	Gravitational constant	G	$\approx$	$6.673 \cdot 10^{-11}\,\mathrm{m^3\,kg^{-1}\,s^{-2}}$
$M_\odot$	Solar mass	$M_\odot$	$\approx$	$1.988 \cdot 10^{30}\,\mathrm{kg}$
M_J	Jupiter mass	M_J	$\approx$	$1.8986 \cdot 10^{27}\,\mathrm{kg}$
$R_\odot$	Solar radius	$R_\odot$	$\approx$	$6.96 \cdot 10^{8}\,\mathrm{m}$
R_J	Jupiter radius	R_J	$\approx$	$7.1492 \cdot 10^{7}\,\mathrm{m}$
AU	Astronomical unit	AU	$\approx$	$149.598 \cdot 10^{9}\,\mathrm{m}$
Myr	Megayear	Myr	$\approx$	$31{,}536{,}000{,}000{,}000\,\mathrm{s}$

FAUST. Ich bin nur durch die Welt gerannt!
Ein jed Gelüst ergriff ich bei den Haaren,
Was nicht genügte, ließ ich fahren,
Was mir entwischte, ließ ich ziehn.
Ich habe nur begehrt und nur vollbracht
Und abermals gewünscht und so mit Macht
Mein Leben durchgestürmt: erst groß und mächtig,
Nun aber geht es weise, geht bedächtig.
Der Erdenkreis ist mir genug bekannt.
Nach drüben ist die Aussicht uns verrannt;
Tor, wer dorthin die Augen blinzelnd richtet,
Sich über Wolken seinesgleichen dichtet!
Er stehe fest und sehe hier sich um:
Dem Tüchtigen ist diese Welt nicht stumm!
Was braucht er in die Ewigkeit zu schweifen?
Was er erkennt, läßt sich ergreifen.
Er wandle so den Erdentag entlang;
Wenn Geister spuken, geh er seinen Gang,
Im Weiterschreiten find er Qual und Glück,
Er, unbefriedigt jeden Augenblick!

SORGE. Wen ich einmal mir besitze,
Dem ist alle Welt nichts nütze:
Ewiges Düstre steigt herunter,
Sonne geht nicht auf noch unter,
Bei vollkommnen äußern Sinnen
Wohnen Finsternisse drinnen,
Und er weiß von allen Schätzen
Sich nicht in Besitz zu setzen.
Glück und Unglück wird zur Grille,
Er verhungert in der Fülle,
Sei es Wonne, sei es Plage,
Schiebt ers zu dem andern Tage,
Ist der Zukunft nur gewärtig,
Und so wird er niemals fertig.

<div align="center">Johann Wolfgang Goethe, "Faust" (Zeilen 11433 – 11466)</div>

Part I

Opening thoughts

Chapter 1

Abstract

With our human self-reflection we embody the fact that the Universe thinks about itself. About 13.75 billion years after a Big Bang, dead matter became something that is able to say "Je pense, donc je suis.", or "I think, therefore I am". For several thousands of years, we are wondering what it means 'to be', what that is which has being, where did it all come from and – why. In quest of answers to these questions, some dig into the shortest scales of matter, so they may penetrate the power that holds the Universe together. Others study the forms of life or explore the human brain, some believe in an omnipotence and some, finally, use devices to look deep into the sky. About 20 years ago, these stargazers – astronomers, who used to name celestial objects in former times, and astrophysicists, who study their physical qualities – discovered the first planet that orbits a distant star. Over the intervening years, the number of such confirmations has increased to several hundreds. Moreover, scientists discovered objects, which are neither stars nor planets, but have intermediate masses. These 'brown dwarfs' constitute the connecting link between the two regimes. And both, stars as well as planets, can only be understood comprehensively in their context with brown dwarfs.

The mere number of these so-called extrasolar planets, or exoplanets, does not tell us too much about our cosmological context. We want to study them. This thesis aims at the gravitational interaction of stellar and substellar objects and at the possibilities for their exploration. The picture of an isolated planet that orbits its host star undeviatingly and forever is obsolete. Recent discoveries have shown that the fate of planets in close orbits is determined by star-planet interaction. And tidal effects turned out to play a key role. Even more, the structure of young brown dwarfs essentially depends on the tidal processes driven by close companions.

Part I of this book, with its Chaps. 2 to 4, gives an introduction to the basic physics and to the objects we will deal with. In Part II, which makes up the cumulative contingent of my publications, Chap. 5 is dedicated to the tidal effects on brown dwarfs. This issue had not been considered before. Here, we point out how tidal processes affect the energy budget of these substellar objects and how they cause deviations from the standard evolution tracks of isolated brown dwarfs. We apply different established tidal models to the case of the currently only known eclipsing brown dwarf binary, and we identify their differences as well as possibilities for their validation or falsification. In the following, I address the impact of tidal effects on the habitability of exoplanets. As we find, the concept of the so-called (circumstellar) 'habitable zone' requires a revision in due consideration of tidal processes. Chapter 6 is devoted to the prediction of extrasolar planet transits and data analysis. We present sky maps of the expectation values of transits as a projection on the celestial plane. We also introduce a mathematical model, which allows for the deduction of the planet's orbital eccentricity, orientation of periastron, geometric albedo, its radius as a fraction of the stellar radius, its orbital period, and the inclination of the orbital plane with respect to the observer's line of sight. In Part III, I take the liberty to conclude, and in the appendix, finally, I present a German popular science publication of my studies on extrasolar transiting planets.

Abriss

Die menschliche Selbstreflexion macht uns zu einem Hort, an dem das Universum über sich selbst nachdenkt. Nach ca. 13,75 Milliarden Jahren ist aus toter Materie etwas entstanden, das „Je pense, donc je suis." sagt, oder „Ich denke, also bin ich". Seit einigen tausend Jahren fragen sich Menschen, was das Sein ist, woher alles Seiende kommt, wie es anfing und – warum. Auf der Suche nach Antworten auf diese Fragen schauen manche in die kleinsten Teilchen, um dort zu finden, was die Welt im Innersten zusammenhält, andere studieren das Leben in seinen unzähligen Phänotypen, diese und jene graben im menschlichen Gehirn, wieder andere danken einer Allmacht und einige schließlich schauen mit Geräten in den Himmel. Diesen Himmelsguckern – solchen, die die Objekte am Himmel beobachten und ihnen dereinst Namen gaben (Astronomen) und denen, die die Vorgängen zwischen und in diesen Körpern studieren (Astrophysikern) – ist es vor ca. 20 Jahren das erste Mal gelungen, einen Planeten zu entdecken, der einen entfernten Stern umrundet. Mittlerweile ist die Anzahl dieser seltsamen Welten um andere Sterne gar auf mehrere hundert gestiegen. Darüber hinaus wurden Objekte entdeckt, die weder Stern noch Planet sind und dennoch ähnliche Massen haben. Diese „Braunen Zwerge" bilden das Bindeglied zwischen Sternen und Planeten. Beide Regime können nur in ihrem Zusammenhang mit Braunen Zwergen verstanden werden.

Die schiere Anzahl der sogenannten extrasolaren Planeten, kurz: Exoplaneten, erzählt uns noch nicht allzuviel über unseren kosmologischen Zusammenhang. Wir wollen sie untersuchen. Mein Anliegen mit dieser Arbeit ist es, einen Beitrag zum Verständnis stellarer und substellarer Wechselwirkungen zu leisten und Möglichkeiten ihrer Erkundung aufzuzeigen. Denn das Bild von einem Planeten, der seinen Mutterstern auf ewig ungestört umrundet, ist obsolet. Die Entdeckungen der vergangenen Jahre haben gezeigt, dass das Schicksal insbesondere der Planeten in engen Orbits von der Wechselwirkung mit dem Zentralgestirn bestimmt wird. Einen wichtigen Einfluss stellt hier die Gezeitenwechselwirkung zwischen Stern und Planet dar. Auch die Struktur Brauner Zwerge in engen Orbits hängt vor allem für junge Objekte stark vom gravitativen Einfluss ihrer Begleiter ab.

Teil I dieses Buches gibt mit seinen Kapiteln 2 bis 4 eine Einführung in die Grundlagen. In Teil II, der den kumulativen Anteil von mir bereits veröffentlichter Arbeiten ausmacht, widme ich Kap. 5 zunächst den Gezeitenwechselwirkungen zwischen Braunen Zwergen, die vorher noch nicht Gegenstand veröffentlichter Forschung waren. Wir zeigen auf, wie Gezeiten das Energiebudget dieser substellaren Körper beeinflussen und Abweichungen von der Standardevolution im gravitativ ungestörten Falle bewirken. Da die Prozesse von Gezeitendissipation längst nicht in einem befriedigenden Maße verstanden sind, wenden wir hier verschiedene, etablierte Modelle an und zeigen deren Unterschiede sowie Möglichkeiten zur Validierung und Falsifikation auf. Im weiteren Verlauf von Kap. 5 wende ich mich dem Einfluss von Gezeiten auf die Bewohnbarkeit von Exoplaneten zu. Hier konnten wir finden, dass Gezeiten eine grundlegende Revision des Konzepts der sogenannten „Habitablen Zone" verlangen. In Kap. 6 stelle ich Studien vor, die Transits von Exoplaneten vor ihrem Mutterstern behandeln. In diesen Arbeiten beschäftigen wir uns mit der Vorhersage von Transits sowie der Datenanalyse. Zum ersten Mal wurden hier Karten erstellt, welche die Transitwahrscheinlichkeit von Exoplaneten an die Himmelssphäre projizieren. Außerdem stellen wir ein mathematisches Modell vor, welches die Ableitung der Exzentrizität, der Orientierung des Periastrons, der geometrischen Albedo eines Transitplaneten, seines Radius im Verhältnis zum Radius des Sterns, seiner Orbitperiode und der orbitalen Inklination gegen die Sichtlinie aus Beobachtungsdaten erlaubt. In Teil III erlaube ich mir, Schlüsse zu ziehen, während der Anhang mit einer populärwissenschaftlichen Ausgabe meiner Studie an extrasolaren Transitplaneten aufwartet.

Chapter 2

Celestial mechanics

2.1 Historical context

At the beginning, there was water, Thales of Miletus said around 600 years B.C. This man is considered the founder of ancient Greek philosophy, thus the father of Occidental Philosophy in general. Although little is known about this man, his period can be dated fairly good since he predicted a Lunar eclipse referred to an event in 585 B.C. (Russell 1945). In this context it seems ironic that the illumination of man's awareness was triggered by an occultation. Thales was followed by Pythagoras, who developed deductive reasoning and thus prepared the bed for modern mathematic and logic. And it was roughly 300 B.C., when Euclid wrote his *Elements*, often mentioned as one of the greatest books ever written. His conception of flat space would not be challenged until the late 19th century by masterminds of relativistic geometries, such as Bernhard Riemann and Hermann Minkowski. At the same epoch as Euclid lived, Eratosthenes was the first man who calculated the circumference of the Earth, simply by measuring the angle of a shadow of a stick in the ground and multiplying two numbers (Sagan 1980). His incredibly tiny error was about 0.6 %. And after Herakleides had recognized that Mercury and Venus orbit the Sun, around 350 B.C, it was Aristarchus of Samos who anticipated Copernican theory, conceiving that all the planets, in particular the Earth, move around the Sun. He also concluded that the Earth performs a rotation every 24 hours. Undoubtedly, Aristarchus had stimulated the later Nikolaus Kopernikus. Greek philosophers even succeeded in calculating the average distance to the Moon. Ptolemy achieved an estimate of 29½ times the radius of the Earth, while the true value is 30.2. And Posidonius estimated the diameter of the Sun to be 6545 the diameter of the Earth, while its true value is 11 726 times the diameter of the Earth.

Of all the available concepts of the Universe it was Ptolemy's version, which dominated after the fall of the ancient Greek culture. In his mechanistic and deterministic construct from between 90 and 168 A.D., the Earth was located in the center while all the remaining celestial bodies – the Sun and the Moon, Mercury, Venus, Mars, Jupiter, Saturn, and the stars – were attached to spheres around it. Man was the center of the Universe, in accord with the picture preached by Christianity as written in the Bible. And it was not until the beginning of the 17th century that this simple model could be confuted. Although the Polish Astronomer Nikolaus Kopernikus had developed his theory of the Universe during the first half of the 16th century, he did not dare to publish it until 1542, one year before he died. His fear for integrity prevented an earlier publication. Although his heliocentric model was much closer to the modern picture of the Solar System, it suffered shortcomings from the assumption of circular orbits. It took another 60 years until Johannes Kepler abandoned the idea of ideal, circular orbits and introduced eccentricity. His more complex and less intuitive theory fitted the wealth of observational data, measured and archived by the Danish astronomer Tycho Brahe, with previously unknown precision. In 1619, when Kepler had found the third of his laws, he published the famous *Harmonice mundi* (Kepler 1619). His theory was supported by observations of the Italian astronomer Galileo Galilei, who found Jupiter's four massive moons Io, Europa, Ganymede, and Callisto, in early 1610. Here, we meet a crucial event in the rise of modern science. As Immanuel Kant writes in his *Kritik der reinen Vernunft* (Kant 1787): "So ging allen Naturforschern ein Licht auf." ("Hence, it dawned on all natural scientists."). Although Sir Isaac Newton never stated officially, his fundamental work *Philosophiae Naturalis Principia*
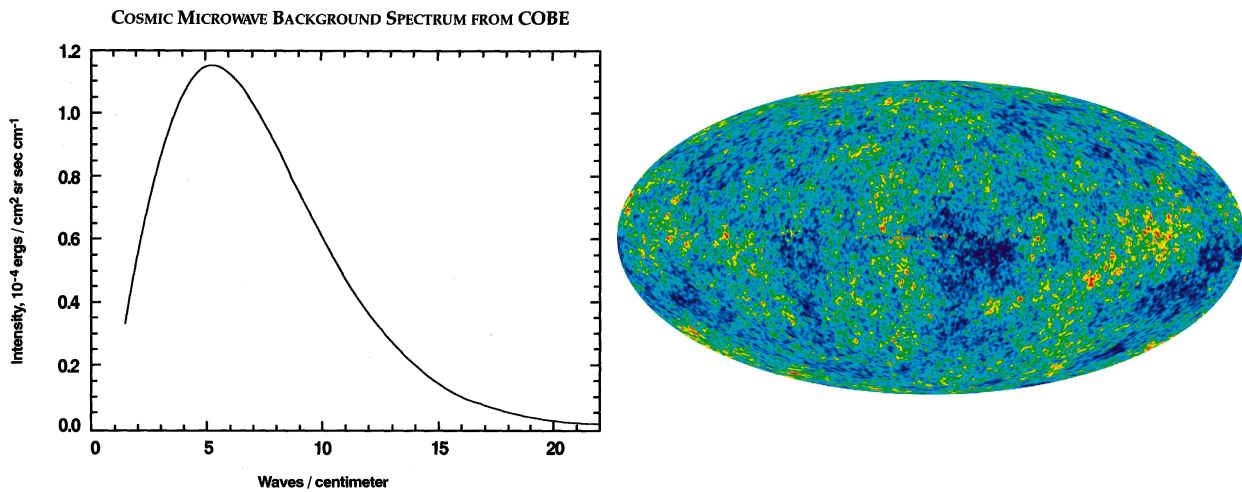
Fig. 2.1: *Left:* Spectrum of the cosmic background radiation as observed with the COBE satellite. *Right:* Combination of images at five different frequencies obtained with the WMAP satellite. This Mollweide projection is in Galactic coordinates. The color scales linearly from -200 to $+200\,\mu$K. Credit: NASA / WMAP Science Team

Mathematica ([Newton 1686](#)) was stimulated by the work of Johannes Kepler. In correspondence with his editor at the Royal Academy of Sciences, Edmund Halley, Newton admits that he had deduced his law of gravitation from Kepler's theorem about 20 years before the submission of his *Principia Mathematica*. However, this book constitutes the birth of classical mechanics. Scientists were multi-talented at that epoch and there was no devision of science into categories such as mathematics, philosophy, physics, chemistry, biology, astronomy, geology, astrology, theology et cetera. All scientists simply were philosophers. Newton himself did not only write the fundamental book of classical physics, he also invented differential and integral calculus as well as calculus of variations, he came up with theories of light and he developed a new, very efficient telescope type, nowadays called 'Newton telescope'. After all, he published on religious issues and indulged himself in occult studies and alchemy.

Philosophers of the following generations became more and more specialized in their respective fields of science. Albert Einstein is often considered the last great mind, who revolutionized our view of the Universe individually. And although he does not give a single reference to another publication in his *Zur Elektrodynamik beweger Körper* from 1905 ([Einstein 1905](#)), except an acknowledgement to his colleague Michele A. Besso, it must be said that he courageously reinterpreted the results of Hippolyte Fizeau, Hendrik Lorentz,

and Henri Poincaré. Nevertheless, his conclusions degraded Newton's classical model of the Universe to a special case of a much less intuitive theory. With his Theory of Relativity, Einstein knocked over the traditional concepts of time, mass, space, and space geometry. The second revolution in physics of the 20th century was induced by quantum theory. In this field, a potpourri of ingenious thinkers started to explore physical scales far from every day experience. Max Planck, Niels Bohr, Werner Heisenberg, Wolfgang Pauli, Erwin Schrödinger, Paul Dirac, Enrico Fermi, and Richard Feynman – to mention just the most popular names – pictured an undetermined, probabilistic Universe. While Aristotle's school explained dead matter based on observations of living matter and mechanists of Newton's school interpreted the fate of living forms as determined by the machinery of Laplace's demon ([Laplace 1814](#)), quantum theorists explain the microscopic and the macroscopic Universe – thus dead as well as living matter – as the result of decoherence: the collapse of multidimensional probability functions of quantum particles.

The theory of relativity in combination with the theory of quantum physics allowed physicists to understand the expansion of the Universe, first described by Georges Lemaître in 1927 ([Lemaître 1927](#)) and observationally confirmed by Edwin Hubble in 1929 ([Hubble 1929](#)), as well as the cosmic background radiation, detected in 1965 by Arno Penzias and Robert W. Wilson ([Penzias &](#)

Wilson 1965). According to the Standard Model, this cosmic microwave background is a remnant of the so-called Big Bang, the ignition of the Universe. It's current spectral distribution corresponds to a temperature of roughly $2.73\,\mathrm{K}$, according to Planck's law from quantum physics (left panel in Fig. 2.1). Fluctuations in the temperature distribution witness anisotropies in the distribution of matter roughly $380\,000$ years after the Big Bang, when the visible Universe became transparent (right panel in Fig. 2.1). These inhomogeneity, likely caused by quantum variations at the ignition of the expansion, provided the seed for the accumulation of matter into stars, galaxies, and galaxy clusters. Thus, this pattern is sometimes called 'the fingerprint of God', whatever one comprehends as 'God'. Measurements of the space missions COBE (Smoot et al. 1992) and WMAP (Spergel et al. 2003) helped cosmologists to constrain the age of the Universe to 13.75 ± 0.11 billion years and to assess space geometry. At the same time as our cosmologic understanding grew, stellar and planetary sciences achieved major progress on the path towards a comprehensive picture of our status in the Universe. Since the end of the 20th century, we know that other stars host planets (Latham et al. 1989; Wolszczan & Frail 1992; Walker et al. 1992; Mayor & Queloz 1995; Marcy & Butler 1995). And most notably, none of the 396 extrasolar systems discovered so far[1] is similar to the one we live in. What can we learn about these strange worlds?

2.2 Classical celestial mechanics

Although the principles of relativity and the statements of quantum physics provided fundamental insights into the formation and structure of the Universe, the equations in this thesis will not require these sophisticated principles. For the mass and time scales under consideration, classical mechanics yields satisfactory results. One of the key equations of two-body dynamics was published by Johannes Kepler as the third of his three laws in 1619. For the planets of the Solar System, each in an elliptical orbit with semi-major axis a and orbital period P around the Sun, he found the relation $P^2 \sim a^3$. This was an empirical fit to Tycho Brahe's observations and Kepler did not understand the underlying physics.

[1]The Extrasolar Planets Encyclopaedia at www.exoplanet.eu as of July 9, 2010

It was Isaac Newton who, based on his three First Principles of Motion, accomplished the analytical derivation of Kepler's law for two bodies with masses M_1 and M_2. With $n = 2\pi/P$ as the orbital mean motion, it can be expressed as

$$n^2 a^3 = G(M_1 + M_2). \qquad (2.1)$$

Here, $G \approx 6.673 \times 10^{-11}\,\mathrm{m}^3/(\mathrm{kg\,s}^2)$ is Newton's gravitational constant.

The mass of a star or a planet is the fundamental parameter. Thus, its determination enjoys highest priority. Imagine the two masses located at cartesian coordinates $\vec{r_1}$ and $\vec{r_2}$ from their barycenter. Their mutual displacement is given by

$$\vec{r} := \vec{r_2} - \vec{r_1} \qquad . \qquad (2.2)$$

In this reference frame the principle of linear momentum can be expressed as

$$M_1\vec{r_1} = -M_2\vec{r_2} \qquad . \qquad (2.3)$$

Equations (2.2) and (2.3) can be used to derive

$$\vec{r_1} = -\frac{M_2}{M_1 + M_2}\vec{r} \qquad (2.4a)$$

$$\vec{r_2} = -\frac{M_1}{M_1 + M_2}\vec{r} \qquad , \qquad (2.4b)$$

which gives

$$\frac{|\vec{r_1}|}{|\vec{r_2}|} = \frac{M_2}{M_1} \qquad . \qquad (2.5)$$

From Eq. (2.5) we learn that the distance of the two masses from the barycenter is always equal to the inverse ratio of their masses. That means that the shapes of their orbits will be the same except for a scaling factor and a mirror-inverted orientation. Thus, in the reference frame of the barycenter both masses will perform eccentric orbits, where a_1 is the semi-major axis of the ellipse of M_1, and a_2 the semi-major axis for the ellipse of M_2. Due to the conservation of angular momentum, this process is two-dimensional. Both orbits will be situated in the same plane, orbiting the common center of mass on the line between them. In this plane, the reference system can be arbitrarily rotated such that the abscissa points in the same direction as the semi-major axes. At apoastron, Eqs. (2.4a) and (2.4b) can be written as

$$a = -\frac{M_1 + M_2}{M_2}a_1 \qquad (2.6a)$$

$$a = -\frac{M_1 + M_2}{M_1}a_2 \qquad , \qquad (2.6b)$$

where $a \equiv a_1 + a_2$ is the semi-major axis of the relative orbit, as used in Eq. (2.1).

2.2.1 Visual binaries

Stars often occur in multiple systems. Abt & Levy (1976) conclude that more than 72 % of stars with spectral types between F3 and G2 (IV and V) exist in multiple systems and Fischer & Marcy (1992) find 42 ± 9 % of M dwarf primaries to be in multiple constellations. In a recent and very extensive study, Raghavan et al. (2010) showed that 54 ± 2 % of a volume-limited sample of stars with spectral types ranging from F6 to K3 exist in multiple constellations. Some of such multiple systems can be resolved on photometric images (see e.g. Heller et al. 2009a, where we presented a sample of optically resolved white dwarf-M star binaries). If both orbits of a visual binary can be observed, it is possible to reconstruct the barycenter as well as the eccentricity e, the orientation of the periastron, and the inclination i between the orbital plane and the observer's line of sight (Bradt 2008). For $i = 0°$ the view on the orbit is 'face-on' and the ellipses are seen from above, while for $i = 90°$ the view is 'edge-on' and the orbits appear as a straight line. If the absolute distance to the system can be determined, e.g. by observations of the parallax, the deprojection of the orbits yields the absolute values of a_1 and a_2, an thus a. As soon as the constituent have performed one orbit during the course of the observations, the period is known. It is thus possible to deduce the sum of the masses with Eq. (2.1) and thus the individual masses from Eqs. (2.6a) and (2.6b).

2.2.2 Double-lined spectroscopic binaries

Close systems with orbital periods less than a few years can typically not be resolved on images. However, their orbits might be accessible via spectroscopy. A physical binary in an orbit around a common barycenter is called a 'double-lined spectroscopic binary' (DLSB) if the spectral lines of both constituents can be resolved in the spectrum. As an example, I show the radial velocity (RV) curve of a recently identified DLSB HD 146875 in Fig. 2.2. As follows from Eq. (2.5), the body with the smaller RV amplitude, the red object in the figure, is the more massive one. Among spectroscopic binaries, these double-lined systems are particularly interesting because they can provide information of the individual masses.
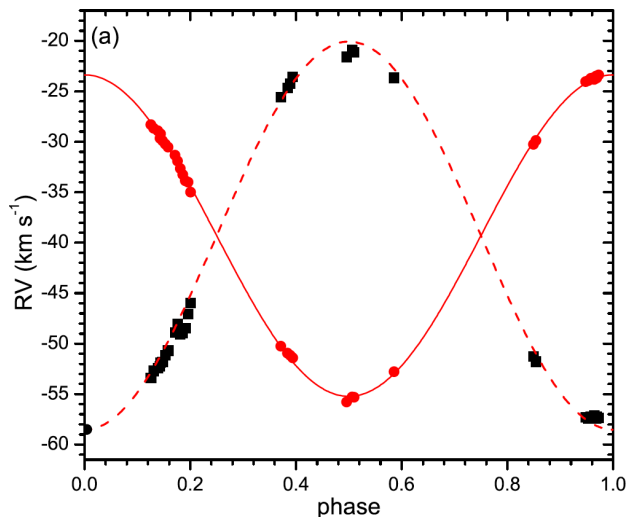

Fig. 2.2: Radial velocity curve of the double-lined spectroscopic binary HD 146875 (from Wang et al. 2009). Points indicate measurements, lines indicate best fits.

Instead of the true semi-major axes, however, the RV curve merely yields information about the projected semi-major axes, which can be derived e.g. by the least-square fitting method. Substituting Eqs. (2.6a) and (2.6b) for a in Eq. (2.1) and multiplying both sides of the equations by $\sin(i)$, one gets

$$\frac{M_2^3 \sin^3(i)}{(M_1 + M_2)^2} = \frac{4\pi}{P^2} \frac{a_1^3 \sin^3(i)}{G} \qquad (2.7a)$$

$$\frac{M_1^3 \sin^3(i)}{(M_1 + M_2)^2} = \frac{4\pi}{P^2} \frac{a_2^3 \sin^3(i)}{G} \qquad . \qquad (2.7b)$$

These formulae are the so-called 'mass functions' for M_1 (Eq. 2.7a) and M_2 (Eq. 2.7b). On the right-hand side we find only variables that can be measured in a DLSB, whereas on the left-hand side there are three unknowns: M_1, M_2, and i. As long as the inclination is not determined, the two mass functions can be divided one by another to compute $M_2/M_1 = a_1/a_2$, while the sum of the masses remains unknown. When the inclination of the system can be constrained, then $a_1 + a_2 \equiv a$ can be used to get the sum of both masses with Kepler's 3rd law (Eq. 2.1), which solves the degeneracy. In Chap. 4 I will review the transit method and its potential to constrain the orbital inclination.

2.3 Tidal distortion

Until 1995, when the discovery of the first extra-solar planet could be confirmed (Mayor & Queloz 1995), the Solar System was the only example of a planetary system. An astonishing aspect of most extrasolar planets found since then is their short orbital period. In the early phase of exoplanet hunting, a family of so-called 'Hot Jupiters' emerged in the detection sample – Jovian gas giants in the close proximity of their host stars.

The short orbital separation between a planet and its host star, or between a moon and a planet, may drive a variety of structural phenomena on both constituents, which give insight in the bodies' structures and evolution. With decreasing semi-major axis the gravitational pull of the star becomes stronger, distorting the structural shape of a planetary companion more and more. Without this tidal deformation, a planet can be described as an oblate sphere, i.e. a spheroid compressed in the direction of the polar diameter. This oblateness is caused by the planetary rotation and the resulting centrifugal acceleration. In the presence of the stellar perturber, however, the planet becomes elongated into the direction of the star. This deformation, the tidal bulge of the planet, does not point directly at the center of mass of the tide raiser (left panel in Fig. 2.3). Due to the time required by the deformed body to respond to the external force, the tidal bulge either lags behind (case A) or goes ahead of (case B) the line connecting the two centers of mass. In case A the planetary day is longer than a year, vice versa for case B. The Earth with respect to the Moon, for example, displays case B: our day is shorter than a month and the tidal bulge precedes to line between the two centers of gravity. This asymmetry exerts a torque acting on the deformed body. In the case of the Earth-Moon system, the rotation speed of the Earth is slowed down. It will settle at an equilibrium state once the mean torque over one orbit (a month) will be zero. If the eccentricity of the Lunar orbit was zero and if the obliquity of the terrestrial rotation axis with respect to the Lunar-terrestrial orbit was zero, then the equilibrium rotation period of the Earth would match the length of a month, while the month would be longer than the current month. This state would be called 'tidal locking'. The Moon is already locked in this rotation state. Since its orbital eccentricity and its obliquity are almost zero, one hemisphere faces the Earth permanently.

2.4 Orbital evolution

Friction in the distorted body causes a time delay between the execution of the gravitational force from the tide raiser and the response of the distorted body, relativistic effects being neglected. Hence, the body heats up, and eventually gets inflated, and the system dissipates energy. This transformation from orbital energy into heat is termed 'tidal heating'. Over the course of the tidal interaction, the total angular momentum of the two-body system is conserved, while it can be exchanged among the two masses. Rotational angular momentum can be converted into orbital angular momentum and vice versa. Since the system dissipates energy at the same time, the semi-major axis a, as well as the eccentricity e, the rotational frequencies of the star and the planet, ω_s and ω_p, and the putative spin-orbit misalignments ψ_s and ψ_p of the star and the planet are subject to changes.

Depending on initial conditions, the semi-major axis of the perturbed body will either be increasing or decreasing until, finally, the body will either be thrown out of the gravitational sphere of influence of the tide raiser, or both objects will collide. The eccentricity will either be driven to zero, a process which is called 'circularization', or it will converge on 1, and the objects will also collide. This yields an observational selection effect. Since tidal processes proceed more rapidly in closer orbits, extrasolar planets at small semi-major axes will show small eccentricities. In Fig. 2.3 I show the correlation between eccentricity and semi-major axis of 464 confirmed planets[2], listed in The Extrasolar Planets Encyclopaedia (TEPE, www.exoplanet.eu) on July 9, 2010. As can be seen in this plot, planets in close orbits typically exhibit small eccentricities, most likely caused by tidal circularization in these systems. Most of these objects at $a < 0.1\,\mathrm{AU}$ show orbits with $e < 0.1$. For a review of processes that may excite significant eccentricities of exoplanets even in tight orbits, see Sect. 5.2. Furthermore, the rotational periods will shift towards an equilibrium state, where the averaged exchange of momentum over one orbit vanishes. This condition is referred to as 'tidal locking' and as long as $e \neq 0$ or $\psi \neq 0$, the equilibrium rotation period will not match the orbital period.

Usually, the tide raiser is assumed to be a point

---

[2]A similar correlation for multiple stellar systems was recently shown by Raghavan et al. (2010).
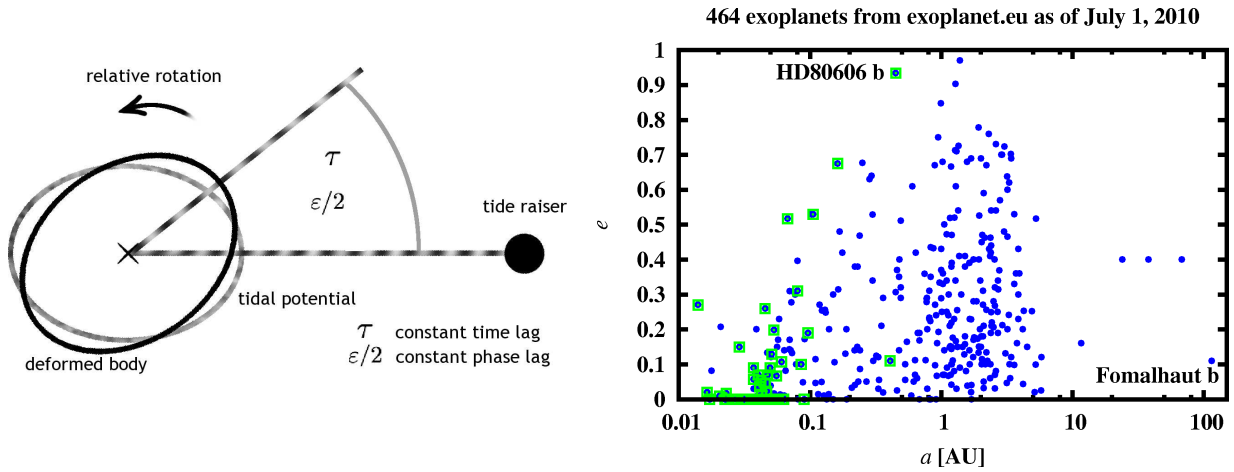
Fig. 2.3: *Left:* Tidal distortion, e.g. of a planetary body. In this sketch, the day of the deformed body is shorter than its year (case B in the text), i.e. the tidal bulge precedes the tidal potential. *Right:* Correlation between eccentricity and semi-major axis of 464 objects from TEPE as of July 9, 2010. Transiting planets are labeled by 87 green squares. For $a < 0.1$ AU there are 85 planets with $e \leq 0.01$ merged in the accumulation of targets at the lower left of the plot.

mass, and only the distortion of one body is considered for the orbital evolution. By switching the role of tide raiser and distorted object and adding both effects, this picture can then be simply applied twice. This approach is justified since only coupling between spin and orbit is relevant and spin-spin coupling is negligible (Hut 1981). In the end, the orbital evolution is given by six equations. In their general form they can be written as

$$\frac{\mathrm{d}a}{\mathrm{d}t} = \frac{\mathrm{d}a}{\mathrm{d}t}\left(a, e, \omega_\mathrm{s}, \omega_\mathrm{p}, \psi_\mathrm{s}, \psi_\mathrm{p}\right) \qquad (2.8a)$$

$$\frac{\mathrm{d}e}{\mathrm{d}t} = \frac{\mathrm{d}e}{\mathrm{d}t}\left(a, e, \omega_\mathrm{s}, \omega_\mathrm{p}, \psi_\mathrm{s}, \psi_\mathrm{p}\right) \qquad (2.8b)$$

$$\frac{\mathrm{d}\omega_i}{\mathrm{d}t} = \frac{\mathrm{d}\omega_i}{\mathrm{d}t}\left(a, e, \omega_i, \psi_i\right) \qquad (2.8c)$$

$$\frac{\mathrm{d}\psi_i}{\mathrm{d}t} = \frac{\mathrm{d}\psi_i}{\mathrm{d}t}\left(a, e, \omega_i, \psi_i\right) \quad , \qquad (2.8d)$$

where the index i can be 's' (for the star) or 'p' (for the planet). Equations (2.8a) - (2.8d) represent a coupled set of differential equations. In Chap. 5 I will present a number of tidal theories that provide different solutions for these equations. In order to simulate the orbital evolution of a two-body system, Eqs. (2.8a) - (2.8d) are integrated numerically. Starting from initial values for a, e, ω_i, and ψ_i, a small but finite time step $\mathrm{d}t$ is used to evaluate $\mathrm{d}a$, $\mathrm{d}e$, $\mathrm{d}\omega_i$, and $\mathrm{d}\psi_i$. These small deviations are then added to the initial values, and

these sums serve as initial values for the next integration step.

2.5 Feedback between structural and orbital evolution

As mentioned above, tidal processes come along with friction inside the bodies involved, leading to energy dissipation of the system. One consequence is tidal heating of the bodies. For gaseous objects, such as giant planets and brown dwarfs (BDs), tidal inflation constitutes another outcome, which results from a transformation of orbital energy into gravitational energy inside the bodies. In Sect. 5.1, where we compute the tidal heating in brown dwarfs, we treat these objects as ideal gases and apply the virial theorem. Hence, we assume that half of the tidal energy flux is converted into heat, while the other half goes into gravitational energy, thus tidal inflation. In addition to a consistent structural treatment, this simplistic approach lacks an evolutionary context.

As reviewed by Pont (2009), tidal processes seem to govern the orbital fate of giant exoplanets in close orbits. In particular, there exists a large sample of planets, which exhibit a radius that is significantly too large compared to predictions from evolutionary models (Ibgui et al. 2010). In the recent decade, various authors have studied the potential of tidal inflation to explain these

bloated radii. A first step towards a realistic description of tidal inflation was presented by Bodenheimer et al. (2001), who computed the tidal inflation of short-period extrasolar planets. However, their approach was not self-consistent because they assumed that tidal heating is constant over the course of the obit. Furthermore, they did not involve a feedback between radial inflation of the planets and a feedback on tidal heating. Since tidal heating of an object is an increasing function of its radius, and since tidal inflation is an increasing function of tidal heating, there will be a constructive interference between both processes until an equilibrium state is reached. For very strong tidal interaction, this feedback might even cause gaseous planets to be disrupted.

Miller et al. (2009) used a more elaborate approach, coupling the structural evolution of Jovian planets with the orbital tidal evolution of the star-planet system. Although they can explain the inflated radii of numerous transiting planets, these planets would require large initial eccentricities and we would need to see them in a very restricted epoch of their evolution. In addition, these authors did not include the possibility of initial planetary obliquities or non-synchronous rotation of the planets, and they used a tidal model, whose equations consider tidal heating only up to second order in e. Ibgui & Burrows (2009) used a similar approach to compute tidal inflation of Jovian planets. They showed that the inflated radii may persists up to a few Gyr, depending on initial conditions.

In none of these studies, however, the authors could consistently reproduce the tidal response of the distorted object, parametrized by a certain tidal dissipation function Q. In fact, their values for Q were fixed at a certain value for a certain model. In reality, the tidal response of an object will depend on its composition and structure.

For terrestrial planets, which are mainly composed of solid compounds rather than gases, tidal heating can be strong enough to drive global volcanism, as observed on the Jovian moon Io. This object is subject to intense tidal distortion from Jupiter. Here, various studies have addressed a coupled evolution of tidal heating an the structural evolution of the moon (Segatz et al. 1988; Fischer & Spohn 1990). On Jupiter's moon Europa, tides are assumed to provide a heat source strong enough for a sub-surface ocean to remain liquid (Greenberg 2005), which might make it a suitable place for life (Greenberg 2010). Another popular example of tidal processes in the Solar System is the Saturn-Enceladus duet. On this moon, tidal heating produces geysers, which seem to be the key source of Saturn's E ring, and it is supposed to maintain a sub-surface ocean below its icy crust (Hansen et al. 2006). Moreover, a variety of terrestrial planets and candidates have been detected over the last few years, such as Gl876 d (Rivera et al. 2005), OGLE-2005-BLG-390L b (Beaulieu et al. 2006), Gl581 c, d, and e (Udry et al. 2007; Mayor et al. 2009a), Gl436 c (Ribas et al. 2008), Gl176 b (Forveille et al. 2009), HD181433 b (Bouchy et al. 2009), HD7924 b (Howard et al. 2009), HD40307 b, c, and d (Mayor et al. 2009b), CoRoT-7 b and c (Léger et al. 2009; Queloz et al. 2009), Gl1214 b (Charbonneau et al. 2009), 61Vir b (Vogt et al. 2010), HD1461 b (Rivera et al. 2010), and 55Cnc e (Dawson & Fabrycky 2010). Since some of them orbit their host stars in close orbits, tidal heating will also play an important role for their structure and evolution (Heller et al. in prep. in Sect. 5.2; Plesa & Breuer 2009; Stamenkovic et al. 2009).

Chapter 3

Brown dwarfs and extrasolar planets

The previous chapter was dedicated to the celestial mechanics and to the gravitational interaction of stellar and sub-stellar objects. But how can one discriminate between these objects? What are the basic physical processes, which define a star, a brown dwarf[1], and a planet? And how can they be explored?

3.1 Formation of sub-stellar objects

At first, it must be stressed that transitions in nature tend to evolve smoothly. Categorization, however, implies discontinuities. Once introduced, these categories – linguistic inventions of humans – can feign the natural, pre-linguistic existence of these categories. The debate about Pluto being a planet or not represents a prominent example for this problem. This bureaucratic, administrative question is neither raised nor answered by an omnipotence, but by humans, who use physical processes in order to categorize. The answer to the question if Pluto is a planet or not, is a working definition, not a law.

Nevertheless, categorizations help to understand the relationships and differences among objects. Their different formation scenarios allows for a discrimination between planets and brown dwarfs. Among planetary bodies, different processes for rocky and gaseous objects are subject to debate. The formation of terrestrial planets is supposed to commence with the microscopic agglomeration of dust particles, which then grows to sizes of meters, embedded in a thin plane around the star (Miguel & Brunini 2010). The runaway growth of planetesimals then leads to the formation of protoplanets (Ida & Makino 1993), while collisions of Mars-sized objects as well as impacts

---

[1]The term 'brown dwarf' for objects below the hydrogen burning limit was introduced by Jill Tarter in her PhD thesis (Tarter 1975).

of such bodies on a terrestrial protoplanet constitute the final formation stage. These encounters explain the former melting of the Earth's crust as well as the formation of the Moon, which probably emerged from the impact of a Mars-sized object on the young Earth (Wetherill 1985).

Besides these cataclysmic encounters, an icy or rocky object with several hundred or thousand km in diameter may also be caught by the gravitational pull of a planet during a fly by. The asteroid-like moons of Mars for example, named Phobos and Deimos, once were trapped in Mars' orbit. Another indicative example is given by Triton, which orbits Neptune in a retrograde sense with respect to the rotation of the planet. The moon may have formed around another planet of a few Earth masses, which then crashed on either Neptune or Uranus, while Triton was captured in Neptune's orbit (Desch & Porter 2010). Traditionally, however, Triton is believed to have formed in the Kuiper belt, far outside Neptune's solar distance. But moons may also form from the accretion disk around giant planets.

These giant planets, meaning planets with masses of the order of magnitude of Jupiter's mass, have conventionally been thought to form via 'core accretion'. At the initial phase of this process, the collisional merging of icy and rocky planetesimals beyond the solar 'snow line' (Sasselov & Lecar 2000) forms solid objects of $\approx$ 10 Earth masses. These dominant-mass objects then drive a concurrent accretion of planetesimals and a gaseous envelope (Pollack et al. 1996). As shown by Boss (2000), this process requires several million years to form Jupiter- and Saturn-like planets from the protoplanetary disk like the solar nebula. However, Uranus and Neptune cannot have formed in situ in their current orbits at 19 and 30 AU, respectively, where accretion rates during the first few million years after the formation of the Sun were much too small (Levison &

Stewart 2001). The 'Nice model', developed by Gomes et al. (2005), Tsiganis et al. (2005), and Morbidelli et al. (2005) – most authors of which were located in Nice at that time – explains the wide orbits of Uranus and Neptune as a consequence of planet-planet scattering among Jupiter, Saturn, Uranus, and Neptune during the first million years after formation of the Solar System.

The discovery of the giant planet 2MASS J04414489+2301513 B (Todorov et al. 2010) indicates a second formation mechanism. This object with a mass between roughly 5 and $10\,M_J$ can hardly have formed by core accretion since its age of a few Myr is much shorter than the time it would have required to form by this mechanism (Lodato et al. 2005). In addition, the recent direct imaging detections of planets around HR8799 (Marois et al. 2008), Fomalhaut (Kalas et al. 2008), and 1RXSJ160929.1−210524 (Lafrenière et al. 2008) and the planet or BD candidates around 2MASSWJ1207334−393254 (Chauvin et al. 2004), AB Pictoris (Chauvin et al. 2005), SCR 1845−6357 (Kasper et al. 2007), GQ Lupi (Neuhäuser et al. 2008), and Gl758 (Thalmann et al. 2009) seem incompatible with the core accretion model for such objects. Alternatively, gravitational instability in protoplanetary disks with masses larger than $0.1\,M_\odot$ can form gas giants within a few hundred years (Boss 2000), making it the favorite formation mechanism for giant planets at orbital distances $\gtrsim 5\,$AU (Dodson-Robinson et al. 2009) and around BDs (Todorov et al. 2010).

There are various formation scenarios for BDs, often labeled as 'failed stars'. The detection of a bipolar jet flowing out from the isolated $24\,M_J$ object 2MASS1207334−393254 with an age of $\approx 8\,$Myr argues for a formation similar to stars, where the fragmentation of large clouds of molecular gas in interstellar space leads to gravitational contraction of the mass and the formation of a gas and dust disk around the center of mass (Lucas et al. 2010). But the formation of BDs and very massive planets can also be initiated by tidal perturbations on the circumstellar disk, when a star passes by (Thies et al. 2010). These encounters lead to fragmentations and gravitational instabilities in the disk, which provide the seeds for local collapses and formation of giant planets and BDs.
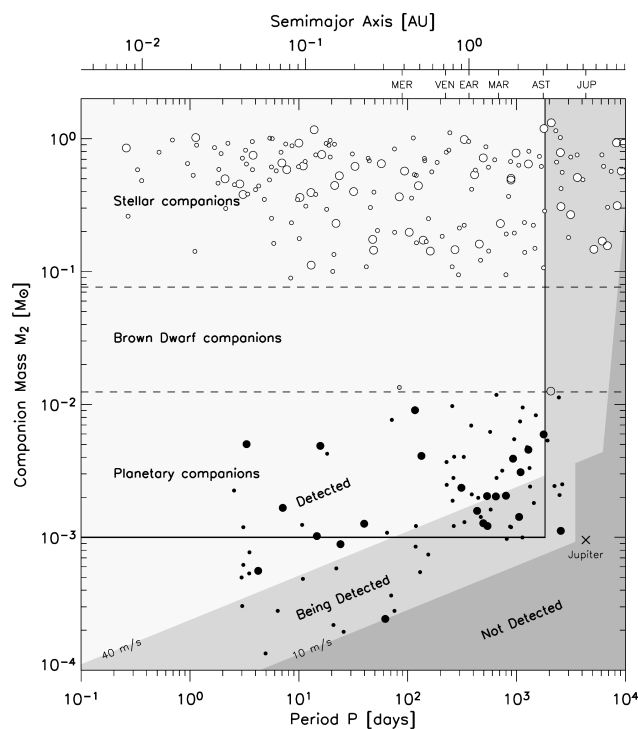

Fig. 3.1: Brown dwarf desert. Shown are the estimated masses and orbital periods of companions to Sun-like stars. Empty circles mark stellar companions, gray circles BDs, and black circles planets. Dashed lines approximate the onset of deuterium and hydrogen burning at $13\,M_J$ and $80\,M_J$, respectively. The rectangle defines the region for $P < 5\,$yr and $M_2 > 10^{-3}\,M_\odot \approx 1\,M_J$. (taken from Grether & Lineweaver 2006)

3.2   The brown dwarf desert

As an irony of history, the first BD candidate HD114762 b (Latham et al. 1989) turned out to be an extrasolar planet some years after publication. At the time of the first announcement, the authors had dissenting opinions about the nature of this object. If they had reported their finding as the detection of an extrasolar planet, they would have advanced empirical exoplanet science for six years. The first widely accepted BD, Gl229 B (Nakajima et al. 1995; Oppenheimer et al. 1995), was announced at the same conference as the first extrasolar planet, orbiting 51 Peg. This anecdote shows, that the categoric boarders between BDs and exoplanets are blurred. It is hard to categorize on the basis of physical characteristics, which are not completely understood. The comprehensive discrimination between BDs and exoplanets remains subject to debate. While internal

processes provide a means for disentanglement of the two species (Sect. 3.3), and different formation scenarios are being discussed (3.1), there is also observational, statistical evidence for different origins of giant planets and BDs.

After five years of BD and exoplanet observations, Marcy & Butler (2000) stated a paucity of sub-stellar companions to stars, as compared to planetary companions and free-floating BDs. They called the span of masses ranging from 5 to 80 M_J, for which stellar companions seemed to be absent in RV surveys sensitive to $P \lesssim 5\,\mathrm{yr}$, the 'brown dwarf desert'. A more recent picture of this scarcely populated mass range is shown in Fig. 3.1, taken from Grether & Lineweaver (2006). This study clearly indicates two distinct mass functions for stellar and sub-stellar companions to a volume-limited sample of Sun-like stars.

The first RV candidate for a BD in the desert was detected by Endl et al. (2004) and the first secure inhabitant of this zone desert is CoRoT-3b (Deleuil et al. 2008). With a mass of $21.66 \pm 1.0\,M_J$ and a radius of $1.01 \pm 0.07\,R_J$, the latter object is particularly interesting since it could either represent the low-mass tail of rare BDs orbiting stars, or it could be a super-massive planet, as predicted by Baraffe et al. (2008).

3.3 Evolution of sub-stellar objects

The distinction between planets and brown dwarfs usually invokes the critical mass required for the ignition of deuterium burning. Depending on the abundance of heavy elements and on the surface gravity (g), this critical mass is simulated to be around $12\,M_J$ (Chabrier & Baraffe 2000). The thermonuclear reaction of deuterium burning describes the fusion of one proton (^1H) and one deuterium particle (^2H) into a helium-3 isotope (^3He) – a process, which releases energy in the form of a gamma quant (γ):

$$^1H + \ ^2H \rightarrow \ ^3He + \gamma \qquad (3.1)$$
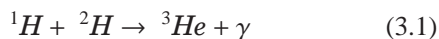
This reaction is not only relevant for BDs but also for very-low-mass stars with masses $\lesssim 0.1\,M_\odot$, and it occurs for central temperatures $\gtrsim 8 \times 10^5\,\mathrm{K}$ (Chabrier & Baraffe 1997). With an initial ^2H mass fraction of 2×10^{-5}, this burning phase lasts less than 1 Myr for a star with a mass $\gtrsim 0.2\,M_\odot$ and almost 20 Myr for a $0.02\,M_\odot$ BD (Ventura &

Zeppieri 1998; Baraffe et al. 2002) – the more massive the object, the faster its ^2H depletion.

For the initial phase of BD and star formation, evolutionary models are uncertain since they depend strongly on the starting conditions (Baraffe et al. 2002). In Fig. 3.2 I show the evolutionary tracks for two BDs in their formation phase. The left panel displays the rapid shrinking of these young objects. In the right panel, it can be seen that during the contraction phase the effective temperatures (T_{eff}, introduced in Stefan 1879; Boltzmann 1884) increase. The slope of the T_{eff} tracks is due to the formation of molecular hydrogen (H_2), which is very sensitive to temperature and pressure. As the brown dwarf cools and gets more compact, i.e. its surface gravity increases, atmospheric pressure increases and more H_2 forms. This favors the onset of convection in the atmosphere, which reaches very small optical depth. Hence, the thermal profile of the atmosphere and thus the H_2 formation undergoes rapid changes. The kinks, as seen in the early-phase T_{eff} evolution, mirror the changes in H_2 abundance at some given T_{eff} and $\log(g)$. Then, after typically 1 Myr, deuterium burning starts, releasing enough nuclear energy to almost stop the contraction and temperature increase untill all deuterium is burned (priv. comm. with Isabelle Baraffe).

Figure 3.3 displays the radial and effective thermal evolution of objects from the planetary, the BD, and the stellar regime, for times between 1 Myr and 10 Gyr after formation. In these simulations of Baraffe et al. (2003), the $75\,M_J$-mass object is massive enough to ignite hydrogen burning, thus it is a star. Thence, it stops shrinking at roughly 1 Gyr, when it reaches the main sequence. A solar-like star would reach the zero-age main sequence in less than 100 Myr. The sub-stellar objects, however, keep on shrinking and cooling for time scales longer than the age of the Universe. This results in the observational selection effect that only young sub-stellar objects can naturally be observed.
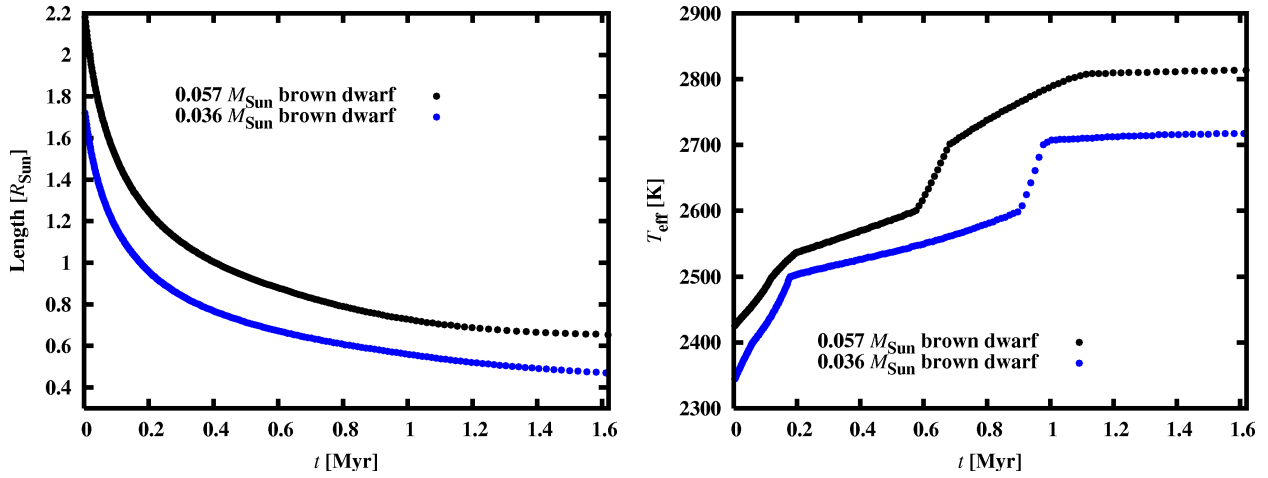
Fig. 3.2: Evolution tracks of young brown dwarfs. These tracks are extremely sensitive to initial conditions of the objects. The masses of the BDs shown here are similar to those of the two constituents of the BD eclipsing binary 2M0535−05, which will be treated in Chap. 5. *Left:* Evolution of brown dwarf radii. *Right:* Evolution of brown dwarf effective temperature. (simulated tables by courtesy of Isabelle Baraffe)

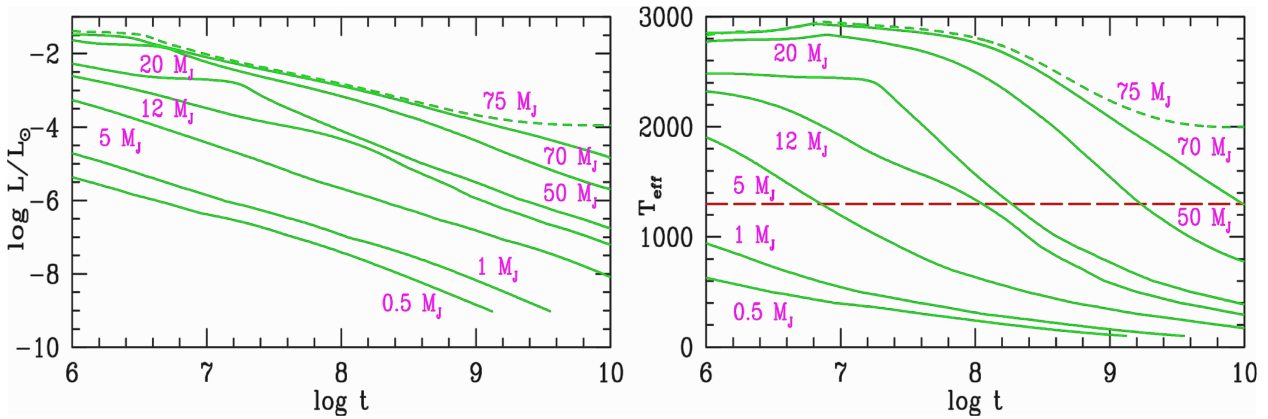Fig. 3.3: Evolution of substellar (solid lines) and stellar (dashed lines) objects (modified from Baraffe et al. 2003). Time t is given in years. *Left:* Luminosity tracks for various planetary and brown dwarfs masses, as well as for a star. *Right:* Effective temperature tracks, in units of Kelvin, for the same set of masses. For temperatures below T_{eff} = 1300 K (dashed line) dust in BD atmospheres settles at lower layers.

Chapter 4

The observational bonanza of transits

Tidal effects, as introduced in Sects. 2.3 - 2.5, are mostly relevant for close orbits. This fact gives the opportunity to investigate those objects, which are subject to significant tidal effects, by the transit method. In close configurations, transits, e.g. of a planet in front of the stellar disk as seen from Earth, are likely to occur. Let e be the orbital eccentricity, R_s and R_p the stellar and the planetary radius, respectively, and ϖ the orientation of the periastron, then the geometric transit probability $\wp_{geo}$, as calculated by Seagroves et al. (2003), can be written as

$$\wp_{geo} \lesssim 0.0045 \, \frac{1 \, \text{AU}}{a} \frac{R_s - R_p}{R_\odot} \frac{1 + e \cos(\pi/2 - \varpi)}{1 - e^2} \quad .$$

(4.1)

Thus, the smaller the semi-major axis and the stronger the impact of tidal heating, the more likely the detection of the stellar companion via the transit method. In Sects. 6.1 and 6.2 we study these and other probabilities, which can be used to compute the detection probabilities of extrasolar transiting planets, as a function of position in the celestial plane.

4.1 Photometry

The exploration of extrasolar planets has blossomed into one of the most rapidly growing fields in science during first decade of the 21st century. The observation of transits constitutes one of the keys to this success. This celestial phenomenon occurs when the exoplanet, as seen from Earth, passes in front of its host star one time per obit. Of course, the so-called 'secondary eclipse', meaning the disappearance of the planet behind the star, can also be observed occasionally. However, these events are very rare and hard to be measured. One way towards a transit detection is offered by systematic photometric observations during one of the two stellar RV minima[1]. If the orbital plane of the transiting object happens to coincide with the observer's line of sight, then the object will block a portion of the stellar surface that is equal to the fraction of its projected area to the stellar disk. If one assumes that the non-irradiated hemisphere of the planet is a totally black circle, this fraction then is equal to R_p^2/R_s^2. Thus, if the radius of the star is known, e.g. if its distance and effective temperature can be estimated or if spectra indicate a star on the main sequence along with a T_{eff} estimate, then the planetary radius can be measured. However easy that reads, there is plenty of effects that complicate the measurements, such as stellar variability (Huber et al. 2009, 2010), limb darkening (Claret 2004), and observational access (Fleming et al. 2008). Moreover, the planetary radius may depend on the wavelength at which it is observed. In Sect. 6.3 we detail which parameters can be deduced from a transit light curve and how.

Although proposals for the observation of such transit events had already been given in the middle of the 20th century (Struve 1952), the first one was partly observed not until the end of the century by Henry et al. (1999) in front of the relatively bright $m_V = 7.65^m$ star HD209458, which was known to host a planet. Based on the ephemeris given by these authors, the full transit light curve could be obtained by Charbonneau et al. (2000). One year after this discovery and famous by now, Brown et al. (2001) published a light curve, which they had obtained with the Hubble Space Telescope (HST). The amazing pre-

---

[1]In the stellar RV curve of a star, which is accompanied by a detectable planet, there are two RV minima. One of them belongs to the planet in inferior conjunction (IC), the other one appears in superior conjunction (SC). Directly before the IC, the star is moving away from the observer and it is moving towards her or him after the transition of the RV minimum, vice versa for the SC. A planetary transit appears in IC, a secondary eclipse in SC.
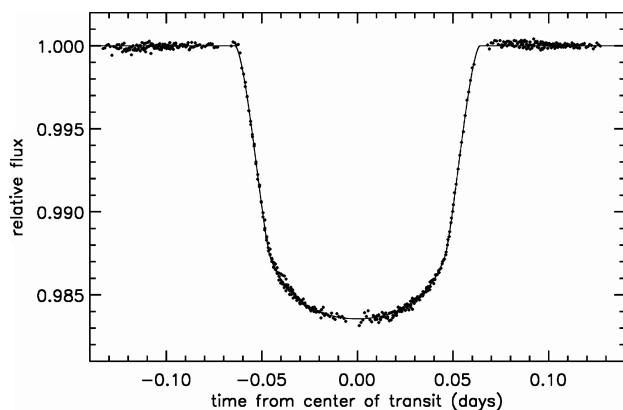
Fig. 4.1: Light curve of the transiting exoplanet HD209458 b. The depth of the curve allows for an estimate of the planetary radius with respect to the stellar radius. The shape of the ingress and egress, as well as the duration and period of the transit provide further insight. (taken from Brown et al. 2001)

cision of these measurements is shown in Fig. 4.1. Aiming at stars, which are known to host planets, is one strategy to detect transits. Another technique, which bases on statistics of a large sample of stars rather than on the selection of single targets, has proven to be very efficient in finding planets. Numerous wide-field, low-budget surveys have been initiated in the past decade and they have revealed a wealth of transiting objects. As of July 9, 2010, there are 87 confirmed planets listed in TEPE. The surveys named XO (5 first detections), Hungarian Automated Telescope Network (HATNet, 16 first detections), and Super Wide Angle Search for Planets (SuperWASP, 25 first detections) have been most fruitful so far. In Sect. 6.1 we present a study of efficiency of these surveys. The planet-hunting instruments of these missions cover a relatively large field of view in the celestial planet, typically a few square degrees, which comprises some thousand stars. Detection software and algorithms are applied to discern the teeny transit dip, usually a percent in depth, from the light intensity of each star.

The launch of the two space-based missions CoRoT, in December 2006, and Kepler, in March 2009, has granted access to high-accuracy, high-cadence data. Outside the Earth's atmosphere, the rapid variations in light intensities and in light distributions on the detector due to scintillation do not occur, crucially improving the data quality. Night and day do also not occur in space, which allows for a continuous coverage of the targets over a long period. Although these mis-

sions have not yet discovered a wealth of exoplanets – there are currently 14 confirmed planets from CoRoT and 5 from Kepler – this picture will change within the next months (Borucki & for the Kepler Team 2010).

4.1.1 Transit dynamics

In addition to the parametrization of the planet and the star, repeated observation of transits provide access to studies of orbital dynamics. As a first step, obstacles that arise from the usage of the terms 'transit center' and 'mid-transit time' need to be removed. The moment when the planet center crosses the center of the star is not generally the same as the mid-point between ingress and egress in the transit light curve Kipping (2008); Kipping et al. (2009). The difference arises from a potential eccentricity of a system. If $e \neq 0$, then the orbital velocities of both the star and the planet will not be constant and thus the planet may enter the stellar disk faster than it leaves it. Hence, the slopes of ingress and egress will differ and the mid-transit time, i.e. the moment when the planet is in the center of the disk, will not be half of the time between ingress and egress.

If a transiting planet is perturbed by another, not necessarily transiting planet, then the gravitational drag of the perturber will induce a shift in the mid-transit time. This shift will display a certain behavior Y in the data, depending on a variety of orbital and physical parameters X of the system. From the mathematical point of view, the study of the transit timing variations (TTVs) is an inverse problem since the independent parameters X of the data $Y = F(X)$, where the function F relates Y to X, need to be found. This situation generates degeneracies in the inverse solutions. Nesvorný & Morbidelli (2008) have applied perturbation theory in order to simulate and fit the observed TTVs of hypothetical systems close to lower-order orbital mean-motion resonances. According to them, more then 20 transit – and ideally also secondary eclipse – observations with high precision are required to get reliable results. As shown by Nesvorný & Beaugé (2010), TTVs provides the – so far – only means to infer the mutual orbital inclination between the orbital plane of the transiting object and the perturber.

Transit duration variations (TDVs) constitute a further dynamical effect on the shape of the light curve. They can be excited by a moon orbiting
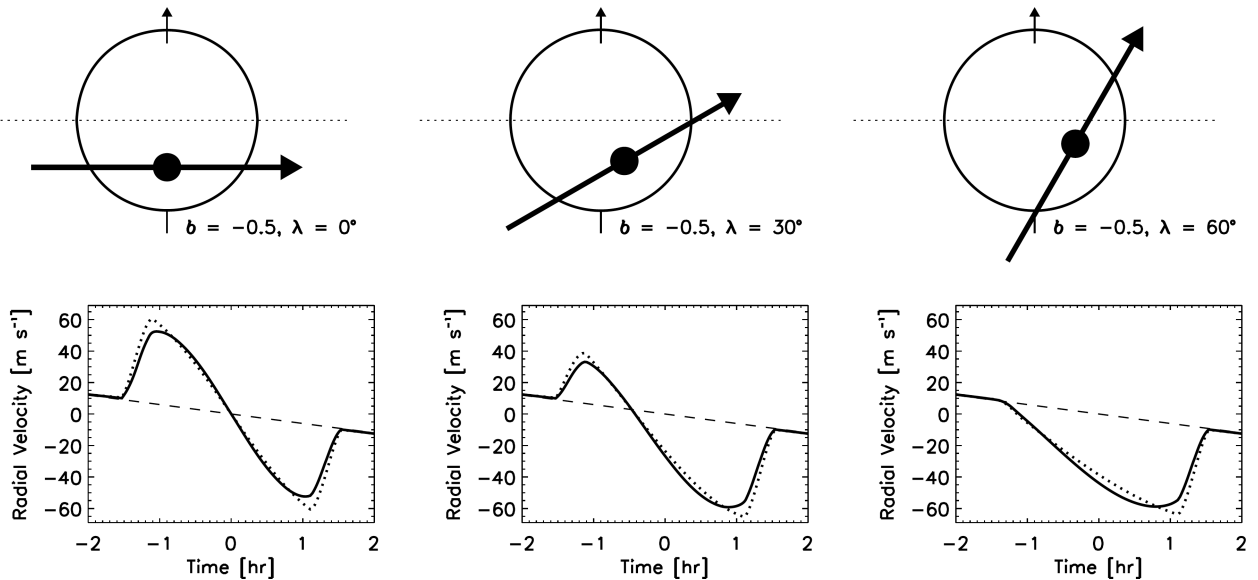
Fig. 4.2: Simulations of the Rossiter-McLaughlin effect. As the path of the planet in front of the stellar disk virtually changes, so does the pseudo radial velocity shift. The cases shown above correspond to planets in prograde orbits. The photometric light curves of all these transits look the same (not shown here). Long-dashed lines indicate the physical RV drift due to the orbital motion of the star. Dotted lines and solid lines indicate different assumptions on the stellar limb darkening. An approximate analytic solution to RM curves has been given by Ohta et al. (2005). (taken from Gaudi & Winn 2007)

the transiting exoplanet. As originally pointed out by Sartoretti & Schneider (1999), TTV measurements alone cannot solve the degeneracy between an exomoon's semi-major axis $a_{e'm.}$ and its mass $M_{e'm.}$. They only allow for the determination of the product $M_{e'm.} \times a_{e'm.}$ via the TTV amplitude. Kipping (2009) could deduce that the TVD amplitude is proportional to $M_{e'm.} \times a_{e'm.}^{-1/2}$ and therefore the ratio of TTV and TDV allows for an independent solution for both the moon's mass and its semi-major axis. In this regard, TTV and TDV measurements are complementary techniques.

The period of the transit may also vary, owing to a phenomenon termed 'light-travel time' (LTT). Originally explained by Woltjer (1922) and explored in more detail by Irwin (1952), this effect on the transit light curve occurs in N-body systems with $N \geq 3$. Assume a 2-body system, represented by transiting planet and its host star, is orbited by a star on a wide orbit. Then the star-planet binary will orbit the common center of gravity with the third body. Occasionally, the transit of the planet will be observed when the tight binary is close to the observer or when it is farther away. The spacial distance between these two configurations will yield a time delay of the transit signals. Then it becomes clear that in the

3-body constellation the effect on the transiting planet gets more significant with increasing semi-major axis of the star-planet binary system in orbit with the 3rd body.

4.2 Spectroscopy

4.2.1 The Rossiter-McLaughlin effect

Even deeper insights into the physics of stars and planets with mutual occultations can be accessed using time-resolved spectroscopy. Far back in time, at the end of the 19th century, astronomers got aware of the fact that the rotation of the Sun induces a broadening of its absorption lines (Abney 1877a,b). And a venturous man even dared to predict that this symmetric broadening would be broken if a stellar binary companion would transit Holt (Holt 1893). Indeed, this effect was observed for the first time about 17 years later by Schlesinger (1910) and again two decades later, independently by Rossiter (Rossiter 1924) and McLaughling (McLaughlin 1924). But there is absolutely no hint in the literature of the prediction of this effect for transiting planets. Of course, these asymmetries would not have been detectable with observational techniques at that

time anyway.

Whoever was the prophet or discoverer of this effect, this pseudo RV shift in the stellar spectrum, mimiced by the transit of a planet in front of the stellar disk, is now commonly termed the 'Rossiter-McLaughlin effect' (RME). Measurements of this effect, caused by planets rather than by stars, have initially been motivated by the detection of the first transiting exoplanet HD 209458 b and an information bulletin by Worek (2000). Indeed, observations of the RME have now been published for 28 of the 87 transiting planets[2] and these measurements have recently caused famous confusion in the exoplanet community. This is why:

The RME allows for measurements of the angle λ_s between the projected spin axis of a star and the projected orbital plane normal of the transiting planet on the celestial plane, as shown in Fig. 4.2. This angle will set a lower limit on the true obliquity ψ_s of the stellar spin axis with respect to the planet's orbital plane. In three spacial dimensions, λ_s and ψ_s are connected via the inclination of the orbit with respect to the observer's line of sight, i, and the inclination of the stellar spin axis with respect to the observer, I_s. Then, as shown by Winn et al. (2005) and Fabrycky & Winn (2009),

$$\cos(\psi_s) = \cos(I_s)\cos(i) + \sin(I_s)\sin(i)\cos(\lambda_s) \quad . \ (4.2)$$

In a press release in April 2010, the SuperWASP consortium announced[3] six new transiting planets and three of which orbit their host star in a retrograde sense, as indicated by RM measurements (Triaud et al. 2010). They sum up all the RM measurements by then, statistically deproject the λ_s distribution into a ψ_s distribution, and conclude that about 4 out of 5 transiting hot Jupiters show obliquities greater than 22°. Interesting enough, their obliquity function matches nicely the prediction of Fabrycky & Tremaine (2007), who applied the coupled effect of tidal processes and the Kozai mechanism to simulate the orbital evolution of exoplanets. These results also indicate that the combined action of tidal processes and the Kozai mechanism produces giant planets in close orbits. May be here is the answer to the question for the origin of hot Jupiters.

---

[2]On www.hs.uni-hamburg.de/EN/Ins/Per/Heller I have installed the 'Holt-Rossiter-McLaughlin Encyclopaedia', which is regularly updated.
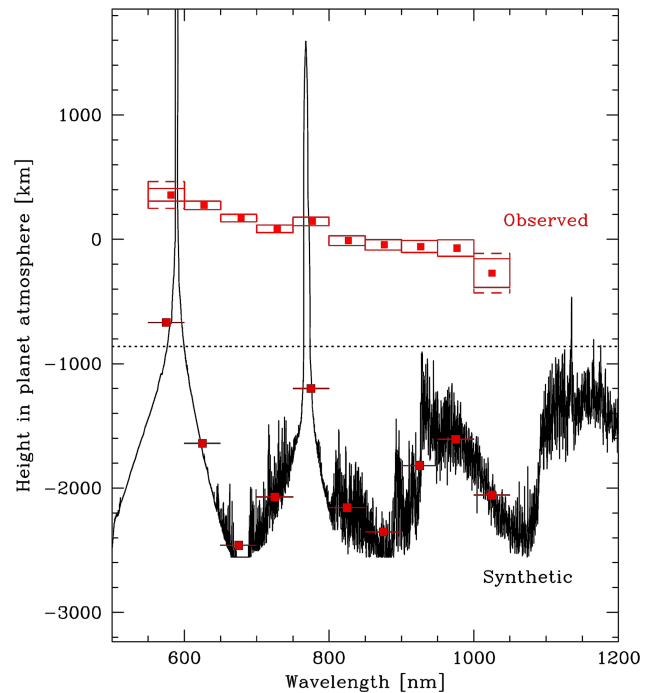
[3]http://www.superwasp.org/publications.htm

Fig. 4.3: Atmospheric transmission spectrum of the transiting exoplanet HD 198733 b. The abscissa denotes a conversion of the transmission spectrum into a scale for the wavelength-dependent transit radius, relative to an arbitrary reference level. Red data points are centered in 50 nm bins. Boxes indicate the bin width horizontally and the photon noise vertically. The black line is the synthetic spectrum from Tinetti et al. (2007) with symbols indicating 50 nm bins analog to the observed ones. (taken from Pont et al. 2008)

4.2.2   Transit spectroscopy

Further prospects for transit observations arise from transmission or transit spectroscopy. This method derives advantage of the wavelength-dependent opacities in the planet's atmosphere, which obscure the transmitted stellar light at different planet radii. During the primary transit, this leads to a wavelength-dependent depth of the light curve. Thus, the detection of relative changes in eclipse depth as a function of wavelength gives insight in the absorption properties of the planet's atmosphere, permitting the confirmation or exclusion of specific chemical species.

The first secure detection of a chemical element in the atmosphere of an exoplanet was presented by Charbonneau et al. (2002), who used the Space Telescope Imaging Spectrograph (STIS) on board the HST to measure the wavelength-dependent

radius of the the transiting planet HD209458 b. They compared the transit depth in a band centered around the Na D lines at 589.3 nm with the average of the flanking bands as a function of time. The Na D dimming could be constrained to be about $2.32 \pm 0.57 \times 10^{-4}$ times deeper than the simultaneous observations of the adjacent bands. Vidal-Madjar et al. (2003) were able to verify escaping hydrogen from HD209458 b by measurements of the Lyman α emission line of the star in the ultra-violet part of the spectrum, at roughly 121.567 nm, with STIS. And one year later, they even announced the detection of oxygen and carbon on HD209458 b (Vidal-Madjar et al. 2004). Moreover, Barman (2007) published results on the detection of water absorption and Richardson et al. (2007) claimed the detection of silicate clouds due to a broad emission peak in the infrared spectrum near 9.65 μm. In a recent article, (Swain et al. 2009) even reported the detection of water, methane, and carbon dioxide in the dayside spectrum of HD209458 b using Hubble's Near Infrared Camera and Multi-Object Spectrometer (NICMOS).

Another very prominent transit target is the exoplanet HD189733 b, orbiting the second brightest transit planet host star with $m_{\mathrm{V}} = 7.67^{\mathrm{m}}$. Measurements of the wavelength-dependent radius at 3.6 μm, 5.8 μm, and 8 μm with the Spitzer Space Telescope Infrared Array Camera (IRAC) revealed that the atmosphere of this planet is rich in water vapour (Tinetti et al. 2007). The data of the 8 μm chanel had already been used by Knutson et al. (2007) to generate a temperature map of the planet. It showed that that hottest spot on the planet is not the sub-stellar point, a fact which can be attributed to strong winds on the planet. Pont et al. (2008) announced the detection of atmospheric haze, based on 675 spectra taken with the Advanced Camera for Surveys (ACA) of the HST. They find that the transmission spectrum is almost featureless, although models suggest strong absorption features due to sodium, potassium, and water. Condensates and clouds, i.e. haze, are called to account for the flat shape of the spectrum. Figure 4.3 shows their data from 600 to 1000 nm, and a comparison to a model spectrum, which is binned to the same of 50 nm ranges as the observations to ease comparison.

Part II

Publications

Chapter 5

Tidal effects on brown dwarfs and extrasolar planets

5.1 Tidal effects on brown dwarfs: application to the eclipsing binary 2MASSJ05352184−0546085

The anomalous temperature reversal in the context of tidal heating

R. Heller, B. Jackson, R. Barnes, R. Greenberg, and D. Homeier

For this study, I adapted the sets of equations of four different tidal models to compute the tidal heating rates and the temperature increase of two BDs in an eclipsing binary system. On the one hand, this approach would allow for a comparison of these established tidal models. On the other hand, we would estimate if tidal heating could be responsible for the observed $T_{\rm eff}$ reversal: the more massive BD (the primary) is cooler than the secondary. One result of this study is the first estimate of the tidal dissipation functions for BDs: $(Q_{\rm BD}) \gtrsim 4.5$. This application of four different tidal theories was inspired by a visit at the Lunar and Planetary Laboratory in Tucson, Arizona, in Dec. 2008.

In addition to the mathematical arrangements, I developed a computer code, written in the programming language 'python', to calculate the tidal heating rates and the orbital evolution of this sub-stellar duet binary. During the numerical integration, the set of differential equations was not coupled, which merely yields a rough – to be more harsh: inconsistent – estimate of the system's orbital evolution. My customizations of another python code, which was originally written by staff members of the Institut für Astrophysik in Göttingen, enabled me to simulate the Rossiter-McLaughlin effect for this binary. After all, I have produced all the figures in this paper and I have written the manuscript.

This work was also presented at the Annual Fall Meeting of the Astronomische Gesellschaft (Germany) on Sept. 22, 2009 in Potsdam, as well as in a seminar talk at the Deutsches Zentrum für Luft- und Raumfahrt in Berlin on June 8, 2010.

Astronomy & Astrophysics

Tidal effects on brown dwarfs: application to the eclipsing binary 2MASS J05352184-0546085

The anomalous temperature reversal in the context of tidal heating

R. Heller[1], B. Jackson[2], R. Barnes[3,4], R. Greenberg[5], and D. Homeier[6]

[1] Hamburger Sternwarte (Universität Hamburg), Gojenbergsweg 112, 21029 Hamburg, Germany
    e-mail: rheller@hs.uni-hamburg.de
[2] Lunar and Planetary Laboratory, University of Arizona, Tucson, AZ 85721, USA
    e-mail: bjackson@lpl.arizona.edu
[3] University of Washington, Dept. of Astronomy, Seattle, WA 98195, USA
[4] Virtual Planetary Laboratory, NASA, USA
    e-mail: rory@astro.washington.edu
[5] Lunar and Planetary Laboratory, University of Arizona, Tucson, AZ 85721, USA
    e-mail: greenber@lpl.arizona.edu
[6] Institut für Astrophysik, Georg-August-Universität Göttingen, Friedrich-Hund-Platz 1, 37077 Göttingen, Germany
    e-mail: derek@astro.physik.uni-goettingen.de

ABSTRACT

Context. 2MASS J05352184−0546085 (2M0535−05) is the only known eclipsing brown dwarf (BD) binary, and so may serve as a benchmark for models of BD formation and evolution. However, theoretical predictions of the system's properties seem inconsistent with observations: i) the more massive (primary) component is observed to be cooler than the less massive (secondary) one; ii) the secondary is more luminous (by $\approx 10^{24}$ W) than expected. Previous explanations for the temperature reversal have invoked reduced convective efficiency in the structure of the primary, connected to magnetic activity and to surface spots, but these explanations cannot account for the enhanced luminosity of the secondary. Previous studies also considered the possibility that the secondary is younger than the primary.
Aims. We study the impact of tidal heating to the energy budget of both components to determine if it can account for the observed temperature reversal and the high luminosity of the secondary. We also compare various plausible tidal models to determine a range of predicted properties.
Methods. We apply two versions of two different, well-known models for tidal interaction, respectively: i) the "constant-phase-lag" model; and ii) the "constant-time-lag" model and incorporate the predicted tidal heating into a model of BD structure. The four models differ in their assumptions about the rotational behavior of the bodies, the system's eccentricity and putative misalignments ψ between the bodies' equatorial planes and the orbital plane of the system.
Results. The contribution of heat from tides in 2M0535−05 alone may only be large enough to account for the discrepancies between observation and theory in an unlikely region of the parameter space. The tidal quality factor Q_{BD} of BDs would have to be $10^{3.5}$ and the secondary needs a spin-orbit misalignment of $\gtrsim 50°$. However, tidal synchronization time scales for 2M0535−05 restrict the tidal dissipation function to $\log(Q_{BD}) \gtrsim 4.5$ and rule out intense tidal heating in 2M0535−05. We provide the first constraint on Q for BDs.
Conclusions. Tidal heating alone is unlikely to be responsible for the surprising temperature reversal within 2M0535−05. But an evolutionary embedment of tidal effects and a coupled treatment with the structural evolution of the BDs is necessary to corroborate or refute this result. The heating could have slowed down the BDs' shrinking and cooling processes after the birth of the system ≈ 1 Myr ago, leading to a feedback between tidal inflation and tidal heating. Observations of old BD binaries and measurements of the Rossiter-McLaughlin effect for 2M0535−05 can provide further constraints on Q_{BD}.

Key words. celestial mechanics – binaries: eclipsing – stars: evolution – stars: individual: 2MASSJ05352184−0546085 – brown dwarfs

1. Introduction

2MASS J05352184−0546085 (2M0535−05) is a benchmark object for brown dwarf (BD) science since it offers the rare opportunity of independent radius and mass measurements on substellar objects. The observed values constrain evolutionary and structural models (D'Antona & Mazzitelli 1997; Baraffe et al. 1998; Chabrier & Baraffe 2000; Baraffe et al. 2002; Chabrier et al. 2007). 2M0535−05 is located in the Orion Nebulae,

a star-forming region with an age of 1 (±0.5) Myr. If both components formed together, as commonly believed, then this system allows for effective temperature (T_{eff}) and luminosity (L) measurements of two BDs at the same age.

However, this system is observed to have an unexpected temperature reversal (Stassun et al. 2006), contravening theoretical simulations: the more massive component (the primary) is the cooler one. From the transit light curve, the ratio of the effective temperatures can be accurately determined to

$T_{\text{eff},2}/T_{\text{eff},1}$ = 1.050 ± 0.002 (Mohanty et al. 2009; Gómez Maqueo Chew et al. 2009). From spectroscopic measurements then, the absolute values can be constrained. The primary, predicted to have $T_{\text{eff},1} \approx 2870$ K (Baraffe et al. 1998), has an observed value of ≈2700 K, whereas the surface temperature of the secondary, predicted to be $T_{\text{eff},2} \approx 2750$ K, is most compatible with $T_{\text{eff},2} \approx 2890$ K.

One explanation for the temperature discrepancies is suppression of convection due to spots on the surface of the primary. If a portion of a BD's surface is covered by spots, its apparent temperature will be reduced, resulting in an increase in the estimated radius in order for the measured and expected luminosities to agree (Chabrier et al. 2007). With a spot coverage of 30–50% and a mixing length parameter $\alpha = 1$ most of the mismatches between predicted and observed radii for low-mass stars (LMS) can be explained (Ribas et al. 2008). Observations of spots on both of the 2M0535−05 components (Gómez Maqueo Chew et al. 2009), as inferred from periodic variations in the light curve, and measurements on the H_α line of the combined spectrum during the radial velocity maxima (Reiners et al. 2007) suggest that enhanced magnetic activity and the accompanying spots on the primary indeed play a key role for its temperature deviation. But even if the spot coverage on the primary serves as an explanation for the primary's reduced T_{eff}, the secondary's luminosity overshoot of ≈2.3 × 10²⁴ W, as compared to the Baraffe et al. (1998) models, suggests some additional processes may be at work.

The temperature reversal between the primary and secondary may result from a difference between their ages. The secondary could be ≈0.5 Myr older than the primary, as proposed by Stassun et al. 2007 (see also D'Antona & Mazzitelli 1997). A difference of 0.5 Myr could allow the secondary to have converted the necessary amount of gravitational energy into heat[1], which would explain its luminosity excess. But evolutionary models are very uncertain for ages ≲1 Myr (Baraffe et al. 2002; Wuchterl 2005; Marley et al. 2007; Mohanty et al. 2007) and, in any case, the age determination and physical nature of these very young objects is subject to debate (Stassun et al. 2008, 2009). Furthermore, the mutual capture of BDs and LMS into binary systems after each component formed independently is probably too infrequent to account for the large number of eclipsing LMS binaries with either temperature reversals or inflated radii (Guenther et al. 2001; Coughlin & Shaw 2007; Ribas et al. 2008; Çakırlı et al. 2009; Morales et al. 2009).

Here, we consider the role that tidal heating may play in determining the temperatures of the BDs. In Table 1 we show the parameters of 2M0535−05 necessary for our calculations. The computed energy rates will add to the luminosity of the BDs in some way (Sect. 2.3) and will contribute to a temperature deviation compared to the case without a perturbing body (Sect. 3). All these energy rates must be seen in the context of the luminosities of the BDs: $L_1 \approx 8.9 \times 10^{24}$ W (luminosity of the primary) and $L_2 \approx 6.6 \times 10^{24}$ W (luminosity of the secondary). At a distance a to the primary component, its luminosity is distributed onto a sphere with area $4\pi a^2$. The secondary has an effective – i.e. a 2D-projected – area of πR_2^2. With $F_{1,a}$ as the flux of the primary at distance a, the irradiation from the primary onto the secondary $L_{1\to2}$ is thus given by

$$L_{1\to2} = \pi R_2^2 F_{1,a} = \pi R_2^2 \frac{L_1}{4\pi a^2} = L_1 \frac{R_2^2}{4 a^2} . \quad (1)$$

---

[1] In contrast to the Baraffe et al. (1998) tracks, the models by D'Antona & Mazzitelli (1997) predict a temperature increase in BDs for the first ≈30 Myr of their existence.

Table 1. Orbital and physical parameters of 2M0535-05.

PROPERTY	OBSERVED VALUE
a, semi-major axis[1]	0.0407 ± 0.0008 AU
e, eccentricity[1]	0.3216 ± 0.0019
P_{orb}, orbital period[1]	9.779556 ± 0.000019 d
i, orbital inclination to the line of sight[1]	88.49 ± 0.06°
age[1]	1 ± 0.5 Myr
$T_{\text{eff},1}$, primary effective temperature[1]	2715 ± 100 K
$T_{\text{eff},2}/T_{\text{eff},1}$, effective temperature ratio[1]	1.050 ± 0.002
M_1, primary mass[1]	0.0572 ± 0.0033 $M_\odot$
M_2, secondary mass[1]	0.0366 ± 0.0022 $M_\odot$
R_1, primary radius[1]	0.690 ± 0.011 $R_\odot$
R_2, secondary radius[1]	0.540 ± 0.009 $R_\odot$
L_1, primary luminosity[3]	8.9 × 10²⁴ ± 3 × 10²⁴ W
L_2, secondary luminosity[3]	6.6 × 10²⁴ ± 2 × 10²⁴ W
P_1, rotational period of the primary[1]	3.293 ±0.001 d
P_2, rotational period of the secondary[1]	14.05 ±0.05 d
$\bar{T}_{\text{eff},1}$, modeled T_{eff} for the primary[2]	2850 K
$\bar{T}_{\text{eff},2}$, modeled T_{eff} for the secondary[2]	2700 K
$\bar{R}_1$, modeled radius for the primary[2]	0.626 $R_\odot$
$\bar{R}_2$, modeled radius for the secondary[2]	0.44 $R_\odot$

Notes. [1] Gómez Maqueo Chew et al. (2009). [2] Baraffe et al. (1998). [3] Assuming an uncertainty of 200 K in $T_{\text{eff},1}$ and $T_{\text{eff},2}$.

Using that equation, we calculate the mutual irradiation of the BDs: $L_{1\to2} \approx 8.5 \times 10^{21}$ W and $L_{2\to1} \approx 1.0 \times 10^{22}$ W. These energy rates are two and three orders of magnitude lower, respectively, than the observed luminosity discrepancy. Hence, we assume that mutual irradiation can be ignored. This simplification is in contrast to the cases of the potentially inflated transiting extrasolar planets WASP-4b, WASP-6b, WASP-12b, and TrES-4, where stellar irradiation (Ibgui et al. 2010) dominates tidal heating by several magnitudes.

Various tidal models haven been used to calculate tidal heating in exoplanets (Bodenheimer et al. 2001; Jackson et al. 2008a,b; Barnes et al. 2009), which may in fact be responsible for previous discrepancies between interior models and radii of transiting exoplanets (Jackson et al. 2008a,b; Ibgui & Burrows 2009). This success in exoplanets motivates our investigation into BDs. While many different tidal models are available, there is no consensus as to which is the best. For this reason, we apply a potpourri of well-established models to the case of 2M0535−05 in order to compare the different results. As we show, tidal heating may account for the temperature reversal and it may have a profound effect on the longer-term thermal evolution of the system.

The coincidence of $P_{\text{orb}}/P_1 \approx 2.9698 \approx 3$, with P_{orb} as the orbital and P_1 primary's rotation period, has been noted before but we assume no resonance between the primary's rotation and the orbit for our calculations. These resonances typically occur in systems with rigid bodies where a fixed deformation of at least one body persists, such as in the Sun-Mercury configuration with Mercury trapped in a 3/2 spin-orbit resonance. We assume that, in the context of tides, BDs may rather be treated as fluids and the shape of the body is not fixed.

With this paper, we present the first investigation of tidal interaction between BDs. In Sect. 2 we introduce four models for tidal interaction and discuss how we convert the computed

R. Heller et al.: Tidal effects on brown dwarfs: application to 2M0535−05

energy rates into an increase in effective temperature. Section 3 is devoted to the results of our calculations, while we deal with the observational implications in Sect. 4. We end with conclusions about tidal heating in 2M0535−05, and in BDs in general, in Sect. 5.

2. Tidal models

Two qualitatively different models of tidal dissipation and evolution have been developed over the last century: The "constant-phase-lag" (Goldreich & Soter 1966; Wisdom 2008; Ferraz-Mello et al. 2008, Wis08 and FM08 in the following), and the "constant-time-lag" model (Hut 1981, Hut81 in the following). In the former model, the forces acting on the deformed body are described by a superposition of a static equilibrium potential and a disturbing potential (FM08). The latter model assumes the time between the passage of the perturbing body overhead and the passage of the tidal bulge is constant. Although both models have been used extensively, it is not clear which model provides a more accurate description of the effects of tides, so we apply formulations of both models.

In the "constant-phase-lag" model of FM08, quantitative expressions have been developed to second order in eccentricity e while the others include also higher orders. Higher and higher order expansions require assumptions about the dependence of a body's tidal response to an increasing number of tidal frequencies, which involves considerable uncertainty. Therefore higher order expansions do not necessarily provide more accuracy (FM08; Greenberg 2009). In the "constant-phase-lag" model of Wis08, expressions in e are developed to 8th order. The "constant-time-lag" model of Hut81 does not include possible obliquities, while an enhanced version of that model by Levrard et al. (2007) (Lev07) does.

Tidal dissipation in BDs has not been observed or even considered previously, and hence, neither model should take precedence when calculating their tidal dissipation, especially since neither tidal model is definitive (Greenberg 2009). As our investigation is the first to consider tidal effects on BDs, we will employ several applicable, previously published models to 2M0535−05. By surveying a range of plausible models and internal properties, usually encapsulated in the "tidal dissipation function" Q (Goldreich & Soter 1966), we may actually be able to determine which model is more applicable to the case of BDs – assuming, of course, that tidal dissipation contributes crucially to the observed temperature inversion.

2.1. Constant phase lag

2.1.1. Tidal model #1

The potential of the perturbed body can be treated as the superposition of periodic contributions of tidal frequencies at different phase lags and the expression for the potential can be expanded to first order in those lags (FM08). Those phase lags $\varepsilon_{k,i \,|\, k=0,1,2,5,8,9}$ of the ith body that we will need for our equations are given by

$$Q_i\,\varepsilon_{0,i} = \Sigma(2\Omega_i - 2n)$$
$$Q_i\,\varepsilon_{1,i} = \Sigma(2\Omega_i - 3n)$$
$$Q_i\,\varepsilon_{2,i} = \Sigma(2\Omega_i - n)$$
$$Q_i\,\varepsilon_{5,i} = \Sigma(n)$$
$$Q_i\,\varepsilon_{8,i} = \Sigma(\Omega_i - 2n)$$
$$Q_i\,\varepsilon_{9,i} = \Sigma(\Omega_i) \qquad i \in \{1,2\}, \qquad (2)$$

where $\Sigma(x)$ is the algebraic sign of x, thus $\Sigma(x) = +1 \vee -1$, $n = 2\pi/P_{\rm orb}$ is the orbital frequency and $\Omega_i = 2\pi/P_i$ are the rotational frequencies of the primary ($i = 1$) and secondary ($i = 2$), P_i being their rotational periods. The tidal frequencies are functions of the tidal quality factor Q of the deformed object, which parametrizes the object's tidal response to the perturber. It is defined as

$$Q^{-1} = \frac{1}{2\pi E_0} \int_0^{P_{\rm orb}} {\rm d}t \left(-\frac{{\rm d}E}{{\rm d}t}\right), \qquad (3)$$

where E_0 is the maximum energy stored in the tidal distortion and the integral over the energy dissipation rate $-{\rm d}E/{\rm d}t$ is the energy lost during one orbital cycle (Goldreich & Soter 1966). Although Ogilvie & Lin (2004) conclude that tidal dissipation rates of giant planets are not adequately represented by a constant Q-value, many parameterized tidal models rely on this quantity. Measurements of the heat flux from Jupiter's moon Io during the fly-by of the Voyager 1 spacecraft, combined with a specific model of the history of the orbital resonance, allowed for an estimate for the quality factor $Q_{\jupiter}$ of Jupiter to be $2\times10^5 < Q_{\jupiter} < 2\times10^6$ (Yoder 1979) while Aksnes & Franklin (2001) used historical changes in Io's orbit to infer that $Q_{\jupiter}$ is around $10^{5.3}$. However, Greenberg et al. (2008) pointed out that $Q = \infty$ is not ruled out (see also Peale & Greenberg 1980; Ioannou & Lindzen 1993). Tides raised by Neptune on its moons help to constrain the planet's quality factor to $10^{3.95} < Q_{\neptune} < 10^{4.56}$ (Zhang & Hamilton 2008). For M dwarfs, $Q_{\rm dM}$ is assumed to be of order 10^5, whereas for rigid bodies like Earth $20 \lesssim Q \lesssim 500$ (Ray et al. 2001; Mardling & Lin 2004, and references therein). For BDs, however, Q is even more uncertain, thus we will handle it as a free parameter in our procedures.

FM08 allows for the tidal amplitude to be different from what it would be if the tide-raising body were fixed in space. This concern is met by the dynamical Love number $k_{\rm d}$ under the assumption that the tidally disturbed body had infinite time to respond. Without better knowledge of a body's response to tides, we assume the dynamical Love number is the same as the potential Love number of degree 2, k_2. For the gas planets of the solar system, this number has been calculated by Gavrilov & Zharkov (1977). BDs may rather be treated as polytropes of order $\mathfrak{n} = 3/2$ (Baraffe, private communication). We infer the Love number from the relation $k_2 = 2k_{\rm aps}$ (Mardling & Lin 2002) and use the tables of apsidal motion constants $k_{\rm aps}$ given in Brooker & Olle (1955). These authors provide numerical calculations for $k_{\rm aps}$ for a polytrope of $\mathfrak{n} = 3/2$. We find $k_{\rm aps} = 0.143$ and thus $k_{\rm d} \equiv k_2 = 0.286$. This places k_2 for BDs well in the regime spanned by the gas giants of the solar system: Jupiter ($k_2 = 0.379$), Saturn ($k_2 = 0.341$), Uranus ($k_2 = 0.104$) and Neptune ($k_2 = 0.127$) (Gavrilov & Zharkov 1977).

Before we proceed to the equations for the tidal heating rates, we sum up those for the orbital evolution of the semi-major axis a, the eccentricity e and the putative obliquity ψ. The latter parameter is the angle between the equatorial plane of one of the two bodies in a binary system and the orbital plane (Winn et al. 2005), frequently referred to as spin-orbit misalignment. We use Eqs. (56), (60) and (61) from FM08 but our equations for a binary system with comparable masses need slight modifications since both constituents contribute significantly to the evolution of a and e. We add both the terms for the secondary being the perturber of the primary ($i = 1$, $j = 2$) and vice versa, since only

spin-orbit coupling is relevant, whereas spin-spin interaction can be neglected. This results in

$$\frac{\mathrm{d}a}{\mathrm{d}t} = \sum_{\substack{i=1,2\\i \neq j}} \frac{3k_{\mathrm{d},i}M_j R_i^5 n}{4M_i a^4}(4\varepsilon_{0,i}+e^2\Big[-20\varepsilon_{0,i}+\frac{147}{2}\varepsilon_{1,i}+\frac{1}{2}\varepsilon_{2,i} \quad (4)$$

$$-3\varepsilon_{5,i}\Big]-4S_i^2[\varepsilon_{0,i}-\varepsilon_{8,i}]), \quad (5)$$

$$\frac{\mathrm{d}e}{\mathrm{d}t} = -\sum_{i=1,2 i\neq j} \frac{3ek_{\mathrm{d},i}M_j R_i^5 n}{8M_i a^5}\left(2\varepsilon_{0,i}-\frac{49}{2}\varepsilon_{1,i}+\frac{1}{2}\varepsilon_{2,i}+3\varepsilon_{5,i}\right), \quad (6)$$

$$\frac{\mathrm{d}\psi_i}{\mathrm{d}t} = \frac{3k_{\mathrm{d},i}M_j R_i^5 n}{4M_i a^5}\, S_i\,(-\varepsilon_{0,i}+\varepsilon_{8,i}+-\varepsilon_{9,i}), \quad (7)$$

where $k_{\mathrm{d},i}$ is the dynamical Love number, M_i the mass and R_i the radius of the deformed BD, $S_i := \sin(\psi_i)$, with ψ_i as the obliquity of the perturbed body, and $\varepsilon_{k,i\,|\,k=0,1,2,5,8,9}$ are the tidal phase lags, given in Eq. (2).

The total energy that is dissipated within the perturbed body, its tidal energy rate, can be determined by summing the work done by tidal torques (Eqs. (48) and (49) in FM08). The change in orbital energy of the ith body due to the jth body is given by

$$\dot{E}_{\mathrm{orb},i}^{\#1} = \underbrace{\frac{3k_{\mathrm{d},i}GM_j^2 R_i^5}{8a^6}}_{p} n(4\varepsilon_{0,i}+e^2[-20\varepsilon_{0,i}+\frac{147}{2}\varepsilon_{1,i}+\frac{1}{2}\varepsilon_{2,i}$$

$$-\;3\varepsilon_{5,i}]-4S_i^2[\varepsilon_{0,i}-\varepsilon_{8,i}]) \quad (8)$$

and the change in rotational energy is deduced to be

$$\dot{E}_{\mathrm{rot},i}^{\#1} = -\frac{3k_{\mathrm{d},i}GM_j^2 R_i^5}{8a^6}\Omega_i(4\varepsilon_{0,i}+e^2[-20\varepsilon_{0,i}+49\varepsilon_{1,i}+\varepsilon_{2,i}]$$

$$+\;2S_i^2\,[-2\varepsilon_{0,i}+\varepsilon_{8,i}+\varepsilon_{9,i}]), \quad (9)$$

where G is Newton's gravitational constant. The total energy released inside the body then is

$$\dot{E}_{\mathrm{tid},i}^{\#1} = -(\dot{E}_{\mathrm{orb},i}^{\#1}+\dot{E}_{\mathrm{rot},i}^{\#1}) > 0. \quad (10)$$

The greater-than sign in this equation is true, since either $\Omega_i < n$ and orbital energy is converted into rotational energy, or $\Omega_i > n$ and the body is decelerated by a transfer of rotational energy into orbital energy. In both cases, the dynamical energy of the system is released within the distorted body. For $\Omega_i = 0$, e.g., Eqs. (8) and (9) yield $\dot{E}_{\mathrm{orb},i}^{\#1} = -p \cdot (4+57e^2+4S_i^2)/Q_i$ and $\dot{E}_{\mathrm{rot},i}^{\#1} = 0$.

The approach for the calculation of tidal energy rates with tidal model #1 depends on processes due to non-synchronous rotation via $\varepsilon_{k,i} = \varepsilon_{k,i}(\Omega_i, n)$ and includes a putative obliquity ψ_i and terms of e up to the second order. After inserting the orbital and rotational periods for 2M0535−05, these equations reduce to

$$\dot{E}_{\mathrm{tid},1}^{\#1} = \frac{3k_{\mathrm{d},1}GM_2^2 R_1^5}{8Q_1 a^6}\left([4+30e^2]\Omega_1-[4+51e^2]n\right),$$

$$\dot{E}_{\mathrm{tid},2}^{\#1} = \frac{3k_{\mathrm{d},2}GM_1^2 R_2^5}{8Q_2 a^6}\left([4+56e^2]n+[2S_2^2-4-28e^2]\Omega_2\right). \quad (11)$$

Interestingly, for these particular values of Ω_1, Ω_2 and n, the S_1-terms for $\dot{E}_{\mathrm{tid},1}^{\#1}$ cancel each other, so that it is not a function of ψ_1, whereas $\dot{E}_{\mathrm{tid},2}^{\#1}$ does depend on ψ_2.

2.1.2. Tidal model #2

The model of Wis08 includes terms in eccentricity up to the 8th order, predicting higher tidal energy rates than for the equations of model #1. Equations for the evolution of the orbital parameters are not given in Wis08. Furthermore, in his theory the perturbed body is assumed to be synchronously rotating with the orbital period. Since this is not the case for either of the BDs in 2M0535−05, the following equations will only yield lower limits for the tidal heating. The tidal heating rates are given by

$$\dot{E}_{\mathrm{tid},i}^{\#2} = \frac{21k_{2,i}GM_j^2 R_i^5 n}{2Q_i a^6}\zeta_{\mathrm{Wis}}(e,\psi_i) \quad (12)$$

with

$$\zeta_{\mathrm{Wis}}(e,\psi_i) = \frac{2}{7}\frac{f_1^{\mathrm{Hut}}}{\beta^{15}}-\frac{4}{7}\frac{f_2^{\mathrm{Hut}}}{\beta^{12}}C_i+\frac{1}{7}\frac{f_5^{\mathrm{Hut}}}{\beta^9}\left(1+C_i^2\right)$$

$$+\;\frac{3}{14}\frac{e^2 f_3^{\mathrm{Wis}}}{\beta^{13}}\,S_i^2\cos(2\Lambda_i), \quad (13)$$

where we used $C_i := \cos(\psi_i)$ and

$$\beta = \sqrt{1-e^2},$$

$$f_1^{\mathrm{Hut}} = 1+\frac{31}{2}e^2+\frac{255}{8}e^4+\frac{185}{16}e^6+\frac{25}{64}e^8,$$

$$f_2^{\mathrm{Hut}} = 1+\frac{15}{2}e^2+\frac{45}{8}e^4+\frac{5}{16}e^6,$$

$$f_5^{\mathrm{Hut}} = 1+3e^2+\frac{3}{8}e^4,$$

$$f_3^{\mathrm{Wis}} = 1-\frac{11}{6}e^2+\frac{2}{3}e^4+\frac{1}{6}e^6, \quad (14)$$

following the nomenclature of Hut (1981) and Wisdom (2008) as indicated. Furthermore, $k_{2,i}$ is the potential Love number of degree 2 for the ith component of the binary system and Λ_i is a measure of the longitude of the node of the body's equator on the orbit plane with respect to the pericenter of its orbit. In order to estimate the impact of Λ_i in the last term in Eq. (13), we assume this impact to be as large as possible, $\Lambda_i = 0$, and compare it to the preceding terms. We find that for the case of 2M0535−05 the first three terms are of order 1, whereas the term connected to Λ_i varies between 10^{-2} and 10^{-5}, depending on ψ_i. These irrelevant contributions give us a justification to neglect the unknown values of Λ_i in 2M0535−05 for our computations, facilitating the comparisons to the other models.

2.2. Constant time lag

2.2.1. Tidal model #3

Instead of assuming phase lags and superposition of frequency-dependent potentials, the "equilibrium tide" model by Hut (1981) invokes a constant time lag τ between the line joining the centers of the two bodies and the culmination of the tidal bulge on the distorted object. With that assumption, the model of Hut81 is mutually exclusive with the assumption of a fixed angle lag (Goldreich & Soter 1966): in general, a fixed time lag and a fixed angle lag result in very different behaviors of the

R. Heller et al.: Tidal effects on brown dwarfs: application to 2M0535−05

tidal bulge[2]. As for the case of the "constant-time-lag" model, we first sum up the equations governing the behavior of the orbital evolution. With the purpose of easing a comparison between Hut81's equations (Eqs. (9)–(11) therein) and Eqs. (4)–(7) from this paper for the theory of the "constant-phase-lag" model #1, we transform the former into

$$\frac{\mathrm{d}a}{\mathrm{d}t} = \sum_{i=1,2i\neq j} \frac{-6k_{\mathrm{aps},i}GM_jR_i^5}{a^7}\, \tau_i \left(1+\frac{M_j}{M_i}\right)\left(\frac{f_1^{\mathrm{Hut}}}{\beta^{15}} - \frac{f_2^{\mathrm{Hut}}}{\beta^{12}}\frac{\Omega_i}{n}\right), (15)$$

$$\frac{\mathrm{d}e}{\mathrm{d}t} = \sum_{i=1,2i\neq j} \frac{-27k_{\mathrm{aps},i}GM_jR_i^5 e}{a^8}\, \tau_i \left(1+\frac{M_j}{M_i}\right)\left(\frac{f_3^{\mathrm{Hut}}}{\beta^{13}} - \frac{11}{18}\frac{f_4^{\mathrm{Hut}}}{\beta^{10}}\frac{\Omega_i}{n}\right), (16)$$

$$\begin{aligned}\frac{\mathrm{d}\psi_i}{\mathrm{d}t} &= \frac{-3k_{\mathrm{aps},i}GM_j^2R_i^3\psi_i}{M_ia^6r_{\mathrm{g},i}^2}\, \tau_i \\ &\times \left(\frac{f_2^{\mathrm{Hut}}}{\beta^{12}}\frac{n}{\Omega_i} - \frac{f_5^{\mathrm{Hut}}}{2\beta^9}\left[1 - \frac{r_{\mathrm{g},i}^2}{\beta}\frac{M_i+M_j}{M_j}\left(\frac{R_i}{a}\right)^2\frac{\Omega_i}{n}\right]\right),\end{aligned} (17)$$

with $k_{\mathrm{aps},i}$ as the apsidal motion constant of the perturbed body (see Sect. 2.1.1), $r_{\mathrm{g},i}^2$ as the radius of gyration of the ith body, which is defined by the body's moment of inertia $I_i = M_i r_{\mathrm{g},i}^2 R_i^2$, and

$$\begin{aligned}f_3^{\mathrm{Hut}} &= 1 + \frac{15}{4}e^2 + \frac{15}{8}e^4 + \frac{5}{64}e^6, \\ f_4^{\mathrm{Hut}} &= 1 + \frac{3}{2}e^2 + \frac{1}{8}e^4.\end{aligned} (18)$$

Hut81 then calculates the energy dissipation rate within a binary system, caused by the influence of one of the two bodies on the other, as the change in the total energy $E = E_{\mathrm{orb}} + E_{\mathrm{rot}}$. Here, E_{orb} and E_{rot} are the orbital and rotational energies of the body (Eqs. (A28)–(A35) in Hut81). For the tidal heating rates of the ith constituent within the binary, this yields

$$\dot{E}_{\mathrm{tid},i}^{\#3} = \frac{3k_{\mathrm{aps},i}GM_j^2R_i^5n^2}{a^6}\, \tau_i\, \zeta_{\mathrm{Hut}}(e,\Omega_i,n), (19)$$

where

$$\zeta_{\mathrm{Hut}}(e,\Omega_i,n) = \frac{f_1^{\mathrm{Hut}}}{\beta^{15}} - 2\frac{f_2^{\mathrm{Hut}}}{\beta^{12}}\frac{\Omega_i}{n} + \frac{f_5^{\mathrm{Hut}}}{\beta^9}\frac{\Omega_i^2}{n^2}. (20)$$

Unfortunately, with these equations for the tidal energy rates model #3 neglects a potential obliquity of the body, which prevents us from a direct comparison with the other tidal models.

2.2.2. Tidal model #4

Lev07 extended Hut81's formula for the tidal energy rate to the case of an object in equilibrium rotation[3] and they included possible obliquities (see also Neron de Surgy & Laskar 1997),

though they do not give the equations for the orbital evolution. Lev07's equations are equivalent to

$$\dot{E}_{\mathrm{tid},i}^{\#4} = \frac{3k_{2,i}GM_j^2R_i^5n}{Q_{\mathrm{n},i}a^6}\, \zeta_{\mathrm{Lev}}(e,\psi_i), (21)$$

where

$$\zeta_{\mathrm{Lev}}(e,\psi_i) = \frac{f_1^{\mathrm{Hut}}}{\beta^{15}} - \frac{(f_2^{\mathrm{Hut}}/\beta^{12})^2}{f_5^{\mathrm{Hut}}/\beta^9}\left(1 + \frac{1}{1-2/S_i^2}\right). (22)$$

The "annual tidal quality factor" is given as $Q_{\mathrm{n}}^{-1} = n\,\tau$. Even though Lev07's equations invoke Q_{n} and their equations resemble those of the models with constant phase lag, their approach still assumes a constant-time-lag. Since Lev07 do not explicitly connect their Q_{n} to the Q of FM08 (model #1) and Wis08 (model #2), we keep Q and Q_{n} as two different constants for our further treatment.

With these expansions, Eq. (21) involves terms in eccentricity up to order e^8. But since model #4 assumes tidal locking, i.e. $\dot{E}_{\mathrm{tid}}^{\#4}$ is not a function of Ω, this model also yields just a lower limit for the heating rates (Wisdom 2008).

2.3. Converting tidal heating into temperature increase

Now that we have set up four distinct models for the calculations of the additional tidal heating term for the BDs, there are two physical processes that will be driven by these energy rates: tidal inflation and temperature increase. Let's take $\bar{L}$ as the luminosity of either of the two 2M0535−05 BDs that it would have if it were a single BD and $\bar{R}$ and $\bar{T}_{\mathrm{eff}}$ as its corresponding radius and effective temperature. Then, by the Stefan-Boltzmann law (Stefan 1879; Boltzmann 1884)

$$\bar{L} = 4\pi\bar{R}^2\sigma_{\mathrm{SB}}\bar{T}_{\mathrm{eff}}^4, (23)$$

where σ_{SB} is the Stefan-Boltzmann constant. The radial expansion in the binary case is given by $\mathrm{d}R = R-\bar{R}$ and the temperature increase by $\mathrm{d}T = T_{\mathrm{eff}} - \bar{T}_{\mathrm{eff}}$. In its present state, the BD has a luminosity

$$L = \dot{E}_{\mathrm{in}} + \bar{L}, (24)$$

where $\dot{E}_{\mathrm{in}}$ is some additional internal energy rate. Solving Eq. (24) for the temperature increase yields:

$$\mathrm{d}T = \left(\frac{\dot{E}_{\mathrm{in}}}{4\pi R^2\sigma_{\mathrm{SB}}} + \left[\frac{\bar{R}}{R}\right]^2\bar{T}_{\mathrm{eff}}^4\right)^{1/4} - \bar{T}_{\mathrm{eff}}. (25)$$

In the next step, we quantify the amount of tidal energy that is converted into internal energy, leading to an increase in effective temperature. Since we will use the virial theorem for an ideal, monoatomic gas to estimate the partition between internal and gravitational energy, we first have to assess the adequacy of treating the 2M0535−05 BDs as ideal gases. We therefore show the degeneracy parameter $\tilde{\Psi} = k_{\mathrm{B}}T/(k_{\mathrm{B}}T_{\mathrm{F}})$ as a function of radius in Fig. 1 (Chabrier & Baraffe 2000; Baraffe, private comm.). Here, k_{B} is the Boltzmann constant, T is the local temperature within the gas and $E_{\mathrm{F}} = k_{\mathrm{B}}T_{\mathrm{F}}$ is the Fermi energy of a partially degenerate electron gas with an electron Fermi temperature T_{F}. With respect to M, T_{eff} and $\log(g)$, g being the body's gravitational acceleration at the surface, the BD structure model corresponds to that of the primary, but with an age of 4.9 Myr. We find that for most of the BD, i.e. that portion of the structure in which the majority of the luminosity is released, $\tilde{\Psi}$ is of order 1. This means that we may indeed approximate the BDs as ideal gases.

---

[2] If $e = 0$ and $\psi = 0$, then there is a single tidal lag angle ε and the tidal dissipation funtion can be written as $Q = 1/\varepsilon = 1/(\tau n)$. For the course of an orbit, where the tidal evolution of n is negligible, both Q and τ can be fixed. However, in a general case where τ is constant in time, Q will decrease as the orbital semi-major axis decays and n increases. So Q would not be constant.

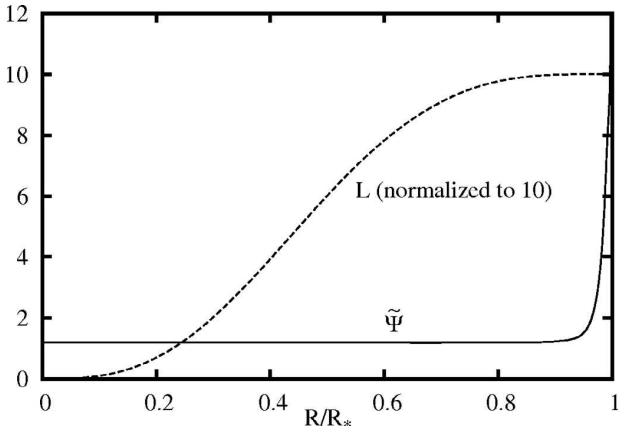[3] Wis08 calls this "asymptotic nonsynchronous rotation".

Fig. 1. Degeneracy parameter $\tilde{\Psi} = k_B T/(k_B T_F)$ (solid line) with model parameters similar to those of the 2M0535−05 primary and radius-integrated luminosity L (dashed line) as a function of radius. To fit into the plot, L is normalized to 10.

With the time derivative of the virial theorem for an ideal monoatomic gas (Kippenhahn & Weigert 1990, Sect. 3.1 therein),

$$L = \dot{E}_{in} = -\dot{E}_G/2, \qquad (26)$$

where $\dot{E}_G$ is the temporal change in gravitational energy, we find that half of the additional tidal energy is converted into internal energy and the other half causes an expansion of the BD. There are currently no models for tidal inflation in BDs and the treatment is beyond the scope of this paper. Instead of including the modeled BD radii $\bar{R}_i$ into Eq. (25) we avoid further uncertainties and fix $\bar{R}/R = 1$ (see Sect. 5 for a discussion of tidal inflation in the evolutionary context). The increase in effective temperature due to tidal heating then becomes

$$dT = \left(\frac{\dot{E}_{tid}/2}{4\pi R^2 \sigma_{SB}} + \bar{T}_{eff}^4 \right)^{1/4} - \bar{T}_{eff}. \qquad (27)$$

For $\bar{T}_{eff,i}$ we took the values predicted by the Baraffe et al. (1998) models (see Table 1).

Our neglect of tidal inflation makes this temperature increase an upper limit. Given that this neglect is arbitrary, we estimate how our constraints for $\log(Q_2) = 3.5$ and $\psi_2 = 50°$ would change, if tidal inflation played a role in 2M0535−05. Comparing the observed radii of both BDs with the model predictions (see Table 1), radial expansions of 10% for the primary and 20% for the secondary seem realistic. Theoretical investigations of tidal heating on the inflated transiting planet HD209458b by (Ibgui & Burrows 2009) support an estimate of tidal inflation by 20%. As a test, we assumed that the secondary BD in 2M0535−05 is tidally inflated, where its radius in an isolated scenario would be 80% of its current value, i.e. $\bar{R} = 0.8 \cdot R$ in Eq. (25). In the non-inflated scenario with $\bar{R}/R = 1$, the BD would reach a temperature increase of $dT = 60$ K at $\log(Q_2) = 3.5$ and $\psi_2 = 50°$ with model #2 (see Sect. 3.3). With the inflation, however, $\log(Q_2) \approx 2.7$ is needed to achieve the same heating at $\psi_2 = 50°$, whereas no obliquity at $\log(Q_2) = 3.5$ would yield significant heating. Thus, if tidal inflation in the secondary BD increases its radius by 20%, then the value for the dissipation function required to yield the same T_{eff} would be about 0.8 smaller in $\log(Q)$ than in the case of no inflation. Therefore, the temperature we report in Sect. 3 may, at worst, correspond to $\log(Q)$ that is smaller by 0.8.

3. Results

3.1. Orbital evolution

In order to get a rough impression of how far the orbital configuration of the system has evolved, we used the equations given in FM08, to compute the change of its eccentricity e and of a possible obliquity ψ_2 of the secondary within the last 1.5 Myr. Since this time span is the upper bound for the system's age, confined by its localization within the Orion Nebulae and indicated by comparison with BD evolutionary tracks, we thus get the strongest changes in e and ψ_2. If any initial obliquity would be washed out already, ψ_i could be neglected in the calculations of tidal heating. Furthermore, the measured eccentricity e could give a constraint to the tidal dissipation function Q. Computations based on the theory of "constant-time-lag" yield qualitatively similar results.

For the evolution of e, we relied on Eq. (6). We took the observed eccentricity $e = 0.3216$ as a starting value and evolved it backwards in time. To evolve the system into the past, we changed the sign of the right side of the equation. Furthermore, we assumed that the quality factors Q_1 and Q_2 of the primary and secondary are equal, leading to $Q_1 = Q_2 =: \tilde{Q}$ and $\tilde{\varepsilon}_{k,i} := \tilde{\varepsilon}_{k,i}(\Omega_i, n, \tilde{Q})$, because we are merely interested in a tentative estimate so far. This assumption should be a good approximation due to the similarity of the both components in terms of composition, temperature, mass, and radius.

The observed eccentricity of the system might give a constraint to the possible values for $\tilde{Q}$ since de/dt depends on $\tilde{Q}$ via $\tilde{\varepsilon}_{k,i}$. Certain $\tilde{Q}$ regimes could be incompatible with the observed eccentricity of the system at a maximum age of 1.5 Myr, if these $\tilde{Q}$ values would have caused the eccentricity to decay rapidly to 0 within this time. However, our simulations (Fig. 2) show that the system has not yet evolved very far for the whole range of $\tilde{Q}$ and that the eccentricity of 2M0535−05 is in fact increasing nowadays. In this system, circularization does not occur. The observed eccentricity of 0.3216 consequently does not constrain $\tilde{Q}$. In this first estimate, we fixed all other parameters in time, i.e. we neglected an evolution of the semi-major axis a, of possible obliquities ψ_i and we used constant radii R_i and rotational frequencies Ω_i. We did this because we cannot yet incorporate the evolutionary behavior of the components' radii R_i in the context of tides and furthermore, there is no knowledge about possible misalignments ψ_i between the orbital plane and the equatorial planes of the primary and secondary, respectively. A consistent evolution of R_i, however, is necessary to evolve da/dt as a function of ψ_1 and ψ_2, as given by Eq. (4). Such a calculation was beyond the scope of this study.

The relative spin-geometry of the two BD rotational axes with respect to the orbital plane and with respect to each other is unknown in 2M0535−05. Anyhow, we can estimate if a possible obliquity that once existed for one of the BDs would still exist at an age of 1.5 Myr or if it would have been washed out up to the present. We used a numerical integration of Eq. (7) to evolve ψ_2 forward in time (Fig. 2). For the secondary's initial obliquity $\psi_{ini,2}$, we plot the state of ψ_2 as a function of the quality factor Q_2 after an evolution of 1.5 Myr. We see that even for a very small quality factor of 10^3 and high initial obliquities the secondary is basically in its natal configuration today. Thus, it is reasonable to include a putative misalignment of the secondary with respect to the orbital plane in our considerations. As shown below, this is crucial for the calculations of the tidal heating and the temperature reversal.
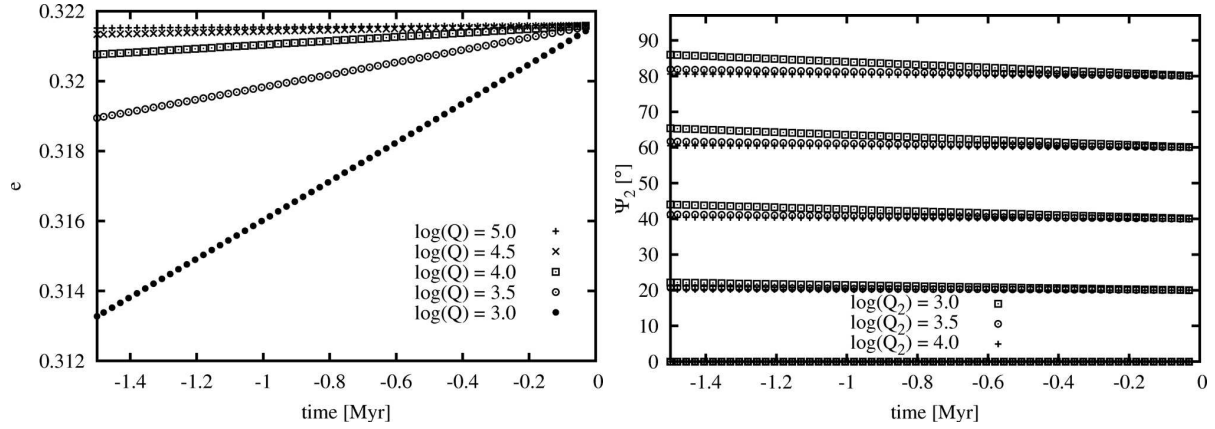
Fig. 2. Orbital evolution of 2M0535-05 after model #1 going back in time for 1.5 Myr. *Left*: eccentricity evolution. Depending on $\tilde{Q}$ and on the age of the system, its initial eccentricity has not been smaller than ≈0.3133, which is ≈97.4% of its current value. *Right*: obliquity evolution of the secondary BD for three different values of Q_2. Simulations started at "time = 0" for $\psi_2 \in \{0°, 20°, 40°, 60°, 80°\}$ and were evolved backwards in time. For $\log(Q_2) > 4$ there is no significant change in ψ_2. For all the treated values of Q_2, the obliquity of the 2 M0535−05 secondary is still close to its natal state.

3.2. Tidal heating in 2M0535−05 with model #1

In Fig. 3, we show the results for the tidal heating rates as computed after tidal model #1. As given by Eq. (11), the tidal heating of the primary does not depend on a putative obliquity, whereas that of the secondary does. Using this model, we find that the luminosity gain of the secondary is, over the whole Q range, smaller than that of the primary, which mainly results from the relation $\dot{E}_{\mathrm{tid},i}^{\#1} \propto R_i^5$. Figure 3 also shows that a growing obliquity shifts the gain in thermal energy towards higher values for a fixed Q_2. The observed overshoot of ≈10^{24} W in the secondary's luminosity can be reproduced with very small quality factors of $Q_2 \approx 10^3$ and high obliquities up to $\psi_2 \approx 90°$.

In Fig. 4, we show the results for the temperature increase as per Eq. (27) with the tidal energy rates coming from model #1. These rates yield only a slight temperature increase for both constituents. Even for low Q values of order 10^4 and high obliquities of the secondary, the heating only reaches values ≲10 K. We also see that the heating for the primary is computed to be greater than that for the secondary and no temperature reversal would be expected. If both BDs have the same Q values, then model #1 is unable to explain the temperature reversal. We cannot rule out a system in which, e.g., $Q_1 = 10^5$ and $Q_2 = 10^3$, for which model #1 could explain the reversal. However, there is no reason to expect that similar bodies have Q values that span orders of magnitude. Hence, we conclude that model #1 can neither reproduce the luminosity overshoot of the secondary nor the system's temperature reversal.

3.3. Tidal heating in 2M0535−05 with model #2

This model yields the highest heating rates and hence temperature increases. The contrast between the absolute energy rates within the primary $\dot{E}_{\mathrm{tid},1}^{\#2}$ and the secondary $\dot{E}_{\mathrm{tid},2}^{\#2}$ is very small. In fact, for any given point in ψ-Q space, the heating rates differ only by $\log(\dot{E}_{\mathrm{tid},1}^{\#2}/\mathrm{W}) - \log(\dot{E}_{\mathrm{tid},2}^{\#2}/\mathrm{W}) \approx 0.1$ (Fig. 5). The tidal energy rates of the secondary become comparable to the observed luminosity overshoot at $\log(Q_2) \approx 3.5$ and $\psi_2 \approx 50°$, where $\dot{E}_{\mathrm{tid},2}^{\#2} \approx 10^{24}$ W. A comparison of the heating rates from model #2 with those of model #1 for either of the BDs shows that model #2 provides higher rates, with growing contrast for increasing obliquities.

The temperature increase arising from the comparable heating rates is inverted for a given spot on the ψ-$\log(Q)$ plane. If both BDs had the same obliquity and the same dissipation factor, the secondary would experience a higher temperature increase. As presented in Fig. 6, the temperature increase after model #2 is significant only in the regime of very low Q and high obliquities. Neglecting any orbital or thermal evolution of the system, the observed temperature reversal could be reproduced by assuming an obliquity for the secondary while the primary's rotation axis is nearly aligned with the normal of the orbital plane. We note that the real heating will probably be greater since model #2 assumes synchronous rotation, which is not the case for both BDs in 2M0535−05 (see Table 1). The values of Q_2 and ψ_2 necessary to account for the observed increase in L_2 and $T_{\mathrm{eff},2}$ may thus be further shifted towards more reasonable numbers, i.e. Q_2 might also be higher than $10^{3.5}$ and the obliquity might be smaller than $50°$. Thus, for a narrow region in the ψ-$\log(Q)$ plane, model #2 yields tidal energy rates for the secondary comparable to its observed luminosity overshoot and in this region the computed temperature increase can explain the observed temperature reversal.

3.4. Tidal heating in 2M0535−05 with model #3

Since the only free parameter in this model is the putative fixed time lag τ, we show the tidal heating rates for both the primary and the secondary only as a function of τ in Fig. 7 with $0\,\mathrm{s} < \tau < 300\,\mathrm{s}$. For this range, model #3 yields energy rates and temperature rises that are compatible with the observed luminosity and temperature overshoot of the secondary. For $\tau \gtrsim 100$ s the heating rate for the secondary becomes comparable to the observed one, namely $\dot{E}_{\mathrm{tid},2}^{\mathrm{Hut}} \approx 10^{24}$ W. However, assuming a similar time lag τ_1 for the primary, the luminosity gain of the primary BD would be significantly higher than that of the secondary, which is not compatible with the observations. The assumption of $\tau_1 \approx \tau_2$ should be valid since both BDs are very similar in their structural properties, such as mass, composition, temperature, and radius.

The corresponding temperature increase is plotted in Fig. 8. It shows that the more massive BD would experience a higher temperature increase than its companion, assuming similar time

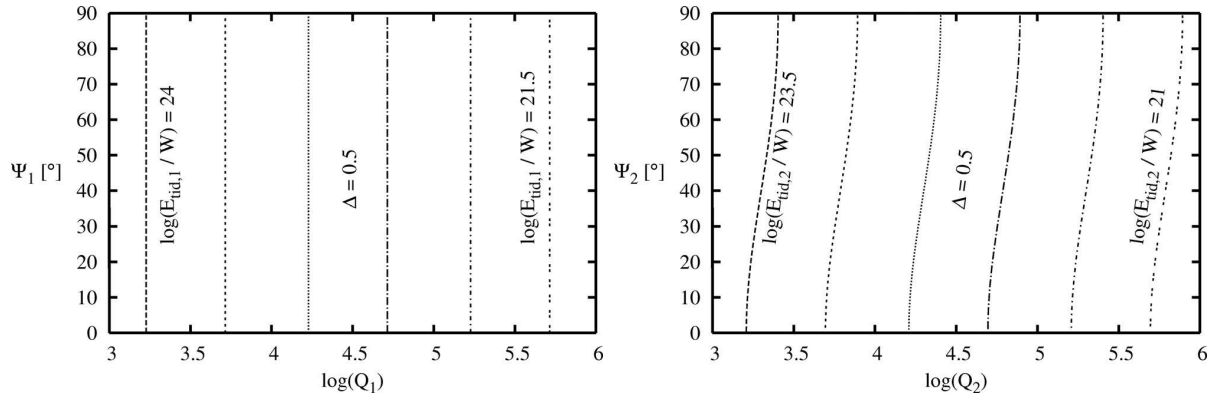**Fig. 3.** Tidal heating after model #1. *Left*: (Primary) Projection of $\dot{E}^{\#1}_{\mathrm{tid},1}$ onto the $\log(Q_1)$-ψ_1 plane. The stepsize between contour lines is chosen to be $\Delta = 0.5$ in $\log(\dot{E}^{\#1}_{\mathrm{tid},1}/\mathrm{W})$. *Right*: (Secondary) Projection of $\dot{E}^{\#1}_{\mathrm{tid},2}$ onto the $\log(Q_2)$-ψ_2 plane. Although there is a dependence on ψ_2, the energy rates at a fixed value for the quality factor are smaller than those for the primary.
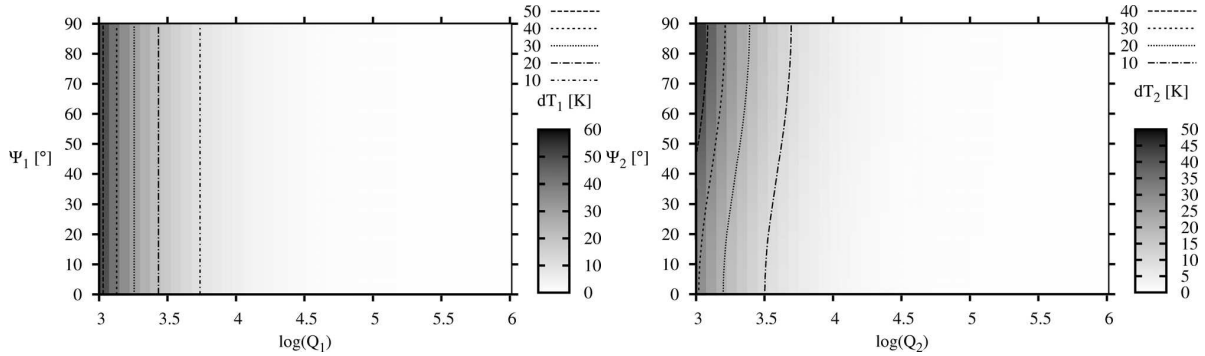
Fig. 4. Temperature increase after model #1. *Left*: (Primary) Projection of $d\mathrm{T}_1$ onto the $\log(Q_1)$-ψ_1 plane. For a significant temperature increase, Q_1 would have to be much smaller than $10^{3.5}$, but such a temperature increase is not observed in the primary. *Right*: (Secondary) Projection of $d\mathrm{T}_2$ onto the $\log(Q_2)$-ψ_2 plane. Even for very low values of Q_2 and high obliquities ψ_2 the observed temperature increase cannot be reconstructed. For any given point in the ψ-$\log(Q)$ plane, $d\mathrm{T}_2 < d\mathrm{T}_1$, which does not support the observed temperature reversal.

lags. Since tidal heating is underway in 2M0535−05 and was probably similar in the past (see Sect. 2.1.1), tidal heating after model #3 would have been more important on the primary, forcing it to be even hotter than it would be without the perturbations of the secondary. The temperature difference between the primary and the secondary, which is anticipated by BD evolutionary models, would be even larger. Thus, the temperature inversion cannot be explained by tidal model #3.

3.5. Tidal heating in 2M0535−05 with model #4

The calculations based on model #4 yield significant heating rates in both BDs. Like in the case of models #1 and #2, the luminosity gain of the secondary at a fixed obliquity is, over the whole Q_n range, smaller than that of the primary (Fig. 9). As for model #2, the difference between $\dot{E}^{\#4}_{\mathrm{tid},1}(\psi)$ and $\dot{E}^{\#4}_{\mathrm{tid},2}(\psi)$ is less pronounced than in model #1. Assuming spin-orbit alignment for the primary and a pronounced obliquity of the secondary, tidal heating rates of $\dot{E}^{\#4}_{\mathrm{tid},2} = 10^{24}$ W can be reached with $\log(Q_{n,2}) \approx 3.5$ and $\psi_2 \approx 50°$.

Like model #2, #4 produces a reversal in temperature increase by means of the modified Stefan-Boltzmann relation in Eq. (27), due to the comparable heating rates of both BDs and the significantly smaller radius of the secondary (Fig. 10). We find a reversal in tidal heating, i.e. $d T_2 > d T_1$ for any given point in ψ-Q_n space. A temperature increase of $\gtrsim 40$ K can be

reached with $\log(Q_{n,2}) \approx 3.5$ and $\psi_2 \approx 50°$. Since the equations of model #4 provide merely a lower limit due to the assumption of asymptotic non-synchronous rotation, $Q_{n,2}$ might also be higher than $10^{3.5}$ and the obliquity might be smaller than $50°$. Similar to model #2, tidal model #4 can reproduce the observed temperature reversal in a narrow region of the ψ-$\log(Q)$ parameter space.

4. Discussion

We employed several tidal models to explore the tidal heating in 2M0535−05. We found that, assuming similar tidal quality factors Q and obliquities ψ for both BDs, the constant-phase-lag model #2 and the constant-time-lag model #4 yield a stronger increase in effective temperature on the secondary mass BD than on the primary. For certain regimes of Q_2 and ψ, the tidal energy rates in the secondary are of the correct amount to explain the larger temperature in the smaller BD. A comparison between our computations based on the models #1 and #2 on the one hand and #3 and #4 on the other hand is difficult. The reference to a fixed tidal time lag might only be reconciled with the assumption of $Q_n^{-1} = n\,\tau$ as done by Lev07, which is at least questionable since the assumption of a fixed time lag is not compatible with a fixed phase lag. Furthermore, model #3 does not invoke obliquities, which also complicates direct comparisons of the model output.

R. Heller et al.: Tidal effects on brown dwarfs: application to 2M0535−05
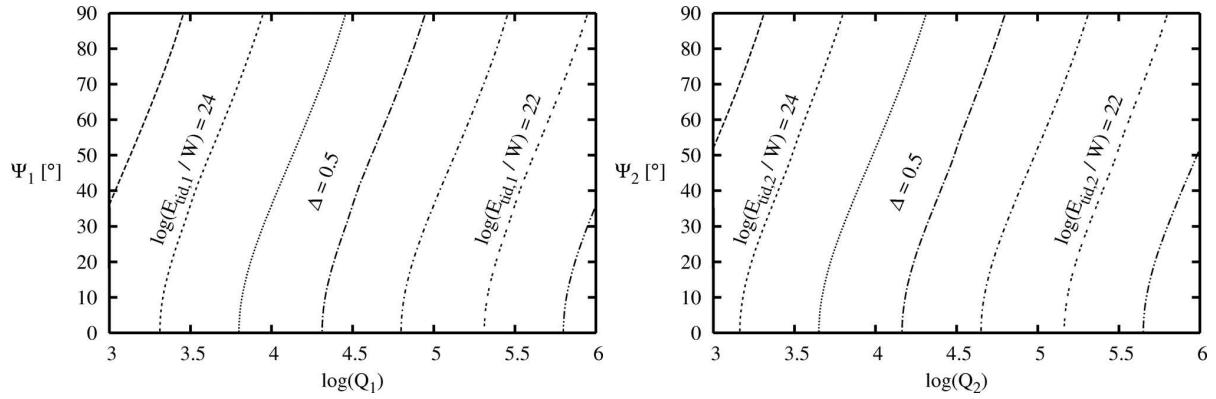

Fig. 5. Tidal heating after model #2. *Left*: (Primary) Projection of $\dot{E}_{\mathrm{tid},1}^{\#2}$ onto the $\log(Q_1)$-ψ_1 plane. The stepsize between contour lines is chosen to be $\Delta = 0.5$ in $\log(\dot{E}_{\mathrm{tid},1}^{\#2}/\mathrm{W})$. The tidal energy rates strongly depend on a putative obliquity, different from model #1. *Right*: (Secondary) Projection of $\dot{E}_{\mathrm{tid},2}^{\#2}$ onto the $\log(Q_2)$-ψ_2 plane. For the three models (#1, #2, and #4) invoking Q and ψ, these rates are the highest of all for any given point in the ψ-$\log(Q)$ plane – for the primary as well as for the secondary.
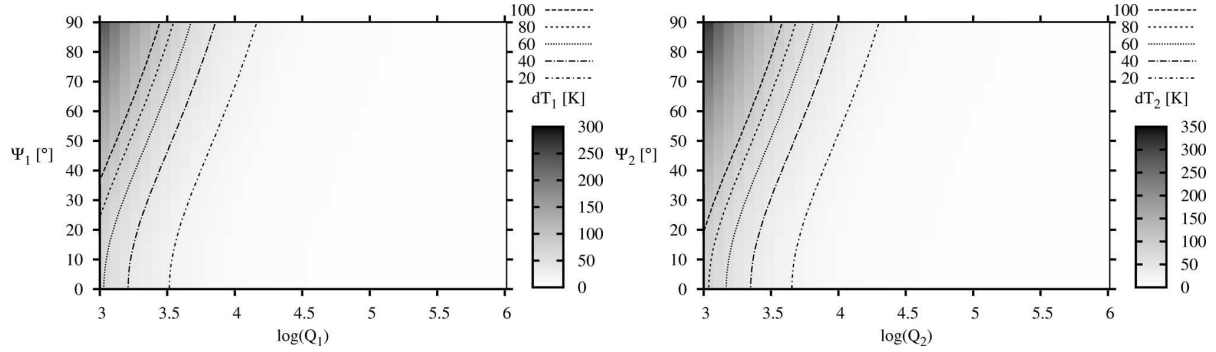

Fig. 6. Temperature increase after model #2. *Left*: (Primary) Projection of dT_1 onto the $\log(Q_1)$-ψ_1 plane. *Right*: (Secondary) Projection of dT_2 onto the $\log(Q_2)$-ψ_2 plane. For any given location in the $\log(Q)$-ψ plane, model #2 yields the strongest temperature increase compared to the other models – both for the primary and the secondary, respectively. For a given spot in Q-ψ space there is an inversion in temperature increase: $dT_2 > dT_1$, i.e. the less massive BD is heated more.
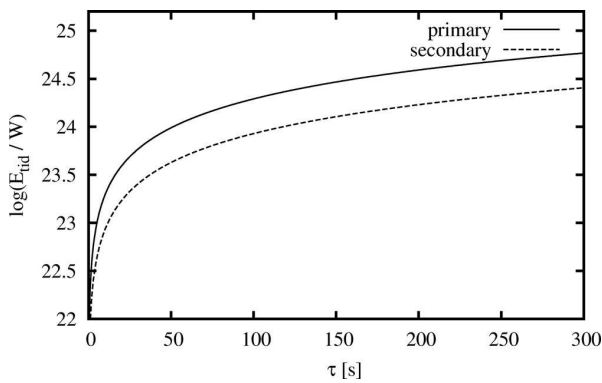

Fig. 7. Tidal heating within the primary (solid line) and secondary (dashed line) after model #3. While the tidal heating rate of the secondary becomes comparable to its observed luminosity overshoot for $\tau \gtrsim 100$ s, if the same τ is applied to the primary, heating within the primary would lead to a larger luminosity than is observed.
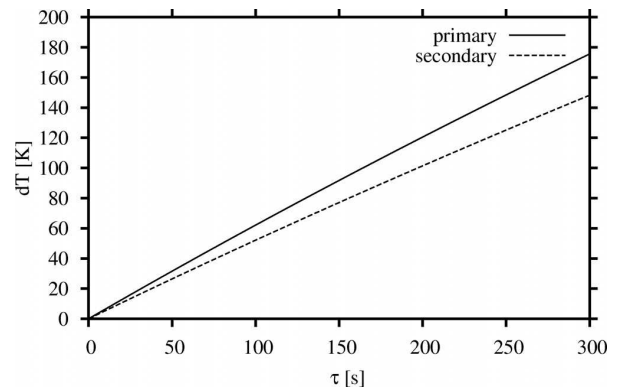
Fig. 8. Temperature increase of the primary (solid line) and secondary (dashed line) after model #3. Contrary to what is observed, the primary would be hotter than the secondary.

4.1. Constraints on the tidal dissipation function for BDs, Q_{BD}

4.1.1. The Rossiter-McLaughlin effect in 2M0535−05

The geometric implication of the most promising tidal models #2 and #4 is that the obliquity of the 2M0535−05 primary is

negligible and that of the secondary is $\psi_2 \approx 50°$ – provided tidal heating accounts for the T_{eff} reversal and the luminosity excess of the secondary. There does exist an observational method to measure the geometric configuration of eclipsing systems, called the Rossiter-McLaughlin effect (RME) (Rossiter 1924; McLaughlin 1924).
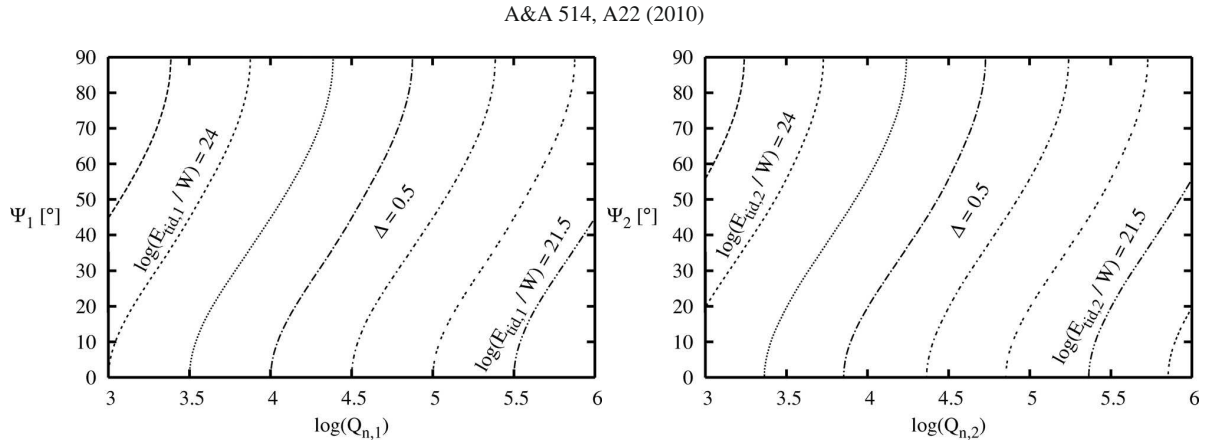
Fig. 9. Tidal heating after model #4. *Left*: (Primary) Projection of $\dot{E}_{\rm tid,1}^{\#4}$ onto the $\log(Q_1)$-ψ_1 plane. The stepsize between contour lines is chosen to be $\Delta = 0.5$ in $\log(\dot{E}_{\rm tid,1}^{\#4}/W)$. *Right*: (Secondary) Projection of $\dot{E}_{\rm tid,2}^{\#4}$ onto the $\log(Q_2)$-ψ_2 plane.
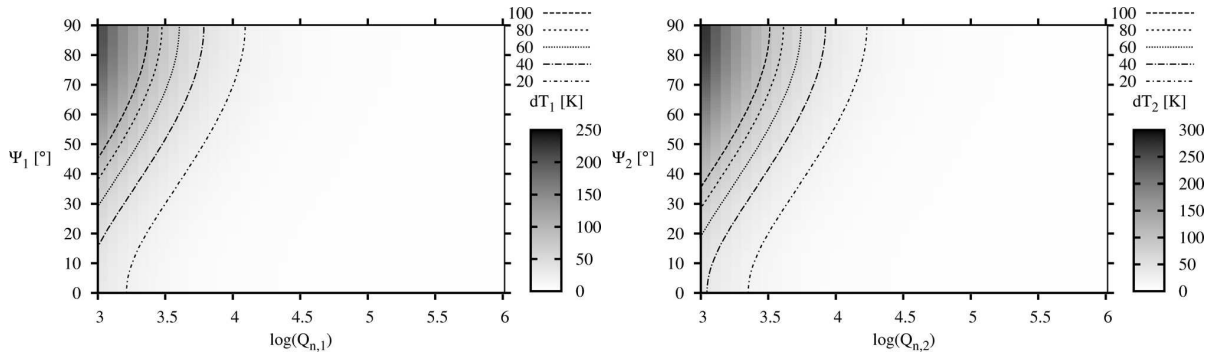

Fig. 10. Temperature increase after model #4. *Left*: (Primary) Projection of dT_1 onto the $\log(Q_1) - \psi_1$ plane. *Right*: (Secondary) Projection of dT_2 onto the $\log(Q_2) - \psi_2$ plane. For $\log(Q_2) \approx 3.5$ and an obliquity of $\psi_2 \approx 70°$ the temperature increase of the secondary becomes similar to the observed one. For the whole range of Q and ψ there is an inversion in temperature increase, similar to model #2: $dT_2 > dT_1$.

The RME appears during transits in front of rotating stars. Hiding a fraction of the star's surface results in the absence of some corresponding rotational velocity contribution to the broadening of the stellar lines. Thus, the changes in the line profiles become asymmetric (except for the midpoint of the transit) and the center of a certain stellar line is shifted during a transit, which induces a change of the star's radial velocity. The shape of the resulting radial velocity curve depends on the effective area covered by the transiting object and its projected path over the stellar surface with respect to the spin axis of the covered object (for a detailed analysis of the RME see Ohta et al. 2005).

Using a code originally presented in Dreizler et al. (2009), we have undertaken simulations of the RME for various geometric configurations of 2M0535−05 during the primary eclipse[4] as it would be seen with the Ultraviolet and Visual Echelle Spectrograph (UVES) at the Very Large Telescope (VLT) (see Fig. 11). For the data quality we assumed the constraints given by the UVES at the VLT exposure time calculator[5] in version 3.2.2. The computations show that, using Th-Ar reference spectra and also the telluric *A* and *B* bands as benchmarks, a time

sampling with one spectrum every 1245 s and a S/N of $\gtrsim 7$ around 8600 Å are necessary to get 21 measurements during the primary eclipse and an accuracy of $\lesssim 100$ m/s.

In principle, there are four parameters for the background object of the transit to be fitted in our simulations of the RME: the rotational velocity $v_{\rm rot}$, the inclination of the spin axes with respect to the line of sight $I_\star$, the angle between the projection of the spin and the projection of the orbital plane normal onto the celestial plane λ, and the orbital inclination with respect to the line of sight i. From light curve analyses, both rotational velocities in 2M0535−05 and the orbital inclination i are known. Thus, for the simulation of the primary eclipse $I_{\star,2}$ and λ_2 are the remaining free parameters.

The obliquities $\psi_{i\,|\,i=1,2}$, i.e. the real 3-dimensional angle between the orbital normal and the spin axis of the occulted object, is related to the other angles as

$$\cos(\psi_i) = \cos(I_{\star,i})\cos(i) + \sin(I_{\star,i})\sin(i)\cos(\lambda_i). \qquad (28)$$

While the two obliquities ψ_i are intrinsic angles of the system, they cannot be measured directly. They can only be inferred from i, $I_{\star,i}$ and λ_i, which depend on the position of the observer with respect to the system. Since we are only interested in the possible options for the measurement of the obliquities in 2M0535−05, we refer the reader to the paper by Winn et al. (2005) for a discussion of Eq. (28) and the geometrical aspects of the RME. With $i = 88.49°$ the first term in Eq. (28) degrades to insignificance, which yields $\cos(\psi_i) \approx \sin(I_{\star,i})\cos(\lambda_i)$.

---

[4] The "primary eclipse" refers to the major flux decrease in the system's light curve. Due to the significantly higher effective temperature of the secondary mass BD the primary eclipse occurs when the primary mass component transits in front of the secondary companion, as seen from Earth.

[5] http://www.eso.org/observing/etcwww.eso.org/ observing/etc

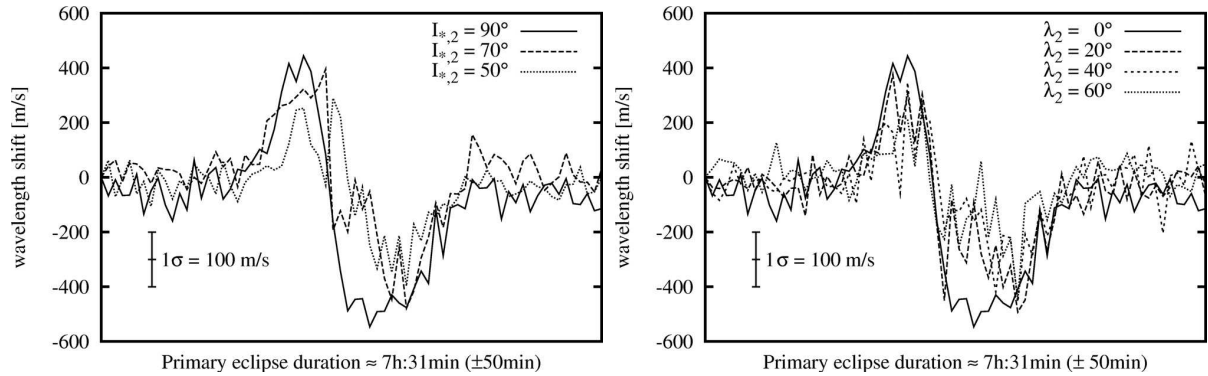R. Heller et al.: Tidal effects on brown dwarfs: application to 2M0535−05

Fig. 11. Simulations for the Rossiter-McLaughlin effect as it would be seen with UVES during the primary eclipse of 2M0535−05, which occurs when the secondary mass BD is occulted by the primary. The S/N is 7. *Left*: the orbital inclination i is fixed at 88.49° (see Table 1) and $\lambda = 0$, which means the transiting primary BD follows a path parallel to the secondary's equator. The alignment of the secondary's spin axis $I_{\star,2}$ varies between 90° (perpendicular to the line of sight) and 50°. *Right*: with i fixed at 88.49° and $I_{\star,2} = 90°$, λ_2 varies between 0° (primary path parallel to the secondary's equator) and 60° (primary path strongly misaligned with the secondary's equator).

At low values for $I_{\star,i}$ and λ_i the fitted solutions to the RME are degenerate and there are multiple solutions within a certain confidence interval. But our simulations for the transit show that the error due to the observational noise is on the same order as the error due to degeneracy and thus we find standard deviations in $I_{\star,2}$ and λ_2 of $\sigma_{I_{\star,2}} \approx 20°$ and $\sigma_{\lambda_2} \approx 20°$, respectively. The uncertainty in ψ_2 depends not only on the uncertainties in $I_{\star,2}$ and λ_2 but also on the actual values of $I_{\star,2}$ and λ_2. But in all cases, the standard deviation in the secondary's obliquity $\sigma_{\psi_2} < 20°$.

If present in 2M0535−05, a considerable misalignment of the secondary BD of 50° could be detected with a 1-σ accuracy of 20° or less. Thus, an observed ψ_2 value of 50° would be a 2.5-σ detection of spin-orbit misalignment. Unless RME measurements suggest $\psi \approx 90°$, RME observations alone are unlikely to provide definitive evidence that any of the tidal models we consider is responsible for the temperature reversal.

4.1.2. Further observations of BD binaries

Besides the option of RME measurements for testing the geometric implications, there does exist a possibility to verify our estimate of $\log(Q) \approx 3.5$ for BDs in general. Comparison of observed orbital properties with values constrained by the equations that govern the orbital evolution might constrain the free parameters, here Q. Using Eq. (6), we find that, assuming only a slight initial eccentricity of 0.05, the eccentricity of a BD binary system similar to 2M0535−05, in terms of masses, radii, rotational frequencies, and semi-major axis would increase to 1 after ≈ 500 Myr if the quality factors of the two BDs are $\lesssim 10^{3.5}$ (see left panel in Fig. 12). A measurement of e in such an evolved state could not constrain Q in a 2M0535−05 analog since either the initial eccentricity could have been relatively large while the orbit evolved rather slowly due to high Q values or a small initial value of e could have developed to a large eccentricity due to small values of Q.

We also simulate the evolution of a 2M0535−05 analog but with a different rotational frequency of the primary constituent in order to let the eccentricity decrease with time. We neglected the evolution of all the other physical and orbital parameters since we are merely interested in a tentative estimate. For a given candidate system the analysis would require a self-consistent coupled evolution of all the differential equations. For the arbitrary case of $P_1 = P_2 = 14.05$ d we find that, even for the most extreme but unrealistic case of an initial eccentricity equal to 1, this fictitious binary would be circularized on a timescale of 100 Myr for $\log(\tilde{Q}) < 5$ (see right panel in Fig. 12). Findings of old, eccentric BD binaries with rotational and orbital frequencies that yield circularization in the respective system would set lower limits to Q.

4.1.3. Rotational periods in 2M0535−05

Another, and in fact a crucial, constraint on Q for BDs comes from the synchronization time scale t_{synch} of the two BDs in 2M0535−05. Following the equation given in Lev07 and taking the initial orbital mean motion and semi-major axis of the system as calculated with an uncoupled system of differential equations from model #1, we derive $t_{\text{synch,1}} = 0.07$ Myr for the primary and $t_{\text{synch,2}} = 0.04$ Myr for the secondary with $\log(Q) = 3.5$. Since the rotation in both BDs is not yet synchronized with the orbit and the age of the system is about 1 Myr, $\log(Q) = 3.5$ is not consistent with the age of 2M0535−05. Both components should have synchronous rotation rates already. We find the consistent value for Q to be $\gtrsim 10^{4.5}$, yielding synchronization time scales $t_{\text{synch,1}} \gtrsim 0.69$ Myr and $t_{\text{synch,2}} \gtrsim 0.37$ Myr.

To make this estimate for Q more robust, we present the evolution of the BDs' rotational periods in Fig. 13 and compare it to the critical period for a structural breakup P_{crit}. The evolutionary tracks are calculated with model #1 and Eq. (30) in FM08. As a rough approach we do not couple this equation with those for the other orbital parameters. The left panel of Fig. 13 shows that for $\log(Q_1) = 3.5$ and $\psi_1 = 0°$ the primary's initial rotation period 1 Myr ago is ≈ 0.3 d. The initial rotation period for the secondary, for $\log(Q_2) = 3.5$ and $\psi_2 = 0°$, is about −0.2 d, where the algebraic sign contributes for a retrograde revolution (right panel in Fig. 13). For most of its lifetime, the secondary would have had a retrograde rotation and just switched the rotation direction within the last few 10 000 yr, which is very unlikely in statistical terms. Since the orbital momentum is on the order of 10^{43} kg m^2/s and the individual angular momenta are about 10^{41} kg m^2/s, the shrinking process might not have had a serious impact on the rotational evolution. Tides have dominated the spin evolutions.

Following Scholz & Eislöffel (2005), the critical breakup period P_{crit} depends only on the body's radius and its mass. The radius evolution for BDs is very uncertain for the first Myr
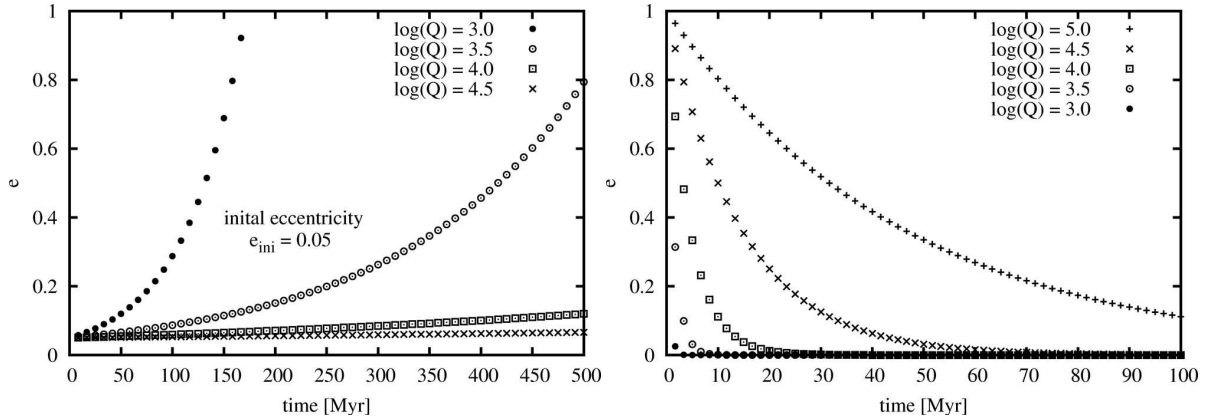
A&A 514, A22 (2010)

Fig. 12. Orbital evolution of a 2M0535−05 analog after model #1. *Left*: eccentricity evolution for different values of $\tilde{Q}$ for the next 500 Myr. The initial eccentricity was arbitrarily chosen: $e_{ini} = 0.05$. For $\log(\tilde{Q}) \lesssim 3.5$ this binary will be disrupted within 500 Myr. *Right*: eccentricity evolution of a 2M0535−05 analog but with $P_1 = P_2 = 14.05$ d for different values of $\tilde{Q}$. Contrary to the scenario in the left figure, the changed rotational period of the primary BD now leads to circularization of the system. Measurements of e in LMS binaries with known ages can give lower limits to $\tilde{Q}$.
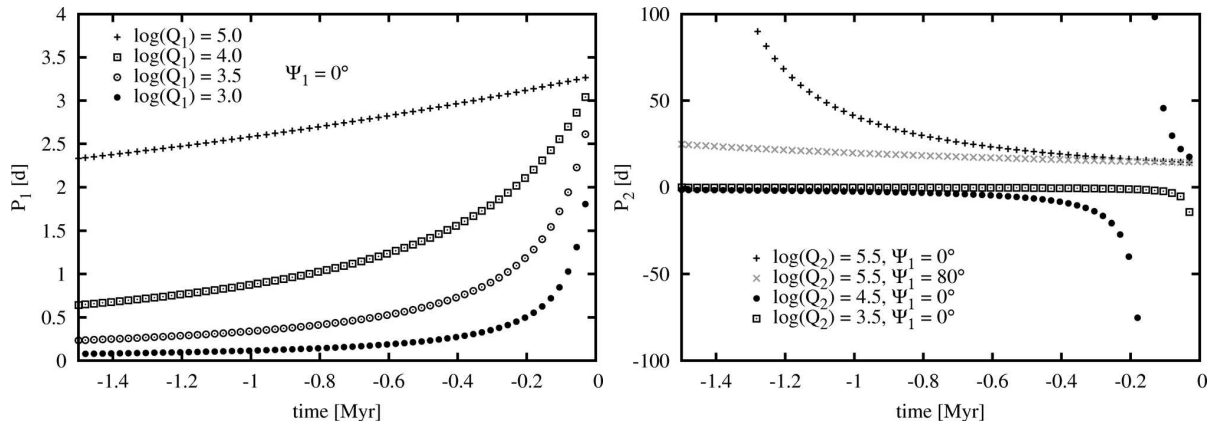

Fig. 13. Rotational evolution of the two BDs in 2M0535−05 after model #1 for different values of Q_1 and Q_2. *Left*: (Primary) Going backwards in time, the rotation period decreases. For $\log(Q_1) = 3.5$, P_1 drops below the critical period for structural breakup of ≈ 0.5 d already before the date of birth around 1 Myr ago. *Right*: (Secondary) For $\log(Q_2) = 5.5$ we show the tracks for $\psi_2 = 0°$ and $80°$ for comparison. For $\log(Q_2) = 4.5$ the rotation direction switches at about -0.18 Myr and for $\log(Q_2) = 3.5$ at roughly $-10\,000$ yr.

after formation but we estimate their initial radii to be as large as the solar radius. This yields $P_{crit,1} \approx 0.5$ d for both the primary and the secondary BD. As stated above, the moduli of the initial rotation periods of both BDs would have been smaller than 0.5 d for Q values of $\lesssim 10^{3.5}$. This inconsistency gives a lower limit to Q_1 and Q_2 since values of $\lesssim 10^{3.5}$ would need an initial rotation periods of both BDs which are smaller than their critical breakup periods. Obliquities larger than 0° would accelerate the (backwards) evolution and yield even larger lower limits for Q_1 and Q_2. Thus, our simulations of the rotational period evolution of both BDs require $\log(Q_{BD}) \gtrsim 3.5$, whereas the tidal synchronization timescale even claims $\log(Q_{BD}) \gtrsim 4.5$.

4.2. Evolutionary embedment of tidal heating

Tidal heating must be seen in the evolutionary context of the system. On the one hand, the tidal energy rates generate a temperature increase on the Kelvin-Helmholtz time-scale, which is ≈ 2 Myr for the BDs in 2M0535−05 – and thus on the order of the system's age, as per Eq. (27). On the other hand, tidal heating will affect the shrinking and cooling process of young BDs in

terms of an evolutionary retardation. As models show (D'Antona & Mazzitelli 1997; Baraffe et al. 1998; Chabrier et al. 2000; Chabrier & Baraffe 2000), single BDs cool and shrink significantly during their first Myrs after formation. Adding an energy source comparable to the luminosity of the object will slow down the aging processes such that the observed temperature and luminosity overshoot at some later point is not only due to the immediate tidal heating but also due to its past evolution. Consequently, the luminosity and temperature overshoot in the secondary might not (only) be due to present-day tidal heating, but it could be a result of an evolutionary retardation process triggered by the presence of the primary as a perturber. Coupled radius-orbit evolutionary models have already given plausible explanations for the inflated radii of some extrasolar planets (Gu et al. 2003; Miller et al. 2009; Ibgui & Burrows 2009; Ibgui et al. 2010, 2009).

For a consistent description of the orbital and physical history of 2M0535−05, one would have to include the evolution of obliquities ψ_i, BD radii R_i, eccentricity e, semi-major axis a, and rotational frequencies Ω_i. Note that there is a positive feedback between radial inflation and tidal heating: as tidal heating

inflates the radius, the tidal heating rate can increase and – in turn – may cause the radius to inflate even more. In a self-consistent orbital and structural simulation of 2M0535−05, tidal inflation, neglected in our computations of the T_{eff} increase in Eq. (27), will result naturally from the additional heating term introduced by tides.

In conjunction with 2M0535−05 that means the actual heating rates necessary to explain the T_{eff} and luminosity excess in the secondary are lower than they would have to be if there would be no historical context. Relating to Figs. 4, 6, 8, and 10, the implied obliquity and Q factor for the secondary are – again – shifted towards lower and higher values, respectively. Embedded in the historical context of tidal interaction in 2M0535−05, $\psi_2 < 50°$ and $\log(Q_2) > 3.5$ may also explain the temperature reversal and the luminosity excess of the secondary.

These trends, however, are contrary to that induced by tidal inflation. If tidal heating is responsible for a radial expansion of 10 and 20% in the primary and secondary, the values of the dissipation factor necessary to explain the T_{eff} reversal would be ≈ 0.8 smaller in $\log(Q_2)$ (see Sect. 2.3).

5. Conclusions

We surveyed four different published tidal models, but neglect any evolutionary background of the system's orbits and the components' radii to calculate the tidal heating in 2M0535−05. Our calculations based on models #2 and #4, which are most compatible with the observed properties of the system, require obliquities $\psi_1 \approx 0$, $\psi_2 \approx 50°$ and a quality factor $\log(Q) \approx 3.5$ in order to explain the luminosity excess of the secondary. Additionally, the observed temperature reversal follows naturally since we may reproduce a reversal in temperature increase due to tides: $\mathrm{d}T_2 > \mathrm{d}T_1$. In model #2, synchronous rotation of the perturbed body is assumed. Since this is not given in 2M0535−05, the actual heating rates will be even higher than those computed here. Our results for the heating rates as per model #2 are thus lower limits, which shifts the implied obliquity of the secondary and its Q factor to lower and higher values, respectively.

Considerations of the synchronization time scale for the BD duet and the individual rotational breakup periods yield constraints on Q_{BD} for BDs. We derive a lower limit of $\log(Q_{\text{BD}}) > 4.5$. This is consistent with estimates of Q-values for M dwarfs, $\log(Q_{\text{dM}}) \approx 5$, and the quality factors of Jupiter, $2 \times 10^5 < Q_{\text{♃}} < 2 \times 10^6$, and Neptune, $10^4 \lesssim \log(Q_{\text{♆}}) \lesssim 10^{4.5}$ (see Sect. 2.1.1). With $\log(Q_{\text{BD}}) > 4.5$ tidal heating alone can neither explain the temperature reversal in the system nor the luminosity excess of the secondary.

An obliquity of 50°, however, would be reasonable in view of recent results from measurements of the RME in several transiting exoplanet systems[6]. Currently, out of 18 planets there are 7 with significant spin-orbit misalignments $\gtrsim 30°$ and some of them are even in retrograde orbits around their host stars. A substantial obliquity ψ_2 might cause an enhanced heating in the 2M0535−05 secondary, while the primary's spin could be aligned with the orbital spin, leading to negligible heating in the primary.

Despite the advantages of distance-independent radius and luminosity measurements of close, low-mass binaries, the comparison of fundamental properties of the constituents with theoretical models of isolated BDs must be taken with care. This applies also to the direct translation from the discrepancies between observed and modeled radii for a fixed metallicity into an apparent age difference as a calibration of LMS models (Stassun et al. 2009). Tidal heating might be a crucial contribution to discrepancies between predicted and observed radii in other eclipsing low-mass binary systems (Ribas et al. 2008). As recently shown by Ibgui & Burrows (2009), tidal heating in extra-solar giant planets in close orbits at $a \lesssim 0.2$ AU with modest to high eccentricities of $e \gtrsim 0.2$ can explain the increased radii of some planets, when embedded in the orbital history with its host star.

Improvement of tidal theories is necessary to estimate the relation between tides and the observed radii of LMS being usually too large as compared to models. A tidal model is needed for higher orders of arbitrary obliquities and eccentricities that also accounts for arbitrary rotation rates. As stated by Greenberg (2009), a formal extension of the simple "lag-and-add" procedure of tidal frequencies the theory of constant phase lag is questionable. Besides the extension, conciliation among the various models is needed. The results from the models applied here should be considered preliminary but are suggestive and indicate the possible importance of tides in binary BD systems.

Several issues remain to be addressed for a more detailed assessment of tidal heating in 2M0535−05: i) reconciliation and improvement of tidal theories; ii) self-consistent simulations of the orbital and physical evolution of the system and the BDs; iii) measurements of the system's geometric configuration; iv.) constraints on the tidal quality factors of BDs.

References

Aksnes, K., & Franklin, F. A. 2001, AJ, 122, 2734
Baraffe, I., Chabrier, G., Allard, F., et al. 1998, A&A, 337, 403
Baraffe, I., Chabrier, G., Allard, F., et al. 2002, A&A, 382, 563
Barnes, R., Jackson, B., Raymond, S. N., West, A. A., & Greenberg, R. 2009, ApJ, 695, 1006
Bodenheimer, P., Lin, D. N. C., & Mardling, R. A. 2001, ApJ, 548, 466
Boltzmann, L. 1884, Annalen der Physik, 258, 291
Brooker, R. A., & Olle, T. W. 1955, MNRAS, 115, 101
Çakırlı, Ö., Ibanoglu, C., & Güngör, C. 2009, New Astron., 14, 496
Chabrier, G., & Baraffe, I. 2000, ARA&A, 38, 337
Chabrier, G., Baraffe, I., Allard, F., et al. 2000, ApJ, 542, 464
Chabrier, G., Gallardo, J., & Baraffe, I. 2007, A&A, 472, L17
Coughlin, J. L., & Shaw, J. S. 2007, Journal of the Southeastern Association for Research in Astronomy, 1, 7
D'Antona, F., & Mazzitelli, I. 1997, Mem. Soc. Astron. Ital., 68, 807
Dreizler, S., Reiners, A., Homeier, D., et al. 2009, A&A, 499, 615
Ferraz-Mello, S., Rodríguez, A., & Hussmann, H. 2008, Celest. Mechan. Dyn. Astron., 101, 171 (FM08)
Gavrilov, S. V., & Zharkov, V. N. 1977, Icarus, 32, 443
Goldreich, P., & Soter, S. 1966, Icarus, 5, 375
Gómez Maqueo Chew, Y., Stassun, K. G., Prša, A., et al. 2009, ApJ, 699, 1196
Greenberg, R. 2009, ApJ, 698, L42
Greenberg, R., Barnes, R., & Jackson, B. 2008, in BAAS, 40, 391
Gu, P., Lin, D. N. C., & Bodenheimer, P. H. 2003, ApJ, 588, 509
Guenther, E. W., Torres, G., Batalha, N., et al. 2001, A&A, 366, 965
Hut, P. 1981, A&A, 99, 126 (Hut81)

---

[6] See www.hs.uni-hamburg.de/EN/Ins/Per/Heller for an overview.

Ibgui, L., & Burrows, A. 2009, ApJ, 700, 1921
Ibgui, L., Spiegel, D. S., & Burrows, A. 2009, ApJ, submitted
  [arXiv:0910.5928]
Ibgui, L., Burrows, A., & Spiegel, D. S. 2010, ApJ, 713, 751
Ioannou, P. J., & Lindzen, R. S. 1993, ApJ, 406, 266
Jackson, B., Barnes, R., & Greenberg, R. 2008a, MNRAS, 391, 237
Jackson, B., Greenberg, R., & Barnes, R. 2008b, ApJ, 681, 1631
Kippenhahn, R., & Weigert, A. 1990, Stellar Structure and Evolution (Stellar
  Structure and Evolution, XVI (Berlin, Heidelberg, New York: Springer-
  Verlag), Also Astronomy and Astrophysics Library
Levrard, B., Correia, A. C. M., Chabrier, G., et al. 2007, A&A, 462, L5
  (Lev07)
Mardling, R. A., & Lin, D. N. C. 2002, ApJ, 573, 829
Mardling, R. A., & Lin, D. N. C. 2004, ApJ, 614, 955
Marley, M. S., Fortney, J. J., Hubickyj, O., Bodenheimer, P., & Lissauer, J. J.
  2007, ApJ, 655, 541
McLaughlin, D. B. 1924, ApJ, 60, 22
Miller, N., Fortney, J. J., & Jackson, B. 2009, ApJ, 702, 1413
Mohanty, S., Baraffe, I., & Chabrier, G. 2007, in IAU Symp., 239, ed. F. Kupka,
  I. Roxburgh, & K. Chan, 197
Mohanty, S., Stassun, K. G., & Mathieu, R. D. 2009, ApJ, 697, 713
Morales, J. C., Ribas, I., Jordi, C., et al. 2009, ApJ, 691, 1400
Neron de Surgy, O., & Laskar, J. 1997, A&A, 318, 975

Ogilvie, G. I., & Lin, D. N. C. 2004, ApJ, 610, 477
Ohta, Y., Taruya, A., & Suto, Y. 2005, ApJ, 622, 1118
Peale, S. J., & Greenberg, R. J. 1980, in Lunar and Planetary Institute Conference
  Abstracts, 11, 871
Ray, R. D., Eanes, R. J., & Lemoine, F. G. 2001, Geophys. J. Int., 144, 471
Reiners, A., Seifahrt, A., Stassun, K. G., Melo, C., & Mathieu, R. D. 2007, ApJ,
  671, L149
Ribas, I., Morales, J. C., Jordi, C., et al. 2008, Mem. Soc. Astron. It., 79,
  562
Rossiter, R. A. 1924, ApJ, 60, 15
Scholz, A., & Eislöffel, J. 2005, A&A, 429, 1007
Stassun, K. G., Mathieu, R. D., & Valenti, J. A. 2006, Nature, 440, 311
Stassun, K. G., Mathieu, R. D., & Valenti, J. A. 2007, ApJ, 664, 1154
Stassun, K. G., Mathieu, R. D., Cargile, P. A., et al. 2008, Nature, 453, 1079
Stassun, K. G., Hebb, L., López-Morales, M., et al. 2009, in IAU Symp. 258, ed.
  E. E. Mamajek, D. R. Soderblom, & R. F. G. Wyse, 161
Stefan, J. 1879, Sitzungsberichte der mathematisch-naturwissenschaftlichen
  Classe der kaiserlichen Akademie der Wissenschaften, 79, 391
Winn, J. N., Noyes, R. W., Holman, M. J., et al. 2005, ApJ, 631, 1215
Wisdom, J. 2008, Icarus, 193, 637 (Wis08)
Wuchterl, G. 2005, Astron. Nachr., 326, 905
Yoder, C. F. 1979, Nature, 279, 767
Zhang, K., & Hamilton, D. P. 2008, Icarus, 193, 267

5.2   Constraints on habitability from obliquity tides

René Heller, Rory Barnes, and Jérémy Leconte
To be submitted to *Astronomy & Astrophysics*
Credit: R. Heller, in preparation for submission to *A&A*, **reproduced with permission ©ESO**

The tidal processes described in the previous chapter also apply to terrestrial exoplanets, except for tidal inflation. We consider here the impact of tidal effects on the habitability of extrasolar Earth-like planets, with a focus on the contribution of obliquity tides. The drive towards synchronous rotation ($P_\mathrm{rot} \rightarrow P_\mathrm{orb}$), as well as 'tilt erosion' ($\psi_\mathrm{p} \rightarrow 0$), fundamentally determines the atmospheric conditions on the planet – thus its habitability. Tidal heating can be strong enough to cause global volcanism and rapid resurfacing on the planet, as observed on the Jovian moon Io, rendering it inhospitable. We find that planets in the insolation habitable zone (IHZ) around low-mass stars (LMSs) experience substantial tidal evolution, making some parts of the IHZ of LMSs in fact non-habitable. The consideration of tidal processes affects the concept of the habitable zone.

My numerical integration routine constitutes the basis of this study. It consists of roughly 500 lines of code, written in the programming language 'python', and performs a coupled numerical evolution of the two-body tidal interaction for the tidal models of Ferraz-Mello et al. (2008) and Leconte et al. (2010). In addition to some mathematical rearrangements of the tidal models, I created all the figures except for Fig. 5, and I authored the writing process.

I presented this work at the Astrobiology Graduate Conference in June 2010 in Tällberg, Sweden, with an oral contribution. In August 2010, I will give another talk on this topic at the Cool Stars 16 Conference in Seattle, USA, in the frame of the splinter session "Habitability of Planets Orbiting Cool Stars".

Constraints on habitability from obliquity tides

R. Heller[1,2], J. Leconte[3], and R. Barnes[4,5]

[1] Hamburger Sternwarte (Universität Hamburg), Gojenbergsweg 112, 21029 Hamburg, Germany
   e-mail: `rheller@hs.uni-hamburg.de`
[2] Graduiertenkolleg 1351 "Extrasolar Planets and their Host Stars" of the Deutsche Forschungsgesellschaft
[3] École Normale Supérieur de Lyon, CRAL (CNRS), Université de Lyon, 46 allée d'Italie, 69007 Lyon, France
   e-mail: `jeremy.leconte@ens-lyon.fr`
[4] University of Washington, Dept. of Astronomy, Seattle, WA 98195
   e-mail: `rory@astro.washington.edu`
[5] Virtual Planetary Laboratory, NASA

ABSTRACT

Context. So far, stellar insolation has been used as the main argument to define a planet's habitability depending on its semi-major axis a and orbital eccentricity e. Nowadays, more and more Earth-like planets are being discovered around low-mass stars (LMSs). Since for these systems tidal processes are significant, it is necessary to review tidal impacts on the habitability of exoplanets. The misalignment between a planet's rotational axis and the orbital plane normal, i.e. the planetary obliquity, turns out to be a key parameter for tidal processes.
Aims. This paper considers the constraints on habitability arising from tidal processes with a focus on the evolution of the planet's spin orientation and rate. Since tidal processes are far from being understood and various tidal models are subject to debate, a comparison of commonly used theories is necessary.
Methods. We apply two of the most recent equilibrium tide theories – one of them a constant-phase-lag model, the other one a constant-time-lag model – to compute the obliquity evolution of an Earth-mass and a 10 Earth-mass planet in orbits around LMSs. The time required for the spin to decrease from an Earth-like obliquity of 23.5° to 5°, the tilt erosion time, is compared to the traditional insolation habitable zone (IHZ) in the a-e plane. We also compute maximum and minimum obliquities as a function of a and e, which yield appropriate tidal heating to neither melt the planetary surface nor freeze it tectonically, assumed tidal heating is the major source of internal heating. The Super-Earth Gl581 d is studied as an example for tidal locking.
Results. Earth-like obliquities of terrestrial planets around stars with masses $\lesssim 0.5\,M_\odot$ are eroded within less than 1 Gyr. Terrestrial planets in the IHZ of stars with masses $\approx 0.25\,M_\odot$ undergo significant tidal heating, whereas in the IHZ of stars with masses $\gtrsim 0.5\,M_\odot$ they require additional sources of heat to drive tectonic activity. Here, the predictions of the two tidal models diverge significantly for $e \gtrsim 0.3$. Gl581 d is most likely in a pseudo-synchronous rotation state. In our two-body simulations, its obliquity is eroded to 0° nowadays and its rotational period is about half its orbital period. In general, obliquity prevents a planet from facing its host star with one fixed hemisphere.
Conclusions. Tidal processes under the consideration of planetary obliquities affect the concept of the habitable zone. Rapid tilt erosion of terrestrial planets orbiting LMSs challenge atmospheric modelers.

Key words. Planets and satellites: dynamical evolution and stability – Celestial mechanics – Planetary systems – astrobiology – Stars: low-mass – Planets and satellites: tectonics

1. Introduction

1.1. The role of obliquity for a planetary atmosphere

The obliquity ψ_{p} of a planet, i.e. the angle between its spin axis and the orbital normal, is a crucial parameter for the possible habitability of a planet. On Earth, the Moon stabilizes ψ at roughly 23.5° against chaotic perturbations from the other solar system planets (Laskar et al. 1993). This steady tilt causes seasons and, together with the rotational period of 1 d, assures a smooth temperature distribution over the whole globe with maximum variations of 150 K. Measurements of oxygen isotope ratios of benthic foraminifera ($\delta^{18}O_{\mathrm{b}}$) in deep-sea sediments suggest that changes in the Earth's obliquity have caused phases of glaciations on a global scale (Drysdale et al. 2009). In general, the coupled evolution of eccentricity (e) and obliquity (ψ) has fundamental impact on the global climate of terrestrial planets Dressing et al. (2010), with higher obliquities rendering planets

habitable at larger semi-major axes. Williams & Kasting (1997) investigated varying obliquities for Earth and conclude that a substantial part of the Earth would not be tolerable for life if its obliquity were as high as 90°. Hunt (1982) studied the impact of zero obliquity on the temperature distribution on Earth's and finds a global contraction of the inhabitable area on Earth for such a case. A discussion of the prospects of eukaryotic life to survive a snowball Earth is given by Hoffmann & Schrag (2002).

For obliquities smaller than $\approx 5°$ the habitability of a terrestrial planet might crucially be hindered. Decreasing obliquities induce less seasonal variation of solar insolation between higher and lower latitudes. Thus, winters get milder and summers become cooler. Given that cool summer temperatures turn out to be more important than cold winters for the emergence of continental ice sheets, smaller tilt angles lead to more glaciation. As a consequence, the temperature contrast between polar and equatorial regions gets very strong (Spiegel et al. 2009), possibly leading to a collapse of the potential atmosphere (priv. comm.

Heller et al.: Constraints on habitability from obliquity tides

with Frank Selsis), which freezes out at the poles or evaporates at the equator.

1.2. Tidal effects and planetary obliquity

Until the end of the last decade, the standard scenario of star and planet formation assumed planets forming in a disk around the host star. This disk would be coplanar with the equatorial plane of the star and the planet's spin axis would be aligned with the orbital normal. Meanwhile, observational evidence points towards a more complex formation scenario, where the stellar obliquity, i.e. the misalignment between the stellar rotation axis and the orbital plane normal, depend on stellar and planetary mass (Winn et al. 2010) as well as on the influence of perturbing bodies (Fabrycky & Tremaine 2007). Thus, the spin axis of the planets themselves is not necessarily perpendicular to the orbital plane. The angle between the planetary spin axis and the orbital plane, the obliquity ψ_p, can have any orientation with values $0 \leq \psi_\mathrm{p} \leq 180°$ (Agnor et al. 1999; Chambers 2001; Kokubo & Ida 2007; Miguel & Brunini 2010), where a rotation prograde with the orbital motion means $0 \leq \psi_\mathrm{p} \leq 90°$ and $\psi_\mathrm{p} > 90°$ defines a retrograde planet rotation.

In the course of the planet's lifetime, this possible spin-orbit misalignment can be subject to lockings or severe perturbations, e.g. by a third or more bodies inducing chaotic interaction (Laskar & Joutel 1993; Laskar et al. 1993) or Milankovitch cycles (Milanković 1941; Spiegel et al. 2010); the putative presence of a moon that stabilizes the planet's obliquity as on Earth (Neron de Surgy & Laskar 1997); a perturber that pumps the planet into Cassini states (Gladman et al. 1996) or drives the Kozai mechanism by leverage effects (Kozai 1962; Fabrycky & Tremaine 2007; Migaszewski & Gozdziewski 2010).

Furthermore, tidal interaction between a planet and its host star alters the orbital and eventually also the structural characteristics of the bodies involved. The effects raised by the planet on the star are usually negligible, whereas the evolution of the planet's semi-major axis a, eccentricity e, its rotational period P_rot, and ψ_p can put constraints on its habitability. In the long term, tidal effects reduce a planet's initial obliquity. We call this effect 'tilt erosion'. Given all the dependencies of a planet's climate on the body's obliquity, as described above, an investigation of tilt erosion is required.

Tidal interaction implies exchange of orbital and/or rotational momentum between the bodies. Since the total angular momentum is conserved, orbital energy is transformed into heat and released in the two bodies. This effect, called 'tidal heating', can alter the planet's geology and thus puts also constraints on habitability.

Besides the impact of tilt erosion on the planet's atmosphere and tidal heating on the planet's geology, another threat for its habitability emerges from 'tidal locking'. If zero eccentricity coincides with zero obliquity, the tidal equilibrium rotational period of a planet will equal its orbital period. In the reference system of the synchronously rotating planet, the host star is then static. This configuration would destabilize the planet's atmosphere, where one side is permanently heated and the other one dark. As we will show, obliquities prevent a planet from this fixed rotation state.

1.3. Obliquities and the insolation habitable zone

In previous studies (Barnes et al. 2009a,b), we have investigated the impact of tidal heating on the habitability of exoplanets but not considered the effect of tilt erosion, i.e. the tidal reduction of a planet's obliquity. We investigate here the timescales for tilt erosion of terrestrial planets orbiting low-mass stars (LMS) on the main-sequence. M dwarf stars are considered favorable hosts for habitable planets (Tarter et al. 2007). We search for those locations in the parameter space of e, a, and stellar mass M_s, where obliquities can withstand tilt erosion for long time. These regions are then compared with the traditional insolation habitable zone (IHZ) (Kasting et al. 1993; Selsis et al. 2007; Barnes et al. 2008; Spiegel et al. 2009). We also examine the amount of tidal heating induced by obliquities and compare maximum and minimum tidal surface heating rates to the IHZ. Our models applied below describe the interaction of two bodies: a star and a planet. We neglect relativistic effects and those arising from the presence of a third or more bodies and assume tidal interaction of the planet with its host star as the dominant gravitational process. Our approach does not invoke the geologic or rheological response of the body to the tidal effects.

This article is structured as follows: After this introduction, we devote in Sect. 2 to the two models of equilibrium tide and we motivate our choice of parameter values. In Sect. 3 we describe the constraints that may arise from tidal obliquity processes on the habitability of terrestrial planets, i.e. tilt erosion, tidal heating, and tidal locking. Section 4 is dedicated to the results, in particular to a comparison with the traditional IHZ, while Sect. 5 is dedicated to a discussion of the results. In Sect. 6 we conclude.

2. Methods

2.1. Parametrizing tidal dissipation

There are two concurrent theories of bodily equilibrium tides. The first one, in terms of historical appearance, assumes that the tidal potential of the body, influenced by a gravitational perturber, can be expressed as the sum of Legendre or Fourier polynomials P_l. Each component is assumed to have its own, constant phase lag ε_l (Darwin 1879; Gerstenkorn 1955; Kaula 1964; Peale 1999; Ferraz-Mello et al. 2008) or constant geometric lag angle $\delta_l = \varepsilon_l/2$ (MacDonald 1964), which drives the physical deformation of the body at its own, particular frequency χ_l. With this approach, $\varepsilon_l \sim \chi_l^0$ is assumed although the relationship between ε_l and χ_l is not known a priori (Goldreich 1963). As long as the tidal deformation of the body is small, deviations from the equilibrium shape are assumed to be proportional to the distorting force. By analogy with the driven harmonic oscillator, the tidal dissipation function Q has been introduced, where $Q^{-1} = \tan(\varepsilon_l) = \tan(2\,\delta)$. This parameter is a measure for the tidal energy dissipated in one cycle (Goldreich & Soter 1966). Seismic data argues for $Q \sim \chi_l^\alpha$, with $0.2 \lesssim \alpha \lesssim 0.4$ and $\mathrm{yr}^{-1} \lesssim \chi_l \lesssim 10^7$ Hz (Efroimsky & Lainey 2007b,a). The key flaw of this theory emerges from the fact that this 'lag-and-add' procedure of polynomials P_l is only reasonable if the decomposed tidal potential involves a tight range of tidal frequencies (Greenberg 2009). Hence, it is inherently constricted to low eccentricities and inclinations.

The second tidal theory assumes $\varepsilon \sim \chi^1$, which is equivalent to a fixed time lag τ between the tidal bulge and the line connecting the centers of the two bodies under consideration (Singer 1972; Mignard 1979, 1980; Hut 1981). Both the constant-time-lag (CTL) model and the constant-phase-lag (CPL) model we use are called 'equilibrium tide models' or 'theories of equilibrium tide' since the distorted body is assumed a homogeneous sphere, which continually adjusts to maintain a state of quasi-

Heller et al.: Constraints on habitability from obliquity tides

hydrostatic equilibrium in the varying gravitational potential of its orbital companion. As an example for a comprehensive dynamical tide model, applied to rotating giant planets, see e.g. Ogilvie & Lin (2004).

We use two of the most recent studies on equilibrium tides, one representing the family of CPL models (Ferraz-Mello et al. 2008, FM08 in the following) and one the family of CTL models (Leconte et al. 2010, Lec10 in the following), to simulate the tidal evolution of terrestrial planets around LMSs. Particular attention is drawn to the evolution of the spin-orbit orientation and the rotational period. As test objects we choose an Earth-mass planet and a terrestrial Super-Earth with $M_{\rm p} = 10\, M_{\rm Earth}$, where $M_{\rm p}$ is the mass of the planet and $M_{\rm Earth}$ is the mass of the Earth.

Terrestrial bodies of such masses may have a variety of compositions (Bond et al. 2010), thus their response to tidal processes can differ a lot. Against this background, we choose a value of 0.5 for the radius of gyration $r_{\rm g,p}$ of the terrestrial planet, while the relationship between $M_{\rm p}$ and the planetary radius $R_{\rm p}$ is taken as $R_{\rm p} = (M_{\rm p}/M_{\rm Earth})^{0.27} \times R_{\rm Earth}$ (Sotin et al. 2007). For both the Earth analog and the Super-Earth we choose a tidal dissipation value of $Q = 100$, owing to the values for Earth given by Ray et al. (2001) and Henning et al. (2009). Measurements of the Martian dissipation function $Q_{\rm Mars} = 79.91 \pm 0.69$ (Lainey et al. 2007), as well as estimates for Mercury, where $Q_{\rm Mercury} < 190$, Venus, with $Q_{\rm Venus} < 17$ (Goldreich & Soter 1966), and the Moon, with $Q_{\rm Moon} = 26.5 \pm 1$ (Dickey et al. 1994), indicate a similar order of magnitude for the tidal dissipation function of all terrestrial bodies. For Super-Earths at distances < 1 AU to their host star, the atmospheres are modeled to be no more massive than $\approx 1 M_{\rm Earth}$ (Rafikov 2006), typically much less massive. We thus neglected their contribution to the tidal dissipation of the body. Over the course of the numerical integrations we use a fixed value for Q. In real bodies, Q is a function of the bodies rigidity μ, viscosity η, and temperature T (Segatz et al. 1988; Fischer & Spohn 1990). A comprehensive tidal model would have to couple the orbital with the structural evolution of the involved bodies since small perturbations in T can result in large variations in Q (Mardling & Lin 2002; Efroimsky & Lainey 2007b). To estimate the impact on our results arising from uncertainties in Q, we will show an example where the tidal dissipation function for the Earth-mass planet is varied by a factor of two, to values of 50 and 200, and the dissipation value for the Super-Earth is varied by factor of 5, to values of 20 and 500. Henning et al. (2009) sum up estimates for Q and the Love number of degree 2 or 'semi-diurnal Love number', k_2, for planets in the solar system. They find $k_2 = 0.3$ and $Q = 50$ the most reasonable choice for an Earth-like planet (for the relationship between Q and k_2 see Henning et al. 2009). We take $Q_{\rm p} = 100$ and $k_2 = 0.3$ (Yoder 1995) for the terrestrial planets, consistent with our previous studies. With $Q' = 3/2 \times Q/k_2$ we thus have $Q'_{\rm p} = 500$. For the CPL model of FM08 we assume the dynamical Love number of the ith body, $k_{\rm d,i}$, to be equal to $k_{2,i}$. As tidal dissipation value for the star we take $Q_{\rm s} = 10^5$ (Heller et al. 2010).

The tidal time lag τ of Earth with respect to the Moon as a tide raiser has been estimated to 638 s (Neron de Surgy & Laskar 1997) and ≈ 600 s (Lambeck 1977, p. 562 therein). We apply the more recent value of 638 s to model the tidal evolution of the Earth-mass planet with the CTL model.

2.2. Tidal model #1: constant phase lag

The reconsideration of Darwin's theory (Darwin 1879, 1880) by FM08 is restricted to low eccentricities and inclinations. To compute the orbital evolution of the star-planet system self-consistently, we numerically integrate a set of six coupled differential equations for the eccentricity e, the semi-major axis a, the two rotational frequencies ω_i ($i \in \{\rm s, p\}$, where the subscripts 's' and 'p' refer to the star and the planet, respectively), and the two obliquities ψ_i given by

$$\frac{{\rm d}e}{{\rm d}t} = -\frac{ae}{8GM_1M_2} \sum_{i \neq j} Z_i' \left(2\varepsilon_{0,i} - \frac{49}{2}\varepsilon_{1,i} + \frac{1}{2}\varepsilon_{2,i} + 3\varepsilon_{5,i} \right) \quad (1)$$

$$\frac{{\rm d}a}{{\rm d}t} = \frac{a^2}{4GM_1M_2} \sum_{i \neq j} Z_i' \left(4\varepsilon_{0,i} + e^2 \Big[-20\varepsilon_{0,i} + \frac{147}{2}\varepsilon_{1,i} + \right.$$
$$\left. \frac{1}{2}\varepsilon_{2,i} - 3\varepsilon_{5,i} \Big] - 4\sin^2(\psi_i)\big[\varepsilon_{0,i} - \varepsilon_{8,i}\big] \right) \quad (2)$$

$$\frac{{\rm d}\omega_i}{{\rm d}t} = -\frac{Z_i'}{8M_i r_{\rm g,i}^2 R_i^2 n} \left(4\varepsilon_{0,i} + e^2 \Big[-20\varepsilon_{0,i} + 49\varepsilon_{1,i} + \varepsilon_{2,i} \Big] + \right.$$
$$\left. 2\sin^2(\psi_i)\big[-2\varepsilon_{0,i} + \varepsilon_{8,i} + \varepsilon_{9,i} \big] \right) \quad (3)$$

$$\frac{{\rm d}\psi_i}{{\rm d}t} = \frac{Z_i' \sin(\psi_i)}{4M_i r_{\rm g,i}^2 R_i^2 n\omega_i} \left(\big[1 - \xi_i\big]\varepsilon_{0,i} + \big[1 + \xi_i\big]\big\{\varepsilon_{8,i} - \varepsilon_{9,i}\big\} \right). \quad (4)$$

In these equations, Z_i' stands for

$$Z_i' := 3G^2 k_{\rm d,i} M_j^2 (M_i + M_j) \frac{R_i^5}{a^9} \frac{1}{nQ_i}, \quad (5)$$

$\xi_i := r_{\rm g,i}^2 R_i^2 \omega_i an/(GM_j)$, G is Newton's gravitational constant, n is the orbital mean motion or orbital frequency, M_i is the mass of the ith body, and R_i its mean radius. The algebraic signs of the tidal phase lags are given by

$$\varepsilon_{0,i} = \Sigma(2\Omega_i - 2n)$$
$$\varepsilon_{1,i} = \Sigma(2\Omega_i - 3n)$$
$$\varepsilon_{2,i} = \Sigma(2\Omega_i - n)$$
$$\varepsilon_{5,i} = \Sigma(n)$$
$$\varepsilon_{8,i} = \Sigma(\Omega_i - 2n)$$
$$\varepsilon_{9,i} = \Sigma(\Omega_i), \quad (6)$$

with $\Sigma(x)$ as the sign of any physical quantity x, thus $\Sigma(x) = +1 \lor -1$.

2.3. Tidal model #2: constant time lag

Lec10 extended the model presented by Hut (1981) to arbitrary eccentricities and inclinations. For convenience and to ease comparison with tidal model #1, we translate their equations for the evolution of the orbital parameters into

Heller et al.: Constraints on habitability from obliquity tides

$$\frac{\mathrm{d}e}{\mathrm{d}t} = \frac{11ae}{2GM_1M_2}\sum_{i\neq j}Z_i\left(\cos(\psi_i)\frac{f_4(e)}{\beta^{10}(e)}\frac{\omega_i}{n} - \frac{18}{11}\frac{f_3(e)}{\beta^{13}(e)}\right) \quad (7)$$

$$\frac{\mathrm{d}a}{\mathrm{d}t} = \frac{2a^2}{GM_1M_2}\sum_{i\neq j}Z_i\left(\cos(\psi_i)\frac{f_2(e)}{\beta^{12}(e)}\frac{\omega_i}{n} - \frac{f_1(e)}{\beta^{15}(e)}\right) \quad (8)$$

$$\frac{\mathrm{d}\omega_i}{\mathrm{d}t} = \frac{Z_i}{2M_ir_{g,i}^2R_i^2n}\left(2\cos(\psi_i)\frac{f_2(e)}{\beta^{12}(e)} - \left[1+\cos^2(\psi)\right]\frac{f_5(e)}{\beta^9(e)}\frac{\omega_i}{n}\right) \quad (9)$$

$$\frac{\mathrm{d}\psi_i}{\mathrm{d}t} = \frac{Z_i\sin(\psi_i)}{2M_ir_{g,i}^2R_i^2n\omega_i}\left(\left[\cos(\psi_i) - \frac{\xi_i}{\beta}\right]\frac{f_5(e)}{\beta^9(e)}\frac{\omega_i}{n} - 2\frac{f_2(e)}{\beta^{12}(e)}\right) \quad (10)$$

where

$$Z_i := 3G^2k_{2,i}M_j^2(M_i + M_j)\frac{R_i^5}{a^9}\tau_i, \quad (11)$$

$k_{2,i}$ is the potential Love number of degree 2 of the ith body, and the extension functions in e are given by

$$\begin{aligned}
\beta(e) &= \sqrt{1-e^2}, \\
f_1(e) &= 1 + \frac{31}{2}e^2 + \frac{255}{8}e^4 + \frac{185}{16}e^6 + \frac{25}{64}e^8, \\
f_2(e) &= 1 + \frac{15}{2}e^2 + \frac{45}{8}e^4 + \frac{5}{16}e^6, \\
f_3(e) &= 1 + \frac{15}{4}e^2 + \frac{15}{8}e^4 + \frac{5}{64}e^6, \\
f_4(e) &= 1 + \frac{3}{2}e^2 + \frac{1}{8}e^4, \\
f_5(e) &= 1 + 3e^2 + \frac{3}{8}e^4,
\end{aligned} \quad (12)$$

following the nomenclature of Hut (1981). For $\tau_i = 1/(nQ_i)$ one finds $Z' = Z$.

Though the total angular momentum of the binary is conserved, the tidal friction induces a conversion from kinetic and potential energy into heat, which is dissipated in the two bodies. The tidal heating rate in the ith body is given by

$$\dot{E}_{\mathrm{tid},i} = Z_i\Big(\frac{f_1(e)}{\beta^{15}(e)} - 2\frac{f_2(e)}{\beta^{12}(e)}\cos(\psi_i)\frac{\omega_i}{n} + \left[\frac{1+\cos^2(\psi_i)}{2}\right]\frac{f_5(e)}{\beta^9(e)}\left\{\frac{\omega_i}{n}\right\}^2\Big). \quad (13)$$

If we assume a pseudo-synchronized orbit of the planet, i.e. $\mathrm{d}\omega/\mathrm{d}t = 0$, where the equilibrium rotation rate is given by

$$\omega_p^{\mathrm{equ.}} = n\frac{f_2(e)}{\beta^3(e)f_5(e)}\frac{2\cos(\psi_p)}{1+\cos^2(\psi_p)} \quad (14)$$

(see also Levrard et al. 2007; Wisdom 2008), then Eq. (13) can be written as

$$\dot{E}_{\mathrm{tid},p}^{\mathrm{equ.}} = \frac{Z_p}{\beta^{15}}\left[f_1 - \frac{f_2^2}{f_5}\frac{2\cos^2(\psi_p)}{1+\cos^2(\psi_p)}\right]. \quad (15)$$

This function of ψ_p has its minimum at $\psi_p = 0°$ and its maximum at $\psi_p = 90°$. Higher obliquities yield higher tidal heating rates as long as $\psi_p < 90°$. For $\psi_p \geq 90°$ tidal heating becomes

less intense and the transformation $\psi_p \rightarrow \pi - \psi_p$ results in identical physical states.

Instead of a fixed value for the tidal dissipation function Q_i this model assumes a fixed time lag τ_i between the tidal bulge of the deformed – the ith – body and the line connecting its center of gravity with the center of mass of the perturber. We estimate τ_p as described at the end of Sect. 2.1, and apply a fixed $\tau_s = 1/(Q_s n_{\mathrm{ini}})$, where n_{ini} is the orbital mean motion at the beginning of the integration. Over the course of the integration, τ_p and τ_s are fixed (see also footnote no. 2 in Heller et al. 2010).

2.4. Comparison of both tidal models

Both models converge for a limiting case, namely when both $e \rightarrow 0$ and $\psi \rightarrow 0$. If we assume that tides have circularized the orbit and the rotation rate of the planet has been driven close to its equilibrium rotation, which corresponds to $n \approx \omega_p$ in the CPL model, then the tidal phase lags become $\varepsilon_{0,i} \approx 0$, $\varepsilon_{1,i} \approx -1$, $\varepsilon_{2,i} \approx 1$, $\varepsilon_{5,i} \approx 1$, $\varepsilon_{8,i} \approx -1$, and $\varepsilon_{9,i} \approx 1$. As an example we consider the differential equation for the evolution of the obliquity. The other equations behave similarly. For $e = 0$ and $\psi_i = 0$ Eq. (4) from the CPL model transforms into

$$\frac{\mathrm{d}\psi_i}{\mathrm{d}t} = -\frac{Z_i'\sin(\psi_i)}{2M_ir_{g,i}^2R_i^2n\omega_i}\left[1+\xi_i\right], \quad (16)$$

while Eq. (10) from the CTL model at first order in ψ and for $e = 0$ gives

$$\frac{\mathrm{d}\psi_i}{\mathrm{d}t} = -\frac{Z_i\sin(\psi_i)}{2M_ir_{g,i}^2R_i^2n\omega_i}\left[1+\xi_i\right]. \quad (17)$$

Equation (16) and Eq. (17) coincide for $\tau_i = 1/(nQ_i)$, which is the value of the specific dissipation function for a quasi-circular pseudo-synchronous planet (see Sect. 3 in Lec10).

3. Constraints on habitability from obliquity tides

3.1. Tilt erosion

As 'tilt erosion time' t_{ero} we here define the time that is required by tidal processes to reduce an initial Earth-like obliquity of 23.5° to 5°. We numerically integrate the two sets of coupled equations from Sects. 2.2 and 2.3, respectively, to derive t_{ero} as a projection onto the e-a plane as well as on the M_s-a plane. We choose two different planetary masses: an Earth-twin of one Earth mass and a Super-Earth of of 10 Earth masses.

Both planets are released with initial rotational periods of 1 d in the relevant regions of the initial e-a space around stars with masses of 0.1, 0.25, 0.5, and 0.75 $M_\odot$. We also place the two planets in a parameter plane spanned by $0 \leq M_s \leq 1 M_\odot$ and initial semi-major axes $0 \leq a \leq 1$ AU with two different initial eccentricities, $e = 0.01$ and $e = 0.5$. Here, AU $:= 149.598 \times 10^9$ m is an abbreviation for an astronomical unit, i.e. the mean distance between the Earth and the Sun.

3.2. Tidal heating from obliquity tides

Various astrophysical phenomena can maintain significant eccentricities and obliquities over time scales much larger than the erosion time scales to be computed with the equations above for the 2-body interaction of a star and a planet. Planets can be caught in Cassini states, they may undergo Kozai oscillations or

4

Milanković cycles and they can mutually scatter their orbital elements. Recently, McArthur et al. (2010) measured the angle between the orbital planes of the two extrasolar planets υ And A c and υ And A d to be $29.9° \pm 1°$. In the planetary system around Gl581, the orbits of planet d and e are likely to be inclined by $\approx 30°$ (Barnes et al. 2010a, submitted). The orbital obliquities, i.e. the angles between the orbital plane normals and the stellar spin axis, of these planets are significant and since orbital oscillations occur on time scales of 10^3 yr (Barnes et al. 2008) bodily obliquities will be significant in those orbital regions where $t_{ero} \gg 10^3$ yr (Barnes et al. 2010b). In general, for those cases where $e \neq 0$ and/or $\psi_p \neq 0$ tidal heating on the planet can significantly alter the body's structure and evolution and can thus raise constraints on its habitability.

On the rocky moon Io, surface heating rates of $2\,W/m^2$ (Spencer et al. 2000), excited by tidal distortions from Jupiter, are correlated with global volcanism. While surface tidal heating rates may serve as an tentative upper limit for a planet's habitability, depending on its structural and compositional nature, another key surface heating rate, to be used as a lower limit in terms of habitability, can be found for such planets, where tidal heating is the major source of inner energy that could drive geologic activity. The role of plate tectonics for the emergence and survival of life is being discussed, e.g. in Kasting & Catling (2003) and Gaidos et al. (2005). In the terrestrial planets of the solar system, as well as in the Moon, the radiogenic decay of long-lived isotopes ^{40} K, ^{232} Th, ^{235} U, and ^{238} U provided an energy source that drove or drives structural convection (Spohn 1991; Gaidos et al. 2005). The today output of radioactive decay on Earth is $0.04\,W/m^2$ (Zahnle et al. 2007). While an Earth-sized object obviously can maintain its radiogenic heat source for several Gyr, the heat flow in a Mars-sized planet decreases much more rapidly. Early Mars tectonically froze when its surface heating rates, driven by radiogenic processes and not by tides, dropped below $0.04\,W/m^2$ Williams et al. (1997). Currently its surface rates due to radiogenic processes are $\approx 0.03\,W/m^2$ (Spohn 1991). Obliquity tides may deliver a source of energy sufficient to drive tectonic mechanisms of exoplanets near or in the IHZ of LMSs.

As given by Eq. (13), tidal heating rates are a function of a body's obliquity. Assume a certain surface heating rate $h_p^{equ.} = \dot{E}_{tid,p}^{equ.}/(4\pi R_p^2)$ is given for a planet in equilibrium rotation, then Eq. (15) can be solved for the corresponding tilt:

$$|\psi_p^{equ.}| = \arccos\left(\sqrt{\cfrac{1}{1 + \left(\cfrac{h_p^{equ.}\,4\pi R_p^2 \beta^{15}(e)}{2Z_p} - f_1(e)\right)\cfrac{f_5(e)}{f_2^2(e)}}} - 1\right)$$

(18)

for $h_i^{equ.}\,4\,\pi\,R_i^2/Z < f_1(e)/\beta^{15}(e)$.

For a given stellar and planetary mass we use Eq. (18) to calculate the obliquities $|\psi_{min}^{equ.}|$ and $|\psi_{max}^{equ.}|$ of a planet corresponding to the minimum and maximum surface heating rates of $0.04\,W/m^2$ and $2\,W/m^2$, respectively, as a projection the e-a plane. Close to the star tidal heating will be $\gg 2\,W/m^2$ even without heating from obliquity tides, whereas in the outer regions obliquity tides may push the rates above the $2\,W/m^2$ threshold or not – depending on the actual obliquity. Further outside, there will be a minimum obliquity necessary to yield $h_p^{equ.} = 0.04\,W/m^2$. We should bare in mind that these key heating rates of $0.04\,W/m^2$ and $2\,W/m^2$ are empirical examples taken from two special cases the Solar System. Depending on

a planet's structure, composition, and age these thresholds may vary significantly. Comprehensive simulations require coupled evolutions of the bodies' orbits and interiors (Segatz et al. 1988).

The model presented by FM08 was developed for the cases of small eccentricities and low inclinations. Thus, an application of the $|\psi_{min}^{equ.}|$ and $|\psi_{max}^{equ.}|$ concept to FM08 would not be reasonable.

3.3. Tidal locking

A widely spread misapprehension is that a tidally locked body permanently turns one side to its host (e.g. in Neron de Surgy & Laskar 1997; Joshi et al. 1997; Grießmeier et al. 2004; Khodachenko et al. 2007). Various other studies only include the impact of eccentricity on tidal locking, neglecting the contribution from obliquity (Goldreich & Soter 1966; Goldreich 1966; Eggleton et al. 1998; Trilling 2000; Showman & Guillot 2002; Dobbs-Dixon et al. 2004; Selsis et al. 2007; Barnes et al. 2008; Ferraz-Mello et al. 2008). As given by Eq. (14), one side of the planet is only permanently orientated towards the star if both $e = 0$ and $\psi = 0$. In this special case, habitability of a planet can potentially be ruled out when the planet's atmosphere freezes out on the dark side and/or evaporates on the bright side (Joshi et al. 1997). As long as e and ψ are not eroded, however, the planet is prevented from an $\omega_p = n$ locking. In addition to atmospheric instabilities arising from $\omega_p = n$, slow rotation may result in small intrinsic magnetic moments of the planet. This may result in little or no magnetospheric protection of planetary atmospheres from dense flows of coronal mass ejection plasma of the host star (Khodachenko et al. 2007). Again, since obliquities prevent a synchronous rotation of the planet with the orbit, its magnetic shield can be maintained.

3.4. Compatibility with the insolation habitable zone

Our constraints on habitability from obliquity tides are embedded in the IHZ as presented by Barnes et al. (2008), who enhanced the model of Selsis et al. (2007) to arbitrary eccentricities. Accordingly, we assume the planets to have a 50 % cloud cover (Selsis et al. 2007).

First forms of life on Earth required between 300 and 1800 Myr to emerge (Gaidos et al. 2005). During this period, before the so-called Great Oxidation Event $\approx 2500\,Myr$ ago (Anbar et al. 2007), microorganisms may have played a major role in the evolution of Earth's atmosphere (Kasting & Siefert 2002), probably enriching it with CH_4 (methane) and CO_2 (carbon dioxide). On geological times it was only recently that life conquered the land, about 450 Myr ago in the Ordovician (Kenrick & Crane 1997; Kenrick 2003). Therefore we assume that a planet needs to provide habitable conditions for at least 1000 Myr for life to imprint its spectroscopic signatures in the planet's atmosphere (Seager et al. 2002; Jones & Sleep 2010) or to leave photometrically detectable traces on the planet's surface (Fujii et al. 2010). This is relevant from an observational point of view since the spectra of Earth-like planets will be accessible with upcoming space-based missions such as Darwin (Ollivier & Léger 2006; Leger & Herbst 2007) and the Terrestrial Planet Finder (Kaltenegger et al. 2010a). Since green is a color often used to symbolize confidence, we fill zones in our plots with $t_{ero} > 10^3$ Myr in green.

Heller et al.: Constraints on habitability from obliquity tides

4. Results

4.1. Time scales for tilt erosion

We plot t_{ero} for an Earth twin and a 10-Earth-mass planet orbiting a 0.1, 0.25, 0.5, and a $0.75\,M_{\odot}$ star, respectively, over a parameter plane spanned by e and a. In Fig. 1 we show the results for FM08, in Fig. 2 we present the outcome for Lec10. In Figs. 3 and 4 we plot t_{ero} for the two planets for a range of stellar masses and semi-major axes, for the two cases of $e = 0.01$ and $e = 0.5$. An error estimate emerging from uncertainties in Q is given in Figs. 1 and 2.

The IHZs are highlighted in blue, whereas the zones for $t_{\text{ero}} > 10^3$ Myr are colored in green. Looking at any panel in Figs. 1 and 2, one finds t_{ero} increasing with increasing initial distance from the star as well as with decreasing eccentricity. In eccentric orbits at short orbital distances the obliquity is eroded most rapidly. For the FM08 model we see that the IHZ does not coincide with the green areas as long as $M_{\text{s}} \lesssim 0.5\,M_{\odot}$ for both planets. While for $M_{\text{s}} = 0.5\,M_{\odot}$ only the outer orbital regions of the IHZ are overlapped by green areas for both planets, for $M_{\text{s}} \approx 0.75\,M_{\odot}$ essentially the whole IHZ is totally covered by the green. Although we do not show the corresponding figures, we find that if the star has a mass $\gtrsim 1\,M_{\odot}$ the IHZ is completely covered with $t_{\text{ero}} > 10^4$ Myr – for all the three reasonable Q values of both planets.

The calculations following Lec10 (Fig. 2) yield qualitatively similar results for small eccentricities. However, for $e \gtrsim 0.3$ their mismatch is of the same order of magnitude as the uncertainty in the tidal dissipation function Q (see the $0.25\,M_{\odot}$ row). For these high eccentricities, the CTL model of Lec10 predicts significantly smaller tilt erosion times, where the discrepancy is also stronger for lower-mass stars.

The projection of t_{ero} onto the M_{s}-a plane using the FM08 model is shown in Fig. 3. While the IHZs of the Earth mass planet are covered by the green zones only for $a \gtrsim 0.3$ AU and $M_{\text{s}} \gtrsim 0.4\,M_{\odot}$ at $e = 0.01$ (upper left panel) and only for $a \gtrsim 0.35$ AU and $M_{\text{s}} \gtrsim 0.45\,M_{\odot}$ at $e = 0.5$ (lower left panel), the physical inertia of the $10\,M_{\text{Earth}}$ Super Earth assures that the initial obliquity of $23.5°$ is washed out on timescales $> 10^3$ Myr even for tighter orbits and lower-mass stars at both eccentricities. Comparing the different lines, corresponding to $e = 0.01$ at the top and $e = 0.5$ at the bottom, one sees that higher eccentricities only tend to erode the spin slightly faster.

The higher order terms of e in the equations of Lec10 produce a large variation of the locations of the green areas between $e = 0.01$ (upper panel) and $e = 0.5$ (lower panel) in Fig. 4. While the results for $e = 0.01$ almost coincide with those of the FM08 model, the discrepancies to the case of $e = 0.5$ are significant. Using Lec10's model, Earth-like planets in such highly eccentric orbits around LMSs turn out to be subject to rapid spin-orbit alignment. The magnification of tidal effects at high eccentricities is due to the plummet of the mean orbital distance in eccentric orbits and is enhanced by the steep dependency of tidal effects on a (Wisdom 2008; Leconte et al. 2010). An initial semi-major axes $\gtrsim 0.45$ AU and a host star with $M_{\text{s}} \gtrsim 0.5\,M_{\odot}$ is required for a terrestrial planet to keep an obliquity $\gtrsim 5°$ longer than $\approx 10^3$ yr if $e \gtrsim 0.5$. The Super-Earth at $e = 0.5$ is resistive to tilt erosion also at smaller orbits and requires only $\gtrsim 0.4$ AU and $M_{\text{s}} \gtrsim 0.45\,M_{\odot}$ to keep $\psi_{\text{p}} \gtrsim 5°$ for the same time.

4.2. Tidal heating from obliquity tides

In Fig. 5 we plot ψ_{max} and ψ_{min} as a function of a and e for the same stellar and planetary masses as used above in Figs. 1 and 2. Calculations are based on the equilibrium CTL model by Lec10. The red zone indicates that even for the case of vanishing spin-orbit misalignment, corresponding to $\psi_{\text{max}} < 1°$, tidal surface heating rates are $> 2\,\text{W/m}^2$. Starting from left, the contours illustrate a maximum obliquity of $1°, 20°, 30°, 40°, 50°, 60°, 70°, 80°$, and $89°$, all of which produce $h_{\text{p}}^{\text{equ.}} = 2\,\text{W/m}^2$ at their respective localization in the a-e plane. Green in Fig. 5 depicts a region where neither any obliquity produces tidal surface heating rates $> 2\,\text{W/m}^2$ nor any minimum obliquity is required to yield tidal surface heating rates $> 0.04\,\text{W/m}^2$. The 9-tuple of contour lines for ψ_{min} refers to obliquities of $1°, 20°, ..., 80°$, and $89°$ providing $h_{\text{p}}^{\text{equ.}} = 0.04\,\text{W/m}^2$ at their respective localization. Smaller obliquities lead to less tidal heating. In the blue zone finally, not even a planet with a rotational axis perpendicular to the orbital plane normal, e.g. $\psi_{\text{p}} = 90°$, yields $h_{\text{p}}^{\text{equ.}} \approx 0.04\,\text{W/m}^2$.

Earth-like planets as well as Super-Earths in the inner IHZ of stars with masses $\approx 0.1\,M_{\odot}$ are subject to intense tidal heating. Only for planets in low-eccentric orbits at the outer IHZ of $\approx 0.1\,M_{\odot}$ stars tidal heating may have minor effects on the planet's structure. With increasing stellar mass the IHZ is shifted to wider orbits, whereas the green stripe of moderate tidal heating is located at roughly the same position in all the 8 panels of Fig. 5. This is due to the weak sensitivity of $\psi_{\text{p}}^{\text{equ.}}$ on M_{s} in Eq. (18). The IHZ of a $0.25\,M_{\odot}$ star nicely covers the zone with moderate tidal heating. In these overlapping regions, adequate stellar insolation meets tolerable tidal heating rates. Only highly eccentric orbits at the inner IHZ are subject to extreme tidal heating. Terrestrial planets in the IHZ of $0.5\,M_{\odot}$ stars do not undergo intense tidal heating. Only at the inner border of the IHZ $h_{\text{p}}^{\text{equ.}} \approx 1\,\text{W/m}^2$ for high obliquities, while at the outer regions tidal heating rates are of order $10\,\text{mW/m}^2$ and smaller. For terrestrial planets in the IHZ of stars with masses $\gtrsim 0.75\,M_{\odot}$ tidal heating has negligible impact on the evolution of the planet's structure and does not induce constraints on the planet's habitability.

4.3. Gl581 d as an example for tidal locking

Gl581 d is a $M_{\text{p}} \gtrsim 7.1\,M_{\text{Earth}}$ Super-Earth, grazing the outer rim of the IHZ of its $M_{\text{s}} \approx 0.31\,M_{\odot}$ host star (Selsis et al. 2007; von Bloh et al. 2007; Beust et al. 2008; Barnes et al. 2009a; Mayor et al. 2009; Wordsworth et al. 2010). The apoastron is situated outside the IHZ whereas the periastron is located inside. While the solar constant, i.e. the solar energy flux per time and area on Earth, is about $1000\,\text{W/m}^2$ when the Sun is in the zenith[1], the stellar incident flux on Gl581 d averaged over an orbit (Williams & Pollard 2002) is

$$f = \frac{L_{\text{Gl581}}}{4\pi a^2 \sqrt{1-e^2}} \approx 432\,\text{W/m}^2, \qquad (19)$$

with the luminosity of the host star $L_{\text{Gl581}} = 0.013\,L_{\odot}$ (Bonfils et al. 2005a; Mayor et al. 2009). If the absorbed stellar flux per unit area is larger than $\approx 300\,\text{W/m}^2$, runaway greenhouse effects may turn a terrestrial planet inhabitable (Zahnle et al. 2007; Selsis et al. 2007, and references therein). Thus, the maximum

---

[1] Outside of the Earth's atmosphere, i.e. at the distance of 1 AU from the Sun, the solar constant is about $1400\,\text{W/m}^2$.

Heller et al.: Constraints on habitability from obliquity tides

bond albedo for Gl 581 d compatible with this habitability criterion is $300/432 \approx 0.7$. Tidal locking in this potentially habitable planet could have a substantial impact on the atmospheric conditions on this planet (Kaltenegger et al. 2010b).

We choose this body as an example to study the evolution of the planet's orbit with a focus on its rotational period. A comparison between the FM08 and the Lec10 model is applied where it is reasonable. As shown in the right panel of Fig. 6, both models tell that the obliquity has been eroded over the course of the system's evolution, assumed no perturbations from other bodies. At an age of $\gtrsim 2$ Myr (Bonfils et al. 2005b) tidal processes would have pushed an Earth-like initial obliquity to zero and the rotation is most likely caught in its equilibrium state. For the model of Lec10, the numeric solution for the equilibrium rotation period of $P_{\text{equ.}} \approx 35$ d (left panel in Fig. 6) can also be calculated analytically with Eq. (14) using the observed eccentricity $e = 0.38^{\pm 0.09}$ and assuming that the spin axis is co-aligned with the orbit normal, $\psi_{\text{p}} = 0°$. We have also calculated the evolution of a and e and find no significant changes during the current lifetime of the system.

As given by Eq. (14) from the CTL theory and as explained in Sect. 3.3, the equilibrium rotational period is a function of e and ψ_{p}. We calculate the equilibrium rotation period $P_{\text{equ.}}$ as a function of the obliquity ψ_{p} for a set of eccentricities (Fig. 7). The most likely true value of $P_{\text{equ.}} \approx 35$ d, corresponding to $e = 0.38$ and $\psi_{\text{p}} \lesssim 40°$, can be inferred from the gray line in Fig. 7 for $e = 0.4$. Since the observed orbital period of Gl 581 d is ≈ 68 d, Fig. 7 shows that Gl 581 d does not permanently turn one hemisphere towards its host star, except for the case of $\psi_{\text{p}} \approx 74°$. Only then $P_{\text{orb.}} \approx P_{\text{rot.}}$.

In Fig. 8 we present the tidal surface heating rate of Gl 581 d as a function of the putative obliquity. Since the orbit is currently tilted against the orbit of Gl 581 e with an angle of $\approx 30°$ (Barnes et al. 2010a, submitted) it is probably subject to considerable interactions with the other planets of the system. Thus, the obliquity of the planet itself might be significant. Between spin-orbit alignment ($\psi_{\text{p}} = 0°$) and a planetary spin axis perpendicular to the orbital plane ($\psi_{\text{p}} = 90°$) tidal surface heating rates range from ≈ 0.007 W/m^2 to ≈ 0.05 W/m^2.

Moreover, the eccentricity of Gl 581 d could be subject to fluctuations. In the history of the planet e might have been significantly larger then its current value, which could have caused tidal surface heating rates of order of a few W/m^2. We find $e = 0.7$ to be the eccentricity, where $h_{\text{Gl581 d}}^{\text{equ.}} > 2$ W/m^2 for any obliquity.

5. Discussion

Our results, especially those for tilt erosion and tidal locking, picture scenarios for atmosphere modelers. Given the mass and the age of a star, as well as the orbital parameters of the planet, our estimates of the tilt erosion time scales indicate whether a significant obliquity of the planet is likely. This evaluation will allow to estimate the equilibrium rotation period of the planet. Both the estimates for the potential of the planet's obliquity and its pseudo-synchronous rotation period will help to model the planet's atmosphere in more detail than only based on its dynamical mass (by radial velocity detection) or true mass (for transiting planets), a, and e.

Our exploration of tidal heating will be relevant for structural evolution models of terrestrial planets. Vice versa, due to the feedback between tidal heating and structural evolution, a self-consistent and coupled treatment of both phenomena will make our results more accurate. Mantle convection is modeled

to be damped in Super-Earths. With increasing, mass a conductive lid forms over the convective lid inside the planet, reducing its efficiency to transport heat from the core to the surface (Stamenkovic et al. 2009). This process counteracts the generation of plate tectonics and of a magnetic field and poses a serious threat for life since cosmic radiation is not shielded on such planets. LMSs are particularly active and may thus sterilize the surface of rocky planet in their IHZ with X-rays. The additional amount of tidal heating in Super-Earths, however, might alter their rheology (Plesa & Breuer 2009), i.e. their viscous qualities, and yield a crucial contribution to their inner heating budget, supporting geological convection. Hence, tidal heating could in fact work in favor for habitability of Super-Earths.

The tidal heating rate, as given by the model of Lec10, is a function of e and ψ_{p}. For Gl 581 d we find that the tidal surface heating rate of Gl 581 d is 0.007 W/m$^2 \lesssim h_{\text{Gl581 d}}^{\text{equ.}} \lesssim 0.5$ W/m^2. This is in line with the value of 0.01 W/m^2 found by Barnes et al. (2009a), who neglected the planet's obliquity. We also explore $h_{\text{Gl581 d}}^{\text{equ.}}$ as a function of the planet's eccentricity and find that if e has ever been $\gtrsim 0.7$, then tidal heating might have posed a threat to putative life on Gl 581 d. Selsis et al. (2007) approximated the rotational synchronization time of the planet to be 10^7 yr, concluding that the planet has one permanent day side and night side. Indeed, with the revised value of $e = 0.38^{\pm 0.09}$ (Mayor et al. 2009) we find that the tidal equilibrium rotation occurs after $\approx 2 \times 10^7$ yr. However, the equilibrium rotational period of the planet, as calculated with Lec10's ansatz, turns out to be $P_{\text{Gl581 d}}^{\text{equ.}} \approx 35$ d $\approx P_{\text{orb.}}/2$. Correia et al. (2008) have approached the issue of equilibrium rotation of terrestrial planets for low eccentricities and obliquities. For Gl 581 d they found $\omega_{\text{Gl581 d}}^{\text{equ.}}/n \approx 1.25 \Leftrightarrow P_{\text{Gl581 d}}^{\text{equ.}} \approx 54.4$ d.

The semantics of the terms 'tidal locking' and 'synchronous rotation' carry the risk to cause confusion. Wittgenstein (1953, PU in the following) has pointed out that the meaning of a word is given by its usage in the language (see §30, 43, and 432 in PU). However, 'tidal locking' and 'synchronous rotation' are used ambiguously in the literature (see Sect. 3.3), thus their meanings remain diffuse. While some authors simply refer to 'tidal locking' as the state where a planet permanently turns one hemisphere towards its host star, others use it in a more general sense of tidal equilibrium rotation. We caution that tidal processes drive the planetary rotation period to be equal to its orbital period only if $e = 0$ and $\psi_{\text{p}} = 0$. If a planet with $e \neq 0$ or $\psi_{\text{p}} \neq 0$ is said to be tidally locked, then it is clear that tidal locking dues not depict the state of the planet turning one hemisphere permanently to its star. And the rotation period of the planet will not be synchronized with respect to its orbit, if 'synchronous' here means 'equal' or 'identical'.

Uncertainties in our calculations arise from the assumption of a constant tidal dissipation in the planets, parametrized by the tidal dissipation factor Q. For one thing, merging all the geophysical effects such as composition, viscosity, temperature distribution, and pressure in one parameter unquestionably is an oversimplification. In addition, it is unknown how Q depends on the respective tidal frequency. Although on Earth Q is constant over a a wide range of frequencies, the behavior will be different for different objects. The Q value of extrasolar planets remains to be estimated, either by observational constraints or theory. For another thing, whatever Q value will turn out to describe terrestrial planets most reasonably, it will be a function of time due to the structural and rheological evolution of the planet. The assumption of a tidal time lag τ between the tidal bulge and the

Heller et al.: Constraints on habitability from obliquity tides

tide raiser may prove to be a more realistic description of tidal interaction.

6. Conclusions

Tidal processes raise severe constraints on the habitability of terrestrial planets in the IHZ of LMSs. First, tidal erosion of the obliquities, i.e. 'tilt erosion', of such planets occurs on time scales much shorter than required for the emergence of life. Planets with masses $\lesssim 10 \, M_{\rm Earth}$ orbiting $\lesssim 0.25 \, M_\odot$ stars in the IHZ lose initial Earth-like spins of $23.5°$ within less than $100 \, {\rm Myr}$, typically much faster. Further gravitational processes, such as the entourage of massive moons, the Kozai mechanism, or planet-planet scattering, are required to maintain significant obliquities.

Second, tidal heating of Earth-like planets in the IHZ of stars with $\lesssim 0.25 \, M_\odot$ is significant. Depending on the body's obliquity, orbital semi-major axis, eccentricity, and its structural composition, a terrestrial planet in the IHZ of a $\lesssim 0.25 \, M_\odot$ host star can undergo intense tidal heating with tidal surface heating rates of order of a few W/m^2. Simulations of coupled orbital-structural evolution of Earth-like planets are necessary to further explore the effect of tidal heating on habitability.

Third, tidal locking is a function of the planet's eccentricity and its obliquity. As long as the planet maintains a significant obliquity or eccentricity, its rotational equilibrium period will not match the orbital period. As an example, the equilibrium rotation period of the extrasolar Super-Earth Gl581 d is about $35 \, {\rm d}$. With an orbital period of $\approx 68 \, {\rm d}$, we find $P_{\rm Gl581d}^{\rm equ.} \approx P_{\rm orb.}/2$.

For low eccentricities ($e \lesssim 0.2$) and low inclinations ($\psi_{\rm p} \lesssim$ a few degrees), the CPL model of FM08 and the CTL model of Lec08 mathematically converge. In our calculations of the time scales required for tilt erosion (Sect. 4) they provide similar results in the low-eccentricity regime. For higher values of e and $\psi_{\rm p}$, tidal processes described by Lec08 occur on significantly shorter time scales than predicted by the FM08 model. Hence, tidal heating computed with Lec08 is also more intense.

The possible detection of exomoons via transit photometry (Sartoretti & Schneider 1999), the Rossiter-McLaughlin effect (Simon et al. 2010), planet-moon eclipses (Cabrera & Schneider 2007), and transit timing and duration variations (Szabó et al. 2006; Kipping 2009) as well as the empirical constraint of the oblateness of a transiting planet (Carter & Winn 2010a,b), are first steps towards the measurement of the obliquity of exoplanets. All these observational effects are only accessible for transiting planets. Since obliquity determines atmospheric conditions as well as the amount of tidal heating and the equilibrium rotation period, it will be indispensable to verify $\psi_{\rm p}$ for planets in the IHZ around their host stars to assess their habitability. Thus, transiting planets are the most promising targets for a comprehensive appraisal of an extrasolar habitat.

References

Agnor, C. B., Canup, R. M., & Levison, H. F. 1999, Icarus, 142, 219

Anbar, A. D., Duan, Y., Lyons, T. W., et al. 2007, Science, 317, 1903
Barnes, R., another, O., another, O., et al. 2010a, ApJ, submitted
Barnes, R., Jackson, B., Greenberg, R., & Raymond, S. N. 2009a, ApJ, 700, L30
Barnes, R., Jackson, B., Greenberg, R., Raymond, S. N., & Heller, R. 2009b, ArXiv e-prints
Barnes, R., Jackson, B., Heller, R., Greenberg, R., & Raymond, S. N. 2010b, LPI Contributions, 1538, 5595
Barnes, R., Raymond, S. N., Jackson, B., & Greenberg, R. 2008, Astrobiology, 8, 557
Beust, H., Bonfils, X., Delfosse, X., & Udry, S. 2008, A&A, 479, 277
Bond, J. C., O'Brien, D. P., & Lauretta, D. S. 2010, ApJ, 715, 1050
Bonfils, X., Delfosse, X., Udry, S., et al. 2005a, A&A, 442, 635
Bonfils, X., Forveille, T., Delfosse, X., et al. 2005b, A&A, 443, L15
Cabrera, J. & Schneider, J. 2007, in Astronomical Society of the Pacific Conference Series, Vol. 366, Transiting Extrapolar Planets Workshop, ed. C. Afonso, D. Weldrake, & T. Henning, 242–+
Carter, J. A. & Winn, J. N. 2010a, ApJ, 709, 1219
Carter, J. A. & Winn, J. N. 2010b, ArXiv e-prints
Chambers, J. E. 2001, Icarus, 152, 205
Correia, A. C. M., Levrard, B., & Laskar, J. 2008, A&A, 488, L63
Darwin, G. H. 1879, Philosophical Transactions of the Royal Society, 170, 447, (repr. Scientific Papers, Cambridge, Vol. II, 1908)
Darwin, G. H. 1880, Royal Society of London Philosophical Transactions Series I, 171, 713
Dickey, J. O., Bender, P. L., Faller, J. E., et al. 1994, Science, 265, 482
Dobbs-Dixon, I., Lin, D. N. C., & Mardling, R. A. 2004, ApJ, 610, 464
Dressing, C. D., Spiegel, D. S., Scharf, C. A., Menou, K., & Raymond, S. N. 2010, ArXiv e-prints
Drysdale, R. N., Hellstrom, J. C., Zanchetta, G., et al. 2009, Science, 325, 1527
Efroimsky, M. & Lainey, V. 2007a, in American Institute of Physics Conference Series, Vol. 886, New Trends in Astrodynamics and Applications III, ed. E. Belbruno, 131–138
Efroimsky, M. & Lainey, V. 2007b, Journal of Geophysical Research (Planets), 112, 12003
Eggleton, P. P., Kiseleva, L. G., & Hut, P. 1998, ApJ, 499, 853
Fabrycky, D. & Tremaine, S. 2007, ApJ, 669, 1298
Ferraz-Mello, S., Rodríguez, A., & Hussmann, H. 2008, Celestial Mechanics and Dynamical Astronomy, 101, 171, (FM08)
Fischer, H. & Spohn, T. 1990, Icarus, 83, 39
Fujii, Y., Kawahara, H., Suto, Y., et al. 2010, ApJ, 715, 866
Gaidos, E., Deschenes, B., Dundon, L., et al. 2005, Astrobiology, 5, 100
Gerstenkorn, H. 1955, Zeitschrift fur Astrophysik, 36, 245
Gladman, B., Dane Quinn, D., Nicholson, P., & Rand, R. 1996, Icarus, 122, 166
Goldreich, P. 1963, MNRAS, 126, 257
Goldreich, P. 1966, AJ, 71, 1
Goldreich, P. & Soter, S. 1966, Icarus, 5, 375
Greenberg, R. 2009, ApJ, 698, L42
Grießmeier, J., Stadelmann, A., Penz, T., et al. 2004, A&A, 425, 753
Heller, R., Jackson, B., Barnes, R., Greenberg, R., & Homeier, D. 2010, A&A, 514, A22+
Henning, W. G., O'Connell, R. J., & Sasselov, D. D. 2009, ApJ, 707, 1000
Hoffmann, P. F. & Schrag, D. P. 2002, Terra Nova, 14, 129
Hunt, B. G. 1982, Journal of the Meteorological Society of Japan. Ser., 60, 309
Hut, P. 1981, A&A, 99, 126
Jones, B. W. & Sleep, P. 2010, ArXiv e-prints
Joshi, M. M., Haberle, R. M., & Reynolds, R. T. 1997, Icarus, 129, 450
Kaltenegger, L., Eiroa, C., Ribas, I., et al. 2010a, Astrobiology, 10, 103
Kaltenegger, L., Segura, A., & Mohanty, S. 2010b, LPI Contributions, 1538, 5613
Kasting, J. F. & Catling, D. 2003, ARA&A, 41, 429
Kasting, J. F. & Siefert, J. L. 2002, Science, 296, 1066
Kasting, J. F., Whitmire, D. P., & Reynolds, R. T. 1993, Icarus, 101, 108
Kaula, W. M. 1964, Reviews of Geophysics, 2, 661
Kenrick, P. 2003, Nature, 425, 248
Kenrick, P. & Crane, P. R. 1997, Nature, 389, 33
Khodachenko, M. L., Ribas, I., Lammer, H., et al. 2007, Astrobiology, 7, 167
Kipping, D. M. 2009, MNRAS, 396, 1797
Kokubo, E. & Ida, S. 2007, ApJ, 671, 2082
Kozai, Y. 1962, AJ, 67, 591
Lainey, V., Dehant, V., & Pätzold, M. 2007, A&A, 465, 1075
Lambeck, K. 1977, Royal Society of London Philosophical Transactions Series A, 287, 545
Laskar, J. & Joutel, F. 1993, Celestial Mechanics and Dynamical Astronomy, 57, 293
Laskar, J., Joutel, F., & Robutel, P. 1993, Nature, 361, 615
Leconte, J., Chabrier, G., Baraffe, I., & Levrard, B. 2010, A&A, 516, A64+
Leger, A. & Herbst, T. 2007, ArXiv e-prints
Levrard, B., Correia, A. C. M., Chabrier, G., et al. 2007, A&A, 462, L5, (Lev07)

Heller et al.: Constraints on habitability from obliquity tides

MacDonald, G. J. F. 1964, Reviews of Geophysics and Space Physics, 2, 467

Mardling, R. A. & Lin, D. N. C. 2002, ApJ, 573, 829

Mayor, M., Bonfils, X., Forveille, T., et al. 2009, A&A, 507, 487

McArthur, B. E., Fritz. Benedict, G., Barnes, R., et al. 2010, ApJ, 715, 1203

Migaszewski, C. & Gozdziewski, K. 2010, ArXiv e-prints

Mignard, F. 1979, Moon and Planets, 20, 301

Mignard, F. 1980, Moon and Planets, 23, 185

Miguel, Y. & Brunini, A. 2010, MNRAS, 800

Milanković, M. 1941, Königliche Serbische Akademie, XX, 633

Neron de Surgy, O. & Laskar, J. 1997, A&A, 318, 975

Ogilvie, G. I. & Lin, D. N. C. 2004, ApJ, 610, 477

Ollivier, M. & Léger, A. 2006, in ESA Special Publication, Vol. 1306, ESA Special Publication, ed. M. Fridlund, A. Baglin, J. Lochard, & L. Conroy, 505–+

Peale, S. J. 1999, ARA&A, 37, 533

Plesa, A. & Breuer, D. 2009, in European Planetary Science Congress 2009, 366–+

Rafikov, R. R. 2006, ApJ, 648, 666

Ray, R. D., Eanes, R. J., & Lemoine, F. G. 2001, Geophysical Journal International, 144, 471

Sartoretti, P. & Schneider, J. 1999, A&AS, 134, 553

Seager, S., Ford, E. B., & Turner, E. L. 2002, in Presented at the Society of Photo-Optical Instrumentation Engineers (SPIE) Conference, Vol. 4835, Society of Photo-Optical Instrumentation Engineers (SPIE) Conference Series, ed. A. M. Dressler, 79–86

Segatz, M., Spohn, T., Ross, M. N., & Schubert, G. 1988, Icarus, 75, 187

Selsis, F., Kasting, J. F., Levrard, B., et al. 2007, A&A, 476, 1373

Showman, A. P. & Guillot, T. 2002, A&A, 385, 166

Simon, A. E., Szabó, G. M., Szatmáry, K., & Kiss, L. L. 2010, ArXiv e-prints

Singer, S. F. 1972, Moon, 5, 206

Sotin, C., Grasset, O., & Mocquet, A. 2007, Icarus, 191, 337

Spencer, J. R., Rathbun, J. A., Travis, L. D., et al. 2000, Science, 288, 1198

Spiegel, D. S., Menou, K., & Scharf, C. A. 2009, ApJ, 691, 596

Spiegel, D. S., Raymond, S. N., Dressing, C. D., Scharf, C. A., & Mitchell, J. L. 2010, ArXiv e-prints

Spohn, T. 1991, Icarus, 90, 222

Stamenkovic, V., Noack, L., & Breuer, D. 2009, in European Planetary Science Congress 2009, 372–+

Szabó, G. M., Szatmáry, K., Divéki, Z., & Simon, A. 2006, A&A, 450, 395

Tarter, J. C., Backus, P. R., Mancinelli, R. L., et al. 2007, Astrobiology, 7, 30

Trilling, D. E. 2000, ApJ, 537, L61

von Bloh, W., Bounama, C., Cuntz, M., & Franck, S. 2007, A&A, 476, 1365

Williams, D. M. & Kasting, J. F. 1997, Icarus, 129, 254

Williams, D. M., Kasting, J. F., & Wade, R. A. 1997, Nature, 385, 234

Williams, D. M. & Pollard, D. 2002, International Journal of Astrobiology, 1, 61

Winn, J. N., Fabrycky, D., Albrecht, S., & Johnson, J. A. 2010, ArXiv e-prints

Wisdom, J. 2008, Icarus, 193, 637, (Wis08)

Wittgenstein, L. J. J. 1953, Philosophische Untersuchungen, bibliothek suhrkamp edn., Vol. BS1372 (Suhrkamp)

Wordsworth, R., Forget, F., Selsis, F., et al. 2010, ArXiv e-prints

Yoder, C. F. 1995, in Global Earth Physics: A Handbook of Physical Constants, ed. T. J. Ahrens, 1–+

Zahnle, K., Arndt, N., Cockell, C., et al. 2007, Space Science Reviews, 129, 35

9

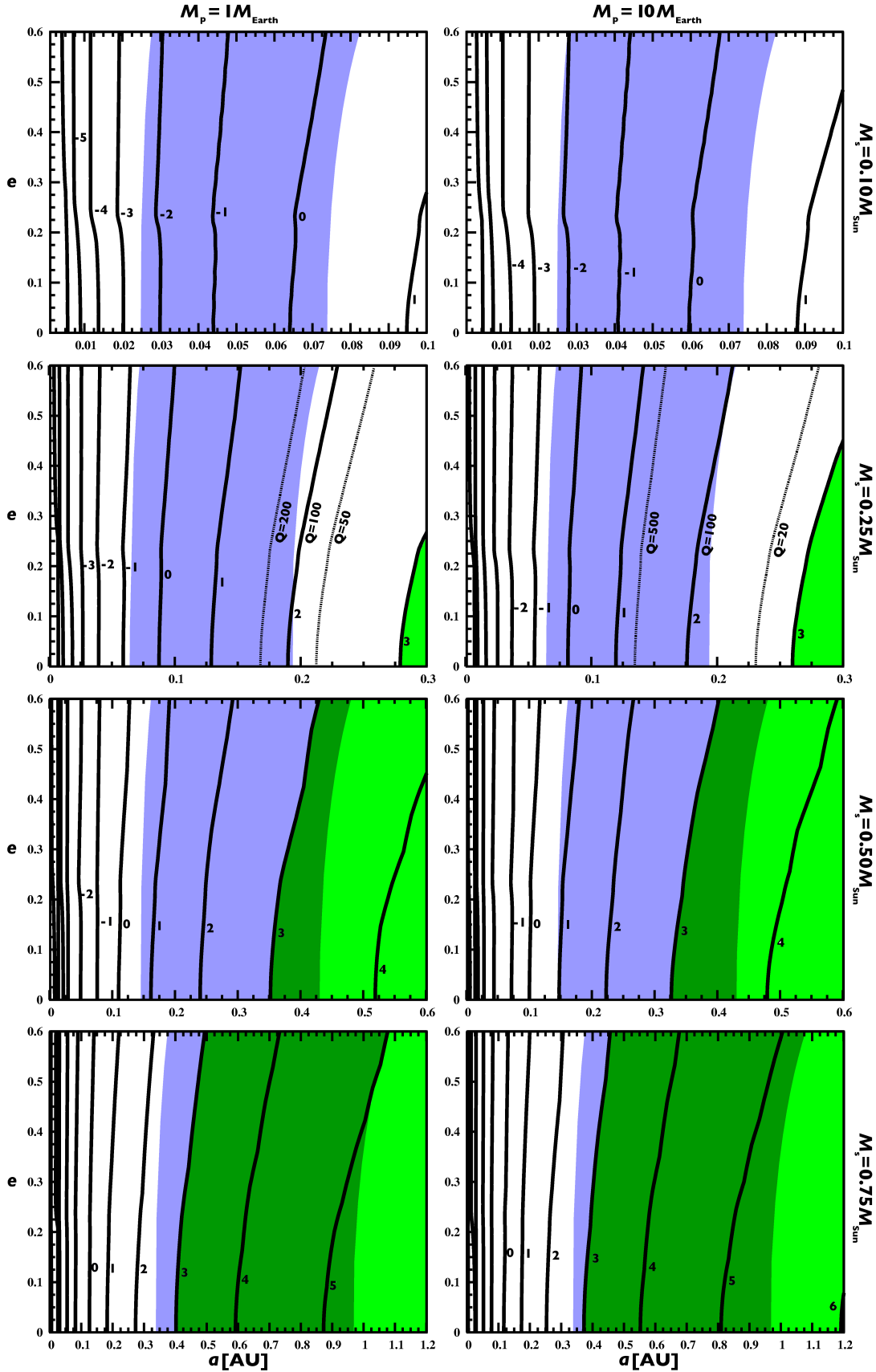Heller et al.: Constraints on habitability from obliquity tides

Fig. 1. Tilt erosion times for FM08. The IHZ is shaded in blue, contours of constant t_{ero} are labeled in units of $\log(t_{ero}/\text{Myr})$. Zones of $t_{ero} > 10^3$ Myr are shaded in green. Error estimates for Q_p are shown for the 0.25 $M_\odot$ star.

10

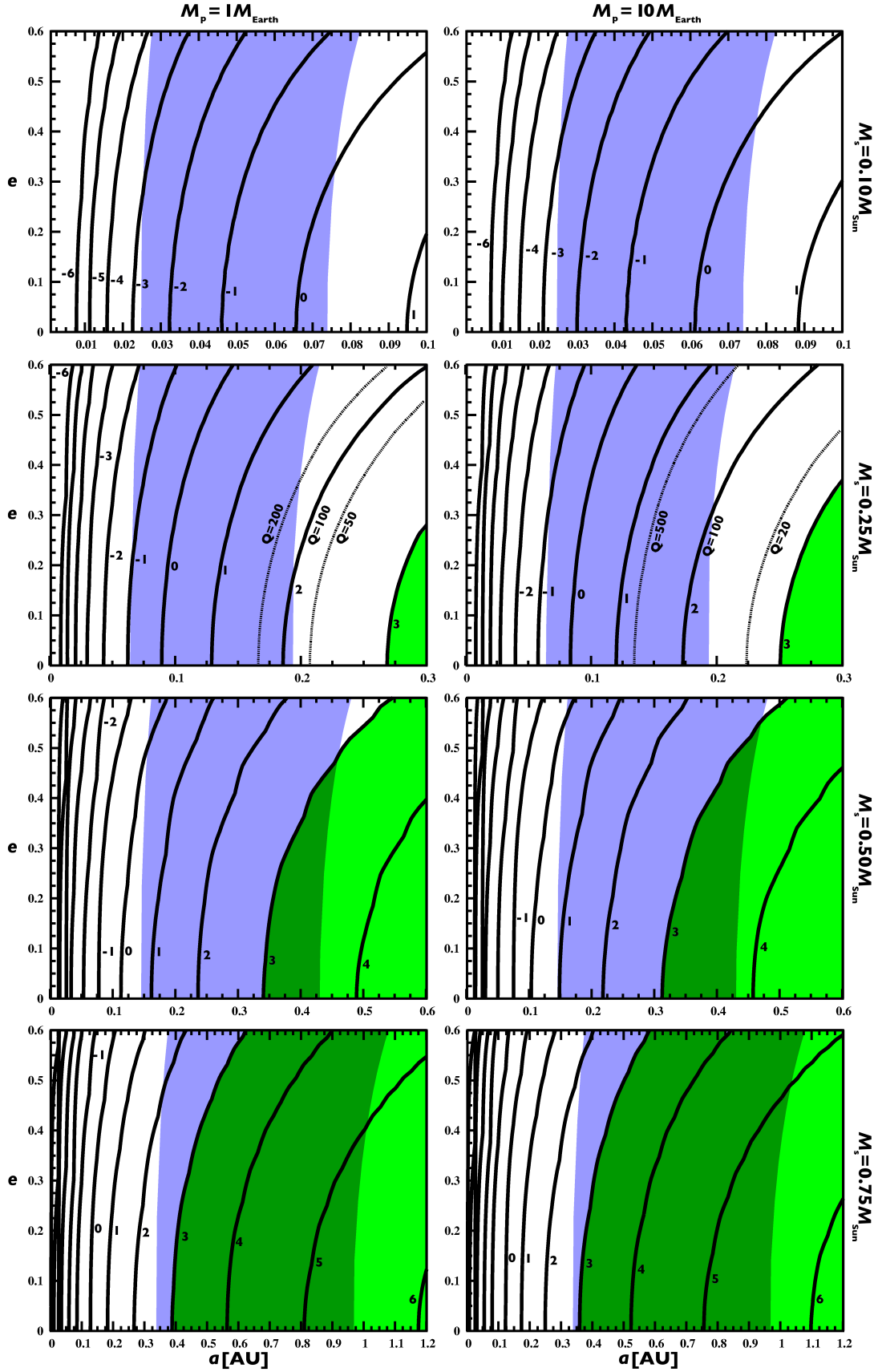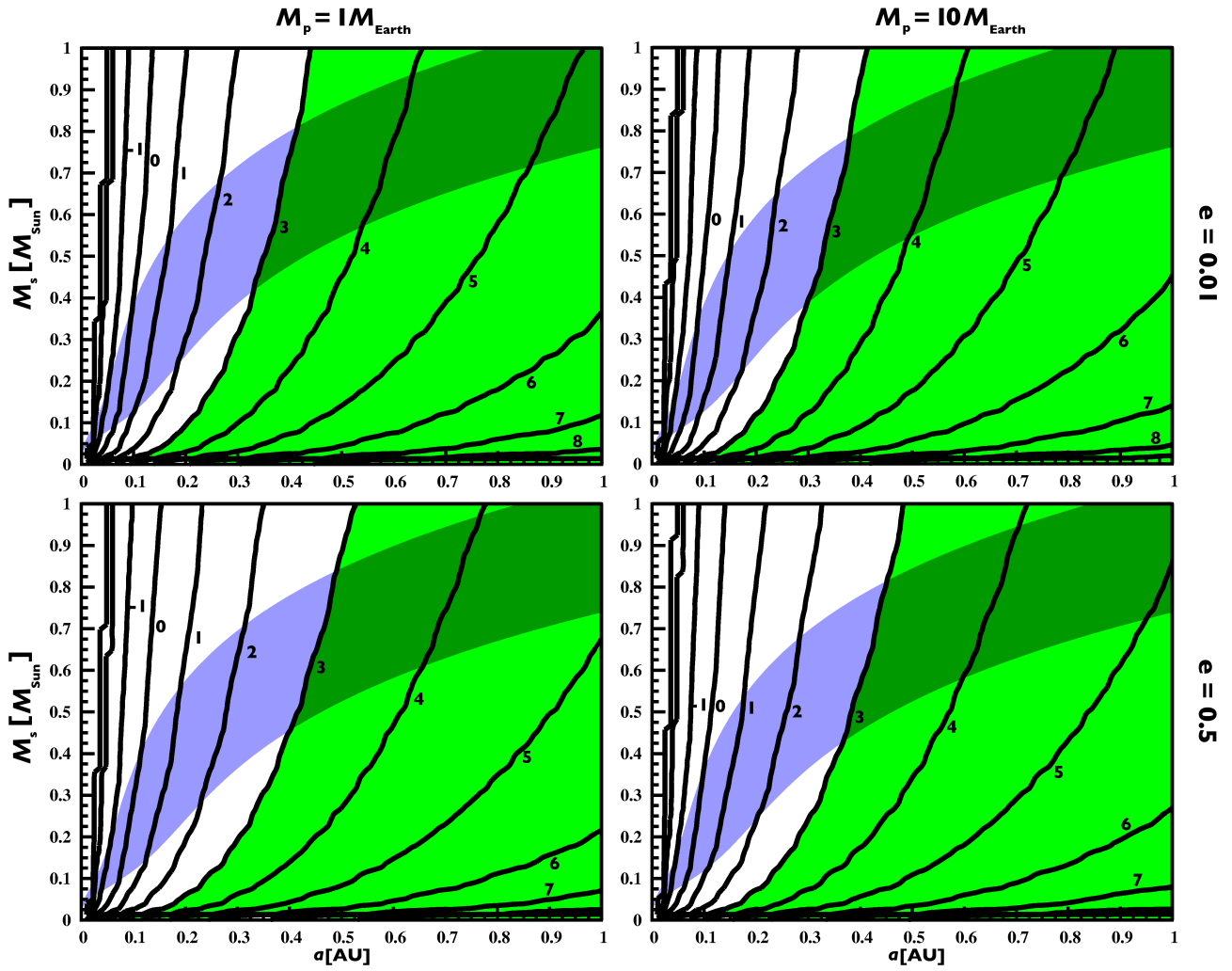Heller et al.: Constraints on habitability from obliquity tides

Fig. 2. Tilt erosion times for Lec10. The IHZ is shaded in blue, contours of constant $t_{\rm ero}$ are labeled in units of $\log(t_{\rm ero}/{\rm Myr})$. Zones of $t_{\rm ero} > 10^3$ Myr are shaded in green. Error estimates for $Q_{\rm p}$ are shown for the 0.25 $M_\odot$ star.

11

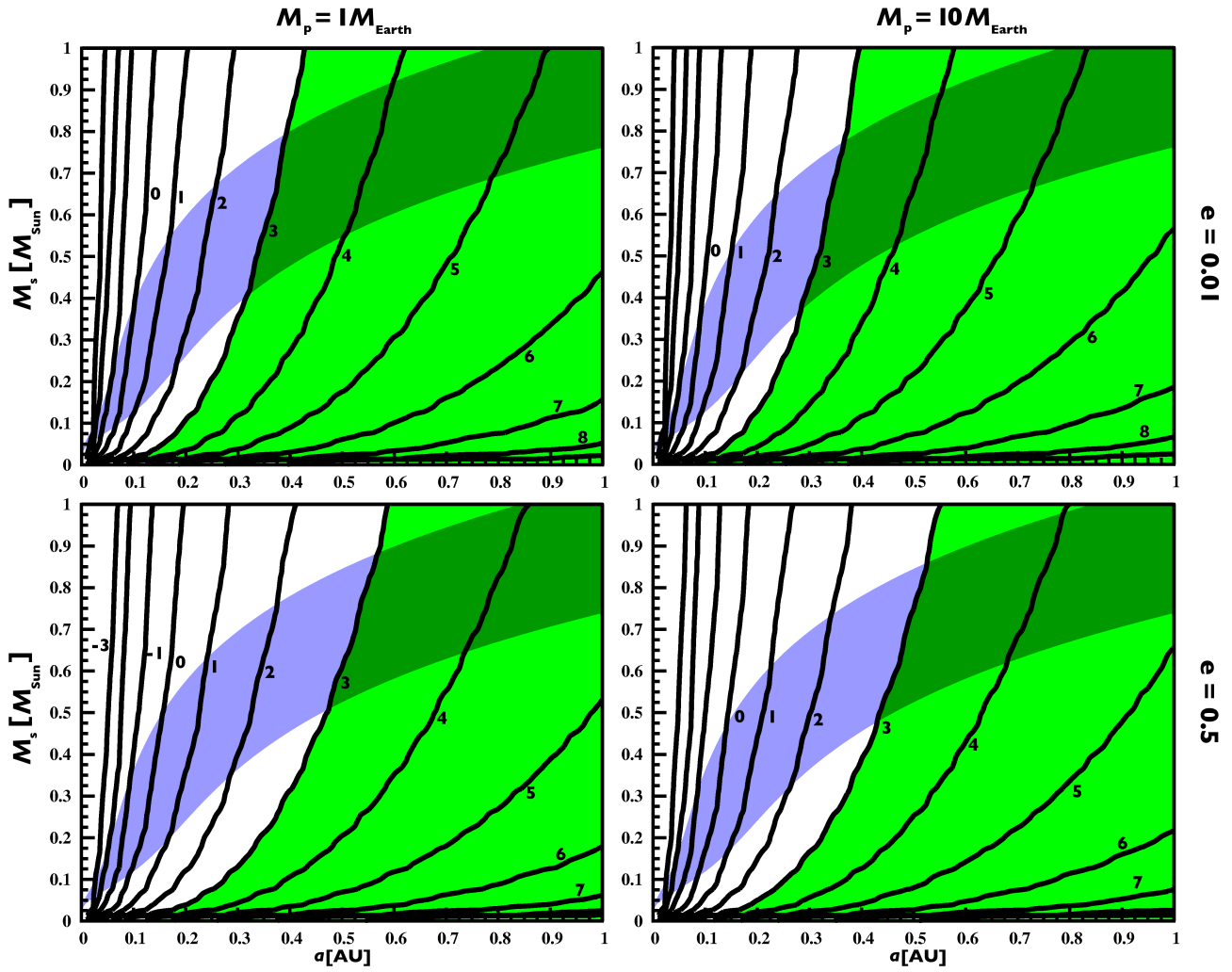Heller et al.: Constraints on habitability from obliquity tides

Fig. 3. Tilt erosion times for FM08. The IHZ is shaded in blue and the contours of constant tilt erosion times are labeled in units of $\log(t_{\mathrm{ero}}/\mathrm{Myr})$. Zones of $t_{\mathrm{ero}} > 10^3$ Myr are shaded in green.

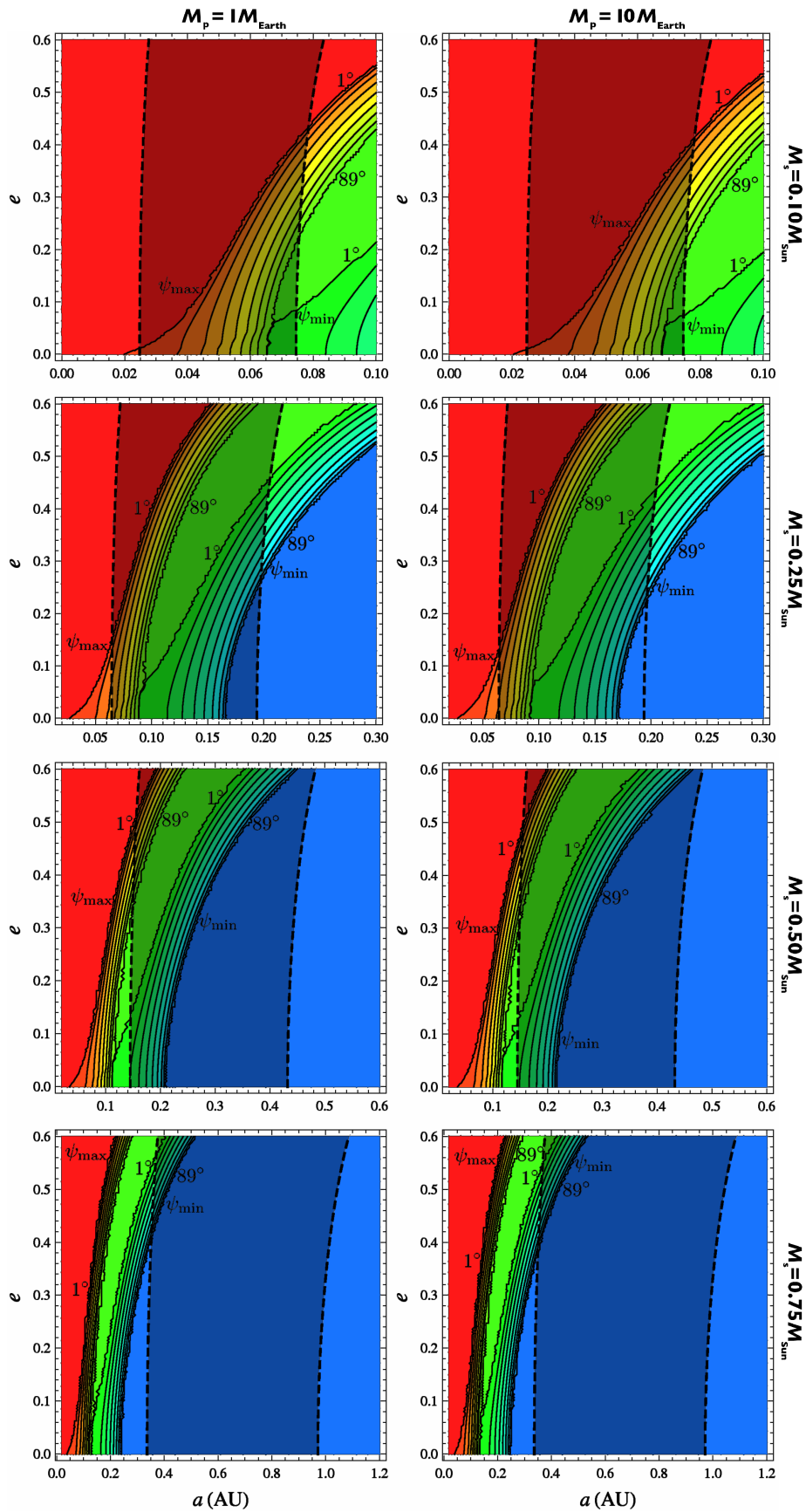Heller et al.: Constraints on habitability from obliquity tides

Fig. 4. Tilt erosion times for Lec10. The IHZ is shaded in blue and the contours of constant tilt erosion times are labeled in units of $\log(t_{\mathrm{ero}}/\mathrm{Myr})$. Zones of $t_{\mathrm{ero}} > 10^3$ Myr are shaded in green.

Heller et al.: Constraints on habitability from obliquity tides

Fig. 5. Obliquity thresholds ψ_{max} and ψ_{min} as explained in the text. For each 9-tuple of contours the lines indicate $\frac{1}{4}°, 20°, 30°, ..., 70°, 80°$, and $89°$. The IHZ is shaded in gray. In the red zone, $h_p^{equ.} > 2\,\mathrm{W/m^2}$ for any obliquity.
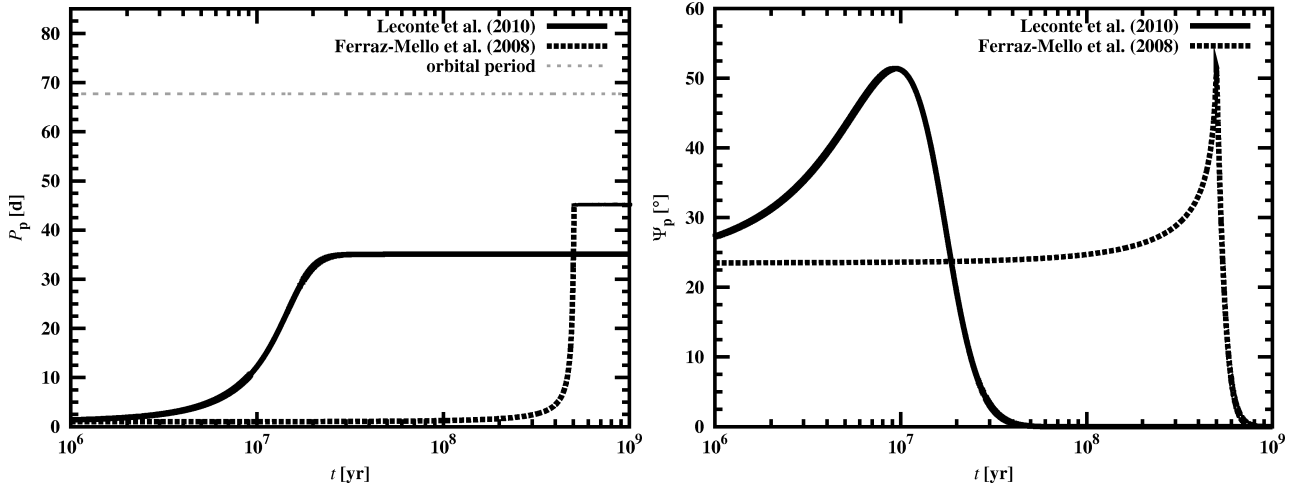
Fig. 6. *Left:* Evolution of the putative rotational period for Gl581 d for both models, FM08 and Lec10. The initial period was taken to be analog to the Earth's current day. *Right:* Evolution of the putative Earth-analog obliquity for Gl581 d for both models, FM08 and Lec10.
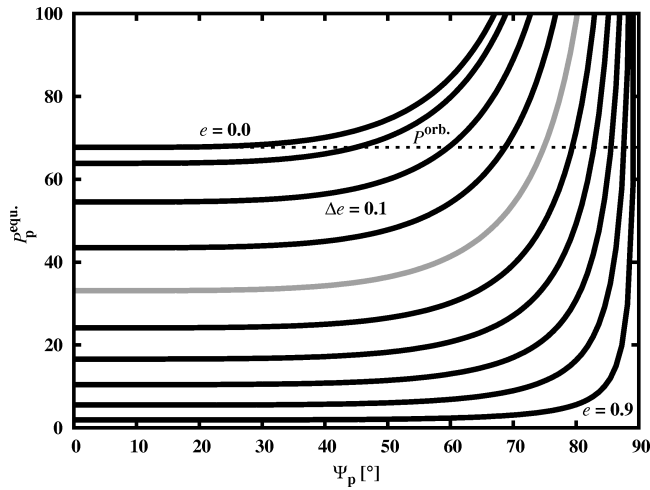
Fig. 7. Equilibrium rotation period of Gl581 d as a function of obliquity for various eccentricities. The gray line corresponds to $e = 0.4$, close to the observed eccentricity of $e = 0.38^{\pm 0.09}$. The observed orbital period is indicated with a dotted line.
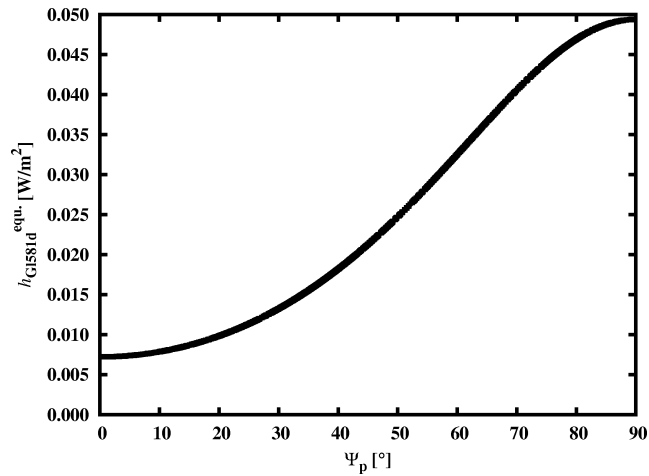
Fig. 8. Tidal surface heating rates on Gl581 d as a function of obliquity, based on the model of Lec10. Equilibrium rotation of the planet is assumed.

5.3 Tidal constraints on planetary habitability

Rory Barnes, Brian Jackson, Richard Greenberg, Sean N. Raymond, and René Heller
Proceedings submitted to "Pathways Towards Habitable Planets" Symposium
To be published in *ASP Conference Series* **as Barnes et al. (2009)**
A free preprint version is available at `http://arxiv.org/abs/0912.2095`**.**

Here we reconsider the effects of tidal interaction on the habitability of extrasolar planets. In addition to tilt erosion, tidal heating, and tidal locking, the progression of orbital shrinking affects the habitability of exoplanets. In this article, we review all these effects and study their impact on a 10 Earth-mass terrestrial planet orbiting a $0.25\,M_\odot$ star. This represents an attractive mass combination in terms of observational accessibility of space-based missions such as 'CoRoT' and 'Kepler'.

For this report, I calculated the time that tides require to reduce a planet's initial obliquity of $23.5°$ to $5°$. This time is projected onto the plane spanned by eccentricity and semi-major axis and depends on the planetary and the stellar masses (Fig. 2). The model I used for these computations is given in Sect. 4 of the paper and is the same as model #4 from the previous chapter (Heller et al. 2010).

This work was presented by Rory Barnes on the Astrobiology Science Conference 2010 with a talk on 'Tidal Constraints on Planetary Habitability'.

Tidal Constraints on Planetary Habitability

Rory Barnes[1,2], Brian Jackson[3,4], Richard Greenberg[5], Sean N. Raymond[2,6], and René Heller[7]

Abstract.   We review how tides may impact the habitability of terrestrial-like planets. If such planets form around low-mass stars, then planets in the circumstellar habitable zone will be close enough to their host stars to experience strong tidal forces. We discuss 1) decay of semi-major axis, 2) circularization of eccentric orbits, 3) evolution toward zero obliquity, 4) fixed rotation rates (not necessarily synchronous), and 5) internal heating. We briefly describe these effects using the example of a 0.25 $M_\odot$ star with a 10 $M_\oplus$ companion. We suggest that the concept of a habitable zone should be modified to include the effects of tides.

1   Introduction

Exoplanet surfaces are probably the best places to look for life beyond the Solar System. Remote sensing of these bodies is still in its infancy, and the technology does not yet exist to measure the properties of terrestrial exoplanet atmospheres directly. Indeed, the scale and precision of the engineering required to do so is breathtaking. Given these limitations, a reliable model of habitability is essential in order to maximize the scientific return of future ground- and space-based missions with the capability to remotely detect exoplanet atmospheres.

Here we review one often misunderstood issue: The effect of tides. If the distance between a star and planet is small, $\lesssim 0.1$ AU, the shape of the planet (and star) can become significantly non-spherical. This asymmetry can change the planet's orbital motion from that of spherical planets. Simulating the deviations from the spherical approximation is difficult and uncertain as observations of the Solar System, binary stars and exoplanets do not yet provide enough information to distinguish between models. Without firm constraints, qualitatively

---

[1]   Department of Astronomy, University of Washington, Seattle, WA, 98195-1580

[2]   Virtual Planetary Lab

[3]   Planetary Systems Laboratory, Goddard Space Flight Center, Code 693, Greenbelt, MD 20771

[4]   NASA Postdoctoral Program Fellow

[5]   Lunar and Planetary Laboratory, University of Arizona, Tucson, AZ 85721

[6]   Center for Astrophysics and Space Astronomy, University of Colorado, UCB 389, Boulder CO 80309-0389

[7]   Hamburger Sternwarte, University of Hamburg, Gojenbergsweg 112, 21029 Hamburg, Germany

2

different models of the planetary response to tides exist. The two most prominent descriptions are the "constant-phase-lag" and "constant-time-lag" models (Greenberg 2009). In the former, the tidal bulge is assumed to lag the perturber by a fixed angle, but in the latter it lags by a fixed time interval. Depending on the mathematical extension in terms of e, the two models may diverge significantly when $e \gtrsim 0.3$. Throughout this review the reader should remember that the presented magnitudes of tidal effects are model-dependent. For more on these differences and the details of tidal models, the reader is referred to recent reviews by Ferraz-Mello *et al.* (2008) and Heller *et al.* (2009).

We consider tidal effects in the habitable zone (HZ) model proposed by Barnes *et al.* (2008) which utilizes the 50% cloud cover HZ of Selsis *et al.* (2007), but assumes that the orbit averaged flux determines surface temperature (Williams and Pollard 2002). We use the example of a 10 $M_\oplus$ planet orbiting a 0.25 $M_\odot$ star. This choice is arbitrary, but we note that large terrestrial planets orbiting small stars will be preferentially discovered by current detection techniques. This chapter is organized as follows: In § 2 we discuss orbital evolution, in § 3 we describe rotation rates, in § 4 we consider the obliquity, and in § 5 we examine tidal heating.

2 Orbital Evolution

Orbital evolution due to tides should be considered for any potentially habitable world. The asymmetry of the tidal bulge leads to torques which transfer angular momentum between rotation and orbits, and the constant flexing of the planet's figure between pericenter and apocenter dissipates energy inside the planet. These two effects act to circularize and shrink most orbits. In the constant-phase-lag model, the orbits of close-in exoplanets evolve in the following way (Goldreich and Soter 1966; see also Jackson *et al.* 2009):

$$\frac{da}{dt} = -\Big(\frac{63}{2}\frac{\sqrt{GM_*^3}R_p^5}{m_p Q_p'}e^2 + \frac{9}{2}\frac{\sqrt{G/M_*}R_*^5 m_p}{Q_*'}\Big[1 + \frac{57}{4}e^2\Big]\Big)a^{-11/2} \qquad (1)$$

$$\frac{de}{dt} = -\Big(\frac{63}{4}\frac{\sqrt{GM_*^3}R_p^5}{m_p Q_p'} + \frac{225}{16}\frac{\sqrt{G/M_*}R_*^5 m_p}{Q_*'}\Big)a^{-13/2}e, \qquad (2)$$

where a is semi-major axis, G is Newton's gravitational constant, m_p is the mass of the planet, Q_p' is the planet's tidal dissipation function divided by two-thirds its Love number, Q_*' is the star's tidal dissipation function divided by two-thirds its Love number, R_p is the planet's radius, and R_* is the stellar radius. The Q' values represent the body's response to tidal processes and combines a myriad of internal properties, such as density, equation of state, etc. It is a difficult quantity to measure, so here we use the standard values of $Q_*' = 10^6$ and $Q_p' = 500$ (Mathieu 1994; Mardling and Lin 2002; Jackson *et al.* 2008a). The first terms in Eqs. $(1 - 2)$ represent the effects of the tide raised on the planet, the second the tide raised on the star.

Eqs. $(1 - 2)$ predict a and e decay with time. As tides slowly change a planet's orbit, the planet may move out (through the inner edge) of the habitable zone (HZ). This possibility was considered in Barnes *et al.* (2008), who showed
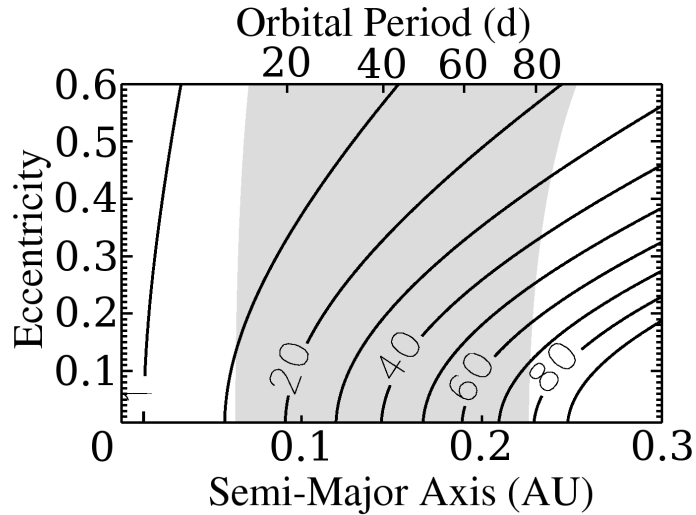
3

Figure 1.   Contours of equilibrium rotation period in days for a 10 $M_\oplus$ planet orbiting a 0.25 $M_\odot$ star. The gray region is the HZ from Barnes *et al.* (2008).

for some example cases the time for a planet to pass through the inner edge of the HZ. Such sterilizing evolution is most likely to occur for planets with initially large eccentricity near the inner edge of the HZ of low mass stars ($\lesssim 0.3\,M_\odot$). Even if a planet does not leave the HZ, the circularization of its orbit can require billions of years, potentially affecting the climatic evolution of the planet.

3   Rotation Rates

Planetary rotation rates may be modified by tidal interactions. Although planets may form with a wide range of rotation rates Ω, tidal forces may fix Ω such that no net exchange of rotational and orbital angular momenta occurs during one orbital period. The planet is then said to be "tidally locked," and the rotation rate is "pseudo-synchronous" or in equilibrium. The equilibrium rotation rate in the constant-phase-lag model is

$$\Omega_{eq} = n(1 + \frac{19}{2}e^2), \tag{3}$$

where n is the mean motion (Goldreich 1966). Note that planets only rotate synchronously (one side always facing the star) if $e = 0$ (the constant-time-lag model makes the same prediction). Therefore, the threat to habitability may have been overstated in the past, as independently pointed out by several recent
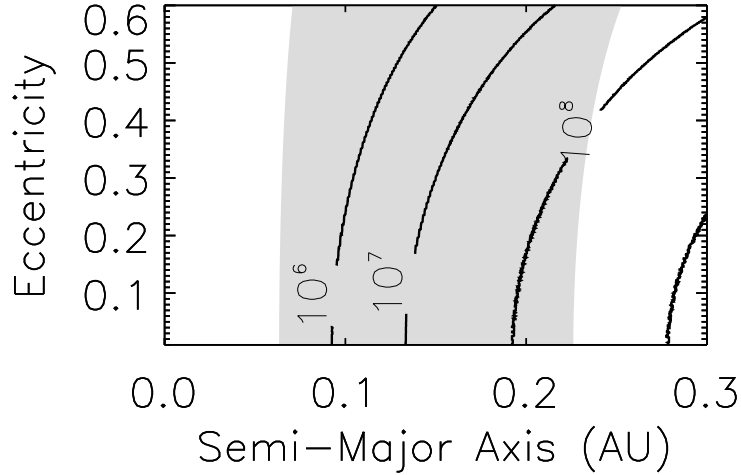
4

Figure 2.   Time in years for a 10 $M_\oplus$ planet orbiting a 0.25 $M_\odot$ star to evolve from an obliquity $\psi = 23°\!.5$ to $5°$. The gray region is the HZ from Barnes *et al.* (2008).

investigations (Barnes *et al.* 2008; Ferraz-Mello *et al.* 2008; Correia *et al.* 2008). Figure 1 shows the values of the equilibrium rotation period for a 10 $M_\oplus$ planet orbiting a 0.25 $M_\odot$ star as a function of a and e.

4   Obliquity

Tidal effects tend to drive obliquities to zero or π. The constant-time-lag model of Levrard *et al.* (2007) found a planet's obliquity ψ changes as

$$\frac{\mathrm{d}\psi}{\mathrm{d}t} = \frac{\sin(\psi)K_\mathrm{p}}{C_\mathrm{p}\Omega_0 n}\left(\frac{\cos(\psi)\epsilon_1\Omega_0}{n} - 2\epsilon_2\right) \tag{4}$$

where

$$\epsilon_1 = \frac{1 + 3e^2 + \frac{3}{8}e^4}{(1-e^2)^{9/2}}, \tag{5}$$

$$K_\mathrm{p} = \frac{3}{2}k_{2,\mathrm{p}}\frac{GM_\mathrm{p}^2}{R_\mathrm{p}}\tau_\mathrm{p}n^2\left(\frac{M_\mathrm{s}}{M_\mathrm{p}}\right)^2\left(\frac{R_\mathrm{p}}{a}\right)^6, \tag{6}$$

$$C_\mathrm{p} = r_{\mathrm{g,p}}^2 M_\mathrm{p}R_\mathrm{p}^2, \tag{7}$$

and

$$\epsilon_2 = \frac{1 + \frac{15}{2}e^2 + \frac{45}{8}e^4 + \frac{5}{16}e^6}{(1-e^2)^6} \quad . \tag{8}$$
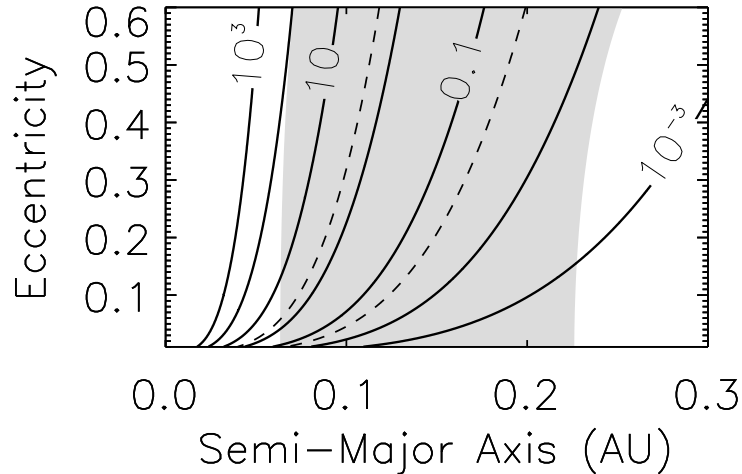
5

Figure 3.   Tidal heating fluxes for a 10 $M_\oplus$ planet orbiting a 0.25 $M_\odot$ star. Contour labels are in W m^{-2}. The dashed contours represent the boundaries of the tidal habitable zone (Jackson *et al.* 2008c; Barnes *et al.* 2009b). The gray region is the HZ from Barnes *et al.* (2008).

In the preceding equations $r_{\mathrm{g,p}}$ $(= 0.5)$ is the planet's radius of gyration (a measure of the distribution of matter inside a body), Ω_0 is the initial rotation frequency, and τ_{p} is the "tidal time lag", which in this constant-time-lag model replaces Q_p'. We assumed $Q_p' = 500$ for the planet at its initial orbital configuration and set $\tau_{\mathrm{p}} = 1/(nQ_{\mathrm{p}}')$, *i.e.* initially the planet responds in the same way as in a constant-phase-lag model. In the course of the orbital evolution, τ_{p} was then fixed while n and Q_{p} evolved in a self-consistent system of coupled differential equations. In Fig. 2 we show the time for a planet with an initial obliquity of 23°.5 to reach 5°, a value which may preclude habitability (F. Selsis, personal communication). However, obliquities may easily be modified by other planets in the system (Atobe *et al.* 2004; Atobe and Ida 2007) or a satellite (Laskar *et al.* 1993).

5   Tidal Heating

As a body on an eccentric orbit is continually reshaped due to the varying gravitational field, friction heats the interior. This "tidal heating" is quantified in the constant-phase-lag model as

$$H = \frac{63}{4} \frac{(GM_*)^{3/2} M_* R_p^5}{Q_p'} a^{-15/2} e^2 \qquad (9)$$

6

(Peale *et al.* 1979; Jackson 2008b). However, in order to assess the surface effects of tidal heating on a potential biosphere, it is customary to consider the heating flux, $h = H/4\pi R_p^2$, through the planetary surface. Jackson *et al.* (2008c; see also Barnes *et al.* 2009b) argued that when $h \geq 2$ W m^{-2} (the value for Io [McEwen *et al.* 2004]) or $h \leq 0.04$ W m^{-2} (the limit for plate tectonics [Williams *et al.* 1997]), habitability is less likely. Barnes *et al.* (2009b) suggested that these limits represent a "tidal habitable zone". In Fig. 3 contours of tidal heating are shown for a 10 M$_\oplus$ planet orbiting a 0.25 M$_\odot$ star. The tidal habitable zone is the region between the dashed curves. Note that a and e evolve as prescribed by Eqs. $(1 - 2)$, and hence the heating fluxes evolve with time as well.

References

Atobe, K., and Ida, S. 2007, Icarus, 188, 1
Atobe, K., Ida, S. and Ito, T. 2004, Icarus, 168, 223
Barnes, R., Jackson, B., Raymond, S.N., West, A.A., and Greenberg, R. 2009a. ApJ, 695, 1006
Barnes, R., Jackson, B., Greenberg, R. and Raymond, S.N. 2009b. ApJ, 700, L30
Barnes, R., Raymond, S.N., Jackson, B. and Greenberg, R. 2008, AsBio, 8, 557
Correia, A.C.M., Levrard, B., and Laskar, J. 2008, A&A, 488, L63
Ferraz-Mello, S., Rodríguez, A. and Hussmann, H. 2008, CeMDA, 101, 171
Goldreich, P. 1966, AJ, 71, 1
Goldreich, P. and Soter, S. 1966, Icarus, 5, 375
Greenberg, R. 2009, ApJ, 698, L42
Heller, R., Jackson, B., Barnes, R., Greenberg, R. and Homeier, D. 2009, A&A, submitted
Jackson, B., Barnes, R. and Greenberg, R. 2008c, MNRAS, 391, 237
———. 2009, ApJ, 698, 1357
Jackson, B., Greenberg, R, and Barnes, R. 2008a, ApJ, 678, 1396
———. 2008b, ApJ, 681, 1631
Laskar, J., Joutel, F., and Robutel, P. 1993, Nature, 361, 615
Lainey, V., Arlot, J.-E., Karatekin, O., and van Hoolst, T. 2009, Nature, 459, 957
Levrard, B. *et al.* 2007, A&A, 462, L5
Mardling, R.A. and Lin, D.N.C. 2002, ApJ, 573, 829
Mathieu, R. 1994, ARA&A, 32, 465
McEwen, A.S., Keszthelyi, L.P., Lopes, R., Schenk, P.M., and Spencer, J.R. 2004, in: Jupiter. The planet, satellites and magnetosphere, ed. F. Bagenal, T.E. Dowling, and W.B. McKinnon (Cambridge, UK: Cambridge UP), 307
Peale, S.J., Cassen, P., and Reynolds, R.T. 1979, Science, 203, 892
Selsis, F. *et al.* 2007, A&A, 476, 137
Williams, D.M., Kasting, J.E., and Wade, R.A. 1997, Nature, 385, 234
Williams, D.M. and Pollard, D. 2002, IntJAsBio 1, 61

5.4   Tidal effects on the habitability of exoplanets: the case of GJ581 d

Rory Barnes, Brian Jackson, René Heller, Richard Greenberg, and Sean N. Raymond
Astrobiology Science Conference 2010
Published in the *LPI Contributions* as Barnes et al. (2010)
A free online version is available at `http://adsabs.harvard.edu/abs/2010LPICo1538.5595B`.
Credit: Barnes, LPI Contributions, 1538, 5595, (2010)

As a side project of our investigations on planetary habitability from Sect. 5.2 of this book, we dedicate this report to the special case of the extrasolar planet Gl581 d. This planet is worth a more detailed study of tidal effects since the planet is located close to the outer rim of the insolation habitable zone. Depending on its cloud coverage, the significant eccentricity of the planet's orbit may render the planet habitable or not: *(i.)* The orbit-averaged flux of a planet scales with $a^{-2} \sqrt[-2]{1 - e^2}$, thus the more eccentric the orbit, the higher the average flux. And *(ii.)*, tidal heating, which scales proportional to e^2 (Peale et al. 1979), might contribute essentially to enable plate tectonics on this planet. Tectonic activity is assumed to be necessary for the formation of life since, on Earth, it maintains the carbon-silicate cycle.

Besides several contributions with regard to the contents of this article, I carried out various calculations on the evolution of the orbit, which were presented at the Astrobiology Science Conference 2010.

This work was presented by R. Barnes on the Astrobiology Science Conference 2010 with a talk on 'Tidal Effects on the Habitability of Exoplanets: The Case of GJ581 d'.

Tidal Effects on the Habitability of Exoplanets: The Case of GJ 581 d

Rory Barnes[1,2], Brian Jackson[3,4], René Heller[5], Richard Greenberg[6], Sean N. Raymond[7], [1]Department of Astronomy, University of Washington, Seattle, WA, 98195-1580, rory@astro.washington.edu, [2]Virtual Planetary Laboratory, [3]Planetary Systems Laboratory, Goddard Space Flight Center, Code 693, Greenbelt, MD 20771, [4]NASA Postdoctoral Program Fellow, [5]Hamburger Sternwarte, University of Hamburg, Gojenbergsweg 112, 21029 Hamburg, Germany, [6]Lunar and Planetary Laboratory, University of Arizona, Tucson, AZ 85721, [7]Laboratoire d'Astrophysique de Bordeaux (CNRS; Université Bordeaux I) BP 89, F-33270 Floriac, France

Tides may be crucial to the habitability of exoplanets. If such planets form around low-mass stars, then those in the circumstellar habitable zone will be close enough to their host stars to experience strong tidal forces. Tides may result in orbital decay and circularization, evolution toward zero obliquity, a fixed rotation rate (not necessarily synchronous), and substantial internal heating [1–4]. Due to tidal effects, the range of habitable orbital locations may be quite different from that defined by the traditional concept of a habitable zone (HZ) based on stellar insolation, atmospheric effects, and liquid water on a planet's surface. Tidal heating may make locations within the traditional HZ too hot, while planets outside the traditional zone could be rendered quite habitable due to tides.

Consider for example GJ 581 d, a planet with a minimum mass of 7 Earth masses, a semimajor axis a of 0.22 AU, and an eccentricity e of 0.38 ± 0.09 ([5]; revised from $a = 0.25$ AU in [6]). The circumstellar habitable zone of [1], which is a synthesis of [7–8], predicts this planet receives enough insolation to permit surface water, albeit with some cloud coverage, see Fig. 1. The small value of a and large value of e suggest that tides may be important, and their potential effects must be taken into consideration. Given the recent revision of its orbit [5], we examine the habitability of this planet in the context of tides. As more planets in the circumstellar HZ of low mass stars are discovered, a similar analysis should be applied.

Rotation Rate The rotation rate of the planet was tidally locked in less than 1 Gyr. Tidal locking, however, does not mean the planet is rotating synchronously, instead it follows the relation

$$\Omega_{\mathrm{eq}} = n(1 + ke^2), \qquad (1)$$

where Ω_{eq} is the equilbrium rotation frequency, n is the mean motion, and k is a prameter that is dependent on the tidal model. If tidal bulges lag by a constant phase, $k = 9.5$ [9,1], but if they lag by a constant time, then $k = 6$ [10]. Therefore, GJ 581 d may rotate faster than synchronous, with a
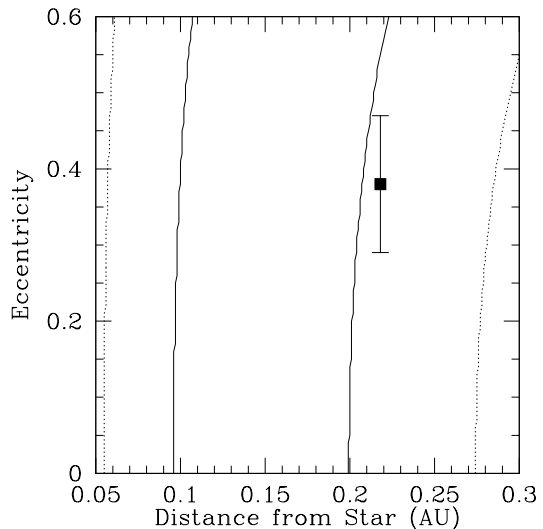

Figure 1: Insolation limits to the habitability of GJ 581 d. Solid curves correspond to the 0% cloud cover HZ model of [1], dotted curves assume 100% cloud coverage. GJ 581 d is the black square, with the 1-σ uncertainty in eccentricity also shown (the errors in a are negligible.)

period of perhaps about half the orbital period of 66.8 days.

Obliquity Tidal evolution tends to drive obliquities to 0 or π (depending on initial conditions). For GJ 581 d, the time for this "obliquity locking" to occur is ~ 100 Myr [4,11]. Should this locking occur, the habitability of GJ 581 d may be in jeopardy, even if it is in the circumstellar HZ, as the poles become a cold trap and can eventually freeze out the atmosphere [12]. However, perturbations from other planets may drive a chaotic obliquity evolution [13]. For this to occur the orbits of the other planets in the system must be inclined relative to GJ 581 d's orbit.

Large mutual inclinations in the GJ 581 system are likely. An earlier phase of planet-planet scattering [14] is evidenced by GJ 581 d's large eccentricity, as protoplanetary disk phenomena are un-

likely to produce values larger than 0.3 [15]. Such scattering would have likely driven large relative inclinations ($\gtrsim 30°$) between planets [14]. So, while tides are driving planet d's obliquity toward 0 or π, interactions with other planets are preventing this situation from occuring. Note that the orbital oscillations occur on $\sim 10^3$ year timescales, which is orders of magnitude shorter than the obliquity locking timescale. Whether these obliquities oscillations from the other planets preclude d's habitability is another matter.

Orbital Evolution The GJ 581 system is estimated to be 8 Gyr old [7]. Therefore tides may have played a role in its orbital history. Tides tend to circularize and shrink orbits with time [16]. Although these effects are operating on GJ 581 d, they have resulted in minimal evolution: GJ 581 d has always been in the circumstellar habitable zone. If we assume standard mass-radius relationships for terrestrial planets [17], then GJ 581 d has not drifted an appreciable amount in the last 8 Gyr.

Internal Heating Plate tectonics may be necessary for habitability [17]. On Earth, the internal energy to drive this process comes from endogenic sources: radioactive decay and energy from formation. The sources combine to provide a current heat flux of 0.08 W m^{-2} [18]. This value is close to the lower limit for plate tectonics, $0.04\,\mathrm{W\,m^{-2}}$ derived by [19]. We use their example to make a crude estimate of endogenic heat flux on GJ 581 d, assuming an age of 8 Gyr [6]. They assumed an exponential cooling law:

$$h_{\mathrm{end}} = h_{\mathrm{end},0} R_{\mathrm{p}} \rho_{\mathrm{p}} e^{-\lambda t}, \qquad (2)$$

where h_{end} are the radiogenic and primordial heating flux (in $\mathrm{W\,m^{-2}}$), $h_{\mathrm{end},0}$ is a proportionailty constant, ρ_{p} is the planetary density, λ is the the reciprocal of the half-life, and t is the age of the system. As a first estimate, [19] set $\lambda = 1.5 \times 10^{-10}$, corresponding to the half-life of ^{238}U. The actual cooling times and initial radiogenic inventory of GJ 581 d could be very different, and Eq. (2) should be considered an order of magnitude estimate. Scaling from the Earth, the heat flux from non-tidal sources on GJ 581 d is $0.12\,\mathrm{W\,m^{-2}}$, about 3 times larger than the tectonics limit. Given the uncertainties in this calculation, plate tectonics is not a given on GJ 581 d.

Perhaps tidal heat, similar to Io's, can provide additional energy. Tidal heating H inside a planet is equal to the change in orbital energy:

$$H = \frac{63}{4} \frac{(GM_*)^{3/2} M_* R_{\mathrm{p}}^5}{Q_p'} a^{-15/2} e^2 \qquad (3)$$

[20–21]. However, in order to assess the surface effects of tidal heating on a potential biosphere, we can consider the heating flux, $h = H/4\pi R_{\mathrm{p}}^2$, through the planetary surface. The tidal heat flux of GJ 581 d, assuming best fit parameters and planetary tidal dissipation parameter $Q' = 500$, is 0.01 W m^{-2} [3], about 4 times too low for plate tectonics, and perhaps an order of magnitude lower than the endogenic heat flux. Therefore tidal heating, which is also uncertain, could provide a signfcant heat source for this planet. Perhaps a combination of endogenic and tidal heat drive plate tectonics, facilitating habitability.

We conclude that tidal effects are an important part of assessing GJ 581 d's potential habitability. As more plausibly terrestrial planets are discovered, these tidal issues need to be applied to them as well in order to assess their potential habitability.

[1] Barnes, R. *et al.* 2008, AsBio, 8, 557. [2] Jackson, B. *et al.* 2008, MNRAS, 391, 237. [3] Barnes, R. *et al.* 2009, ApJ, 700, L30. [4] Barnes, R. *et al.* 2010, in Conference Proceedings to *Pathways Towards Habitable Planets*, Eds: D. Gallindo & I. Ribas, in press. [5] Mayor, M. *et al.* 2009. A&A, 507, 487. [6] Udry, S. *et al.* 2007, A&A 469, L43. [7] Selsis, F. *et al.* 2007, A&A, 476, 137. [8] Williams, D. M. & Pollard, D. 2002, Int J. AsBio, 1, 61. [9] Goldreich, P. 1966, AJ, 71, 1. [10] Ferraz-Mello, S. *et al.* 2008, CeMDA, 101, 171. [11] Levrard, B. *et al.* 2007, A&A, 462, L5. [12] Selsis, F., personal communication. [13] Atobe, K., & Ida, S. 2007, Icarus, 188, 1. Marzari, F. & Weidenschilling, S. 2002, Icarus, 156, 570. [15] D'Angelo, G. *et al.* 2003 ApJ, 586, 540. [16] Jackson, B. *et al.* 2008, ApJ, 678, 1396. [17] Sotin, C. *et al.* 2007, Icarus, 191, 337. [18] Davies, G. 1999, Dynamic Earth (Cambridge, UK; Cambridge UP) [19] Walker, J. C. G., *et al.* 1981, JGR, 86, 9776. [20] Williams, D. M. *et al.* 1997, Nature, 385, 234. [20] Peale, S. J. *et al.* 1979, Science, 203, 892. 19. [21] Jackson, B. *et al.* 2008, ApJ, 681, 1631.

Chapter 6

Transits of extrasolar planets

6.1 Transit detections of extrasolar planets around main-sequence stars

I. Sky maps for hot Jupiters

R. Heller, D. Mislis, and J. Antoniadis

While the previous chapter addressed the tidal processes in stars, brown dwarfs, and exoplanets, we now turn to the observational aspects of exoplanet transits. We use data of roughly 1 million stars from the Tycho catalog from 1997, which are based on observations of the space-based Hipparcos satellite between 1989 and 1993. Some of the basic parameters of each star are taken to infer the individual stellar metallicities and the probability of these stars to host a Jovian planet in a close orbit. From these probabilities we deduce the expectation values of transit observations per $8° \times 8°$ field of view and project them on the celestial plane. Finally, we use the instrumental parameters of some ongoing ground-based transit surveys to reproduce the transit sky maps as seen through the glasses of the respective survey. This allows not only for a comparison of the efficiencies of these surveys but also for a prediction of the number of bright-star transits still to be discovered.

This publication emerged from inspiring discussions with Dimitris Mislis who had the initial idea for these sky maps. He had set up a procedure to plot the detection probabilities of transiting extrasolar planets based on Tycho catalog input data. While he assumed that each star has a planet, I proposed to include the stellar metallicity, which is empirically connected to the occurrence of (detectable) planets. I also set up the mathematical tools for the computation of the expectation values for the number of transiting planets, which is a more concrete value compared to the transit probabilities. Finally, I structured our procedure, I introduced Fig. 2, and I authored the paper.

A German review of this study is published in the popular science magazine *Sterne und Weltraum* (6/2010). My article comprises six pages and is written for a broader audience, scientists as well as amateurs. It is entitled "Auf der Suche nach extrasolaren Transitplaneten". With permission to reprint, granted by Axel M. Quetz and the editorial staff of *Sterne und Weltraum*, this article is presented in Sect. A.1.

Astronomy
&
Astrophysics

Transit detections of extrasolar planets around main-sequence stars

I. Sky maps for hot Jupiters[*]

R. Heller[1], D. Mislis[1], and J. Antoniadis[2]

[1] Hamburger Sternwarte (Universität Hamburg), Gojenbergsweg 112, 21029 Hamburg, Germany
   e-mail: [rheller;dmislis]@hs.uni-hamburg.de
[2] Aristotle University of Thessaloniki, Dept. of Physics, Section of Astrophysics, Astronomy and Mechanics,
   541 24 Thessaloniki, Greece
   e-mail: iantonia@physics.auth.gr

ABSTRACT

Context. The findings of more than 350 extrasolar planets, most of them nontransiting Hot Jupiters, have revealed correlations between the metallicity of the main-sequence (MS) host stars and planetary incidence. This connection can be used to calculate the planet formation probability around other stars, not yet known to have planetary companions. Numerous wide-field surveys have recently been initiated, aiming at the transit detection of extrasolar planets in front of their host stars. Depending on instrumental properties and the planetary distribution probability, the promising transit locations on the celestial plane will differ among these surveys.
Aims. We want to locate the promising spots for transit surveys on the celestial plane and strive for absolute values of the expected number of transits in general. Our study will also clarify the impact of instrumental properties such as pixel size, field of view (FOV), and magnitude range on the detection probability.
Methods. We used data of the Tycho catalog for ≈ 1 million objects to locate all the stars with $0^{\mathrm{m}} \lesssim m_{\mathrm{V}} \lesssim 11.5^{\mathrm{m}}$ on the celestial plane. We took several empirical relations between the parameters listed in the Tycho catalog, such as distance to Earth, m_{V}, and $(B-V)$, and those parameters needed to account for the probability of a star to host an observable, transiting exoplanet. The empirical relations between stellar metallicity and planet occurrence combined with geometrical considerations were used to yield transit probabilities for the MS stars in the Tycho catalog. Magnitude variations in the FOV were simulated to test whether this fluctuations would be detected by BEST, XO, SuperWASP and HATNet.
Results. We present a sky map of the expected number of Hot Jupiter transit events on the basis of the Tycho catalog. Conditioned by the accumulation of stars towards the galactic plane, the zone of the highest number of transits follows the same trace, interrupted by spots of very low and high expectation values. The comparison between the considered transit surveys yields significantly differing maps of the expected transit detections. While BEST provides an unpromising map, those for XO, SuperWASP, and HATNet show FsOV with up to 10 and more expected detections. The sky-integrated magnitude distribution predicts 20 Hot Jupiter transits with orbital periods between 1.5 d and 50 d and $m_{\mathrm{V}} < 8^{\mathrm{m}}$, of which two are currently known. In total, we expect 3412 Hot Jupiter transits to occur in front of MS stars within the given magnitude range. The most promising observing site on Earth is at latitude $= -1$.

Key words. planetary systems – occultations – solar neighborhood – Galaxy: abundances – instrumentation: miscellaneous – methods: observational

1. Introduction

A short essay by Otto Struve (Struve 1952) provided the first published proposal of transit events as a means of exoplanetary detection and exploration. Calculations for transit detection probabilities (Rosenblatt 1971; Borucki & Summers 1984; Pepper & Gaudi 2006) and for the expected properties of the discovered planets have been done subsequently by many others (Gillon et al. 2005; Fressin et al. 2007; Beatty & Gaudi 2008). Until the end of the 1990s, when the sample of known exoplanets had grown to more than two dozen (Castellano et al. 2000), the family of so-called "Hot Jupiters", with 51 Pegasi as their prototype, was unknown and previous considerations had been

based on systems similar to the solar system. Using geometrical considerations, Rosenblatt (1971)[1] found that the main contribution to the transit probability of a solar system planet would come from the inner rocky planets. However, the transits of these relatively tiny objects remain undetectable around other stars as yet.

The first transit of an exoplanet was finally detected around the sun-like star HD209458 (Charbonneau et al. 2000; Queloz et al. 2000). Thanks to the increasing number of exoplanet search programs, such as the ground-based Optical Gravitational Lensing Experiment (OGLE) (Udalski et al. 1992), the Hungarian Automated Telescope (HAT) (Bakos et al. 2002, 2004), the Super Wide Angle Search for Planets (SuperWASP) (Street et al. 2003), the Berlin Exoplanet Search Telescope (BEST) (Rauer et al. 2004), XO (McCullough et al. 2005), the

---

[*] Sky maps (Figs. 1 and 3) can be downloaded in electronic form at the CDS via anonymous ftp to
cdsarc.u-strasbg.fr (130.79.128.5) or via
http://cdsweb.u-strasbg.fr/cgi-bin/qcat?J/A+A/508/1509

[1] A correction to his Eq. (2) is given in Borucki & Summers (1984).

Transatlantic Exoplanet Survey (TrES) (Alonso et al. 2007), and the Tautenburg Exoplanet Search Telescope (TEST) (Eigmüller & Eislöffel 2009) and the space-based missions "Convection, Rotation & Planetary Transits" (CoRoT) (Baglin et al. 2002) and Kepler (Christensen-Dalsgaard et al. 2007), the number of exoplanet transits has grown to 62 until September 1st 2009[2] and will grow drastically within the next years. These transiting planets have very short periods, typically <10 d, and very small semimajor axes of usually <0.1 AU, which is a selection effect based on geometry and Kepler's third law (Kepler et al. 1619). Transiting planets with longer periods present more of a challenge, since their occultations are less likely in terms of geometrical considerations and they occur less frequently.

Usually, authors of studies on the expected yield of transit surveys generate a fictive stellar distribution based on stellar population models. Fressin et al. (2007) use a Monte-Carlo procedure to synthesize a fictive stellar field for OGLE based on star counts from Gould et al. (2006), a stellar metallicity distribution from Nordström et al. (2004), and a synthetic structure and evolution model of Robin et al. (2003). The metallicity correlation, however, turned out to underestimate the true stellar metallicity by about 0.1 dex, as found by Santos et al. (2004) and Fischer & Valenti (2005). In their latest study, Fressin et al. (2009) first generate a stellar population based on the Besançon catalog from Robin et al. (2003) and statistics for multiple systems from Duquennoy & Mayor (1991) to apply then the metallicity distribution from Santos et al. (2004) and issues of detectability (Pont et al. 2006). Beatty & Gaudi (2008) rely on a Galactic structure model by Bahcall & Soneira (1980), a mass function as suggested by Reid et al. (2002) based on Hipparcos data, and a model for interstellar extinction to estimate the overall output of the current transit surveys TrES, XO, and Kepler. In their paper on the number of expected planetary transits to be detected by the upcoming Pan-STARRS survey (Kaiser 2004), Koppenhoefer et al. (2009) also used a Besançon model as presented in Robin et al. (2003) to derive a brightness distribution of stars in the target field and performed Monte-Carlo simulations to simulate the occurrence and detections of transits. These studies include detailed observational constraints such as observing schedule, weather conditions, and exposure time and issues of data reduction, e.g. red noise and the impact of the instrument's point spread function.

In our study, we rely on the extensive data reservoir of the Tycho catalog instead of assuming a stellar distribution or a Galactic model. We first estimate the number of expected exoplanet transit events as a projection on the complete celestial plane. We refer to recent results of transit surveys such as statistical, empirical relationships between stellar properties and planetary formation rates. We then use basic characteristics of current low-budget but high-efficiency transit programs (BEST, XO, SuperWASP, and HATNet), regardless of observational constraints mentioned above, and a simple model to test putative transits with the given instruments. With this procedure, we yield sky maps, which display the number of expected exoplanet transit detections for the given surveys, i.e. the transit sky as it is seen through the eyeglasses of the surveys.

The Tycho catalog comprises observations of roughly 1 million stars taken with the Hipparcos satellite between 1989 and 1993 (ESA 1997; Hoeg 1997). During the survey, roughly 100 observations were taken per object. From the derived astrometric and photometric parameters, we use the right

ascension (α), declination (δ), the color index ($B - V$), the apparent visible magnitude m_V, and the stellar distance d that have been calculated from the measured parallax. The catalog is almost complete for the magnitude limit $m_V \lesssim 11.5^m$, but we also find some fainter stars in the list.

2. Data analysis

The basis of our analysis is a segmentation of the celestial plane into a mosaic made up of multiple virtual fields of view (FsOV). In a first approach, we subdivide the celestial plane into a set of $181 \times 361 = 65\,341$ fields. Most of the current surveys do not use telescopes, which typically have small FsOV, but lenses with FsOV of typically $8° \times 8°$. Thus, we apply this extension of $8° \times 8°$ and a stepsize of $\Delta\delta = 1° = \Delta\alpha$, with an overlap of $7°$ between adjacent fields, for our automatic scanning in order to cover the complete sky. We chose the smallest possible step size in order to yield the highest possible resolution and the finest screening, despite the high redundancy due to the large overlap. A smaller step size than $1°$ was not convenient due to limitations of computational time. An Aitoff projection is used to fold the celestial sphere onto a 2D sheet.

2.1. Derivation of the stellar parameters

One key parameter for all of the further steps is the effective temperature $T_{\rm eff}$ of the stars in our sample. This parameter is not given in the Tycho catalog but we may use the stellar color index ($B - V$) to deduce $T_{\rm eff}$ by

$$T_{\rm eff} = 10^{[14.551-(B-V)]/3.684} \text{ K}, \tag{1}$$

which is valid for main-sequence (MS) stars with $T_{\rm eff} \lesssim 9100$ K as late as type M8 (Reed 1998). Although we apply this equation to each object in the catalog, of which a significant fraction might exceed $T_{\rm eff} = 9100$ K, this will not yield a serious challenge since we will dismiss these spurious candidates below. From the object's distance to Earth d and the visible magnitude m_V, we derive the absolute visible magnitude M_V via

$$M_V = m_V - 5^m \log\left(\frac{d}{10 \text{ pc}}\right), \tag{2}$$

where we neglected effects of stellar extinction. In the next step, we compute the stellar radius $R_\star$ in solar units via

$$\frac{R_\star}{R_\odot} = \left[\left(\frac{5770 \text{ K}}{T_{\rm eff}}\right)^4 10^{(4.83-M_V)/2.5}\right]^{1/2} \tag{3}$$

and the stellar mass $M_\star$ by

$$M_\star = \left(4\pi R_\star^2 \sigma_{\rm SB} T_{\rm eff}^4\right)^{1/\beta}, \tag{4}$$

where $\sigma_{\rm SB}$ is the Stefan-Boltzmann constant. The coefficient β in the relation $L \propto M^\beta$ depends on the stellar mass. We use the values and mass regimes that were empirically found by Cester et al. (1983), which are listed in Table 1 (see also Smith 1983).

We deduce the stellar metallicity [Fe/H]$_\star$ from the star's effective temperature $T_{\rm eff}$ and its color index ($B - V$) by

$$[{\rm Fe/H}]_\star = \frac{1}{411}\left(\frac{T_{\rm eff}}{\rm K} - 8423 + 4736(B-V) - 1106(B-V)^2\right), \tag{5}$$

as given in Santos et al. (2004). This relation, however, is only valid for stars with $0.51 < (B-V) < 1.33$, 4495 K $< T_{\rm eff} <$ 6339 K, $-0.7 <$ [Fe/H]$_\star < 0.43$, and $\log(g) > 4$. We reject

---

Table 1. Empirical values for β in the mass-luminosity relation Eq. (4) as given in Cester et al. (1983).

β	Stellar mass regime
3.05 ± 0.14	$M_\star \lesssim 0.5\ M_\odot$
4.76 ± 0.01	$0.6\ M_\odot \lesssim M_\star \lesssim 1.5\ M_\odot$
3.68 ± 0.05	$1.5\ M_\odot \lesssim M_\star$

those stars from the sample that do not comply with all these boundary conditions. On the one hand we cleanse our sample of non-MS stars, on the other hand the sample is reduced seriously. While our original reservoir, our "master sample", consists of 1 031 992 stars from the Tycho catalog, all the restrictions mentioned above diminish our sample to 392 000 objects, corresponding to roughly 38%.

3. Transit occurrence and transit detection

3.1. Transit occurrence

Now that we derived the fundamental stellar parameters, we may turn towards the statistical aspects of planetary occurrence, geometric transit probability and transit detection. We start with the probability for a certain star of the Tycho catalog, say the ith star, to host an exoplanet. For F, G, and K dwarfs with $-0.5 < [\mathrm{Fe/H}]_i < 0.5$, Fischer & Valenti (2005) found the empirical relationship

$$\wp_{\exists\,\mathrm{planet},i} = 0.03 \cdot 10^{2 \cdot [\mathrm{Fe/H}]_i} \tag{6}$$

for a set of 850 stars with an analysis of Doppler measurements sufficient to detect exoplanets with radial velocity (RV) semi-amplitudes $K > 30\ \mathrm{ms}^{-1}$ and orbital periods shorter than 4 yr (see Marcy et al. 2005; Wyatt et al. 2007, for a discussion of the origin of this formula and its implications for planet formation). These periods are no boundary conditions for our simulations since we are only interested in surveys with observing periods of ≤ 50 d. The additional constraint on the metallicity does not reduce our diminished sample of 392 000 stars since there is no star with $-0.7 < [\mathrm{Fe/H}]_i < -0.5$ in the Tycho catalog. Similar to the correlation we use, Udry & Santos (2007) found a metallicity distribution of exoplanet host stars equivalent to $\wp_{\exists\,\mathrm{planet},i} = 0.044 \times 10^{2.04 \cdot [\mathrm{Fe/H}]_i}$. However, this fit was restricted to stars with $[\mathrm{Fe/H}]_\star > 0$ since they suspect two regimes of planet formation. Sozzetti et al. (2009) extended the uniform sample of Fischer & Valenti (2005) and found the power-law $\wp_{\exists\,\mathrm{planet},i} = 1.3 \times 10^{2 \cdot [\mathrm{Fe/H}]_i + C}$, $C \in \{0, 0.5\}$, to yield the best data fit. These recent studies also suggest that there exists a previously unrecognized tail in the planet-metallicity distribution for $[\mathrm{Fe/H}]_\star < 0$. Taking Eq. (6) we thus rather underestimate the true occurrence of exoplanets around the stars from the Tycho catalog. The metallicity bias of surveys using the RV method for the detection of exoplanets is supposed to cancel out the bias of transit surveys (Gould et al. 2006; Beatty & Gaudi 2008).

In the next step, we analyze the probability of the putative exoplanet to actually show a transit. Considering arbitrary inclinations of the orbital plane with respect to the observer's line of sight and including Kepler's third law, Gilliland et al. (2000) found the geometric transit probability to be

$$\wp_{\mathrm{geo},i} = 23.8 \left(\frac{M_i}{M_\odot}\right)^{-1/3} \left(\frac{R_i}{R_\odot}\right) \left(\frac{P}{\mathrm{d}}\right)^{-2/3}, \tag{7}$$

where P is the orbital period. A more elaborate expression – including eccentricity, planetary radius, the argument of periastron and the semi-major axis instead of the orbital period – is given by Seagroves et al. (2003). Note that $\wp_{\mathrm{geo},i}$ in Eq. (7) does not explicitly but implicitly depend on the semi-major axis a via $P = P(a)$! The probability for an exoplanetary transit to occur around the ith star is then given by

$$\wp_{\mathrm{occ},i} = \wp_{\exists\,\mathrm{planet},i} \cdot \wp_{\mathrm{geo},i}, \tag{8}$$

where P is the remaining free parameter, all the other parameters are inferred from the Tycho data. Since we are heading for the expectation value, i.e. the number of expected transits in a certain field of view (FOV), we need a probability density for the distribution of the orbital periods of extrasolar planets. On the basis of the 233 exoplanets listed in the EPE on July 6th 2007, Jiang et al. (2007) used a power-law fit $\delta(P) = C(k) \cdot (P/\mathrm{d})^{-k}$, with $C(k)$ as the normalization function, and the boundary condition for the probability density $\int_0^\infty \mathrm{d}P\,\delta(P) = 1$ to get

$$\delta(P) = \frac{1-k}{B^{1-k} - A^{1-k}} \left(\frac{P}{\mathrm{d}}\right)^{-k} \tag{9}$$

with $A = 1.211909$ d and $B = 4517.4$ d as the lower and upper limits for the period distribution and $k = 0.9277$. This function is subject to severe selection effects and bases on data obtained from a variety of surveys and instruments. It overestimates short-period planets since Jiang et al. (2007) included transiting planets and the associated selection effects. While the function presumably does not mirror the true distribution of orbital periods of exoplanets, it is correlated to the period distribution to which current instruments are sensitive, in addition to geometric selection effects as given by Eq. (7).

We now segment the celestial plane into a mosaic made up of multiple virtual FsOV, as described at the beginning of Sect. 2, to calculate the number of expected transits in that field. In Sect. 3.2 we will attribute the FOV of the respective instrument to that mosaic and we will also consider the CCD resolution. The number of stars comprised by a certain FOV is n. The number of expected transits around the ith star in that field, N_i, with periods between P_1 and P_2 is then given by

$$
\begin{aligned}
N_i &= \int_{P_1}^{P_2} \mathrm{d}P\,\delta(P)\,\wp_{\mathrm{occ},i} \\
&= \wp_{\exists\,\mathrm{planet},i} \cdot 23.8 \left(\frac{M_i}{M_\odot}\right)^{-1/3} \left(\frac{R_i}{R_\odot}\right) \frac{1-k}{B^{1-k} - A^{1-k}} \\
&\quad \times \frac{1}{1/3 - k} \left(P_2^{1/3-k} - P_1^{1/3-k}\right) \mathrm{d}^{2/3} {}_{\mid A < P_1 < P_2 < B},
\end{aligned}
\tag{10}
$$

and the number of expected transits in the whole FOV is

$$N = \sum_{i=1}^{n} N_i. \tag{11}$$

We emphasize that this is not yet the number of expected transit detections within a certain FOV (see Sect. 4) but the number of expected transits to occur within it.

A graphical interpretation of this analysis is presented in Fig. 1, where we show a sky map of the expected number of exoplanet transits around MS stars with $m_V \lesssim 11.5^{\mathrm{m}}$ for orbital periods between $P_1 = 1.5$ d and $P_2 = 50$ d. This map bases on several empirical relationships and on substantial observational bias towards close-in Jupiter-like planets, but nevertheless it represents the transit distribution to which current instrumentation
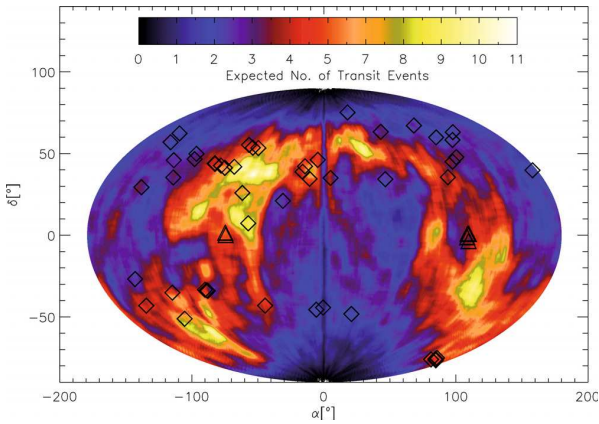
Fig. 1. Sky map of the expected number of exoplanet transit events, N, with orbital periods between $P_1 = 1.5$ d and $P_2 = 50$ d on the basis of 392 000 objects from the Tycho catalog. The published positions of 58 transiting planets from the EPE as of September 1st 2009 are indicated with symbols: 6 detections from the space-based CoRoT mission are labeled with triangles, 52 ground-based detections marked with squares. The axes only refer to the celestial equator and meridian.

has access to. The pronounced bright regions at the upper left and the lower right are the anti-center and the center of the Milky Way, respectively. The absolute values of $0.5 \lesssim N \lesssim 5$ for the most of the sky are very well in line with the experiences from wide-field surveys using a $6° \times 6°$ field. Mandushev et al. (2005) stated 5 to 20 or more exoplanet transit candidates, depending on Galactic latitude, and a ratio of $\approx 25{:}1$ between candidates and confirmed planets, which is equivalent to $0.2 \lesssim N \lesssim 1$. Our values are a little higher, probably due to the slightly larger FOV of $8° \times 8°$ used in Fig. 1 and due to the effect of blends and unresolved binaries (see discussion in Sect. 5).

In the left panel of Fig. 2, we show the distribution of expected transits from our simulation as a function of the host stars' magnitudes compared to the distribution of the observed transiting exoplanets. The scales for both distributions differ about an order of magnitude, which is reasonable since only a fraction of actual transits is observed as yet. For $m_V < 8^m$, only HD209458b and HD189733b are currently know to show transits whereas we predict 20 of such transits with periods between 1.5 d and 50 d to occur in total. We also find that the number of detected transiting planets does not follow the shape of the simulated distribution for $m_V > 9^m$. This is certainly induced by a lack of instruments with sufficient sensitivity towards higher apparent magnitudes, the much larger reservoir of fainter stars that has not yet been subject to continuous monitoring, and the higher demands on transit detection pipelines.

Our transit map allows us to constrain convenient locations for future ground-based surveys. A criterion for such a location is the number of transit events that can be observed from a given spot at latitude l on Earth. To yield an estimate, we integrate N over that part of the celestial plane that is accessible from a telescope situated at l. We restrict this observable fan to $l - 60° < \delta < l + 60°$, implying that stars with elevations $>30°$ above the horizon are observable. The number of the transit events with $m_V \lesssim 11.5^m$ that is observable at a certain latitude on Earth is shown in the right panel of Fig. 2. This distribution resembles a triangle with its maximum almost exactly at the equator. Its smoothness is caused by the wide angle of $120°$ that flattens all the fine structures that can be seen in Fig. 1.

3.2. Transit detection

So far, we have computed the sky and magnitude distributions of expected exoplanet transits with orbital periods between 1.5 d and 50 d, based on the stellar parameters from the Tycho data and empirical relations. In order to estimate if a possible transit can actually be observed, one also has to consider technical issues of a certain telescope as well as the efficiency and the selection effects of the data reduction pipelines. The treatment of the pipeline will not be subject of our further analysis. The relevant aspects for our concern are the pixel size of the CCD, its FOV, the m_V range of the CCD-telescope combination, and the declination fan that is covered by the telescope.

To detect a transit, one must be able to distinguish the periodic transit pattern within a light curve from the noise in the data. Since the depth of the transit curve is proportional to the ratio $A_P/A_\star$, where A_P and $A_\star$ are the sky-projected areas of the planet and the star, respectively, and $R_P/R_\star = \sqrt{A_P/A_\star}$, with R_P as the planetary radius, the detection probability for a certain instrument is also restricted to a certain regime of planetary radii. Assuming that the transit depth is about 1%, the planetary radius would have to be larger than $\approx R_\star/10$. We do not include an elaborate treatment of signal-to-noise in our considerations (see Aigrain & Pont 2007). Since our focus is on MS stars and our assumptions for planetary occurrence are based on those of Hot Jupiters, our argumentation automatically leads to planetary transits of exoplanets close to $\approx R_\star/10$.

We also do not consider observational aspects, such as integration time and an observer on a rotating Earth with observation windows and a finite amount of observing time (see Fleming et al. 2008, for a review of these and other observational aspects). Instead, we focus on the technical characteristics of four well-established transit surveys and calculate the celestial distribution of expected exoplanet transit detections in principle by using one of these instruments. The impact of limited observing time is degraded to insignificance because the span of orbital periods we consider in Eq. (10) reaches only up to $P_2 = 50$ d. After repeated observations of the same field, such a transiting companion would be detected after $\lesssim 3$ yr, which is the typical duty cycle of current surveys.

Our computations are compared for four surveys: BEST, XO, SuperWASP, and HATNet. This sample comprises the three most fruitful surveys in terms of first planet detections and BEST – a search program that used a telescope instead of lenses. While observations with BEST have been ceased without any confirmed transit detection, XO has announced detections and SuperWASP and HATNet belong the most fruitful surveys to date. An overview of the relevant observational and technical properties of these surveys is given in Table 2. For each survey, we first restrict the Tycho master sample to the respective magnitude range, yielding an m_V-restricted sample. In the next step, we virtually observe the subsample with the fixed FOV of the survey telescope, successively grazing the whole sky with steps of $1°$ between adjacent fields. The FOV is composed of a number of CCD pixels and each of these pixels contains a certain number of stars, whose combined photon fluxes merge into a count rate. Efficient transit finding has been proven to be possible from the ground in crowded fields, where target objects are not resolved from neighbor stars. To decide whether a hypothetical transit around the ith star in the pixel would be detected, we simulate the effect of a transiting object that reduces the light flux contribution l_i of the ith star on the combined flux $\sum_k^n l_k$ of the stars within a pixel. If the ith magnitude variation on the pixel-combined light is $\Delta m_{V,i} \geq 0.01^m$, which is a typical
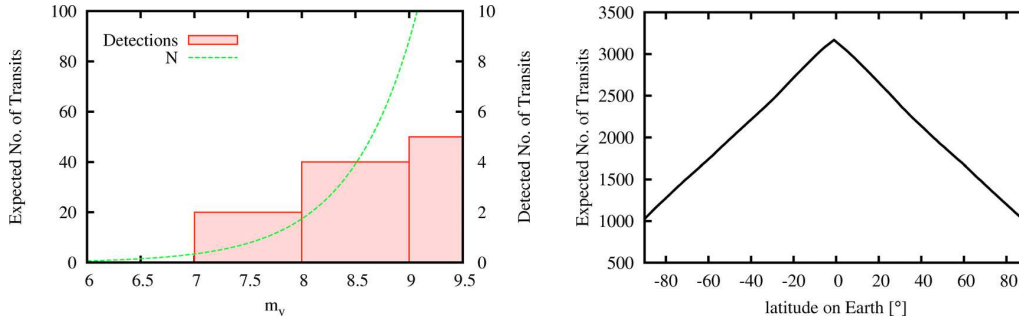
Fig. 2. Sky-integrated number of transits per magnitude (*left panel*) and as a function of latitude (*right panel*). *Left*: while the green line represents our simulations, the rosy bars show the number of transiting planets per magnitude bin discovered so far. Note the different scales at the left and right ordinates! *Right*: the triangle represents the expected number of transits that can be seen at elevations higher than 30° over the horizon at a given latitude on Earth.

Table 2. Instrumental properties of the treated surveys.

Survey	δ range	FOV	CCD Pixel size	m_V Range [Mag.]	δ & m_V Limited sample	δ, m_V & Δm_V Limited sample	δ, m_V, Δm_V & MS Limited sample
BEST	$-16° < \delta < 90°$	3.1°	5.5″/mm	$8 < m_V < 14$	546 382 (52.94%)	516 524 (50.05%)	222 854 (21.59%)
XO	$-39° < \delta < 90°$	7.2°	25.4″/mm	$9 < m_V < 12$	620 477 (60.12%)	597 842 (57.93%)	263 213 (25.51%)
SuperWASP	$-44° < \delta < 90°$	7.8°	13.8″/mm	$7 < m_V < 12$	745 227 (72.21%)	703 707 (68.19%)	311 404 (30.18%)
HATNet	$-28° < \delta < 90°$	8.3°	14.0″/mm	$7 < m_V < 12$	721 473 (69.91%)	686 927 (66.56%)	283 350 (27.46%)

In the last three columns we list the reduced Tycho master sample of 1 031 992 stars after we applied the subsequent boundary conditions: the survey's sky-coverage (δ range), its m_V limitation, magnitude variation $\Delta m_V > 0.01^m$ for the transit of a Jupiter-sized object around the ith star in a pixel, and the boundary conditions for MS stars, for which the empirical relationships hold (see Sect. 2.1). In braces we indicate the portion of the Tycho master sample.

accuracy limit of current ground-based surveys, then we keep this star for further analysis of the transit detection as described in Sects. 2 and 3.1, otherwise it is rejected. The fluxes, however, are not listed in the Tycho catalog; instead, we can use the visible magnitude $m_{V,i}$ of a star and calculate its relative flux f_i/f_0 with respect to a reference object with flux f_0 at magnitude $m_{V,0}$:

$$\frac{f_i}{f_0} = 10^{(m_{V,0}-m_{V,i})/2.5}. \qquad (12)$$

The magnitude variation can then be computed via

$$0.01 \overset{!}{\leq} \Delta m_{V,i} = -2.5 \cdot \log\left(\frac{0.99 \cdot f_i + \sum_{k \neq i}^{n} f_k}{\sum_{k}^{n} f_k}\right) \qquad (13)$$

$$= -2.5 \cdot \log\left(\frac{0.99 \cdot \frac{f_i}{f_0} + \sum_{k \neq i}^{n} \frac{f_k}{f_0}}{\sum_{k}^{n} \frac{f_k}{f_0}}\right).$$

Without loss of generality we chose $m_{V,0} = 30^m$ as reference magnitude.

4. Results

We develop a procedure for the calculation of the number of expected transit events to *occur* around MS stars based on empirical relations between the stars and planets. This procedure is

then applied to more than 1 million stars from the Tycho catalog to visualize the transit probability for all stars with $m_V \lesssim 11.5^m$ as a sky map. We also compute the celestial distribution of the number of expected transit *detections* for four different, well-established wide-field surveys.

In Fig. 3 we present the number of expected transit detections for the technical properties of BEST, XO, SuperWASP, and HATNet. As a general result from these maps, we find that the size of the FOV governs the detection efficiency of a camera. For the method applied here, the CCD resolution, i.e. the pixel size, has almost no impact since we neglect effects of noise, whereas in general the detection limits for transiting planets depend on the CCD resolution in terms of noise (Kovács et al. 2005; Tamuz et al. 2005; Pont et al. 2006). In Table 2 you see that the restriction of $\Delta m_V > 0.01^m$ almost doesn't reduce the sample. A large FOV, collecting the light of relatively many stars, outweighs a lower CCD resolution – at least for the range of pixel sizes considered here. Even for the zones around and in the galactic center and anti-center where the stellar density increases drastically, the number of detectable transit events reaches its maximum. This was not foreseeable since blending, simulated by Eq. (13), could have reduced the efficiency of transit detection within the crowded zones.

The four survey sky maps portray the very distinct efficiencies of the telescopes. The map of BEST reflects the stellar distribution of the Tycho data best due to the relatively high resolution of the CCD. However, the small FOV leads to very few expected transit detections. BEST's visible magnitude cut at the upper end is 14^m while the Tycho catalog is complete only up to 11.5^m. Thus, a significant contribution of stars inside this range is excluded in Fig. 3a. BEST also covers the smallest portion of the sky, compared to the other surveys. The XO project yields
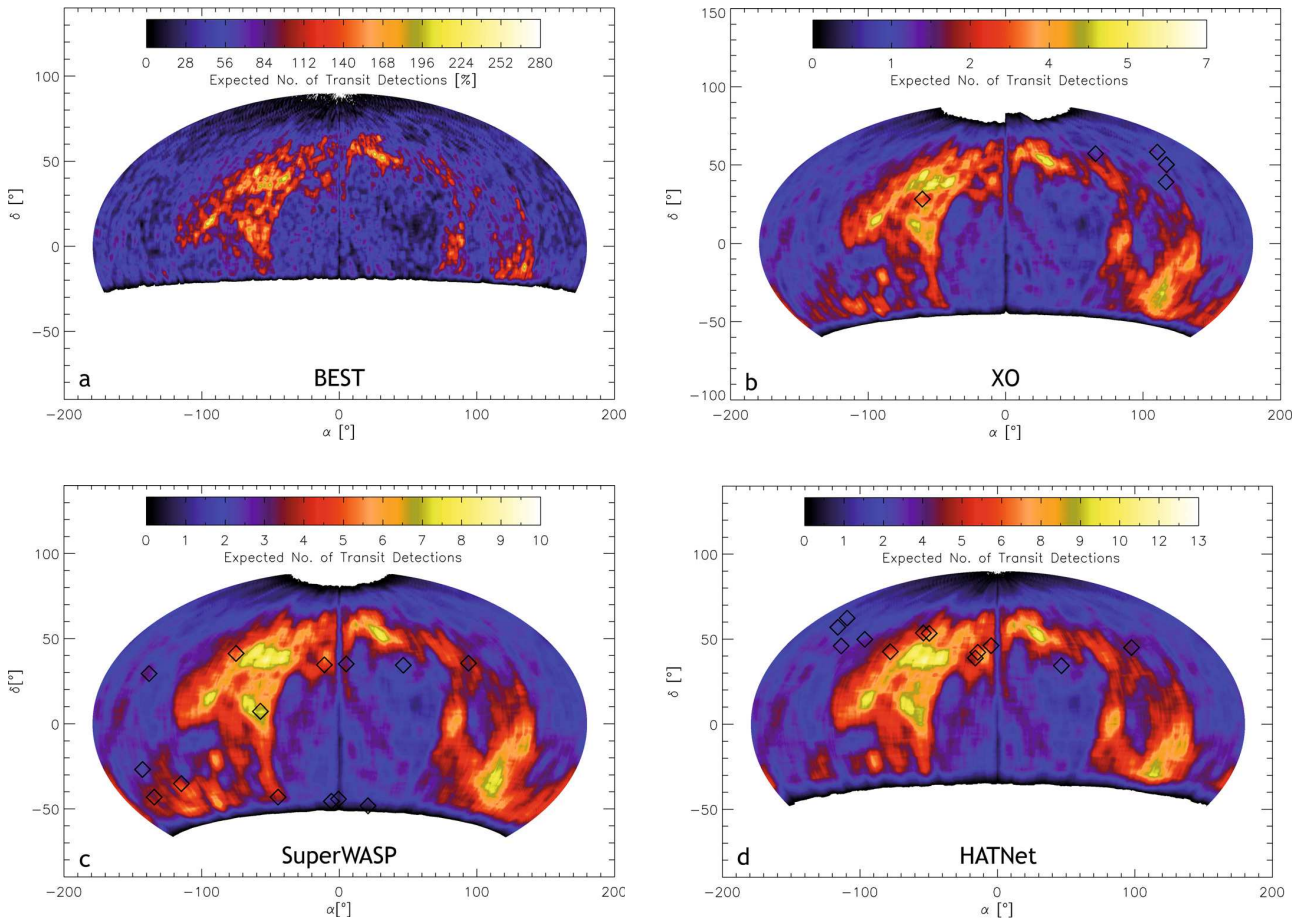
Fig. 3. Sky maps with expected number of transit detections for BEST **a)**, XO **b)**, SuperWASP **c)**, and HATNet **d)**. Note the different scales of the color code! The published detections of the surveys, taken from the EPE as of September 1st 2009, are indicated with symbols.

a much more promising sky map, owed to the larger FOV of the lenses. But due to the relatively large pixel size and an adverse magnitude cut of $9 < m_V$, XO achieves lower densities of expected detections than SuperWASP and HATNet. As for SuperWASP and HATNet, the difference in the magnitude cuts with respect to the Tycho catalog is negligible for XO but tends to result in an underestimation of the expected detections. That part of the SuperWASP map that is also masked by HATNet looks very similar to the map of the latter one. While HATNet reaches slightly higher values for the expected number of detections at most locations, the covered area of SuperWASP is significantly larger, which enhances its efficiency on the southern hemisphere.

The total of expected transiting planets in the whole sky is 3412 (see Fig. 1). By summing up all these candidates within an observational fan of 30° elevation above the horizon, we localize the most convenient site on Earth to mount a telescope for transit observations (see right panel in Fig. 2): it is situated at geographical latitude $l = -1°$. Given that the rotation of the Earth allows a ground-based observer at the equator, where both hemispheres can be seen, to cover a larger celestial area than at the poles, where only one hemisphere is visible, this result could have been anticipated. Due to the non-symmetric distribution of stars, however, the shape of the sky-integrated number of expected transits as a function of latitude is not obvious. Figure 2 shows that the function is almost symmetric with

respect to the equator, with slightly more expected transits at the northern hemisphere. Furthermore, the number of expected transits to be observable at the equator is not twice its value at the poles, which is due to the inhomogeneous stellar distribution. In fact, an observer at the equator triples its number of expected transits with respect to a spot at the poles and can survey almost all of the 3412 transiting objects.

Based on the analysis of the magnitude distribution (left panel in Fig. 2), we predict 20 planets with $m_V < 8$ to show transits with orbital periods between 1.5 d and 50 d, while two are currently known (HD209458b and HD189733b). These objects have proven to be very fruitful for follow-up studies such as transmission spectroscopy (Charbonneau et al. 2002; Vidal-Madjar et al. 2004; Knutson et al. 2007; Sing et al. 2008; Grillmair et al. 2008; Pont et al. 2008) and measurements of the Rossiter-McLaughlin effect (Holt 1893; Rossiter 1924; McLaughlin 1924; Winn et al. 2006, 2007; Wolf et al. 2007; Narita et al. 2007; Cochran et al. 2008; Winn et al. 2009). Our analysis suggests that a significant number of bright transiting planets is waiting to be discovered. We localize the most promising spots for such detections.

5. Discussion

Our values for the XO project are much higher than those provided by Beatty & Gaudi (2008), who also simulated the

expected exoplanet transit detections of XO. This is due to their much more elaborate inclusion of observational constraints such as observational cadence, i.e. hours of observing per night, meteorologic conditions, exposure time, and their approach of making assumptions about stellar densities and the Galactic structure instead of using catalog-based data as we did. Given these differences between their approach and ours, the results are not one-to-one comparable. While the study of Beatty & Gaudi (2008) definitely yields more realistic values for the expected number of transit detections considering all possible given conditions, we provide estimates for the celestial distribution of these detections, neglecting observational aspects.

In addition to the crucial respects that make up the efficiency of the projects, as presented in Table 2, SuperWASP and HATNet benefit from the combination of two observation sites and several cameras, while XO also takes advantage of twin lenses but a single location. Each survey uses a single camera type and both types have similar properties, as far as our study is concerned. The transit detection maps in Fig. 3 refer to a single camera of the respective survey. The alliance of multiple cameras and the diverse observing strategies among the surveys (McCullough et al. 2005; Cameron et al. 2009) bias the speed and efficiency of the mapping procedure. This contributes to the dominance of SuperWASP (18 detections, 14 of which have published positions)[3] over HATNet (13 detections, all of which have published positions)[3], XO (5 detections, all of which have published positions)[3], and BEST (no detection)[3].

It is inevitable that a significant fraction of unresolved binary stars within the Tycho data blurs our results. The impact of unresolved binaries without physical interaction, which merely happen to be aligned along the line of sight, is significant only in the case of extreme crowding. As shown by Gillon & Magain (2007), the fraction of planets not detected because of blends is typically lower than 10%. The influence of unresolved physical binaries will be higher. Based on the empirical period distribution for binary stars from Duquennoy & Mayor (1991), Beatty & Gaudi (2008) estimate the fraction of transiting planets that would be detected despite the presence of binary systems to be $\approx 70\%$. Both the contribution of binary stars aligned by chance and physically interacting binaries result in an overestimation of our computations of $\approx 40\%$, which is of the same order as uncertainties arising from the empirical relationships we use. Moreover, as Willems et al. (2006) have shown, the density of eclipsing stellar binary systems increases dramatically towards the Galactic center. To control the fraction of false alarms, efficient data reduction pipelines, and in particular data analysis algorithms, are necessary (Schwarzenberg-Czerny & Beaulieu 2006).

Recent evidence for the existence of ultra-short period planets around low-mass stars (Sahu et al. 2009), with orbital periods <1 d, suggests that we underestimated the number of expected transits to occur, as presented in Sect. 3.1. The possible underestimation of exoplanets occurring at $[Fe/H]_\star < 0$ also contributes to a higher number of transits and detections than we computed here. Together with the fact that the Tycho catalog is only complete to $m_V \lesssim 11.5^m$, whereas the surveys considered here are sensitive to slightly fainter stars (see Table 2), these trends towards higher numbers of expected transit detections might outweigh the opposite effect of unresolved binary stars.

A radical refinement of both our maps for transits occurrence and detections will be available within the next few years, once the "Panoramic Survey Telescope and Rapid Response System"

(Pan-STARRS) (Kaiser et al. 2002) will run to its full extent. Imaging roughly 6000 square degrees every night with a sensitivity down to $m_V \approx 24$, this survey will not only drastically increase the number of cataloged stars – thus enhance our knowledge of the localization of putative exoplanetary transits – but could potentially detect transits itself (Dupuy & Liu 2009). The Pan-STARRS catalog will provide the ideal sky map, on top of which an analysis presented in this paper can be repeated for any ground-based survey with the aim of localizing the most appropriate transit spots on the celestial plane. The bottleneck for the verification of transiting planets, however, is not the localization of the most promising spots but the selection of follow-up targets accessible with spectroscopic instruments. The advance to fainter and fainter objects thus won't necessarily lead to more transit confirmations. Upcoming spectrographs, such as the ESPRESSO@VLT and the CODEX@E-ELT (Pepe & Lovis 2008), can be used to confirm transits around fainter objects. These next-generation spectrographs that will reveal Doppler fluctuations on the order of cm s^{-1} will also enhance our knowledge about Hot Neptunes and Super-Earths, which the recently discovered transits of GJ 436 b (Butler et al. 2004), HAT-P-11 b (Bakos et al. 2009), and CoRoT-7b (Leger et al. 2009) and results from Lovis et al. (2009) predict to be numerous.

Further improvement of our strategy will emerge from the findings of more exoplanets around MS stars and from the usage of public data reservoirs like the NASA Star and Exoplanet Database[4], making assumptions about the metallicity distribution of planet host stars and the orbital period distribution of exoplanets more robust.

References

Aigrain, S., & Pont, F. 2007, MNRAS, 378, 741
Alonso, R., Brown, T. M., Charbonneau, D., et al. 2007, in Transiting Extrapolar Planets Workshop, ed. C. Afonso, D. Weldrake, & T. Henning, ASP Conf. Ser., 366, 13
Baglin, A., Auvergne, M., Barge, P., et al. 2002, in Stellar Structure and Habitable Planet Finding, ed. B. Battrick, F. Favata, I. W. Roxburgh, & D. Galadi, ESA SP, 485, 17
Bahcall, J. N., & Soneira, R. M. 1980, ApJS, 44, 73
Bakos, G. Á., Lázár, J., Papp, I., Sári, P., & Green, E. M. 2002, PASP, 114, 974
Bakos, G., Noyes, R. W., Kovács, G., et al. 2004, PASP, 116, 266
Bakos, G. Á., Torres, G., Pál, A., et al. 2009, ApJ, submitted [arXiv:0901.0282]
Beatty, T. G., & Gaudi, B. S. 2008, ApJ, 686, 1302
Borucki, W. J., & Summers, A. L. 1984, Icarus, 58, 121
Butler, R. P., Vogt, S. S., Marcy, G. W., et al. 2004, ApJ, 617, 580
Cameron, A. C., Pollacco, D., Hellier, C., et al. the WASP Consortium, & the SOPHIE & CORALIE Planet-Search Teams 2009, in IAU Symp., 253, 29
Castellano, T., Jenkins, J., Trilling, D. E., Doyle, L., & Koch, D. 2000, ApJ, 532, L51
Cester, B., Ferluga, S., & Boehm, C. 1983, Ap&SS, 96, 125
Charbonneau, D., Brown, T. M., Latham, D. W., et al. 2000, ApJ, 529, L45
Charbonneau, D., Brown, T. M., Noyes, R. W., et al. 2002, ApJ, 568, 377
Christensen-Dalsgaard, J., Arentoft, T., Brown, T. M., et al. 2007, Commun. Asteroseismol., 150, 350
Cochran, W. D., Redfield, S., Endl, M., et al. 2008, ApJ, 683, L59
Dupuy, T. J., & Liu, M. C. 2009, ApJ, 704, 1519
Duquennoy, A., & Mayor, M. 1991, A&A, 248, 485
Eigmüller, P., & Eislöffel, J. 2009, in IAU Symp., 253, 340

---

[3] EPE as of September 1st 2009.

[4] http://nsted.ipac.caltech.edu

ESA 1997, VizieR Online Data Catalog, 1239, 0
Fischer, D. A., & Valenti, J. 2005, ApJ, 622, 1102
Fleming, S. W., Kane, S. R., McCullough, P. R., et al. 2008, MNRAS, 386, 1503
Fressin, F., Guillot, T., Morello, V., et al. 2007, A&A, 475, 729
Fressin, F., Guillot, T., & Nesta, L. 2009, A&A, 504, 605
Gilliland, R. L., Brown, T. M., Guhathakurta, P., et al. 2000, ApJ, 545, L47
Gillon, M., & Magain, P. 2007, in Transiting Extrapolar Planets Workshop, ed.
    C. Afonso, D. Weldrake, & T. Henning, ASP Conf. Ser., 366, 283
Gillon, M., Courbin, F., Magain, P., et al. 2005, A&A, 442, 731
Gould, A., Dorsher, S., Gaudi, B. S., et al. 2006, Acta Astron., 56, 1
Grillmair, C. J., Burrows, A., Charbonneau, D., et al. 2008, Nature, 456, 767
Hoeg, E. 1997, in ESA SP, 402, Hipparcos – Venice '97, 25
Holt, J. R. 1893, A&A, 12, 646
Jiang, I.-G., Yeh, L.-C., Chang, Y.-C., et al. 2007, AJ, 134, 2061
Kaiser, N., Aussel, H., Burke, B. E., et al. 2002, in SPIE Conf. Ser. 4836, ed.
    J. A. Tyson, & S. Wolff, 154
Kaiser, N. 2004, in SPIE Conf. Ser. 5489, ed. J. M. Oschmann, Jr., 11
Kepler, J., Ptolemaeus, C., & Fludd, R. 1619, Harmonices mvndi libri v. qvorvm
    primus geometricvs, de figurarum regularium, quae proportiones harmonicas
    constituunt, ortu & demonstrationibus, secundus architectonicvs, SEU EX ge-
    ometria figvrata, de figurarum regularium congruentia in plano vel solido: ter-
    tius proprie harmonicvs, de proportionum harmonicarum ortu EX figuris, ed.
    J. Kepler, C. Ptolemaeus, & R. Fludd
Knutson, H. A., Charbonneau, D., Allen, L. E., et al. 2007, Nature, 447, 183
Koppenhoefer, J., Afonso, C., Saglia, R. P., et al. 2009, A&A, 494, 707
Kovács, G., Bakos, G., & Noyes, R. W. 2005, MNRAS, 356, 557
Leger, A., Rouan, D., Schneider, J., et al. 2009, A&A, 506, 287
Lovis, C., Mayor, M., Bouchy, F., et al. 2009, in IAU Symp., 253, 502
Mandushev, G., Torres, G., Latham, D. W., et al. 2005, ApJ, 621, 1061
Marcy, G., Butler, R. P., Fischer, D., et al. 2005, Progr. Theor. Phys. Suppl., 158,
    24
McCullough, P. R., Stys, J. E., Valenti, J. A., et al. 2005, PASP, 117, 783
McLaughlin, D. B. 1924, ApJ, 60, 22
Narita, N., Enya, K., Sato, B., et al. 2007, PASJ, 59, 763
Nordström, B., Mayor, M., Andersen, J., et al. 2004, A&A, 418, 989
Pepe, F. A., & Lovis, C. 2008, Phys. Scrip. Vol. T, 130, 014007

Pepper, J., & Gaudi, B. S. 2006, Acta Astron., 56, 183
Pont, F., Zucker, S., & Queloz, D. 2006, MNRAS, 373, 231
Pont, F., Knutson, H., Gilliland, R. L., Moutou, C., & Charbonneau, D. 2008,
    MNRAS, 385, 109
Queloz, D., Eggenberger, A., Mayor, M., et al. 2000, A&A, 359, L13
Rauer, H., Eislöffel, J., Erikson, A., et al. 2004, PASP, 116, 38
Reed, B. C. 1998, JRASC, 92, 36
Reid, I. N., Gizis, J. E., & Hawley, S. L. 2002, AJ, 124, 2721
Robin, A. C., Reylé, C., Derrière, S., et al. 2003, A&A, 409, 523
Rosenblatt, F. 1971, Icarus, 14, 71
Rossiter, R. A. 1924, ApJ, 60, 15
Sahu, K. C., Casertano, S., Valenti, J., et al. 2009, in IAU Symp., 253, 45
Santos, N. C., Israelian, G., & Mayor, M. 2004, A&A, 415, 1153
Schwarzenberg-Czerny, A., & Beaulieu, J.-P. 2006, MNRAS, 365, 165
Seagroves, S., Harker, J., Laughlin, G., et al. 2003, PASP, 115, 1355
Sing, D. K., Vidal-Madjar, A., Désert, J.-M., Lecavelier des Etangs, A., &
    Ballester, G. 2008, ApJ, 686, 658
Smith, R. C. 1983, The Observatory, 103, 29
Sozzetti, A., Torres, G., Latham, D. W., et al. 2009, ApJ, 697, 544
Street, R. A., Pollaco, D. L., Fitzsimmons, A., et al. 2003, in Scientific Frontiers
    in Research on Extrasolar Planets, ed. D. Deming, & S. Seager, ASP Conf.
    Ser., 294, 405
Struve, O. 1952, The Observatory, 72, 199
Tamuz, O., Mazeh, T., & Zucker, S. 2005, MNRAS, 356, 1466
Udalski, A., Szymanski, M., Kaluzny, J., Kubiak, M., & Mateo, M. 1992, Acta
    Astron., 42, 253
Udry, S., & Santos, N. C. 2007, ARA&A, 45, 397
Vidal-Madjar, A., Désert, J.-M., Lecavelier des Etangs, A., et al. 2004, ApJ, 604,
    L69
Willems, B., Kolb, U., & Justham, S. 2006, MNRAS, 367, 1103
Winn, J. N., Johnson, J. A., Marcy, G. W., et al. 2006, ApJ, 653, L69
Winn, J. N., Johnson, J. A., Peek, K. M. G., et al. 2007, ApJ, 665, L167
Winn, J. N., Johnson, J. A., Fabrycky, D., et al. 2009, ApJ, 700, 302
Wolf, A. S., Laughlin, G., Henry, G. W., et al. 2007, ApJ, 667, 549
Wyatt, M. C., Clarke, C. J., & Greaves, J. S. 2007, MNRAS, 380, 1737

6.2 Transit detections of extrasolar planets around main-sequence stars

II. Extrasolar planets in the habitable zones of their host stars

D. Mislis, R. Heller, J. H. M. M. Schmitt, E.W. Guenther, and J. Antoniadis
Credit: D. Mislis et al., submitted to *A&A*, reproduced with permission ©ESO

While we presented sky maps for the transit detection of hot Jupiters in our first paper (Heller et al. 2009b, previous chapter), the following article is dedicated to the transit probabilities of extrasolar planets in the habitable zone of their host stars. Due to the magnitude limit of Earth-based transit surveys and due to the relatively long orbital periods of these planets, as compared to hot Jupiters, ground-based detections of such planets are very unlikely. However, space-based telescopes, such as the ongoing 'CoRoT' and 'Kepler' missions, cover thousands of stars simultaneously with accuracies high enough to discern the planetary imprint in the light curve of a star.

To this study, which emerged again from inspiring discussion with Dimitris Mislis, I contributed the black-and-white figures and I composed a significant part of the manuscript.

Transit detections of extrasolar planets around main-sequence stars

II. Extrasolar planets in the habitable zones of their host stars

D. Mislis[1], R. Heller[2], J. Schmitt[3], E. W. Guenther[4], and J. Antoniadis[5]

[1] Hamburger Sternwarte (Universität Hamburg), Gojenbergsweg 112, 21029 Hamburg, Germany
     e-mail: dmislis@hs.uni-hamburg.de
[2] Hamburger Sternwarte (Universität Hamburg), Gojenbergsweg 112, 21029 Hamburg, Germany
     e-mail: rheller@hs.uni-hamburg.de
[3] Hamburger Sternwarte (Universität Hamburg), Gojenbergsweg 112, 21029 Hamburg, Germany
     e-mail: jschmitt@hs.uni-hamburg.de
[4] Thüringer Landessternwarte Tautenburg, Sternwarte 5, D-07778 Tautenburg, Germany
     e-mail: guenther@tls-tautenburg.de
[5] Max Planck Instutute fuer Radioastronomie, Auf dem Huegel 69, 53121 Bonn, Germany
     e-mail: jantoniadis@mpifr-bonn.mpg.de

ABSTRACT

Context. Recent discoveries of transiting Super-Earths and transiting extrasolar planets at the edge or even far outside the traditional habitable zone (THZ) prove the existence and accessability of such objects. Since their formation process is not yet understood and their occurrence has only recently become subject to science the question about their detection probability remains obscure.
Aims. Using simple but reasonable assumptions about planetary occurrence, we want to assess the prospects of current transit surveys – ground-based as well as space-based. We also aspire to classify the basic observational properties of the planets and stars that will most likely be found to be transiting systems.
Methods. We first evaluate the chances of success for ground based transit surveys. Therefore, we employ the data of roughly 1 million stars from the Tycho catalog to derive the location and the fundamental physical parameters of almost all the stars on the celestial plane with $m_V < 11.5$. We then use geometrical considerations and an assumption of the planetary occurrence in a star's THZ to derive a sky map of the probability distribution for the occurrence of transits from exoplanet in the THZ of their host stars. Finally, we use data from the CoRoT field IR01 to simulate the detection probabilities of planets in the THZs of their host stars for CoRoT depending on stellar and planetary features, such as the radii of both constituents and the visible stellar magnitude.
Results. The sky map for ground-based observations of exoplanet transits in the THZ of their host stars shows dismal prospects of success. Within a field of view of a typical ongoing survey, the detection probability does not exceed 1.4 %. A common value for the celestial plane is 0.2 % per field of view. Current space-based missions, on the other hand, will presumably discover transiting planets in their THZs. Assuming each star in IR01 hosts one planet of at least eight times the size of the Earth in its THZ, it is very likely that at least one of them will be detected by CoRoT.
Conclusions.

Key words. Stars: planetary systems – Occultations – Astrobiology – Methods: statistical – Techniques: photometric – Methods: observational

1. Introduction

Transiting extrasolar planets are promising targets for the field of astrobiology since they offer direct measurements of the atmospheric composition of potentially inhabited worlds (Webb & Wormleaton 2001; Ehrenreich et al. 2006; Selsis et al. 2007a; Kaltenegger & Traub 2009). The recent detections of the transiting Super-Earths CoRoT-7b (Léger et al. 2009, space-based discovery) and GJ1214b (Charbonneau et al. 2009, ground-based detection) have shown that today's technology is mature for the exploration of terrestrial planets and their habitability. While most of the transiting planets have been discovered with ground-based instruments, the two space-based missions CoRoT (Deleuil et al. 1997) and Kepler (Borucki et al. 1997) have so far discovered a handful of transiting planets (see Barge et al. (2008); Alonso et al. (2008); Deleuil et al. (2008); Aigrain et al.

(2008); Rauer et al. (2009); Léger et al. (2009); Dvorak et al. (2009) for CoRoT and Borucki et al. (2010b); Koch et al. (2010); Dunham et al. (2010); Latham et al. (2010); Jenkins et al. (2010); Borucki et al. (2010a) for Kepler). All of these planets, except for the two mentioned above, are Jupiter-like in terms of mass and radius, and none of them is located in the habitable zone (HZ) of its host star. Thus, none of the currently known transiting planets can be regarded as habitable.

In this paper, we examine the statistical prospects of ground-based as well as space-based surveys for the detection of planets in the HZs of their host stars. In terms of ground-based instrumentation, we rely on a method described in Heller et al. (2009, paper I in the following), where we used the data of roughly one million objects listed in the Tycho catalog, taken with the Hipparcos satellite between 1989 and 1993 (ESA 1997; Hoeg

1997). For the analysis of the space-based perspectives, we simulate exoplanet transits in front of the 14 007 stars located in the CoRoT field IR01, and also examine the impact of the planetary radius on the detection probability in the field; this part will also include terrestrial planets.

2. Derivation of stellar properties

2.1. Habitable zones around the stars

The method for the derivation of the stellar properties such as T_{eff}, $R_\star$, and $M_\star$ from the parameters given in the Tycho catalog are described in paper I. In this recent study, we use a relationship stated by Fischer & Valenti (2005) between $(B - V)$, as provided by the Tycho catalog, and the stellar metallicity $[\mathrm{Fe/H}]_\star$, to firstly derive $[\mathrm{Fe/H}]_\star$ and finally the probability for planetary occurrence around the stars in the Tycho sample. However, this approach is inappropriate for the calculation of planetary existence in HZs since the empirical relationships are strongly biased towards Hot Jupiters, i.e., planets in orbits with semi-major axes of mostly < 0.1 AU. Up to now, no exoplanet has been discovered that is unambiguously located in the HZ of its host star[1], conection between stellar properties and occurrence of planetary companions in the HZs is not yet assessable. For the following calculations, we thus assume a scenario in which each star has one extrasolar planet in its HZ. Although this approach is rather optimistic, reasonable arguments in favor for this assumption are given in Grether & Lineweaver (2006) and our existence shows that this setting is not totally irrational. If this approximation is too optimistic, our results for the transit probabilities will serve as upper limits.

For the calculations of the transit probability $\wp_{\mathrm{geo}}$ of a given exoplanet within the HZ, we do not include any assumptions about the habitability times of the putative systems. Since the distances of the stars in our sample are typically of order 300 pc, we also do not take into account effects of the Galactic habitable zone (Gonzalez 2005; Prantzos 2008). We rely on the Eq. (1) from Seagroves et al. (2003) and assume that the planetary radius R_P is small compared to the stellar radius $R_\star$, thus $R_\star - R_P \approx R_\star$. Then the formula transforms into an upper limit for the geometric transit probability:

$$\wp_{\mathrm{geo}} \lesssim 0.0045 \, \frac{1\,\mathrm{AU}}{a} \frac{R_\star}{R_\odot} \frac{1 + e\cos(-\varpi)}{1 - e^2} \quad , \qquad (1)$$

which includes eccentricity e, the argument of periastron ϖ and the semi-major axis a. Since we are looking for planets within the stellar HZ, a will be given by the range of relevant orbits at orbital distances $d_{\mathrm{THZ}}^{\mathrm{in}} < a < d_{\mathrm{THZ}}^{\mathrm{out}}$, with $d_{\mathrm{THZ}}^{\mathrm{in}}$ and $d_{\mathrm{THZ}}^{\mathrm{out}}$ as the critical inner and outer radius of the traditional habitable zone (THZ). A simple and established expression for its extent, only as a function of the stellar luminosity $L_\star$, is given by Kasting et al. (1993):

$$d_{\mathrm{THZ}} = 1\,\mathrm{AU} \left(\frac{L_\star/L_\odot}{S_{\mathrm{eff}}} \right)^{0.5} \quad , \qquad (2)$$

where S_{eff} is the effective solar flux, necessary to maintain a certain surface temperature on a planet, in dimensionless units. The

latter parameter depends on the planetary albedo and the atmospheric composition of the planet.

Refinements of this THZ include formation and orbital stability of extrasolar planets, geologic activity, abundant water and the planet's atmospheric composition and structure (for a review see Gaidos et al. 2005). A more elaborate definition of a HZ is given by Selsis et al. (2007b), which includes different, putative atmospheric compositions on the planet, i.e. cloud coverage and albedo. Furthermore, the presence of other planets may render planets in the THZ inhabitable due to gravitational perturbations, which slingshot the potentially habitable planet (Dvorak et al. 2003; Schwarz et al. 2005; Sándor et al. 2007). Tidal processes, raised by the host star, can lead to tidal heating on the planet, which can be strong enough as to drive plate tectonics and global volcanism (Jackson et al. 2008; Barnes et al. 2009), or they may generate subsurface oceans analogous to Europa's (Greenberg 2005), thus customizing the HZ to the individual orbital and physical parameters of the planet. Tides may also drive a significant evolution of a planet's orbit and lead to tidal locking (Barnes et al. (2008)). We confine ourselves to using the less complex description by Kasting et al. (1993) since the planetary parameters are unknown.

To obtain an extent of the THZ, we take the values for S_{eff} as provided by Kasting et al. (1993) for a Venus-like planet to maintain liquid water at the inner edge of the THZ ($S_{\mathrm{eff}}^{\mathrm{in}} = 1.9114$) and a Martian planet at the outer edge, modified to exhibit a maximum greenhouse effect ($S_{\mathrm{eff}}^{\mathrm{out}} = 0.36$). These two values for S_{eff} define an inner and an outer boundary $d_{\mathrm{THZ}}^{\mathrm{in}}$ and $d_{\mathrm{THZ}}^{\mathrm{out}}$ of the THZ around a star as a function of $L_{\star, S_{\mathrm{eff}}}$. To translate it into a function of $(B - V)_{S_{\mathrm{eff}}}$, we use the relationship given in Parenago (1958) to derive M_{V} from the given color index. Using Eq. (3) from paper I, we then deduce the stellar radius and finally, by means of Eq. (4) in that paper, the stellar mass based on several empirical relations. Using Kepler's 3rd law and assuming $M_{\mathrm{p}} \ll M_\star$, the radial boundaries for the THZ can then be converted into limits in terms of orbital period, independent of the planetary radius or mass. In Fig. 1 we show the borders of the THZ, i.e. the period limits as a function of the stellar color index $(B - V)$. While the Earth, with $(B - V)_\odot = 0.642$ (Holmberg et al. 2006), is situated well inside the THZ, Gl581d is slightly too far away from its host star. The only known transiting rocky planet so far, CoRoT-7b (Léger et al. 2009), is far too close to its star.

2.2. Constraints of eccentricity on the habitability

Now that we can infer the extent of the THZ on the basis of the parameters as provided by the Tycho data, we still have the two free parameters e and ϖ for the computation of $\wp_{\mathrm{geo}}$, which are not known for a certain, putative system. We denote the transit probability for circular orbits with $\wp_{\mathrm{geo}}^{\mathrm{circ}}$. To eliminate the dependence on the stellar radius and the semi-major axis in Eq. (1), we present a plot of $\wp_{\mathrm{geo}}(e, \varpi)/\wp_{\mathrm{geo}}^{\mathrm{circ}}$ in Fig. 2, which shows that any given eccentricity $\neq 0$ increases the detection probability for the most part of the orbit. With rising eccentricity, the fraction of the orbit that yields detection probabilities higher than for the circular case increases gently. For an arbitrary but fixed eccentricity, say $\tilde{e}$, the geometric transit probability $\wp_{\mathrm{geo}}^{\tilde{e}}(\varpi)$ reaches its minimum at $\varpi_{\mathrm{min}} = \pi$, while the maximum is at $\varpi_{\mathrm{max}} = 0 \vee 2\pi$.

Of course, for the planetary orbit to be fully situated within the THZ, the eccentricity cannot take arbitrary values. For $e = 0$, it is clear that this circle can be well located within the THZ, however, for the other extreme of $e = 1$, this line will cross the inner and the outer edges of the THZ. Obviously, there does exist a highest value e_{max} for the eccentricity at which the whole orbit
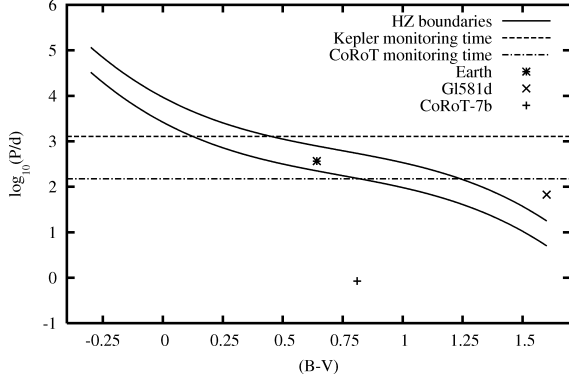
---

[1] There is ongoing discussion about whether Gl581d is located inside or outside its HZ, owed to different concepts of a HZ, uncertainties in the planetary parameters and the planet's non-circular orbit: The apoastron is situated outside the HZ whereas the periastron is located inside (Selsis et al. 2007b; von Bloh et al. 2007; Beust et al. 2008; Barnes et al. 2009; Mayor et al. 2009, and this paper).

Fig. 1. Extent of the THZ as given by Eq. (2) with $S_{\mathrm{eff}}^{\mathrm{in}} = 1.9114$ for the inner limit and $S_{\mathrm{eff}}^{\mathrm{out}} = 0.36$ for the outer bound. Transiting planets with P less than the Kepler or CoRoT monitoring time will show at least one transit, higher periods leading to smaller detection probabilities. The positions of the Earth, Gl581d, and CoRoT-7b are indicated.
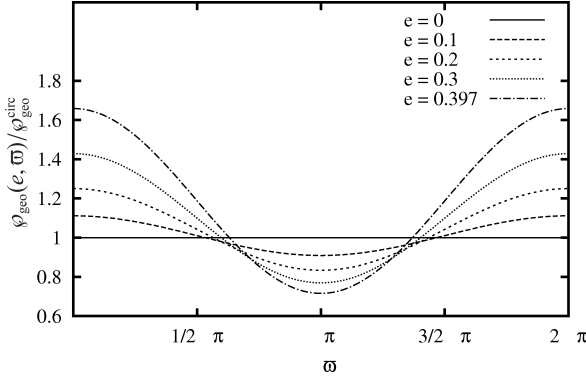

Fig. 2. Geometric transit probability from Eq. (1) as function of ϖ for five different values of e. The highest eccentricity of 0.397 is the theoretical maximum value for an orbit to be fully located in the THZ.

of the planet still is embedded in the THZ. Using the relation of a being centered within the inner and the outer edge of the THZ, $a = (d_{\mathrm{THZ}}^{\mathrm{in}} + d_{\mathrm{THZ}}^{\mathrm{out}})/2$, and constraining that the closest orbital approximation $d^{\mathrm{close}} = a(1 - e)$ between the host star and the planet remains larger than the extent of the inner edge of the THZ, $d^{\mathrm{close}} \geq d_{\mathrm{THZ}}^{\mathrm{in}}$, we derive

$$ e \leq \frac{d_{\mathrm{THZ}}^{\mathrm{out}} - d_{\mathrm{THZ}}^{\mathrm{in}}}{d_{\mathrm{THZ}}^{\mathrm{out}} + d_{\mathrm{THZ}}^{\mathrm{in}}} \quad , \tag{3} $$

and, applying Eq. (2), we find

$$ e \leq \frac{\sqrt{1/S_{\mathrm{eff}}^{\mathrm{out}}} - \sqrt{1/S_{\mathrm{eff}}^{\mathrm{in}}}}{\sqrt{1/S_{\mathrm{eff}}^{\mathrm{out}}} + \sqrt{1/S_{\mathrm{eff}}^{\mathrm{in}}}} \quad . \tag{4} $$

For the values $S_{\mathrm{eff}}^{\mathrm{in}} = 1.9114$ and $S_{\mathrm{eff}}^{\mathrm{out}} = 0.36$ this yields $e_{\max} = 0.397$. Thus, the maximum eccentricity for a planet to remain within the THZ of its host star, as defined by Kasting et al. (1993), is independent of any stellar properties.

3. Application to survey data

3.1. Tycho catalog

We now apply our method to the Tycho data and produce a sky map of the transit probability of exoplanets in the THZs of their host stars. We combine the geometric considerations expressed in Eq. (1) with the assumption of one exoplanet in the THZ of the respective host star[2]. With the premise of one planet in the center of the THZ around each star, the probability for planet to exits around a certain star, $\wp_{\exists\,\mathrm{planet}}$, takes the value 1. Hence, the overall probability for a transit to occur, $\wp_{\mathrm{occ}}$, coincides with the geometric probability:

$$ \wp_{\mathrm{occ}} = \wp_{\exists\,\mathrm{planet}} \cdot \wp_{\mathrm{geo}} = \wp_{\mathrm{geo}} \quad . \tag{5} $$

In the next step, as described in paper I, we scan the sky with a fixed field of view (FOV) spanning $8° \times 8°$, with an overlap of $7°$ between adjacent fields for a smooth distribution, and calculate the transit probability for each of these FsOV. Due to the magnitude cut of the Tycho catalog at $m_{\mathrm{V}} \lesssim 11.5^{\mathrm{m}}$ and the chosen FOV, the results will be adaptive to current ground-based wide-field surveys, e.g. SuperWASP and HATNet, although we do not make any assumption about the instrumental properties such as pixel size, CCD resolution, focal length, observational windows etc. Our virtual instrument, in that sense, has an infinite resolution.

There is a tendency in the Tycho data towards more giant stars and early-type main sequence (MS) stars, caused by the magnitude cut at $m_{\mathrm{V}} \lesssim 11.5^{\mathrm{m}}$. Planetary transits in front of these stars will not be detectable with ground-based instruments due to the limited accuracy achievable from the ground. In addition to our optimistic assumption of one planet in the THZ of each star, this bias leads to an upper limit for the transit probabilities.

To plot $\wp_{\mathrm{occ}}$ for each FOV as a function of the right ascension α and declination δ, e and ϖ must be fixed for each putative planet. We assume circular orbits, thus $e = 0$, for a planet located in the center of the THZ of its host star, $a = (d_{\mathrm{THZ}}^{\mathrm{in}} + d_{\mathrm{THZ}}^{\mathrm{out}})/2$.

3.2. CoRoT field

As an example for the prospects of space-based transit surveys, we refer to CoRoT, one of the two current space-based missions aiming at the detection of extrasolar planet transits. We base our analysis on real data[3], i.e., the light curves (LCs) of 14 007 stars observed with CoRoT in the 'initial run' field IR01, which is located at $\alpha = 06^{\mathrm{h}}57^{\mathrm{m}}18^{\mathrm{s}}, \delta = -01°42'00''$ (J2000.0) (Kabath et al. 2007). The stellar color index $(B - V)$ and the star's visible magnitude m_{V} are known properties. We first derive the stellar effective temperature T_{eff} from $(B - V)$ (see paper I) and then calculate $R_\star$ from a fit to the data given in Habets & Heintze (1981),

$$ \frac{R_\star}{R_\odot} = -7.52082 + 2.2959 \cdot \log_{10}(T_{\mathrm{eff}}) \quad , \tag{6} $$

assuming that the stars in the CoRoT sample are all on the MS. We used a sample of 1000 non-variable LCs, to calculate the standard deviation σ. Given that m_{V} is known, we then apply a fit to the correlation between m_{V} and σ and deduce the lower limit for the apparent brightness, or in mathematical terms: an

---

[2] In paper I we described how these probabilities of transit occurrence are related to the actual transit detection probabilities for certain instruments.

[3] http://idoc-corot.ias.u-psud.fr

upper limit for the visible magnitude $m_{\mathrm{V}}^{\min}$, that is necessary for CoRoT to discern the transit. This correlation is given by

$$m_{\mathrm{V}}^{\min} = 11.761 + 0.170 \cdot \left(\frac{R_{\mathrm{p}}}{R_{\star}}\right)^2 \quad . \tag{7}$$

We now use $\sigma(m_{\mathrm{V}}) = 1.00921 - 7.8 \cdot 10^{-4} m_{\mathrm{V}}$ to simulate CoRoT LCs. Therefore, we model the transit of an extrasolar planet for the two cases of a circular orbit at the inner edge of the THZ as well as at its outer border. To test whether the transit depth D is larger than the standard deviation, we grasp a range of planetary radii $0 < R_{\mathrm{p}} < 10\,R_{\mathrm{E}}$ and stellar radii $0.1\,R_{\odot} < R_{\star} < 1.5\,R_{\odot}$, corresponding to spectral types between F0 and M6 (Habets & Heintze 1981). R_{E} and $R_{\odot}$ are the radius of the Earth and the Sun, respectively. If a LC for a certain R_{p}-$R_{\star}$ combination shows $D > \sigma$, then we assume the transit can be detected. In that case we calculate the individual probability for transit occurrence of that star with Eq. (5).

As an example, we exhibit a very promising configuration of a relatively bright ($m_{\mathrm{V}} = 13$) K5 star, transited by a planet in a circular orbit at the inner edge of the THZ and an unfavorable system where an apparently dim ($m_{\mathrm{V}} = 15$) F5 star shows occultations of a planet located at the outer border of the THZ (Fig. 4). For each of these two configurations, we show the three cases of a $2\,R_{\mathrm{E}}$, a $3\,R_{\mathrm{E}}$, and a $4\,R_{\mathrm{E}}$ planet. The upper row in Fig. 4 shows the favorable star-planet configuration. In all the three LCs the transit is clearly distinguished from the noise. For the transits of the unfavorable system, however, the transit can only be detected in the case of a planet with $4\,R_{\mathrm{E}}$ radius.

Finally, we take into account the geometric concerns of the transit probability as given by Eq. (5). Although $\wp_{\mathrm{occ}}$ is only a function of $R_{\star}$ and a, since we assume $e = 0$, and not a function of R_{p}, the result of our procedure will depend on the planetary radius. This is due to the perceptibility of the transit, which strongly depends on R_{p}. Only if the respective transit of a certain R_{p}-$R_{\star}$ duet yields $D > \sigma$, this pair will be selected for the computation of $\wp_{\mathrm{occ}}$ via Eq. (5), otherwise $\wp_{\mathrm{occ}} = 0$ by default. Another dependence of $\wp_{\mathrm{occ}}$ on $R_{\star}$ arises from Eq. (2). We study the case of a planet transiting at the inner limit of the THZ, thus $a = d_{\mathrm{THZ}}^{\mathrm{in}}$, and the case of a transit at the outer periphery where $a = d_{\mathrm{THZ}}^{\mathrm{out}}$. And as expressed in Eq. (2), these boundaries depend on $L_{\star}$ and thus on $R_{\star}$.

4. Results

4.1. Prospects for ground-based surveys

The sky map for the occurrence probability of extrasolar planet transits in the THZ of their MS host star is shown in Fig. 3. Circular orbits in the center of the THZ are assumed. To apply a certain eccentricity and orientation of periastron for all stars, this map has to be multiplied with the corresponding factor provided by Fig. 2. Of course, the distributions of eccentricity values and orbital orientations will not be uniform in the sky but they will follow some statistical functions. Most of the eccentricities will be close to 0 due to the proximity of transiting planets to their host stars and consequential orbital decay due to tidal interactions on time scales much shorter than the typical life time of a MS star.

The Galactic plane is clearly visible in the sky map. Obviously, its path yields the highest transit probabilities, which is simply due to the increased stellar density in the FOV. The absolute values for $\wp_{\mathrm{occ}}$ are typically around 1 % in the Galactic zone, but only about 2 ‰ for the most part of the sky. These values are upper limits, based on the likely overestimate that each
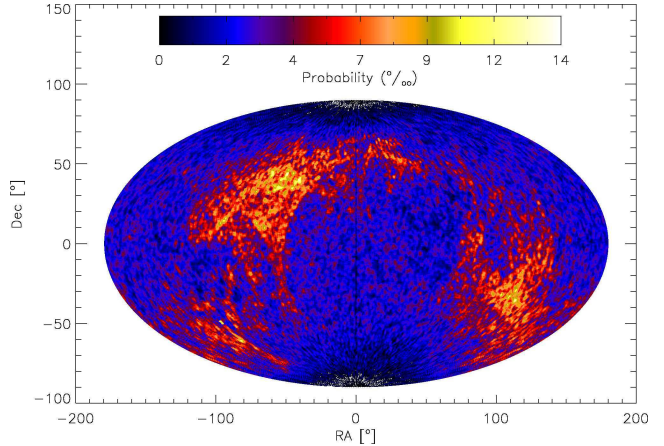

Fig. 3. Sky map of the transit probability $\wp_{\mathrm{occ}}$ for extrasolar planets in the center of the THZs of their host stars in units of per mill. To include e and ϖ, this color map has to be multiplied by the respective values from Fig. 2.

star hosts a planet in its THZ and on a bias in the Tycho data towards giants and early-type stars.

4.2. Prospects for space-based surveys

In Fig. 5 we highlight the radii of the prospective transiting exoplanets and their host stars to be discovered by CoRoT. For the left panel we assumed that each star in IR01 entails a transiting planet at the inner border of its THZ, $d_{\mathrm{THZ}}^{\mathrm{in}}$, whereas the planet is assumed to be at the outer edge $d_{\mathrm{THZ}}^{\mathrm{out}}$ in the right panel. Both plots show the color-coded contours of the R_{p}-$R_{\star}$-projected probability that at least one transit would be observed in IR01 if each of the stars in the field hosted a planet with the respective radius, $\wp_{\mathrm{IR01}}$. The differences in the absolute values between the left and the right panel are as high as 0.5 in some regions but the general shapes of the probability distributions for these putative planets in the CoRoT field IR01 are similar. The comparison of both panels visualizes the fact that, due to the geometrical aspects, the detection probabilities for transiting planets at the inner edge of the THZ are higher than for bodies at the outer edge.

Planets with radii larger than 10 times the radius of the Earth could easily be detected in the THZs of all the stars that we took into account, i.e. $\wp_{\mathrm{IR01}} = 100\,\%$ for $0 \leq R_{\star} \leq 1.5\,R_{\odot}$. The interesting limits for the transit detectability appear for Super Earths with $R_{\mathrm{p}} < 10\,R_{\mathrm{E}}$. Down to $R_{\mathrm{p}} \approx 8\,R_{\mathrm{E}}$ we find $\wp_{\mathrm{IR01}} = 100\,\%$, whereas an Earth-like planet with $R_{\mathrm{p}} = 1\,R_{\mathrm{E}}$ could only be detected around very small MS stars. Nevertheless, the search for an Earth twin in the THZs of IR01 stars will succeed if these planets are common.

The magnitude cuts for CoRoT are indicated with lines. An R_{p}-$R_{\star}$ combination below a certain magnitude line could not be detected as a transiting system, provided that the host star shows the respective apparent magnitude.

5. Discussion

For ground-based surveys, the values for the occurrence probability of exoplanets in the THZ of their hosts stars are small compared to the transit probabilities of hot Jupiters (see paper I). While exoplanet transits in the THZs of their host stars would be observed with probabilities $\lesssim 1\,\%$, passages of hot Jupiters
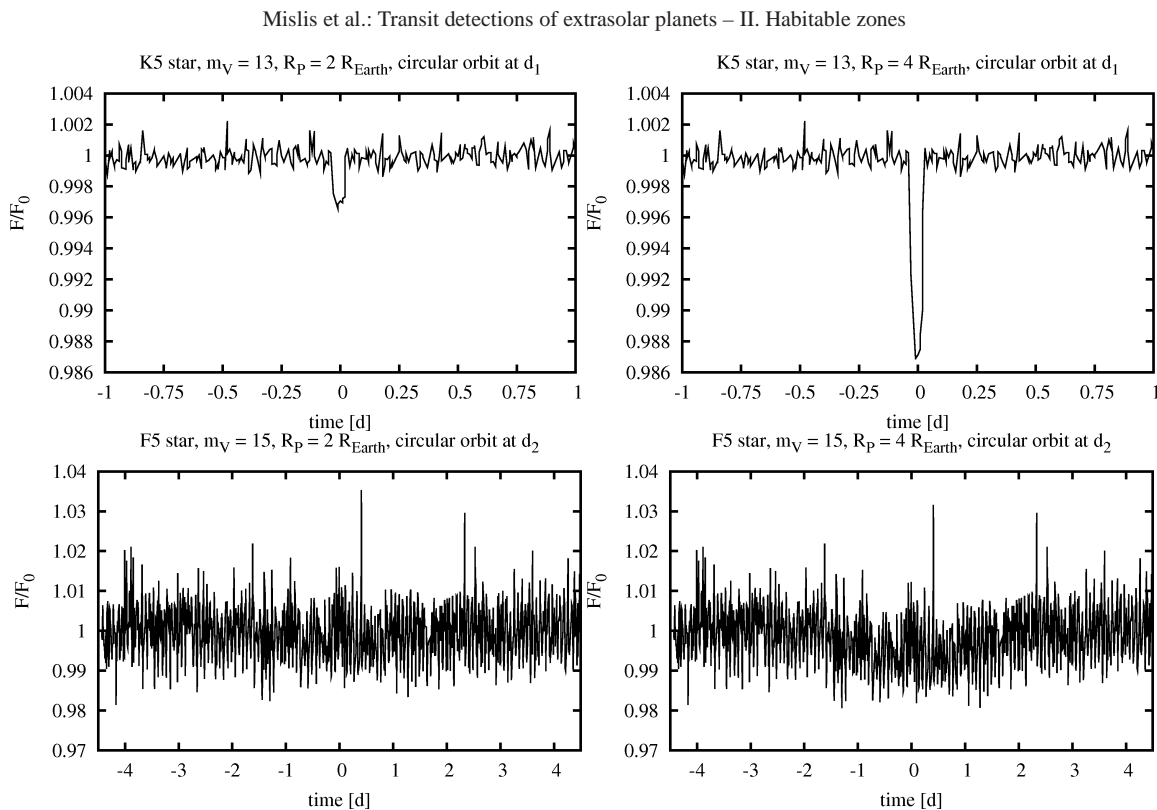
Fig. 4. Simulated CoRoT LCs of stars with transiting planets of 2, and $4\,R_\oplus$ (from left to right). F/F_0 is the relative flux with F as the number of photons and F_0 as the mean photon flux outside the transit. *Upper row:* These transits occur around a K5 star at $m_V = 13$, while the transiting planet is at the inner edge of the THZ. *Lower row:* Here, we consider an F5 star at $m_V = 15$ and for the planetary orbit we assume the outer edge of the THZ. Only for $R_p = 4\,R_\oplus$ the transit becomes distinguishable from the noise between ≈ -1.5 and $\approx 1.5\,$d around the center.

turned out to appear typically on the order of 15 % outside the Galactic plane and $\approx 80\,\%$ inside within a comparable FOV. To increase the chances of success for the detection of an exoplanet in the THZ, one would have to observe a large amount of stars and moreover, the respective field would have to be monitored for a relatively long time due to the relatively long periods of the planets of $\gtrsim 100\,$d (see Fig. 1). The method we present here to compute the probabilities for transit *occurrence* of extrasolar planets around MS stars in the THZs, does not invoke any observational constraints such as observing schedule, weather conditions, and exposure time. We also neglect issues of data reduction, e.g. red noise, the impact of the instrument's point spread function, and efficiency and selection effects of the data reduction pipelines. A consideration of these parameters would allow for the calculation of the actual *detection* probabilities of such transits and these values will be much smaller than those presented here. This makes ground-based surveys not a very promising tool for the detection of such events.

Fortunately, there are two ongoing space based missions that come into consideration for the detection of such planets: CoRoT and Kepler. Planets in the THZs to be discovered by the former mission will most likely be located in the inner part of the zones and will show radii larger than $\approx 8\,R_E$. Smaller planets down to the size of the Earth might also be detected and would orbit stars of the size of the Sun and smaller. The probability distribution in Fig. 5 shows that, if exoplanets with $R_p \gtrsim R_E$ in the THZ are common, then they are very likely to be detected with CoRoT. As long as their non-detections are not due to flaws in the data reduction and if they do not have systematic origin, their absence around stars with THZs that are covered by CoRoT in terms of orbital and observational period (see Fig. 1) constrains the occurrence of Earth-like planets.

References

Aigrain, S., Collier Cameron, A., Ollivier, M., et al. 2008, A&A, 488, L43

Alonso, R., Auvergne, M., Baglin, A., et al. 2008, A&A, 482, L21

Barge, P., Baglin, A., Auvergne, M., et al. 2008, A&A, 482, L17

Barnes, R., Jackson, B., Greenberg, R., & Raymond, S. N. 2009, ApJ, 700, L30

Barnes, R., Raymond, S. N., Jackson, B., & Greenberg, R. 2008, Astrobiology, 8, 557

Beust, H., Bonfils, X., Delfosse, X., & Udry, S. 2008, A&A, 479, 277

Borucki, W. J., Koch, D., Basri, G., et al. 2010a, in American Astronomical Society Meeting Abstracts, Vol. 215, American Astronomical Society Meeting Abstracts, 101.01–+

Borucki, W. J., Koch, D. G., Brown, T. M., et al. 2010b, ArXiv e-prints

Borucki, W. J., Koch, D. G., Dunham, E. W., & Jenkins, J. M. 1997, in Astronomical Society of the Pacific Conference Series, Vol. 119, Planets Beyond the Solar System and the Next Generation of Space Missions, ed. D. Soderblom, 153–+

Charbonneau, D., Berta, Z. K., Irwin, J., et al. 2009, Nature, 462, 891

Deleuil, M., Barge, P., Leger, A., & Schneider, J. 1997, in Astronomical Society of the Pacific Conference Series, Vol. 119, Planets Beyond the Solar System and the Next Generation of Space Missions, ed. D. Soderblom, 259–+

Deleuil, M., Deeg, H. J., Alonso, R., et al. 2008, A&A, 491, 889

Dunham, E. W., Borucki, W. J., Koch, D. G., et al. 2010, ArXiv e-prints

Dvorak, R., Pilat-Lohinger, E., Funk, B., & Freistetter, F. 2003, A&A, 410, L13

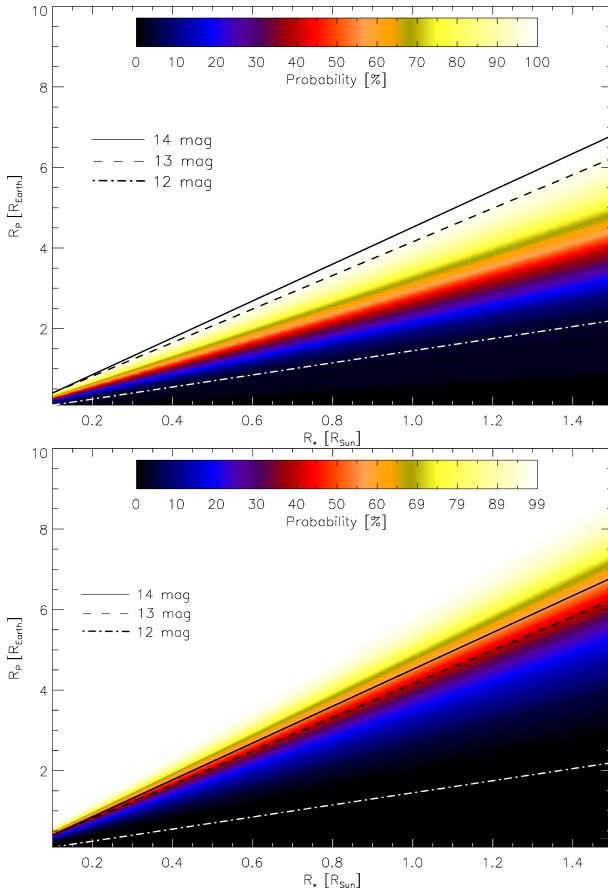Dvorak, R., Schneider, J., Lammer, H., Barge, P., & Wuchterl, G. 2009, ArXiv e-prints

Fig. 5. Transit detection probability of CoRoT for field IR01 ($\wp_{\mathrm{IR01}}$) as a function of stellar and planetary radius. Limits for the visible magnitudes are overplotted. *Top*: The transiting planets are assumed to have a circular orbit at the inner edge $d_{\mathrm{THZ}}^{\mathrm{in}}$ of the THZ. This corresponds to the highest geometrical detection probabilities. *Bottom*: The transiting planets are assumed to have a circular orbit at the outer edge $d_{\mathrm{THZ}}^{\mathrm{out}}$ of the THZ, yielding lower probabilities.

Ehrenreich, D., Tinetti, G., Lecavelier Des Etangs, A., Vidal-Madjar, A., & Selsis, F. 2006, A&A, 448, 379
ESA. 1997, VizieR Online Data Catalog, 1239, 0
Fischer, D. A. & Valenti, J. 2005, ApJ, 622, 1102
Gaidos, E., Deschenes, B., Dundon, L., et al. 2005, Astrobiology, 5, 100
Gonzalez, G. 2005, Origins of Life and Evolution of the Biosphere, 35, 555
Greenberg, R. 2005, Europa - the Ocean Moon : search for an alien biosphere, ed. R. Greenberg
Grether, D. & Lineweaver, C. H. 2006, ApJ, 640, 1051
Habets, G. M. H. J. & Heintze, J. R. W. 1981, A&AS, 46, 193
Heller, R., Mislis, D., & Antoniadis, J. 2009, A&A, 508, 1509
Hoeg, E. 1997, in ESA Special Publication, Vol. 402, Hipparcos - Venice '97, 25–30
Holmberg, J., Flynn, C., & Portinari, L. 2006, MNRAS, 367, 449
Jackson, B., Barnes, R., & Greenberg, R. 2008, MNRAS, 391, 237
Jenkins, J. M., Borucki, W. J., Koch, D. G., et al. 2010, ArXiv e-prints
Kabath, P., Eigmüller, P., Erikson, A., et al. 2007, AJ, 134, 1560
Kaltenegger, L. & Traub, W. A. 2009, ApJ, 698, 519
Kasting, J. F., Whitmire, D. P., & Reynolds, R. T. 1993, Icarus, 101, 108
Koch, D. G., Borucki, W. J., Rowe, J. F., et al. 2010, ArXiv e-prints
Latham, D. W., Borucki, W. J., Koch, D. G., et al. 2010, ArXiv e-prints
Léger, A., Rouan, D., Schneider, J., et al. 2009, A&A, 506, 287
Mayor, M., Bonfils, X., Forveille, T., et al. 2009, A&A, 507, 487
Parenago, P. P. 1958, Soviet Astronomy, 2, 151
Prantzos, N. 2008, Space Science Reviews, 135, 313
Rauer, H., Queloz, D., Csizmadia, S., et al. 2009, A&A, 506, 281
Sándor, Z., Süli, Á., Érdi, B., Pilat-Lohinger, E., & Dvorak, R. 2007, MNRAS, 375, 1495
Schwarz, R., Pilat-Lohinger, E., Dvorak, R., Érdi, B., & Sándor, Z. 2005, Astrobiology, 5, 579
Seagroves, S., Harker, J., Laughlin, G., Lacy, J., & Castellano, T. 2003, PASP, 115, 1355
Selsis, F., Chazelas, B., Bordé, P., et al. 2007a, Icarus, 191, 453
Selsis, F., Kasting, J. F., Levrard, B., et al. 2007b, A&A, 476, 1373
von Bloh, W., Bounama, C., Cuntz, M., & Franck, S. 2007, A&A, 476, 1365
Webb, J. K. & Wormleaton, I. 2001, Publications of the Astronomical Society of Australia, 18, 252

6.3 Planetary albedo and eccentricity determination of exoplanets using transit light curves

D. Mislis, R. Heller, and J. H. M. M. Schmitt

From the observational aspects of extrasolar planet transits we now come to the data analysis. As described in Chap. 4, transits provide access to fundamental planetary parameters, such as the the ratio of the planetary and the stellar radius, and the orbital inclination. The combination with RV follow-up provides a means to deduce the true mass of the planet. Here, we present a comprehensive model, which allows for the assessment of various system parameters only based on the light curve of the system. As we show, if the primary transit can be observed as well as the secondary eclipse, and if the phase curve of the system is available with high enough accuracy, then it is possible to conclude the orbital eccentricity of the planet, the orientation of the periastron, the geometric albedo of the planet, the planetary radius as a fraction of the stellar radius, the orbital period, and the orbital inclination.

I worked out the original idea for this study initially with Dimitris Mislis. As our explorations progressed, I contributed to some mathematical composition and I reviewed the figures and the text.

Planetary albedo and eccentricity determination of exoplanets using transit light curves

D. Mislis[1], R. Heller[1] & J.H.M.M. Schmitt[1]

[1]Hamburger Sternwarte, Gojenbergsweg 112, D-21029 Hamburg
e-mail: mdimitri@hs.uni-hamburg.de

ABSTRACT

We present a new approach to estimate the parameters of transiting extrasolar planetary systems using photometric light curves (LCs). The first results of the current space-based missions CoRoT and Kepler reveal a previously unknown wealth of details in the LCs. An analysis that combines a treatment of various phenomena in these LCs, such as primary and secondary eclipses, as well as the overall shape of a LC between the occultations, allows a derivation of orbital and physical parameters. The complete decipherment of a LC yields information about eccentricity, orientation of periastron, and the planet's albedo. These parameters were impossible to be extracted from low-accuracy data of ground-based surveys. Here, we give a consistent set of equations for the determination of orbital and planetary parameters and present simulations for high-accuracy LCs. For our procedure, we do not use the timing of the primary and secondary eclipses to constrain the eccentricity. Our analysis shows that the minimum accuracy of the observational data to be useful for an application of our method is 10^{-4}, which coincides with the accuracy of the Kepler mission. Future space missions, such as the James Webb Space Telescope, with photometric accuracies of about 10^{-7} can reduce the error in all parameters.

1. Introduction

Two observational methods so far have dominated the studies of extrasolar planets: radial velocity (RV) measurements and transit light curve (LC) analyses. Both have advantages and disadvantages. While the RVs provide estimates of the planetary mass (M_p), the eccentricity (e) and the semi-major axis (a), it does not constrain the inclination (i) of the orbital plane with respect to the observer, thus only lower limits to M_p can be determined. The transit method, on the other hand, provides information on i, the ratio of the planetary radius and the stellar radius (R_p/R_s), and the duration of the transit (D). So far, only a combination of both strategies yielded a full set of orbital and physical parameters for extrasolar planets.

Currently, there are two space missions aiming at the detection of extrasolar planet transits in front of their host stars: CoRoT launched in 2006 (Deleuil et al. 1997) and Kepler launched in 2009 (Borucki et al. 1997). Their instruments are monitoring thousands of stars, supposed to yield hundreds of transit events, whose RV follow-up could take years. Since only RV measurements allow planetary mass determinations, the most fundamental parameter of an extrasolar planet remains undetermined; the planetary mass is the crucial parameter classifying an object as a planet, brown dwarf or a star. Some transiting planets have been subject to detailed studies and various observational techniques, such as transmission spectroscopy during the primary transit and infrared observations of the secondary eclipse (Snellen et al. 2009). In addition, high-accuracy photometry has proven that the planetary thermal emission as well as the reflection of the stellar light from the planet are detectable. In this study, we demonstrate the wealth of information that is hidden in high-accuracy LCs and show that a lot of information

that is normally obtained from RV follow-up can actually be obtained from high-precision photometry.

2. Theoretical background

2.1. Transiting Planets

Standard models of LCs that have been used before the advent of space missions based on a flat curve out of transit and a limb darkening during the transit. Seager & Mallén-Ornelas (2003) proved analytically that each transiting system shows a unique LC. Analyses of high-accuracy data from space required a revision of this simple approach. Nowadays, models incorporate the reflected light from the planet, which deforms the overall shape of the LC, and the secondary eclipse (Fig. 1).

In Fig. 2 we show the geometry of an arbitrary transiting system assuming an elliptical orbit. Let i denote the angle between the observers's line of sight and the orbit plane normal, the angle between the observer's line of sight projected onto the orbit plane and the periastron is labeled ω. The star is in the center of the reference frame and d is the distance between the star and the planet; the distance between the star and the planet during the primary transit is denoted by $d_{\star,p}^{PT}$, during the secondary eclipse both bodies are separated by the distance $d_{\star,p}^{SE}$.

To decode the geometry of the system from the LC we split it into three sub LCs. The light curve f_1 describes the course of the primary transit, when the planet blockes the star's light, f_2 describes the form of the secondary eclipse, when the star blocks and planetary light, and f_3 the rest of the light curve, when both star and planet contribute to the total light.

2   D. Mislis, R. Heller & J.H.M.M. Schmitt: Planetary albedo and eccentricity determination of exoplanets
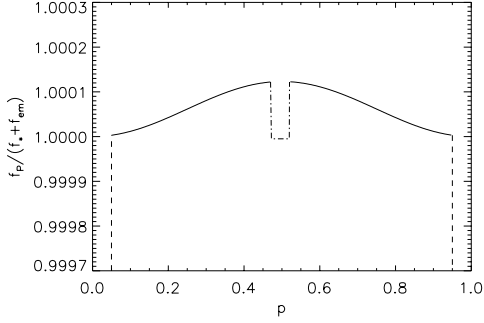

Fig. 1. The current transit model includes the primary transit f_1 (dashed line centered at orbital phase $p = 0$), the secondary eclipse f_2 (dashed-dotted line around $p = 0.5$) and the reflected light from the planet f_3 (solid line).
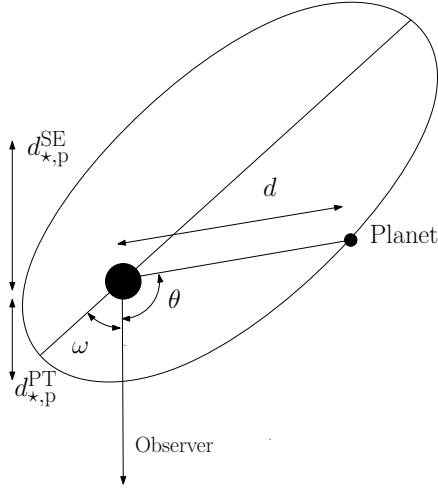

Fig. 2. This sketch of the transiting planetary system as seen from above explains the variables used in our calculations.

$$D \simeq \frac{PR_\star}{\pi a_d^2} \frac{d_{\star,p}^{PT}}{\sqrt{1-e^2}} \sqrt{\left(1 + \frac{R_p}{R_\star}\right)^2 - b^2}, \qquad (1)$$

where a_d is the semi-major axis of the system, P is the orbital period, $R_\star$ and R_p are the radius of the star and the planet, respectively, e is the orbital eccentricity, i is the inclination of the orbital plane with respect to the observer's line of sight, and $b = d_{\star,p}^{PT} \cos i / R_\star$ is the impact parameter. To model the shape of the primary transit, f_1, we use Eq. 1 (Ford et al. 2008) and the limb darkening equation

$$\frac{I_\mu}{I_0} = 1 - u_1(1 - \mu) - u_2(1 - \mu)^2, \qquad (2)$$

with u_1 and u_2 as the two limb darkening coefficients (Claret 2004; Sozzetti et al. 2007), μ as the cosine of the angle between the surface normal and the observer, and I_0 and I_μ as the intensities at the stellar disk center and at μ, respectively. Once the period is known from observations, one can fit the model to the observations to deduce $R_\star$, R_p, i, and $d_{\star,p}^{PT}$. The transit of the secondary eclipse, f_2, is fitted with the same model but without effects of limb darkening.

The total light curve f_3 contains a contributions from the star, which we assume to be constant, a contribution from reflected light, which is phase dependent, and possibly contributions from intrinsic planetary emission, which depends sensitively on the spectral range considered. The phase pattern of the reflected stellar flux depends on the phase angle α, i.e., the angle between star and observer as seen from the planet. Counting the orbital phase θ from primary minimum, the angles α, i and θ are related through

$$\cos(\alpha) = -sin(i)\cos(\theta). \qquad (3)$$

The reflected flux f_{ref} can then be expressed as

$$f_{ref}(\alpha) = \alpha_g f_\star \left(\frac{R_P}{2d}\right)^2 \Phi(\alpha), \qquad (4)$$

where α_g is the geometric albedo of the planet, $f_\star$ is the stellar flux at a distance d from the star, and $\Phi(\alpha)$ the so-called phase function. It is not entirely clear what phase functions should be used for the description of extrasolar planets. A popular choice is to assume

$$\Phi_L(\alpha) = \frac{1}{\pi}\left(\sin \alpha + (\pi - \alpha)\cos \alpha\right), \qquad (5)$$

which models the planet as a Lambert sphere, assuming that the intensity of the reflected light is constant. An alternative choice would be

$$\Phi_C(a) = \frac{1}{2}\left(1 + \cos(\alpha)\right), \qquad (6)$$

which assumes that the reflected light is simply proportional to the size of the star-lit crescent, and many other choices of phase functions are possible.

We next note that the combination $\omega + \theta$ is related to the eccentric anomaly E through

$$\omega + \theta = 2\tan^{-1}\left(\frac{\sqrt{1+e}}{\sqrt{1-e}}\tan(E/2)\right), \qquad (7)$$

and E is related to the meam anomaly M through Kepler's equation

$$E = M - e\cos(E). \qquad (8)$$

We normalise - as usual - the LC by the stellar flux, which can be determined as the minimum flux observed during secondary transit:

$$f_3(\theta) = \frac{f_\star + f_{ref} + f_{em}}{f_\star}. \qquad (9)$$

The question of intrinsic emission from extrasolar planets is a bit more complicated. Clearly we expect those planets just like the solar system planets to be in equilibrium in the sense that the absorbed stellar flux must be re-emitted. If we assume a fast rotating planet this reemission should take place more or less homogeneously over its entire surface and this thermal flux should be almost constant with phase. If, on the other hand, we consider the case of a rotationally locked planet, one expects significant temperature changes between day and night side and hence the emitted thermal flux should show a phase dependence similar to the the reflected star light.

Combining Eqs. (4) - (9), we can derive the equation for the total flux from the planet. For a typical Hot Jupiter the relative planet's emitted flux in the optical band is $f_{em}/f_\star \sim 10^{-7}$ (Alonso et al. 2009). For our analysis we assume $f_{em}/f_\star = 0$.

$$f_3(\alpha) = 1 + \frac{a_g \Phi(\alpha) R_p^2}{4(r_\star + r_p)^2}. \tag{10}$$

So far, we have constructed models that can be fitted to the observed curves of the primary transit f_1, to the secondary eclipse f_2, and to the overall shape f_3. But there is more information hidden in the LC. In the last moments before (or after) the secondary eclipse $\alpha = \alpha_S$ ($\theta = \pi$), so that the normalized total flux becomes

$$f_3(\alpha_S) = 1 + \frac{1}{4} \left(\frac{R_p}{d_{\star,p}^{SE}} \right)^2 \left(a_g \Phi(\alpha_S) \right). \tag{11}$$

In the ideal, noiseless case $f_3(\alpha_S)$ is the last data point before the ingress of the secondary eclipse as well as the first data point afterwards. Using Eqs. (10) - (11) we rewrite Eq. (10) as

$$f_3(\alpha) = 1 + (f_3(\alpha_S) - 1) \left(\frac{1 + e\cos(\omega + \theta)}{1 - e\cos(\omega)} \right)^{-2} \frac{\Phi(\alpha)}{\Phi(\alpha_S)} \tag{12}$$

From the equation above we are able to measure eccentricity and ω of the planetary orbit and using information from the primary transit modeling ($\gamma = a_d/R_p$) we could re-write Eq. 11 as the planet.

$$a_g = 4\gamma^2 \left(\frac{1 - e^2}{1 - e\cos(\omega)} \right)^{-2} \left(\frac{f_3(\alpha_S) - 1}{\Phi(\alpha_S)} \right) \tag{13}$$

This system of equations shows that LCs of transiting extrasolar planetary systems alone already provide access to some more physical and orbital parameters such e, ω and a_g.

2.2. Non-Transiting Planets

Clearly, if photometric accuracy is high enough to detect the reflected light from the planet, many non-transiting planets will be discovered. From a non-transiting planet LC we can expect many information but using equation Eq. 12 we are able to measure eccentricity, ω and the inclination of the orbit because inclination is a function of the orbital phase α (Eq. 3). For R_p (and for the mass) RV follow-up observations are nessesery. The next section will be devoted to the observational accuracy that is necessary to yield robust parameterizations.

3. Simulations - Results

To test our model, we simulate two LCs using the equations above. One of the underlying planetary systems is an analog to the transiting hot Jupiter HAT-P-2b (Pál et al. 2009), whereas the other one resembles the transiting Super-Earth CoRoT-7b (Queloz et al. 2009). We customized these models in terms of the geometric albedo, for which we optimistically applied $\alpha_g = 0.3$ in both cases (Sudarsky et al. 2000). Though observations of CoRoT-7b are reconcilable with $e = 0$, we chose $e = 0.05$. After all, we are not heading for a reconstruction of these systems but we want to estimate how accurate comparable systems could be parameterized and, as an example, if a putative eccentricity of CoRoT-7b could be determined.

To these models, we add increasingly more noise to simulate a data accuracy between 10^{-7} and 10^{-4}. The phase effect in the LCs, i.e. the contribution of f_3, is significant only for accuracies $\lesssim 10^{-4}$, which is why this phenomenon could not be detected in

Table 1. Physical parameters of our two models.

Stellar parameter	hot Jupiter	Super-Earth
$R_\star$	$1.64\,R_\odot$	$0.87\,R_\odot$
$M_\star$	$1.36\,M_\odot$	$0.93\,M_\odot$
$T_{\mathrm{eff},\star}$	6290 K	5275 K
Planetary parameter	hot Jupiter	Super-Earth
R_p	$1.16\,R_J$	$0.15\,R_J$
M_p	$9.08\,M_J$	$0.0151\,M_J$
α_g	0.30	0.30
u_1	0.34	0.20
u_2	0.35	0.57
Orbital parameter	hot Jupiter	Super-Earth
P	5.63347 d	0.85360 d
i	86.72°	80.10°
e	0.52	0.05
ω	185°	5°

the LCs of CoRoT (Costes et al. 2004). We then fit the noiseless model from Sect. 2.1 to each of these – more or less – noisy LCs and use 1000 Monte Carlo simulations to calculate the standard deviations for each parameter in each fit. For the transit fits we use the model of Pál (2008). With this procedure, we simulate the standard deviation as a function of data accuracy.

In Fig. 3 we show the standard deviations resulting from these fits for the planetary geometrical albedo a_g (σ_{a_g}), eccentricity (σ_e), and orientation of periastron (σ_ω) as a function of the root mean square (RMS) of the data. With an accuracy provided by the current Kepler mission of 10^{-4}, the eccentricity of a CoRoT-7b-like planet could merely be determined with a useless standard deviation of roughly 0.8. For a planet similar to HAT-P-2b, however, the standard deviation in e is only about 0.08. The orientation of periastron for the CoRoT-7b twin could be constrained to approximately ±50° while for the HAT-P-2b analog the accuracy is as low as 5°. Restrictions of the geometrical albedo a_g are ±0.02 in the best case (Hot jupiter - RMS 10^{-7}) to ± 1.0 in the worst case (Earth like - RMS 10^{-4}) with no physical meaning.

High-accuracy LCs of transiting systems, as shown in Fig. 1, provide a complete set of orbital and physical parameters. For the case of a non-transiting exoplanet one still might be able to detect variations in the overall shape of the LC, f_3. In this case, two more parameters, namely f_2 and Δf, would have to be fitted since they cannot be inferred directly from the LC and furthermore RV follow-up would be necessary for an assessment of the companion's nature − whether it would be a star or a substellar object. But anyway, e and ω can nevertheless be estimated from observations of f_3 alone. In Fig. 4 we show the contribution of f_3 to the LC (for HAT-P-2b system) in a system with high inclination and without a transit for various values of e and ω.

4. Conclusions

The mathematical tools presented in this article can be used for a complete parametrization of transiting exoplanet systems on the basis of high-accuracy LCs. In our model, RV measurements are not necessary to constrain the eccentricity (e), the orientation of periastron (ω) and the geometric albedo of the planet (α_g). Our model also incorporates the characterization of the ratio of planetary and stellar radius ($R_p/R_\star$), orbital period (P), and the orbital inclination (i).
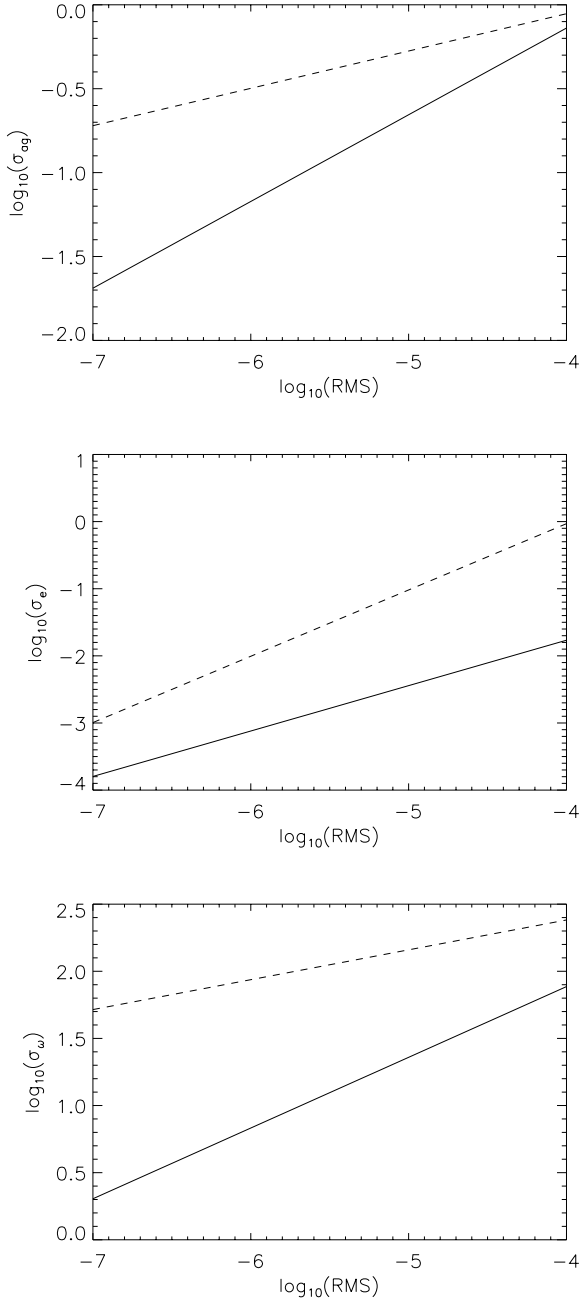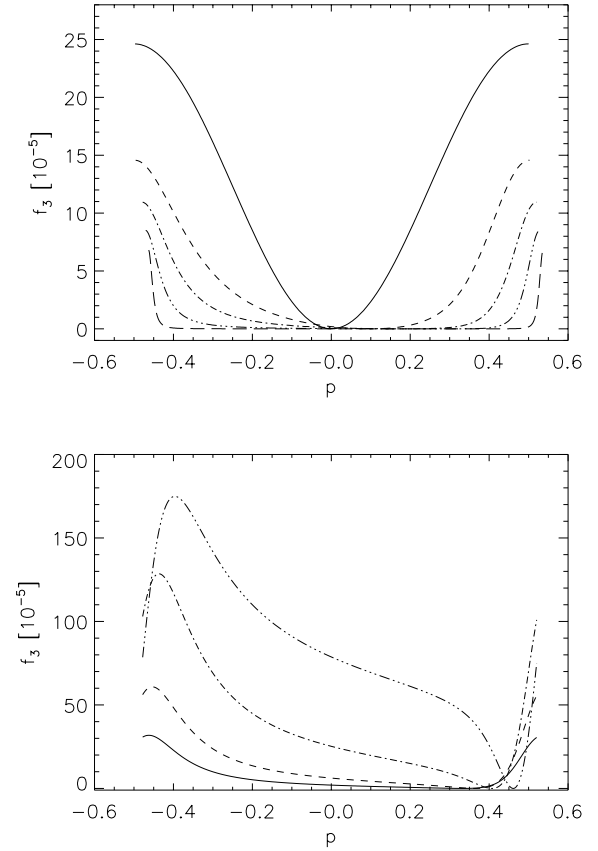
Fig. 4. Contribution of the phase-dependent flux f_3 to LCs without transits. *Top:* f_3 for various eccentricities (from above: e = 0.0, 0.3, 0.5, 0.7, 0.9) while ω is fixed to 0. *Bottom:* f_3 for various orientations of periastron (from above: ω = 50°, 70°, 100°, 140°) while e is fixed to 0.5.

References

Alonso, R., Guillot, T., Mazeh, T., et al. 2009, A&A, 501, L23
Borucki, W. J., Koch, D. G., Dunham, E. W., & Jenkins, J. M. 1997, in Astronomical Society of the Pacific Conference Series, Vol. 119, Planets Beyond the Solar System and the Next Generation of Space Missions, ed. D. Soderblom, 153–+
Claret, A. 2004, A&A, 428, 1001
Costes, V., Bodin, P., Levacher, P., & Auvergne, M. 2004, in ESA Special Publication, Vol. 554, 5th International Conference on Space Optics, ed. B. Warmbein, 281–284
Deleuil, M., Barge, P., Leger, A., & Schneider, J. 1997, in Astronomical Society of the Pacific Conference Series, Vol. 119, Planets Beyond the Solar System and the Next Generation of Space Missions, ed. D. Soderblom, 259–+
Deming, D., Seager, S., Winn, J., et al. 2009, PASP, 121, 952
Ford, E. B., Quinn, S. N., & Veras, D. 2008, ApJ, 678, 1407
Pál, A. 2008, MNRAS, 390, 281
Pál, A., Bakos, G. Á., Torres, G., et al. 2009, MNRAS, 1781
Queloz, D., Bouchy, F., Moutou, C., et al. 2009, A&A, 506, 303
Seager, S. & Mallén-Ornelas, G. 2003, ApJ, 585, 1038
Snellen, I. A. G., de Mooij, E. J. W., & Albrecht, S. 2009, Nature, 459, 543
Sozzetti, A., Torres, G., Charbonneau, D., et al. 2007, ApJ, 664, 1190
Sudarsky, D., Burrows, A., & Pinto, P. 2000, ApJ, 538, 885

Fig. 3. Errors in a_g, e, and ω as functions of data accuracy. The solid line denotes the HAT-P-2b twin while the dashed line labels the CoRoT-7b analog.

The current space missions Kepler could provide the first transiting planets to which our procedure can suitably applied. Our technique will benefit from future space missions such as the James Webb Space Telescope (Deming et al. 2009) with RMS $\lesssim 10^{-6}$.

6.4 The Photometric Software for Transits (PhoS-T)

Precise transit timing for the extrasolar planet XO-2b

D. Mislis, J. Fernandez, R. Heller, and U. Seemann

With the last of my publications in this book, I present the Photometric Software for Transits (PhoS-T), which I helped to build up. Designed not for the detection of exoplanet transits but for the follow-up characterization of these events, it offers an easy-to-use graphical interface to compute the time of the transit center, its duration, the orbital inclination of the transiting object, its orbital period and its radius as a fraction of the stellar radius. If the stellar radius and mass are known from RV measurements, then the planetary radius can be constrained to an absolute value. With the assumption $M_\mathrm{s} \gg M_\mathrm{p}$ the orbital semi-major axis can also be estimated. To infer these parameters from the data, PhoS-T comprises subroutines for bias, dark, and flat field handling, for noise reduction, for the use of comparison targets, and for the consideration of observing time and airmass. The final light curve can then be analyzed with a parametrized χ^2-fit.

My contributions to this publication consisted of the text and mathematical arrangements, as well as of various reviews of the graphical layout of the software.

The Photometric Software for Transits (PhoS-T)*

Precise transit timing for the extrasolar planet XO-2b

D. Mislis[1], J. Fernandez[2], R. Heller[1] & U. Seemann[2]

[1]Hamburger Sternwarte, Gojenbergsweg 112, D-21029 Hamburg, Germany
[2]Institut für Astrophysik, Georg-August-Universität Göttingen, 37077 Göttingen, Germany
e-mail: mdimitri@hs.uni-hamburg.de

ABSTRACT

We present the Photometric Software for Transits (Phos-T), a user-friendly stand-alone astronomical software built to study in detail photometric data of transiting extra-solar planets. Through a simple and clean graphical environment, PhoS-T can perform data calibration, point-source differential photometry, and transit light curve modeling. The software also includes a special mode optimized to analyze public data from the CoRoT mission. Here we present a detailed description of the software, together with the analysis of a recent transit of the extra-solar planet XO-2b, observed with the MONET robotic telescope. The results obtained using PhoS-T are in good agreement with previous works, and provide a precise time-of-transit for XO-2b.

Key words. Methods: data analysis – Techniques : photometry – Stars : planetary systems

1. Introduction

Transiting extra-solar planets provide an enormous amount of information if compared to non-transiting systems, like mass, radius, chemical composition, surface temperature, orbit-rotation inclination, etc. (Charbonneau et al. 2007). In the past 10 years, several research groups have invested a significant amount of resources in order to detect transiting systems (Udalski et al. 1992; McCullough et al. 2004; Street et al. 2003; Bakos et al. 2002). Dedicated space telescopes have been put in orbit to detect more of these systems (Deleuil et al. 1997; Borucki et al. 1997), and follow-up observing programs using ground- and space-based instruments have been crucial for our understanding of these distant worlds (McDowell 2001; Gehrz et al. 2004).

An interesting development in the field of transiting extrasolar planets is the participation of several small observatories in the follow-up programs (e.g. the Fred L. Whipple Observatory, FLWO in the following). Most of the systems discovered by TrES, XO, WASP and HAT have magnitudes between $V = 10^{m}$ and 13^{m}, a range where millimagnitude relative photometry can be achieved with 1m-class telescopes. This level of photometric precision allows a detailed modeling of the transit light curves, and precise measurements of the duration and time of the transits ($\sim 30\,\text{s}$ for events longer than 2 hrs). Significant differences between observed and expected values for timings and duration of transits could indicate the presence of an additional object in a planetary system, which can have a mass as low as the Earth. The potential of 1m-class telescopes should not be underestimated, but the impact of their contributions depends strongly on the quality of the analysis of their data, and how fast their results can become public.

In this context, we present PhoS-T, a user-friendly standalone astronomical software built to study in detail photomet-

ric data of transiting extra-solar planets. PhoS-T can perform high-quality data calibration, point-source differential photometry, and transit light curve modeling in a very short time, using a simple and clean graphical environment. PhoS-T comes from "**Pho**tometric **S**oftware for **T**ransits", and takes its name from the Greek word for light (Phos=ΦΩΣ=light).

2. Theoretical background

2.1. Data reduction function

The first mode of PhoS-T is based on a standard procedure of data reduction. The input data is a fits file, which is passed through standard bias subtraction, dark correction, and flat fielding. The function *Data reduction* uses the two sub-routines *Master Frames* and *Noise Reduction*. *Master Frames* creates the master noise frames. For the purpose of bias subtraction, it creates an average bias value $B_{i,j}$ for each pixel, where the index i runs through the columns and j runs through the lines of the image. With N as the total number of bias frames taken and $b_{i,j}$ as the individual bias values we get

$$B_{i,j} = \frac{1}{N} \sum_{k=1}^{N} (b_{i,j})_k. \tag{1}$$

We call this averaged bias frame the master bias. To obtain the master dark ($D_{i,j}$) and the master flat ($F_{i,j}$) frames, we use similar equations

$$D_{i,j} = \left(\frac{1}{N} \sum_{k=1}^{N} d_{i,j} c_k \right) - B_{i,j} \tag{2}$$

&

$$F_{i,j} = \frac{1}{\overline{F}} \left(\frac{1}{N} \sum_{k=1}^{N} (f_{i,j})_k c_f \right) - B_{i,j} - D_{i,j} \tag{3}$$

2   D. Mislis et. al.: The Photometric Software for Transits (PhoS-T)

where $c_k = 1/(t_{exp}^D)_k$ normalizes the exposure time of the kth dark frame and $c_f = 1/(t_{exp}^F)_k$ which normalizes the exposure time of the kth flat frame. Moreover, $(d_{i,j})_k$ and $(f_{i,j})_k$ are the dark and flat pixels of the kth dark and flat field image and $\overline{F}$ is the mean value of the sum of all flat frames.

The second sub-routine, *Noise Reduction*, then extracts the reduced light $L_{i,j}$ frame via

$$L_{i,j} = \frac{R_{i,j} - B_{i,j} - D_{i,j}t_{exp}^R}{F_{i,j}}, \qquad (4)$$

where $R_{i,j}$ is the jth pixel in the ith column of the raw science image and the t_{exp}^R is the exposure time of each light frame. Finally, PhoS-T applies a "hot pixel" algorithm to remove all the bad pixels from the image. We use a mask of 10×10 pixels, which is applied to each pixel brighter than $40\,000$ analog-to-digital units (ADUs). This mask estimates how isolated these potentially bad pixels are or if they might be part of a point spread function (PSF).

2.2. Align function

For the parametrization of transiting exoplanet systems, telescopes with mirrors larger than $1\,m$ are typically being used nowadays. These are significantly larger and have a much smaller field of view (FOV) than the instruments used by most survey teams, which prefer large FOVs and very often lenses instead of mirrors. The photometric data obtained for the detailed (follow-up) characterization of the transit is thus assumed to be not crowded with stars. Based on this assumption, the *Align* function of PhoS-T includes the two sub-routines *Offset & Rotation* and *Target & Comparison Selection*. The former one selects the two brightest stars of the FOV by

$$S_i = \sum_{j=1}^{J} L_{i,j} \ , \quad 1 \le i \le I \ \ \& \ \ S_j = \sum_{i=1}^{I} L_{i,j} \ , \quad 1 \le j \le J \quad (5)$$

where S_i and S_j are the sums of ADUs per column and line and I and J are the number of columns and lines of the frame, respectively (typically $I = J$). The impact of bad pixels is diminished to insignificance because we are using the sum of a full line or column. As an output we have two graphs with various peaks (Fig. 1). Each peak represents to a star of which PhoS-T selects the two highest for the alignment of the images. The combination of the two largest peaks in both dimensions yields the coordinates of the two brightest stars. If, for any reason, a combination of the two brightest stars does not suit well – they might be located at the edge of the frame or the tracking might be bad – the software selects the next most plausible pair of bright stars. With two stars as references we can then calculate the offset and the rotation angle of each frame with respect to the reference frame. Figure 2 shows an example for the offset in both axes. Moreover *Offset & Rotation* has a focus on the center of the CCD to minimize the risk that the reference stars might move outside the frame in the course of the observation. If the offset is large enough to set the reference stars out of the FOV, this frame is ignored and labeled as "bad frame".

With the *Target & Comparison Selection* the user chooses the window for the transit analysis. First, the reference frame appears divided into four sub-frames, one of which contains the target star to be selected by the user. The new sub-frame is again divided into four sub-frames and the user zooms in until only the target remains (Fig. 3). The same technique is applied for the
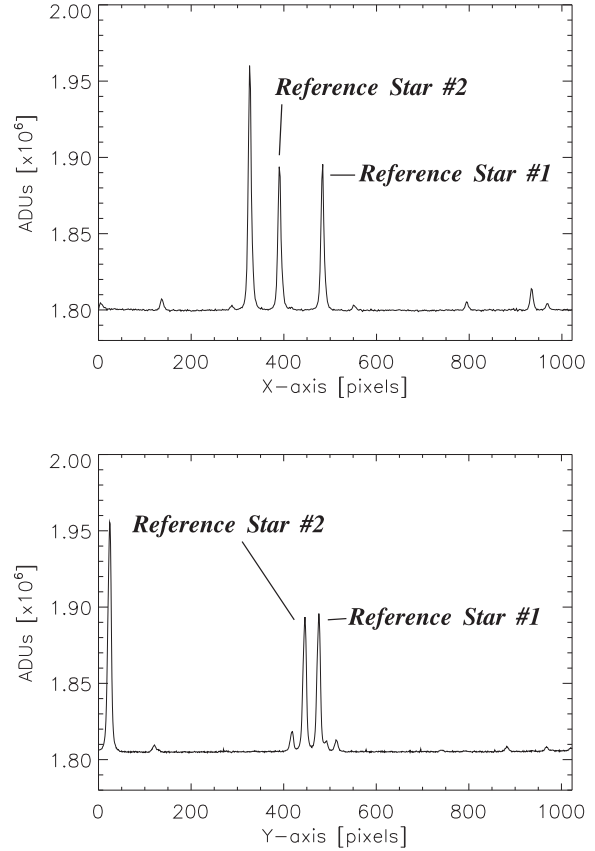

Fig. 1. Sum of ADUs per line (upper panel) and column (lower panel) for the reference frame. As an example we point out the two brightest stars which serve as reference for the orientation of the frame.

comparison star. Finally, the user has defined the photometric window and a comparison star, which is why PhoS-T does not use apertures for photometry. The same technique is applied to the comparison star. Finally, the user has defined the photometric window and a comparison star. This is why PhoS-T does not use apertures for photometry. Although we confined to one comparison star in our example, the user can select as many references as he/she wants to.

2.3. Photometry function

The *Photometry* function uses the three sub-routines *Aperture Photometry*, *Time & Airmass*, and *Final LC*, where LC stands for light curve. The *Aperture Photometry* is different from the usual methods (Mighell 1999). First, it calculates the frame coordinates of the target star and then applies the *Offset & Rotation* sub-routines of the *Align* function to each frame. Then, it finds the new coordinates of the star and creates a sub-frame with the same measures as the photometric window. The software now finds the standard deviation σ_{sky} of the sky using the pixel values of the sky background:

$$\sigma_{sky} = 0.5 * \left(\sqrt{\frac{1}{i} \sum_i (G_{i,1} - \bar{G})^2} + \sqrt{\frac{1}{j} \sum_j (G_{1,j} - \bar{G})^2} \right), \quad (6)$$
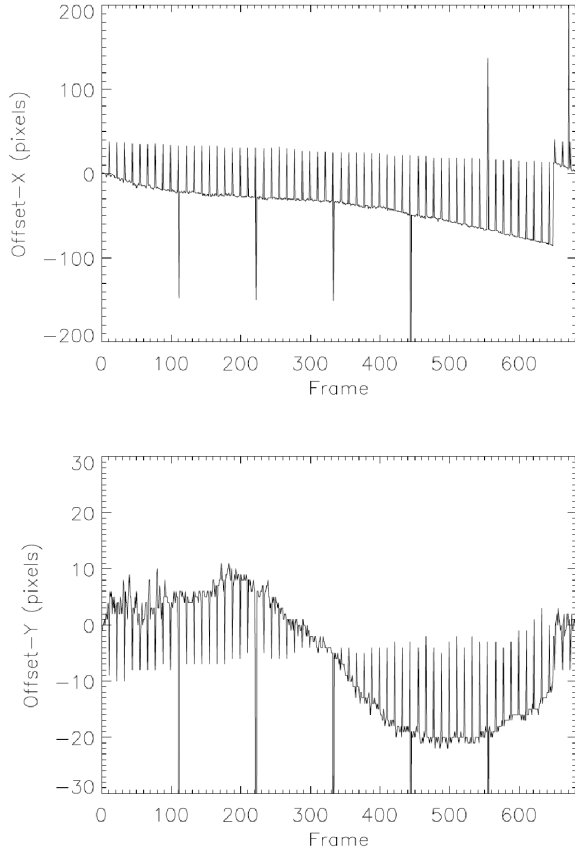
Fig. 2. Offset in both image dimensions after application of the *Offset & Rotation* function. The plots show the shift in X-axis (upper panel) & Y-axis (lower panel) as a function of frame number. In both dimensions MONET shows a guiding periodic offset (varius peaks).

with $G_{i,j}$ as the value of the background in the i, jth pixel and $\bar{G}$ as the mean value of the sky background of the first column and line in the photometric window. All the pixels with values 1.5 σ higher than $\bar{G}$ are replaced with the new sky values. To derive the new sky values, we are using random numbers from a Gaussian distribution where σ equals with the sky standard deviation σ_{sky}. The new frame is called *Sky Frame*. The *Sky Frame* is subtracted from each raw frame. The result of this subtraction, the *Final Frame* with values $\mathfrak{f}_{i,j}$, has a very dim background and an enhanced contrast to the flux values of the target. With this method it is not necessary to define an aperture because the flux of the star $\mathfrak{F}$ is the sum of all pixel values in the *Final Frame*.

$$\mathfrak{F} = \sum_{i=1}^{I} \sum_{j=1}^{J} \mathfrak{f}_{i,j} \tag{7}$$

PhoS-T does not use apertures, thus it can easily handle defocused data, which is common for follow-up observations of transiting planets around bright stars.

The *Time and Airmass* sub-routine simply extracts the Julian date (JD) t and the airmass $a(t)$ from the fits header of the raw image. If there is no JD or modified JD (MJD) given in the header then the JD is calculated from the observing time and date. Using the JD the Heliocentric Julian Date (HJD) could be calculated. For the case of missing information about airmass, PhoS-T calculates the airmass using the coordinates of the pointing.

The *Final LC* sub-routine creates the final light curve $T(t)$ of the transit. First, it finds the correlation between airmass and the light curve of the comparison star(s) $C(t)$ and subtracts the airmass pattern from both the raw comparison light curve C_{raw} and the raw target light curve T_{raw}:

$$T(t) = \frac{T_{\text{raw}}(t)/(\gamma_1 + \alpha \cdot a(t))}{C_{\text{raw}}(t)/(\gamma_2 + \beta \cdot a(t))}. \tag{8}$$

Here, α, β, γ_1 and γ_2 are the free parameters of a linear fit to T_{raw} and C_{raw}, respectively. In Fig. 4 we show the final light curve after the airmass correction of the example object exoplanet XO-2b including a model fit (see Sects. 2.4 and 4).
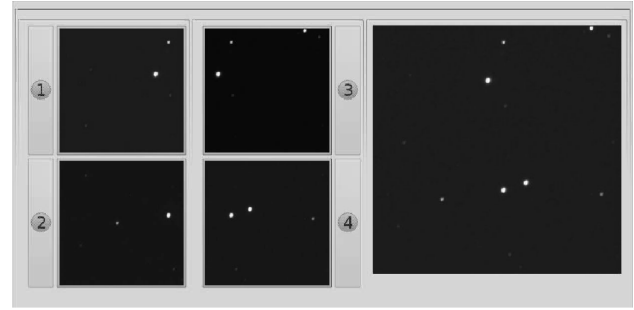

Fig. 3. The *Target & Comparison Selection* screen of PhoS-T. **Right:** The original frame. **Left:** The original frame divided in four sub-frames. The user selects the target and the comparison star by clicking on the sub-frame. The software automatically defines the photometric window.

2.4. Analysis function

The *Analysis* function includes the two sub-routines *Model Fit* and *Errors*. *Model Fit* uses the analytical transit model from Pál (2008). As mentioned above, PhoS-T is a follow-up software. It is most efficient, if a rough parametrization of the transiting system, consistent of the host star and the transiting object, is already available. Provided that the period P is given, PhoS-T can fit the radius of the star R_s, the radius of the planet R_p (of course the output value is the ratio R_p/R_s), the semi-major axis α (again the output is the ratio of α/R_s) and the orbital inclination i with respect to the line of sight. Another set of input parameters are the limb darkening coefficients u_1 & u_2. However, the user is free to select the parameters to be fitted and she/he can choose which parameters should be fixed. After the user has defined the range of the parameters, a χ^2 fit of the model is applied to the full range (Fig. 4).

The *Errors* sub-routine relies on the bootstrap method (Alonso et al. 2008). After 1000 Monte Carlo simulations, a Gaussian distribution is fitted to define errors in all output parameters: the time of the center of the transit T_c, the transit duration (D), i, the ration α/R_s and the ratio of R_p/R_s.

2.5. CoRoT function

The *CoRoT* function is based on two sub-routines: *CDA* (CoRoT Detrend Algorithm (Mislis et. al. 2010) and *BLS* (Box Least
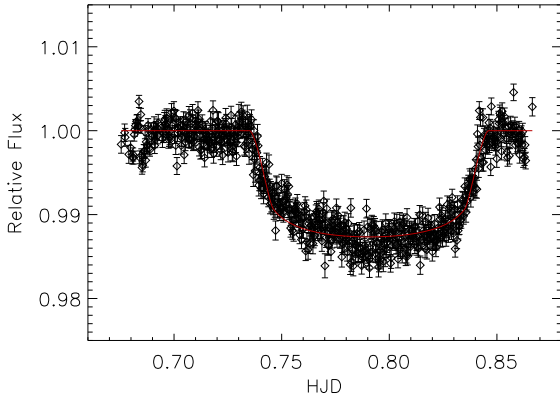
Fig. 4. Final light curve of XO-2b (diamonds) and the transit model (red solid line). The model fit is not perfect at the first part of the transit because the data quality. The light curve shows a small asymmetry.

Square Algorithm - Kovács et al. (2002)). In the *CDA* mode the user can analyze raw CoRoT light curves. It deduces the transit period and removes trends and jumps from raw the light curves. *BLS* searches for transits in a light curve and calculates its period. When the period is known and the folded light curve is prepared, the user can go back at the *Analysis* function and apply a model fit for further analysis.

3. Graphical environment & technical details

The graphical environment of PhoS-T is built with the programming language GTK. For the majority of the sub-routines we have mainly used Python and AWK but also Fortran and Bash-scripting. The PhoS-T main screen is separated in two windows. The first one is the operating window where the user can select the functions and routines as described above. The second window is the display window, which shows output frames after the reduction, such as the aligned plots, the final light curve and the transit model fit. To ease the handling of the procedure, we have incorporated a few display dialogs.

In our example XO-2b (Sect. 4), we have used 774 frames, 22 bias frames, 40 dark frames, 26 flat frames, and 686 scientific frames with a virtual size of 1.5 Gb in total. Using a 4 GHz processor, PhoS-T needed roughly an hour for the full procedure, starting with the master frames creation and ending with the error calculation of the transit model.

4. PhoS-T in action: Photometric Follow up of XO-2b

We used PhoS-T to analyze follow-up photometric data of the transiting extrasolar planet XO-2b. This planet was announced and analyzed in detail by Burke et al. (2007), having an orbital period $P = 2.6$ days, mass $M_p = 0.57 M_J$ and radius $R_p = 0.97 R_J$. The host star, a K0 dwarf, has $V = 11.2$ mag and belongs to a proper-motion binary system, with an apparent distance of 30″ between the stars. The companion star has the same brightness and shares the same spectral characteristics of the planet-bearing star. Ground-based follow-up photometry has refined the transit ephemeris and confirmed the original transit parameters (Fernandez et al. 2009), and space-based infrared

Table 1. Physical Parameters of XO-2b exoplanet. We compare PhoS-T values with Burke et al. (2007), Torres et al. (2008) and Fernandez et al. (2009) (second third and fourth column respectively). The PhoS-T value of α/R_s is higher that the other values because the data quality (Fig. 4 - 6).

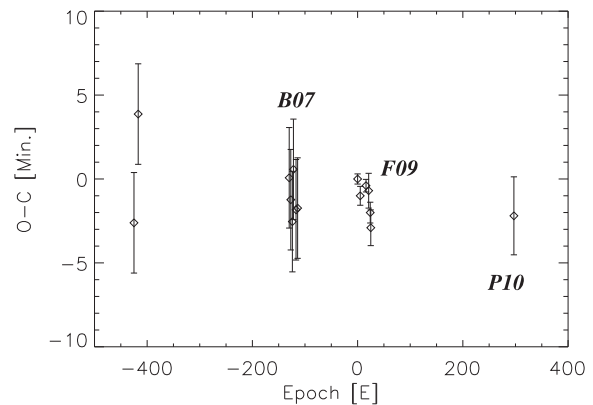| $XO - 2b$				
Parameters	Burke	Torres	Fernandez	PhoS − T	Errors
R_s/R_p	0.1040	0.1040	0.1049	0.1039	± 0.006
α/R_s	7.93	8.23	8.13	8.48	± 0.044
Inclination	88.90	88.90	88.87	88.95	± 0.028 [deg.]
Duration	160.72	160.28	161.74	159.70	± 0.860 [min.]

Fig. 5. O-C diagram using values from Burke et al. (2007) (B07) and Fernandez et al. (2009) (F09). Our results (P10) match with previous results.

observations have detected thermal emission and a weak temperature inversion layer in the atmosphere of XO-2b (Machalek et al. 2009). Here we analyze a new transit of this extrasolar planet, obtaining a precise timing for the event which may be used to the search for evidence of a low-mass planetary companion (Agol et al. 2005; Holman & Murray 2005).

4.1. Observations and Results

To provide a high-quality light curve for the analysis of the transit of XO-2, we used the MONET 1.2-m telescope at McDonald Observatory (Hessman 2001). Data were obtained during the night between February 15 and 16, 2010, in remote observing mode. MONET has a 1K×1K Apogee Alta E47 CCD that gives a 5′×5′ field and a pixel size of 0.30″ when the binning is 1×1. To minimize limb darkening effects on the shape of the transit light curve, observations were made using a Sloan i band filter. We used 15-second exposures, which provided and effective cadence of $\sim 25^{-1}$. Data calibration, photometry and light-curve analysis were performed using PhoS-T (Sec 9.2). Light-curve modeling results, including time of center-of-transit, are presented in Table 1, with previous results from Burke et al. (2007) (B07), Torres et al. (2008) (T08) and Fernandez et al. (2009) (F09). Also Fig. 5 shows the T_c results compare with previous values and Fig. 6 shows the residuals between PhoS-T and IRAF light curve.
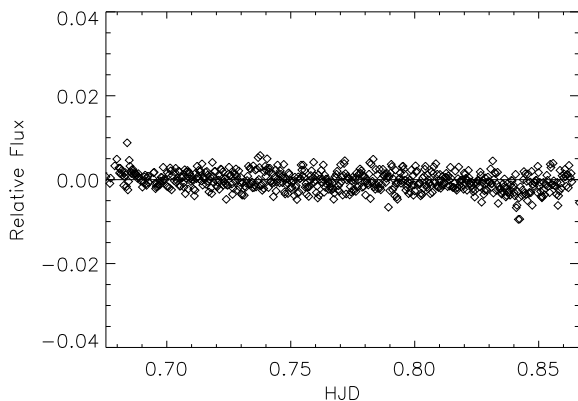
D. Mislis et. al.: The Photometric Software for Transits (PhoS-T)   5

Fig. 6. Residuals between PhoS-T photometry and IRAF pho-
tometry. The light curves obtained with both programs are in
very good agreement.

5. Results & Conclusions

PhoS-T is a new software for data reduction, photometry and
follow-up analysis of transiting planets. The software includes
also functions for reduction and detection transit events in
CoRoT light curves (CDA & BLS). The advantage of PhoS-T
over established software flows from its graphical environment
and its highly automatic operation. It comprises all the routines
required for the standard analysis of transit light curves. In or-
der to test the software, we re-examine new light curves of the
well-known transiting planet XO-2b, obtained with the robotic
1.2m telescope MONET. We successfully reproduce the previ-
ously published values of the system and conclude that data re-
duction, photometry, and the model fitting procedures of PhoS-T
are coequal with well-established software.

References

Agol, E., Steffen, J., Sari, R., & Clarkson, W. 2005, MNRAS, 359, 567
Alonso, R., Barbieri, M., Rabus, M., et al. 2008, åp, 487, L5
Bakos, G. Á., Lázár, J., Papp, I., Sári, P., & Green, E. M. 2002, PASP, 114, 974
Borucki, W. J., Koch, D. G., Dunham, E. W., & Jenkins, J. M. 1997, in
    Astronomical Society of the Pacific Conference Series, Vol. 119, Planets
    Beyond the Solar System and the Next Generation of Space Missions, ed.
    D. Soderblom, 153–+
Burke, C. J., McCullough, P. R., Valenti, J. A., et al. 2007, ApJ, 671, 2115
Charbonneau, D., Brown, T. M., Burrows, A., & Laughlin, G. 2007, Protostars
    and Planets V, 701
Deleuil, M., Barge, P., Leger, A., & Schneider, J. 1997, in Astronomical Society
    of the Pacific Conference Series, Vol. 119, Planets Beyond the Solar System
    and the Next Generation of Space Missions, ed. D. Soderblom, 259–+
Fernandez, J. M., Holman, M. J., Winn, J. N., et al. 2009, AJ, 137, 4911
Gehrz, R. D., Reach, W., & Woodward, C. E. 2004, in COSPAR, Plenary
    Meeting, Vol. 35, 35th COSPAR Scientific Assembly, 1222–+
Hessman, F. V. 2001, in Astronomical Society of the Pacific Conference Series,
    Vol. 246, IAU Colloq. 183: Small Telescope Astronomy on Global Scales, ed.
    B. Paczynski, W.-P. Chen, & C. Lemme, 13–+
Holman, M. J. & Murray, N. W. 2005, Science, 307, 1288
Kovács, G., Zucker, S., & Mazeh, T. 2002, åp, 391, 369
Machalek, P., McCullough, P. R., Burrows, A., et al. 2009, ApJ, 701, 514
McCullough, P. R., Stys, J., Valenti, J., et al. 2004, in Bulletin of the American
    Astronomical Society, Vol. 36, Bulletin of the American Astronomical
    Society, 1566–+
McDowell, J. 2001, S&T, 102, 30

Mighell, K. J. 1999, in Astronomical Society of the Pacific Conference Series,
    Vol. 189, Precision CCD Photometry, ed. E. R. Craine, D. L. Crawford, &
    R. A. Tucker, 50–+
Pál, A. 2008, MNRAS, 390, 281
Street, R. A., Pollaco, D. L., Fitzsimmons, A., et al. 2003, in Astronomical
    Society of the Pacific Conference Series, Vol. 294, Scientific Frontiers in
    Research on Extrasolar Planets, ed. D. Deming & S. Seager, 405–408
Torres, G., Winn, J. N., & Holman, M. J. 2008, ApJ, 677, 1324
Udalski, A., Szymanski, M., Kaluzny, J., Kubiak, M., & Mateo, M. 1992, Acta
    Astronomica, 42, 253

Part III

Closing thoughts

Chapter 7

Summary and outlook

In Part I of this book, I gave a review of the physical principles that govern the mechanical behavior of celestial objects, I have summarized the evolution of sub-stellar objects, and I have explained the promising techniques and methods of exoplanet transit observations. The latter, combined with RV measurements of exoplanet and brown dwarf hosting stars and brown dwarfs, provide the means to assess theories of tidal interaction by measurements of tidally inflated radii as well as system dynamics. The orbital parameters, such as the transit center, the transit duration, and the transit period, might change in the course of time due to gravitational interaction of an exoplanet with a 3rd body or due to tidal interaction with its host star. Thus, I conclude that repeated, high-quality transit observations, which are currently taken by the space-based missions CoRoT and Kepler, will enable us to improve tidal models and to better evaluate tidal effects.

On the theoretical side, considerable improvement of tidal models can be achieved by coupling orbital and structural evolution of sub-stellar objects. This may allow for a better description of tidal effects in the anomalous sub-stellar eclipsing binary 2M0535−05 and may help to resolve the observed T_{eff} reversal. The further inclusion of stellar irradiation may permit to explain the numerous transiting exoplanets with inflated radii. Orbital and structural coupling is also necessary to better assess the habitability of Earth-like planets, expected to be found in the current or the next decade, and the coupling might turn out to be an essential piece of the jigsaw of hot Jupiters and hot Neptunes.

In Part II, beginning with Chap. 5, I firstly treated the tidal effects on brown dwarfs and extrasolar planets. We have shown that tidal heating alone cannot account for the observed T_{eff} reversal. In addition to the orbital-structural coupling, observations of the Rossiter-McLaughlin effect in this system, which might constrain the obliquities of the two bodies, could further enhance our understanding of the tidal effects in 2M0535−05. Tidal effects on extrasolar planets play a crucial role in the appraisal of habitability of these worlds. As we found, the concept of the habitable zone requires urgent review under consideration of tilt erosion, tidal heating, and tidal locking.

In Chap. 6 I presented various studies on extrasolar planet transits in front of their host stars. We were able to show that there is a considerable pool of transiting planets around bright stars waiting to be discovered and our sky maps point out the most promising sites on the celestial plane where they can be found. At this point, I dare to introduce an interesting gedankenexperiment:

Not only do some extrasolar planets transit their host stars but so does the Earth, too. On the celestial plane, there exists a narrow corridor in which transits of the Earth in front of the Sun can be observed, provided that there is an entity capable of observing. I show this corridor in Fig. 7.1. In order to find habitable worlds we explore the atmospheres of transiting planets in search of chemical compounds suggestive of exobiological life (as we suspect it to be). Imagine the inverse situation: Couldn't there be intelligent species that observe 'our' transits and our atmospheric biomarkers? If so, and if they take stock in contacting other civilizations, they might be calling us. This corridor might represent an interstellar phone booth for humans.
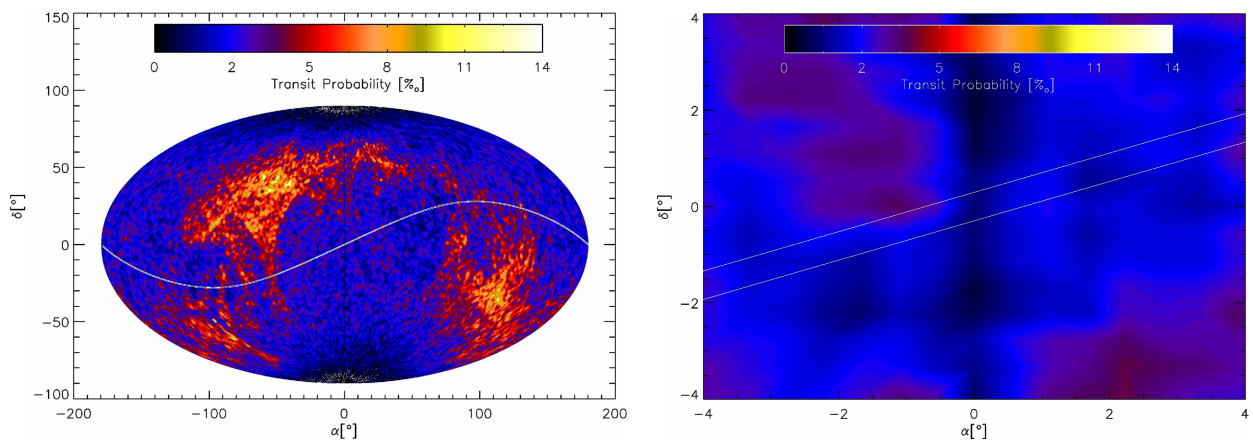
Fig. 7.1: Transit path of the Earth as a projection on the celestial plane. The color-coded transit probabilities correspond to $\wp_{occ}$ as given by Eq. (5) in Sect. 6.2. The white corridor depicts the interstellar phone booth, in which civilizations could observe the transit of the Earth in front of the Sun. Vice versa, the colors indicate where we might be able to detect transiting planets.

Appendix A

Appendix

A.1   Auf der Suche nach extrasolaren Transitplaneten

R. Heller

This article is a popular science reading of Heller et al. (2009b) from Chap. 6.1.

Auf der Suche nach extrasolaren
Transitplaneten

Planeten um andere Sonnen, die von der Erde aus gesehen einmal während ihres Orbits vor ihrem Zentralstern vorbeiziehen, eröffnen eine bis vor Kurzem ungeahnte Palette an Möglichkeiten zu ihrer Untersuchung. Nur: Wo am Himmel lassen sich diese Kandidaten für Sternbedeckungen eigentlich finden?

Von René Heller

Im Jahr 1995 gelang zwei Wissenschaftlerteams unabhängig voneinander die Entdeckung eines jupitergroßen Planeten um den Stern 51 Pegasi. Seitdem vergrößerte sich die Anzahl der mit verschiedenen Methoden aufgespürten Exoplaneten auf mehr als 450 Exemplare. Einige von ihnen nehmen für irdische Beobachter eine so günstige geometrische Konstellation ein, dass sie einmal pro Umlauf um ihr Muttergestirn direkt vor dessen winziger Scheibe vorbeiziehen. Dabei verringert sich die von der Erde aus gemessene Helligkeit für einige Stunden um ungefähr ein Prozent. Im Jahr 2000 gelang Astronomen erstmals die Beobachtung eines solchen Transits, und zwar um den Stern HD 209458. Heute zählt man 79 Sterne, deren periodische Lichtabfälle von der Passage eines planetaren Begleiters herrühren.

Dank solcher Transitplaneten erfuhren Astronomen in den letzten Jahren auf der einen Seite viel über die strukturelle und atmosphärische Zusammensetzung dieser Welten. Auf der anderen Seite gewannen sie auch Aufschlüsse über die Oberflächen der während des Transits teilweise verdeckten Sterne. Auch ließ sich in einigen Fällen die geometrische Ausrichtung der Rotationsachse eines bedeckten Sterns in Bezug auf die Bahnebene des Planeten ermitteln. Die Entdeckung von Monden um Transitplaneten, der so genannten Exomonde, steht noch aus, ebenso der Nachweis chemi-

scher Signaturen von Leben in den Atmosphären von Transitplaneten. Beides notieren die Astronomen an hoher Stelle auf ihrer Agenda, und sie analysieren dies derzeit mit Hilfe theoretischer Modelle.

Die Strategie der Transitjäger

Seit Anfang dieses Jahrtausends starteten die Forscher mehrere Projekte, deren Ziel die Entdeckung dieser begehrten Transitobjekte ist. Die meisten dieser Projekte verwenden erdgebundene Teleskope. Zwei weitere, CoRoT und Kepler, nutzen im Weltall stationierte Teleskope. Da solche geometrischen Bahnlagen von Exoplaneten, die einen Transit ermöglichen, sehr selten sind, besteht die Strategie der Suchprojekte darin, viele hunderte oder tausende von Sternen in einem bestimmten Himmelsfeld über mehrere Nächte hinweg immer wieder zu beobachten. Die gemessenen Helligkeiten lassen sich dann per Software durchforsten und nach Lichtschwankungen einzelner Sterne in dem überwachten Feld durchsuchen.

Das Ziel, möglichst viele Sterne gleichzeitig einzufangen, könnten die Astronomen durch das Ausrichten der Teleskope auf die Gebiete mit den höchsten Sterndichten am Himmel erreichen. Alternativ ließe sich ein Teleskop-Kamera-System mit einem riesigen Gesichtsfeld konstruieren. Während die letztgenannte Option aus technischen und finanziellen

Gründen schwer umsetzbar ist, verbieten physikalische Gründe die blinde Wahl bei der ersten Option: In Gebieten mit sehr dichten Sternpopulationen mag es nämlich vorkommen, dass mehrere Sterne auf ein und dasselbe Pixel der verwendeten CCD-Kamera abgebildet werden. Die eventuelle Schwankung in der Helligkeit eines Sterns könnte so durch das Licht eines störenden anderen Sterns übertrumpft werden und der für die Helligkeitsschwankung ursächliche Transit bliebe unentdeckt. Sollte die Schwankung dennoch de-

Was sich aus den Daten des

Der umfangreiche Tycho-Katalog, unter Astronomen kurz TYC genannt, enthält die Positionsangaben von rund einer Million Sterne. Die Messungen führte der europäische Astrometriesatellit Hipparcos zwischen August 1989 und März 1993 durch. Neben den Positionen vermaß Hipparcos auch die Helligkeit der Sterne in zwei Farben, die annähernd den bekannten Farben *B* and *V* des Farbsystems UBV nach Johnson entsprechen, das der amerikanische Astronom Harold Lester Johnson in den 1950er Jahren aufstellte. Die Präzision dieser Messungen war bis dato unerreicht. Die Positionswerte sind auf plus/

René Heller / SuW-Grafik

◇ Entdeckungen vom Erdboden aus   △ Entdeckungen vom Weltraum aus
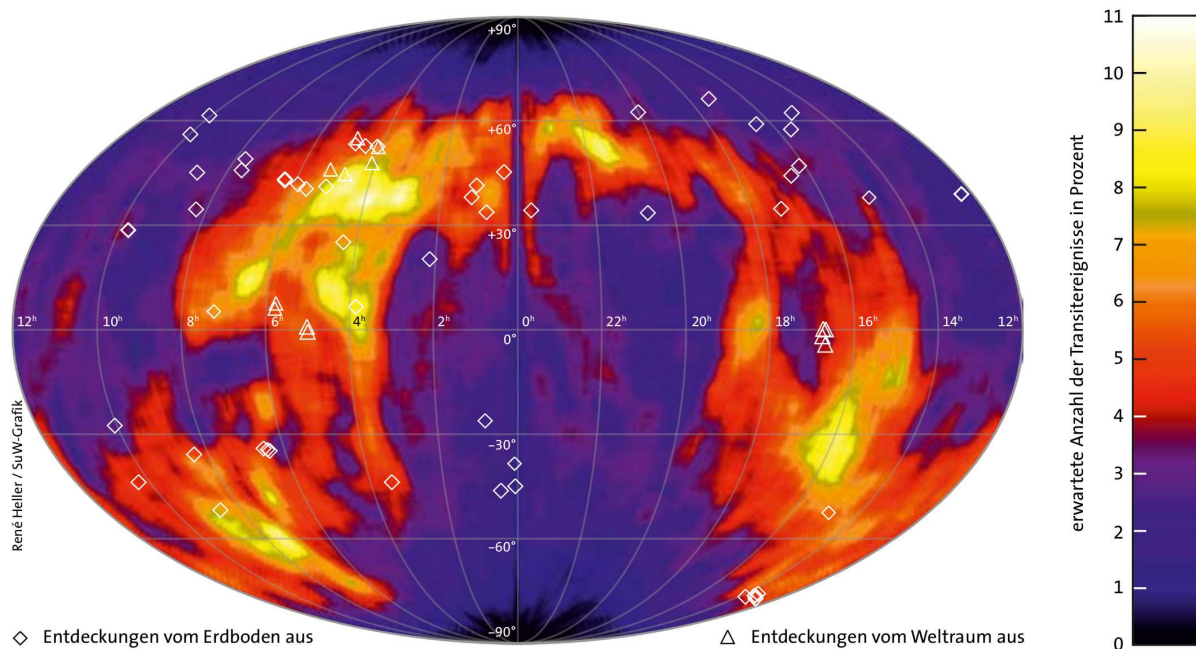
**Die Karte zeigt farbig kodiert die erwartete Anzahl von Transits pro virtu-
ellem 8×8-Grad-Gesichtsfeld am Himmel. Die Positionen der 79 bis zum
April 2010 bekannt gewordenen Transitplaneten sind markiert.**

tektiert werden, ließe sich ihre Quelle un-
ter Umständen trotzdem nicht auflösen.
Die höhere Dichte an stellaren Doppel-
und Dreifachsystemen, deren Komponen-
ten durch gegenseitige Bedeckungen einen
Planetentransit imitieren und die automa-
tisierten Suchalgorithmen foppen mögen,
erschweren die Suche in solchen Gebieten
weiter. Auch ist die Wahl des Beobach-
tungsfelds durch den Aufstellungsort des
Instruments auf der Erde eingeschränkt.

Hier stellt sich die Frage: Wo liegt ei-
gentlich der für die Suche nach Transitpla-
neten günstigste Beobachtungsstandort
auf der Erde? Von wo aus lassen sich die
meisten Transits beobachten? Die Antwor-
ten hängen natürlich von der Verteilung
der Sterne am Himmel ab, dürften aber
aufgrund der unterschiedlichen CCD-Auf-
lösungen und der verschieden großen Ge-
sichtsfelder nicht für jedes Instrument
gleich ausfallen. Wäre es nicht schön, die
Astronomen könnten sich eine Brille mit
den speziellen Eigenschaften eines be-
stimmten Instruments aufsetzen und am
Himmel nur noch jene Sterne sehen, die

einen hinreichend großen Transitplaneten
beherbergen und mit dem jeweiligen In-
strument zu beobachten sind? Dann ließe
sich das Teleskop ganz einfach auf diese
Objekte richten, und man müsste nur noch
warten, bis sich der Durchgang ereignet.

Die Transitvorhersage für morgen…

So einfach ist es zwar nicht, aber mit einem
damit verwandten und durchaus verhei-
ßungsvollen Ansatz lassen sich zumindest
die Transitwahrscheinlichkeiten an den

Tycho-Katalogs lernen lässt

minus 0,02 Bogensekunden genau, die
Helligkeitsmessungen auf wenigstens
0,06 mag. Als ganz wichtigen Parameter
enthält der Katalog auch die Parallaxen
der Sterne, also den Winkel, um den sie am
Himmel hin- und herwackeln, je nachdem,
auf welcher Seite der Erdbahn sich die Erde
und Hipparcos gerade befinden. Aus der
Parallaxe π lässt sich die Entfernung des
Sterns berechnen: $d = 1/\pi$, wobei sich d in
der astronomischen Längeneinheit Parsec
(= 3,26 Lichtjahre) ergibt, sofern man π in
Bogensekunden angibt.

Für Hauptreihensterne existiert eine
stabile Beziehung zwischen dem Farbin-
dex $B - V$ und der Oberflächentemperatur

der Sterne, auch effektive Temperatur T_{eff}
genannt. Für solche Sterne zeigte sich, dass
die Beziehung

$$T_{eff} = 10^{\left(\frac{14{,}5501\,\mathrm{mag} - (B-V)}{3{,}684\,\mathrm{mag}}\right)} \text{Kelvin}$$

eine sehr gute Näherung ist. Beispielswei-
se folgt für die Sonne mit ihrem Farbindex
$B - V \approx 0{,}65$ mag eine Oberflächentem-
peratur von rund 5900 Kelvin. Das kommt
recht nahe an den tatsächlichen Wert
5778 Kelvin heran.

Neben dieser empirischen Beziehung
zwischen Farbindex und effektiver Tempe-
ratur lassen sich für Hauptreihensterne
noch andere Beziehungen nutzen, um den
Radius, die Masse und sogar die Metallizität

[Fe/H] eines Sterns aus den Daten im Tycho-
Katalog abzuleiten. Aus Messungen der
Radialgeschwindigkeiten von 850 Sternen
fanden Astronomen eine bestimmte Wahr-
scheinlichkeit P_{Planet} für das Auftreten von
jupiterähnlichen Planeten in engen Um-
laufbahnen um einen Stern. Die Planeten-
häufigkeit hängt dabei erstaunlicherweise
lediglich von der Sternmetallizität ab:

$$P_{Planet} = 0{,}03 \cdot 10^{2 \cdot [Fe/H]}.$$

Zusammen mit dieser statistischen Aus-
sage lässt sich aus den im Tycho-Katalog
enthaltenen Daten damit die Wahrschein-
lichkeit für das Auftreten eines Planeten
um einen bestimmten Stern errechnen.
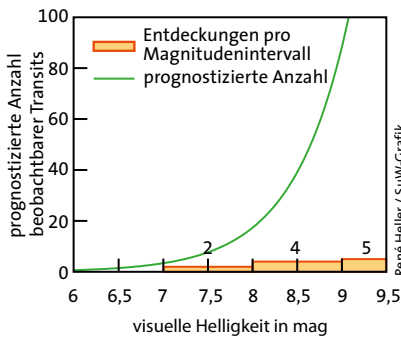
Die Anzahl beobachteter Transitplaneten sollte gemäß der Voraussage der Grafik auf S. 31 mit abnehmender Helligkeit der Zentralsterne – also zunehmender Magnitude – stark zunehmen (grüne Linie). Detektiert wurde bisher eine weit geringere Anzahl (orangefarbene Balken, geordnet pro Helligkeitsstufe von einer Magnitude im sichtbaren Licht der Zentralsterne). Das Potenzial ist also enorm.

Himmel projizieren. Diese Projektion vermag dann den Beobachtern zumindest eine Empfehlung zu liefern. Dazu möchten wir erst einmal wissen, an welchen Positionen am Himmel es überhaupt Sterne gibt. Unsere Wahl fiel auf den Tycho-Katalog. Dort sind die Positionen von etwas mehr als einer Million Sterne aufgeführt. Der Katalog basiert auf den Daten des Astrometriesatelliten Hipparcos und wurde Anfang der 1990er Jahre erstellt. In ihm findet man neben der Position noch weitere Parameter der vermessenen Sterne, etwa ihre scheinbare Helligkeit, ihren Farbindex und für die meisten von ihnen auch die Entfernung zur Erde.

Für Sterne auf der Hauptreihe gelten stabile Beziehungen zwischen dem Farbindex und der Oberflächentemperatur (siehe Kasten auf S. 30). Neben dieser empirischen Beziehung existieren noch andere, mit deren Hilfe sich der Radius, die Masse und sogar die Metallizität eines Sterns aus den Daten im Tycho-Katalog ableiten lassen. Als Metallizität bezeichnen die Astronomen den Anteil aller Elemente schwerer als Helium relativ zum leichtesten und zugleich häufigsten Element Wasserstoff.

An dieser Stelle ist man der Vorhersage eines Transits um einen bestimmten Stern schon sehr nahe. Es gilt noch eine weitere empirische Relation zu nutzen: Auf der Basis von Radialgeschwindigkeitsmessun-

gen an 850 Sternen konnten Astronomen nämlich eine bestimmte Wahrscheinlichkeit für das Auftreten von jupiterähnlichen Planeten in engen Bahnen um einen Stern finden. Der erstaunliche Zusammenhang ist, dass die Planetenhäufigkeit in statistischer Weise lediglich von der Metallizität des Stern abhängt (siehe Kasten auf S. 30). Mit der Kenntnis der Metallizität ist es also an dieser Stelle gelungen, die Wahrscheinlichkeit für das Auftreten eines Planeten um einen bestimmten Stern zu errechnen. Berücksichtigt man nun noch den geometrischen Aspekt der Wahrscheinlichkeit eines Transits und beschränkt man sich auf einen bestimmten Beobachtungszeitraum, in unserem Fall auf 50 Tage, so kann man den statistischen Erwartungswert der um einen Stern auftretenden Transits innerhalb des Beobachtungszeitraums vorhersagen.
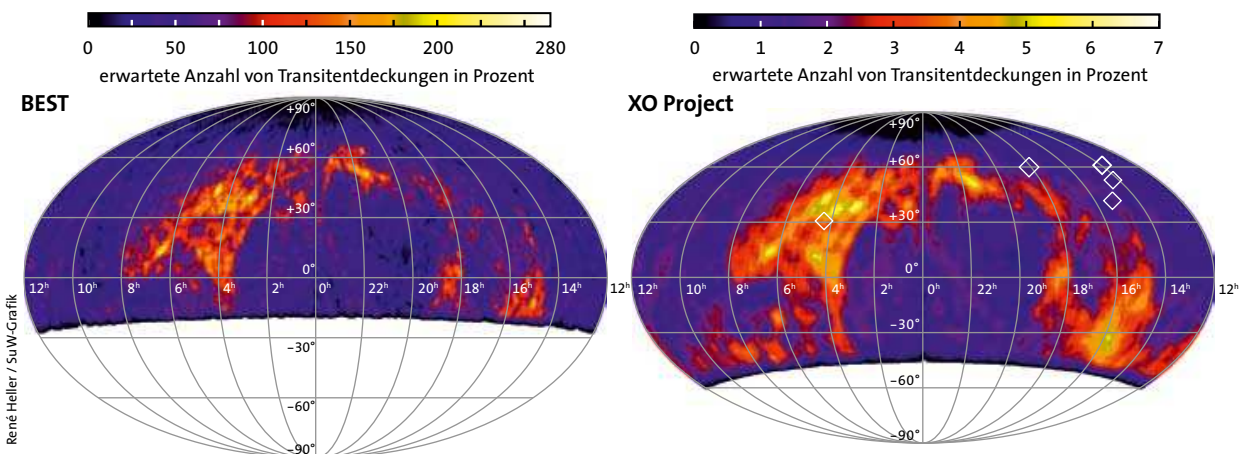
Ist der Erwartungswert für alle Hauptreihensterne im Tycho-Katalog berechnet, so lässt sich eine Himmelskarte erstellen, in der diese Erwartungswerte für Transits aufgetragen sind (siehe Bild auf S. 31). Deutlich zeichnet sich in der Grafik eine Verteilung ab, die jener der Sternverteilung sehr ähnlich ist und dem Band der Milchstraße folgt (siehe Infografik auf S. 36).

Die Auswertung dieser Karte verheißt Gutes für Transit(planeten)jäger und ist

im Bild links dargestellt. Die Grafik zeigt die Anzahl der tatsächlich beobachteten Transitplaneten, aufgetragen gegen die scheinbare visuelle Helligkeit der Sterne, und zum direkten Vergleich die entsprechende Auswertung der Karte mit den Erwartungswerten. Die Vorhersage lautet, dass am Himmel rund zwanzig Transits um Sterne heller als 8 mag sichtbar sein sollten, während aktuell nur zwei bekannt sind, nämlich die um die Sterne HD 209458 und HD 189733. Hier schlummert also ein gewaltiges Entdeckungspotenzial.

Empfehlungen für laufende Durchmusterungen

Die erwartete Verteilung von Transitplaneten über den Himmel liefert eine weitere Erkenntnis: Die meisten Transits dürften von einer bestimmten geografischen Breite aus sichtbar sein: ein Grad südlich. Wäre die Verteilung der Sterne und ihrer Eigenschaften am Himmel homogen, so hätte man dieses Resultat bereits ahnen können. Denn am Äquator einer idealen rotierenden Kugel stehend, vermag ein Beobachter innerhalb nur eines Umlaufs, also im Verlauf eines Tages, von Pol zu Pol blickend die gesamte Himmelssphäre zu sondieren. Befindet sich der Standpunkt jedoch an einem der Pole, so erlangt der Beobachter lediglich Zugang zur halben Sphäre, also nur zur Hälfte der Sterne bei einer homogenen Sternverteilung. Die ungleichmäßige Verteilung der Sterne am Himmel ist bedingt durch die Neigung der Erdrotationsachse gegen die Scheibe der Milchstraße mit ihrer darüber hinaus inhomogenen Sternverteilung entlang des Milchstraßenbands. Sie ließe eigentlich auch andere Breitengrade als aussichtsreichste Standorte zu. Unsere Untersuchung zeigt jedoch: Will man ein Instrument zur Entde-

BEST

erwartete Anzahl von Transitentdeckungen in Prozent

XO Project

erwartete Anzahl von Transitentdeckungen in Prozent

ckung und Messung von Transits aufstellen, dann sollte man seine Ausrüstung am besten einen Breitengrad südlich des Äquators aufstellen.

Doch wie steht es um die Programme zum Auffinden von Transits, die bereits im Gange sind? Lässt sich aus der Himmelskarte der erwarteten Transits vielleicht gar für jedes dieser Instrumente eine Einsicht in die potenziell ertragreichsten Plätze am Himmel gewinnen? Eine Empfehlung wäre doch schön.

Zunächst gilt es zu begutachten, welche Parameter die Effizienz eines Instruments bestimmen. Da ist zum einen die Pixelgröße der verwendeten CCD-Kamera. Sie bestimmt das Auflösungsvermögen und liegt für Weitfeld-Durchmusterungen typischerweise in der Größenordnung von einigen Bogensekunden am Himmel pro Millimeter auf dem CCD-Chip. Je kleiner dieses Verhältnis ist, desto höher ist die Auflösung und umso besser ließe sich ein Stern, der Lichtfluktuationen von einem Transitobjekt aufweist, von einem benachbarten Stern getrennt beobachten. Des Weiteren muss die Größe des Gesichtsfelds berücksichtigt werden. Mit zunehmender Größe gewinnt man mehr Sterne, die sich gleichzeitig beobachten lassen, und erhöht so die Chance, im überwachten Feld einen Transit zu erhaschen. Die Sensibilität des Chips bestimmt schließlich den Helligkeitsbereich, welcher der Instrumentierung zugänglich ist. Die drei bis heute erfolgreichsten erdgebundenen Transitprogramme HATNet, SuperWASP und XO haben Zugang zu Objekten im Helligkeitsbereich von ungefähr 8 bis 12 mag. In diesem Bereich befinden sich auch die meisten Sterne des Tycho-Katalogs.

Die Pixelgröße, das Gesichtsfeld und die Empfindlichkeit des CCDs definieren also die virtuelle Brille eines Instruments,
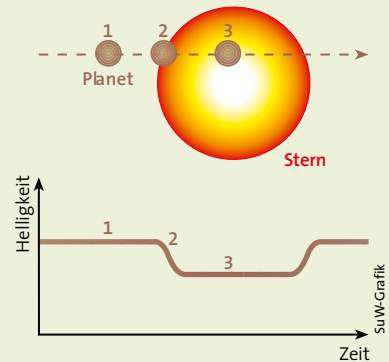
Transits und Suchprogramme

BEST – Zum »Berlin Exoplanet Search Telescope« BEST in Südfrankreich gesellte sich mittlerweile ein zweites Weitwinkelteleskop BEST II in Chile. Das Institut für Planetenforschung des Deutschen Zentrums für Luft- und Raumfahrt betreibt die beiden kleinen automatischen 25-Zentimeter-Teleskope zur Suche nach Transits, die von jupitergroßen Exoplaneten verursacht werden.

XO Project – Auf dem Haleakala auf Maui, Hawaii, sucht ein automatisches System aus Objektiv und CCD-Kamera mit 20 Zentimeter Öffnung nach Transits. Das von der NASA getragene Projekt vereint Wissenschaftler vom Space Telescope Science Institute und von mehreren amerikanischen Universitäten.
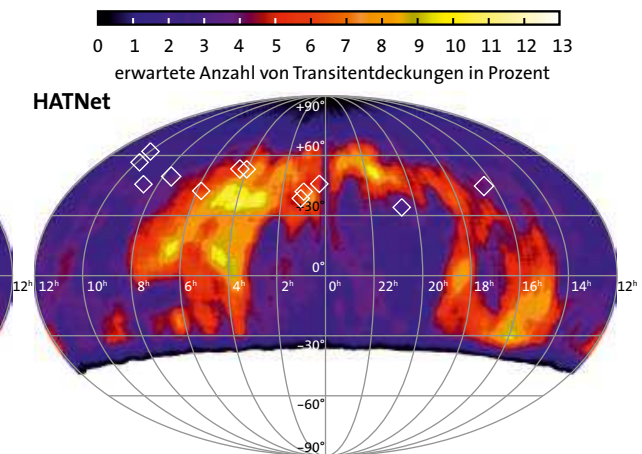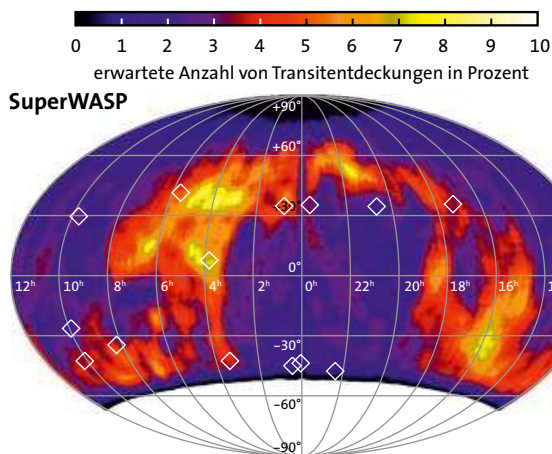
SuperWASP – Das britische Projekt »Wide Angle Search for Planets« zur Suche nach Transits betreibt zwei robotische Observatorien, je eines pro Hemisphäre. Super-WASP-North befindet sich auf La Palma, SuperWASP-South steht auf dem Gelände des südafrikanischen astronomischen Observatoriums SAAO. Jeweils acht Weitwinkelkameras überwachen simultan Millionen Sterne.

HATNet – Das ursprünglich von der ungarischen Astronomischen Gesellschaft HAA entwickelte automatische Teleskop mit elf Zentimeter Öffnung HAT (Hungarian-made Automated Telescope) ist mittlerweile Teil eines Netzwerks von sechs gleichartigen Teleskopen. Das HATNet wird nun vom Harvard-Smithsonian Center for Astrophysics betreut. Die zwei Hauptstationen befinden sich beim Fred Lawrence Whipple Observatory auf dem Mount Hopkins in Arizona und beim Submillimeter Array SMA auf dem Mauna Kea, Hawaii.
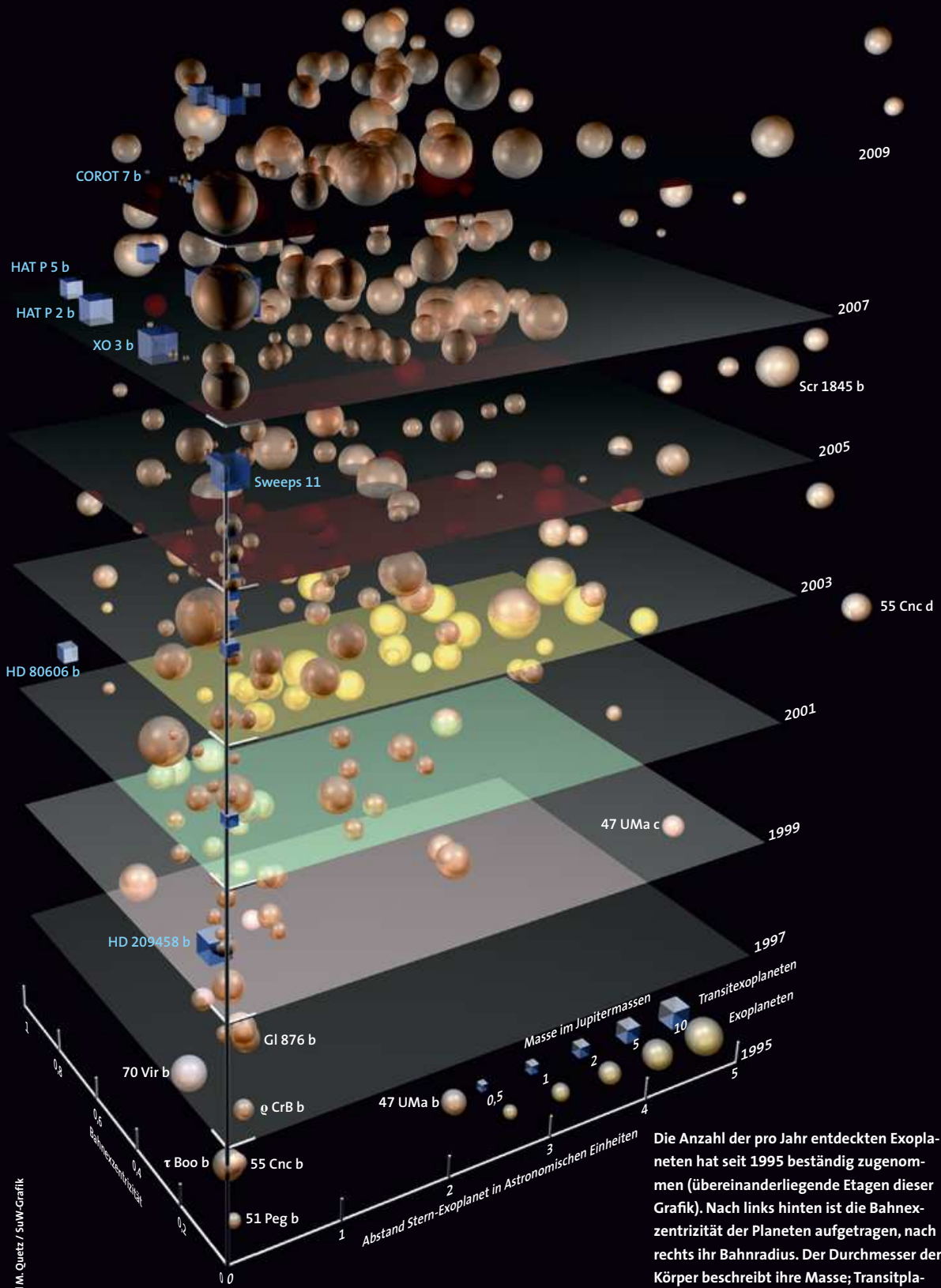
Liegt die Bahnebene eines Exoplaneten um seinen Zentralstern nahe der Sichtlinie zur Erde, so kann es zu einem Transit kommen, bei dem der Exoplanet vor seinem Stern vorbeizieht. Dabei schwächt er dessen Licht geringfügig ab. Die bisher gefundenen Transitplaneten überstreichen die Sternscheibe in wenigen Stunden und senken dessen Helligkeit dabei um etwa ein Prozent, was sich recht einfach nachweisen lässt – ist das Objekt erst einmal gefunden.

Die Erwartungswerte der zu beobachtenden Transits im Gesichtsfeld der vier etablierten Transitsuchprogramme BEST, XO, SuperWASP und HATNet sind hier farbig kodiert. Die Rauten markieren die Erstentdeckungen der Durchmusterungen. Die weißen Areale liegen permanent unter dem Horizont.

Seit 1995 entdeckte Exoplaneten

2009

COROT 7 b

HAT P 5 b

HAT P 2 b

XO 3 b

2007

Scr 1845 b

2005

Sweeps 11

2003

55 Cnc d

HD 80606 b

2001

47 UMa c

1999

1997

HD 209458 b

Transitexoplaneten

Masse im Jupitermassen

Exoplaneten

Gl 876 b

1995

70 Vir b

10

ϱ CrB b

47 UMa b

0,5

τ Boo b

55 Cnc b

2

5

51 Peg b

1

3

4

5

Abstand Stern-Exoplanet in Astronomischen Einheiten

Bahnexzentrizität

1

0,8

0,6

0,4

0,2

0 0

Axel M. Quetz / SuW-Grafik

Die Anzahl der pro Jahr entdeckten Exoplaneten hat seit 1995 beständig zugenommen (übereinanderliegende Etagen dieser Grafik). Nach links hinten ist die Bahnexzentrizität der Planeten aufgetragen, nach rechts ihr Bahnradius. Der Durchmesser der Körper beschreibt ihre Masse; Transitplaneten sind als Würfel dargestellt.

ZUM NACHDENKEN

Metallizität aus Tycho-Daten

Ein wichtiger Punkt bei der Analyse der Transithäufigkeiten mit Hilfe des eine Million Sterne umfassenden Tycho-Katalogs ist die Möglichkeit, aus den Daten weitere, nicht direkt erfasste stellare Parameter abzuleiten.

Die Metallizität beschreibt den Gehalt an chemischen Elementen mit Massen größer als derjenigen von Helium bezogen auf die Menge an Wasserstoff: $[Fe/H] = \lg(N_{Fe}/N_H) - \lg(N_{Fe}/N_H)_\odot$. Sie wird relativ zur Sonne angegeben: $\lg(N_{Fe}/N_H)_\odot = -1,8$.

Die Metallizität $[Fe/H]$ lässt sich nach einer Untersuchung von Nuno C. Santos, Garik Israelian und Michel Mayor (Spectroscopic [Fe/H] for 98 extrasolar planet-host stars. In: A&A 415, S. 1153-1166, 2004) für Sterne innerhalb bestimmter Randbedingungen allein aus dem Farbindex $(B-V)$ berechnen:

$$[Fe/H] = a \cdot T_{eff} - b + c \cdot (B-V) - d \cdot (B-V)^2.$$

mit $a = 2,43 \, 10^{-3}$/K, $b = 20,49$, $c = 11,52$/mag und $d = 2,69$/mag^2. In dieser Gleichung steckt auch die Temperatur T_{eff} der Sternoberfläche. Auch sie lässt sich aus dem Farbindex gewinnen:

B- und V-Helligkeiten aus dem Tycho-Katalog

Stern	V_{Ty} [mag]	B_{Ty} [mag]
HD 209458	7,703	8,334
COROT 7	10,775	11,828

$$T_{eff} = 10^\beta \text{ K}, \beta = \frac{14,55 \text{ mag} - (B-V)}{3,684 \text{ mag}}.$$

Die Wahrscheinlichkeit für einen Transitplaneten vom Typ Heißer Jupiter ist:

$$P_{Planet} = 0,03 \, 10^{2 \cdot [Fe/H]}.$$

Aufgabe 1: Man berechne für die beiden in der Tabelle aufgeführten Sterne Temperatur und Metallizität.

Aufgabe 2: Wie groß ist die Wahrscheinlichkeit für einen Transitplaneten? AMQ

Ihre Lösungen senden Sie bitte bis zum **15. Juni 2010** an: Redaktion SuW – Zum Nachdenken, Max-Planck-Institut für Astronomie, Königstuhl 17, D-69117 Heidelberg. Fax: +49(0)62 21–52 82 46. Einmal im Jahr werden unter den erfolgreichen Lösern **Preise** verlost: siehe S. 117.

mel. Die Methode der virtuellen Transitbrille für die jeweiligen Suchprogramme gibt konkrete Hinweise auf fruchtbare Beobachtungsfelder. Das geplante »Panoramic Survey Telescope and Rapid Response System« Pan-STARRS wird schon bald mit hoher Auflösung den Himmel bis zu extrem leuchtschwachen Sternen der Helligkeit 24 mag kartieren und die Erstellung noch deutlich detaillierterer Karten zulassen. In der Zukunft kommen auch neue, weitaus empfindlichere Spektrografen zum Einsatz. Dazu gehören zum Beispiel ESPRESSO für das Very Large Telescope der europäischen Südsternwarte ESO und CODEX für das European Extremely Large Telescope E-ELT. Im Zusammenspiel mit ihnen lassen sich dann für viele leuchtschwache Objekte auch die stellaren Radialgeschwindigkeiten messen, welche die Transitkandidaten konkret bestätigen oder aber als Fehlalarm enttarnen. Auf Basis des schnellen Reaktionssystems Pan-STARRS und unter Berücksichtigung der Kapazitäten der dann möglichen spektralen Nachuntersuchung der Kandidaten eröffnen sich neue Möglichkeiten: Mit der hier vorgestellten Methode lassen sich nach den zuvor erstellten Transitkarten regelrechte Transitsurveys beginnen und die instrumentellen Eigenschaften bereits im Voraus an die geografische Lage anpassen.

RENÉ HELLER promoviert an der Hamburger Sternwarte über die Entwicklung Brauner Zwerge und die Eigenschaften extrasolarer Planeten.

Literaturhinweise

Mayor M., et al.: A Jupiter-mass companion to a solar-type star. In: Nature 378, S. 355–359, 1995.

Marcy, G. W., et al.: The planet around 51 Pegasi. In: The Astrophysical Journal 481, S. 926–935, 1997.

Charbonneau, D., et al.: Detection of planetary transits across a sun-like star. In: The Astrophysical Journal 529, S. L45–L48, 2000.

Fischer, D. A. und Valenti, J.: The planet-metallicity correlation. In: The Astrophysical Journal 622, S. 1102–1117, 2005.

Heller, R., et al.: Transit detections of extrasolar planets around main-sequence stars – I. A sky map for Hot Jupiters. In: Astronomy and Astrophysics 508, S. 1509–1514, 2009 (arxiv:0910.2887).

durch die hindurch man sich nun die Grafik auf S. 31 erneut anschauen kann. In unserer Arbeit berücksichtigten wir die Standorte der Instrumente der Programme BEST, XO, SuperWASP und HATNet (siehe Kasten auf S. 33). Das Ergebnis zeigen die Grafiken auf S. 32 und 33 unten. Hier ist nun nicht mehr die erwartete Anzahl der auftretenden Transits um die Sterne gezeigt, sondern der Erwartungswert der tatsächlich beobachtbaren Ereignisse für das Gesichtsfeld des jeweiligen Instruments. Dabei zeichnet sich ab, dass BEST mit seinem Teleskop eher mäßig abschneidet. Grund hierfür ist das kleine Gesichtsfeld von 3,1 × 3,1 Grad, das trotz der relativ hohen Auflösung des CCDs von 5,5 Bogensekunden pro Millimeter nur geringe »Fangquoten« zulässt. Die drei erfolgreichsten Programme nutzen hingegen nicht Teleskope, sondern Linsensysteme mit weitaus größeren Gesichtsfeldern. So umfasst beispielsweise dasjenige von SuperWASP immerhin 7,8 × 7,8 Grad. Die in der Reihenfolge steigender Effizienz geordnete Vorhersage für die vier Surveys – also BEST, XO, SuperWASP und HATNet – deckt sich fast mit der Erfahrung: Während BEST keine Erstdetektion vorweisen kann, waren XO mit fünf, SuperWASP mit 26 und HATNet mit 13 weitaus erfolgreicher. Der Verbund mehrerer Instrumente an verschiedenen Standorten und die unterschiedlichen Beobachtungsstrategien und Prozeduren in der Datenauswertung der einzelnen Programme verzerren unsere optimistische Vorhersage für HATNet zugunsten von SuperWASP, der bisher erfolgreichsten Unternehmung.

Mit diesen Transithimmelskarten erhalten Astronomen eine Abschätzung der noch zu erwartenden Anzahl an beobachtbaren exoplanetaren Transits, insbesondere um helle Sterne, sowie ihrer Verteilung am Him-

References

Abney, W. D. W. 1877a, MNRAS, 37, 278

Abney, W. D. W. 1877b, The Observatory, 1, 134

Abt, H. A. & Levy, S. G. 1976, ApJS, 30, 273

Baraffe, I., Chabrier, G., Allard, F., & Hauschildt, P. H. 2002, A&A, 382, 563

Baraffe, I., Chabrier, G., & Barman, T. 2008, A&A, 482, 315

Baraffe, I., Chabrier, G., Barman, T. S., Allard, F., & Hauschildt, P. H. 2003, A&A, 402, 701

Barman, T. 2007, ApJ, 661, L191

Barnes, R., Jackson, B., Greenberg, R., Raymond, S. N., & Heller, R. 2009, ArXiv e-prints

Barnes, R., Jackson, B., Heller, R., Greenberg, R., & Raymond, S. N. 2010, LPI Contributions, 1538, 5595

Beaulieu, J., Bennett, D. P., Fouqué, P., et al. 2006, Nature, 439, 437

Beaulieu, J., Tinetti, G., Kipping, D. M., et al. 2010, ArXiv e-prints

Bodenheimer, P., Lin, D. N. C., & Mardling, R. A. 2001, ApJ, 548, 466

Boltzmann, L. 1884, Annalen der Physik, 258, 291

Borucki, W. J. & for the Kepler Team. 2010, ArXiv e-prints

Boss, A. P. 2000, ApJ, 536, L101

Bouchy, F., Mayor, M., Lovis, C., et al. 2009, A&A, 496, 527

Bradt, H. 2008, Astrophysics Processes: The Physics of Astronomical Phenomena (Cambridge University Press)

Brown, T. M., Charbonneau, D., Gilliland, R. L., Noyes, R. W., & Burrows, A. 2001, ApJ, 552, 699

Burke, C. J., McCullough, P. R., Bergeron, E., et al. 2010, ArXiv e-prints

Chabrier, G. & Baraffe, I. 1997, A&A, 327, 1039

Chabrier, G. & Baraffe, I. 2000, ARA&A, 38, 337

Charbonneau, D., Berta, Z. K., Irwin, J., et al. 2009, Nature, 462, 891

Charbonneau, D., Brown, T. M., Latham, D. W., & Mayor, M. 2000, ApJ, 529, L45

Charbonneau, D., Brown, T. M., Noyes, R. W., & Gilliland, R. L. 2002, ApJ, 568, 377

Chauvin, G., Lagrange, A., Dumas, C., et al. 2004, A&A, 425, L29

Chauvin, G., Lagrange, A., Zuckerman, B., et al. 2005, A&A, 438, L29

Claret, A. 2004, A&A, 428, 1001

Dawson, R. I. & Fabrycky, D. C. 2010, ArXiv e-prints

Deleuil, M., Deeg, H. J., Alonso, R., et al. 2008, A&A, 491, 889

Desch, S. & Porter, S. 2010, in Lunar and Planetary Institute Science Conference Abstracts, Vol. 41, Lunar and Planetary Institute Science Conference Abstracts, 2625–+

Dodson-Robinson, S. E., Veras, D., Ford, E. B., & Beichman, C. A. 2009, ApJ, 707, 79

Einstein, A. 1905, Annalen der Physik, 322, 891

Endl, M., Hatzes, A. P., Cochran, W. D., et al. 2004, ApJ, 611, 1121

Fabrycky, D. & Tremaine, S. 2007, ApJ, 669, 1298

Fabrycky, D. C. & Winn, J. N. 2009, ApJ, 696, 1230

Ferraz-Mello, S., Rodríguez, A., & Hussmann, H. 2008, Celestial Mechanics and Dynamical Astronomy, 101, 171

Fischer, D. A. & Marcy, G. W. 1992, ApJ, 396, 178

Fischer, H. & Spohn, T. 1990, Icarus, 83, 39

Fleming, S. W., Kane, S. R., McCullough, P. R., & Chromey, F. R. 2008, MNRAS, 386, 1503

Forveille, T., Bonfils, X., Delfosse, X., et al. 2009, A&A, 493, 645

Gaudi, B. S. & Winn, J. N. 2007, ApJ, 655, 550

Gomes, R., Levison, H. F., Tsiganis, K., & Morbidelli, A. 2005, Nature, 435, 466

Greenberg, R. 2005, Europa - the Ocean Moon : search for an alien biosphere (Springer)

Greenberg, R. 2010, Astrobiology, 10, 275

Grether, D. & Lineweaver, C. H. 2006, ApJ, 640, 1051

Hansen, C. J., Esposito, L., Stewart, A. I. F., et al. 2006, Science, 311, 1422

Heller, R. 2010a, SuW, 6

Heller, R. 2010b, Sterne und Weltraum, 6, 30

Heller, R., Homeier, D., Dreizler, S., & Oestensen, R. 2009a, A&A, 496, 191

Heller, R., Jackson, B., Barnes, R., Greenberg, R., & Homeier, D. 2010, A&A, 514, A22+

Heller, R., Mislis, D., & Antoniadis, J. 2009b, A&A, 508, 1509

Henry, G. W., Marcy, G., Butler, R. P., & Vogt, S. S. 1999, IAU Circ., 7307, 1

Holman, M. J. & Murray, N. W. 2005, Science, 307, 1288

Holt, J. R. 1893, Astronomy and Astrophysics, XII

Howard, A. W., Johnson, J. A., Marcy, G. W., et al. 2009, ApJ, 696, 75

Hubble, E. 1929, Proceedings of the National Academy of Science, 15, 168

Huber, K. F., Czesla, S., Wolter, U., & Schmitt, J. H. M. M. 2009, A&A, 508, 901

Huber, K. F., Czesla, S., Wolter, U., & Schmitt, J. H. M. M. 2010, A&A, 514, A39+

Hut, P. 1981, A&A, 99, 126

Ibgui, L. & Burrows, A. 2009, ApJ, 700, 1921

Ibgui, L., Burrows, A., & Spiegel, D. S. 2010, ApJ, 713, 751

Ida, S. & Makino, J. 1993, Icarus, 106, 210

Irwin, J. B. 1952, ApJ, 116, 211

Kalas, P., Graham, J. R., Chiang, E., et al. 2008, Science, 322, 1345

Kant, I. 1787, Kritik der reinen Vernunft (Königliche Akademie der Wissenschaften in Berlin)

Kasper, M., Biller, B. A., Burrows, A., et al. 2007, A&A, 471, 655

Kepler, J. 1619, Harmonices mvndi libri v. qvorvm primus geometricvs, de figurarum regularium, quae proportiones harmonicas constituunt, ortu & demonstrationibus, secundus architectonicvs, SEU EX geometria figvrata, de figurarum regularium congruentia in plano vel solido: tertius proprie harmonicvs, de proportionum harmonicarum ortu EX figuris

Kipping, D. M. 2008, MNRAS, 389, 1383

Kipping, D. M. 2009, MNRAS, 392, 181

Kipping, D. M., Ribas, I., & Font-Ribera, A. 2009, in IAU Symposium, Vol. 253, IAU Symposium, 490–491

Knutson, H. A., Charbonneau, D., Allen, L. E., et al. 2007, Nature, 447, 183

Lafrenière, D., Jayawardhana, R., & van Kerkwijk, M. H. 2008, ApJ, 689, L153

Laplace, P.-S. 1814, Essai philosophique sur les probabilités (Paris)

Latham, D. W., Stefanik, R. P., Mazeh, T., Mayor, M., & Burki, G. 1989, Nature, 339, 38

Leconte, J., Chabrier, G., Baraffe, I., & Levrard, B. 2010, A&A, 516, A64+

Léger, A., Rouan, D., Schneider, J., et al. 2009, A&A, 506, 287

Lemaître, G. 1927, Annales de la Societe Scietifique de Bruxelles, 47, 49

Levison, H. F. & Stewart, G. R. 2001, Icarus, 153, 224

Lodato, G., Delgado-Donate, E., & Clarke, C. J. 2005, MNRAS, 364, L91

Lucas, P. W., Tinney, C. G., Burningham, B., et al. 2010, ArXiv e-prints

Maciejewski, G., Dimitrov, D., Neuhaeuser, R., et al. 2010, ArXiv e-prints

Marcy, G. W. & Butler, R. P. 1995, in Bulletin of the American Astronomical Society, Vol. 27, Bulletin of the American Astronomical Society, 1379–+

Marcy, G. W. & Butler, R. P. 2000, PASP, 112, 137

Marois, C., Macintosh, B., Barman, T., et al. 2008, Science, 322, 1348

Mayor, M., Bonfils, X., Forveille, T., et al. 2009a, A&A, 507, 487

Mayor, M. & Queloz, D. 1995, Nature, 378, 355

Mayor, M., Udry, S., Lovis, C., et al. 2009b, A&A, 493, 639

McLaughlin, D. B. 1924, ApJ, 60, 22

Miguel, Y. & Brunini, A. 2010, ArXiv e-prints

Miller, N., Fortney, J. J., & Jackson, B. 2009, ApJ, 702, 1413

Morbidelli, A., Levison, H. F., Tsiganis, K., & Gomes, R. 2005, Nature, 435, 462

Nakajima, T., Oppenheimer, B. R., Kulkarni, S. R., et al. 1995, Nature, 378, 463

Nesvorný, D. & Beaugé, C. 2010, ApJ, 709, L44

Nesvorný, D. & Morbidelli, A. 2008, ApJ, 688, 636

Neuhäuser, R., Mugrauer, M., Seifahrt, A., Schmidt, T. O. B., & Vogt, N. 2008, A&A, 484, 281

Newton, I. 1686, Philosophiae Naturalis Principia Mathematica (The Royal Academy of Science)

Ohta, Y., Taruya, A., & Suto, Y. 2005, ApJ, 622, 1118

Oppenheimer, B. R., Kulkarni, S. R., Matthews, K., & Nakajima, T. 1995, Science, 270, 1478

Peale, S. J., Cassen, P., & Reynolds, R. T. 1979, Science, 203, 892

Penzias, A. A. & Wilson, R. W. 1965, ApJ, 142, 419

Plesa, A. & Breuer, D. 2009, in European Planetary Science Congress 2009, 366–+

Pollack, J. B., Hubickyj, O., Bodenheimer, P., et al. 1996, Icarus, 124, 62

Pont, F. 2009, MNRAS, 396, 1789

Pont, F., Knutson, H., Gilliland, R. L., Moutou, C., & Charbonneau, D. 2008, MNRAS, 385, 109

Queloz, D., Bouchy, F., Moutou, C., et al. 2009, A&A, 506, 303

Raghavan, D., McAlister, H. A., Henry, T. J., et al. 2010, ArXiv e-prints

Ribas, I., Font-Ribera, A., & Beaulieu, J. 2008, ApJ, 677, L59

Richardson, L. J., Deming, D., Horning, K., Seager, S., & Harrington, J. 2007, Nature, 445, 892

Rivera, E. J., Butler, R. P., Vogt, S. S., et al. 2010, ApJ, 708, 1492

Rivera, E. J., Lissauer, J. J., Butler, R. P., et al. 2005, ApJ, 634, 625

Rossiter, R. A. 1924, ApJ, 60, 15

Russell, B. 1945, A History of Western Philosophy (George Allen & Unwin. London)

Sagan, C. 1980, Cosmos (Carl Sagan Productions, Inc.)

Sartoretti, P. & Schneider, J. 1999, A&AS, 134, 553

Sasselov, D. D. & Lecar, M. 2000, ApJ, 528, 995

Schlesinger, F. 1910, Publications of the Allegheny Observatory of the University of Pittsburgh, 1, 123

Seagroves, S., Harker, J., Laughlin, G., Lacy, J., & Castellano, T. 2003, PASP, 115, 1355

Segatz, M., Spohn, T., Ross, M. N., & Schubert, G. 1988, Icarus, 75, 187

Smoot, G. F., Bennett, C. L., Kogut, A., et al. 1992, ApJ, 396, L1

Spergel, D. N., Verde, L., Peiris, H. V., et al. 2003, ApJS, 148, 175

Stamenkovic, V., Noack, L., & Breuer, D. 2009, in European Planetary Science Congress 2009, 372–+

Stefan, J. 1879, Sitzungsberichte der mathematisch-naturwissenschaftlichen Classe der kaiserlichen Akademie der Wissenschaften, 79, 391

Struve, O. 1952, The Observatory, 72, 199

Swain, M. R., Tinetti, G., Vasisht, G., et al. 2009, ApJ, 704, 1616

Tarter, J. C. 1975, PhD thesis, California Univ., Berkeley.

Thalmann, C., Carson, J., Janson, M., et al. 2009, ApJ, 707, L123

Thies, I., Kroupa, P., Goodwin, S. P., Stamatellos, D., & Whitworth, A. P. 2010, ApJ, 717, 577

Tinetti, G., Vidal-Madjar, A., Liang, M., et al. 2007, Nature, 448, 169

Todorov, K., Luhman, K. L., & McLeod, K. K. 2010, ArXiv e-prints

Triaud, A. H. M. J., Cameron, A. C., Queloz, D., et al. 2010, A&A

Tsiganis, K., Gomes, R., Morbidelli, A., & Levison, H. F. 2005, Nature, 435, 459

Udry, S., Bonfils, X., Delfosse, X., et al. 2007, A&A, 469, L43

Ventura, P. & Zeppieri, A. 1998, A&A, 340, 77

Vidal-Madjar, A., Désert, J., Lecavelier des Etangs, A., et al. 2004, ApJ, 604, L69

Vidal-Madjar, A., Lecavelier des Etangs, A., Désert, J., et al. 2003, Nature, 422, 143

Vogt, S. S., Wittenmyer, R. A., Butler, R. P., et al. 2010, ApJ, 708, 1366

Walker, G. A. H., Bohlender, D. A., Walker, A. R., et al. 1992, ApJ, 396, L91

Wang, H. J., Wei, J. Y., Shi, J. R., & Zhao, J. K. 2009, A&A, 500, 1215

Wetherill, G. W. 1985, Science, 228, 877

Winn, J. N., Noyes, R. W., Holman, M. J., et al. 2005, ApJ, 631, 1215

Wolszczan, A. & Frail, D. A. 1992, Nature, 355, 145

Woltjer, Jr., J. 1922, Bull. Astron. Inst. Netherlands, 1, 93

Worek, T. F. 2000, Information Bulletin on Variable Stars, 4838, 1

Danksagung

Diese Arbeit habe ich nicht aus mir allein heraus und eingebettet in das Nichts geschrieben. Denn als Mensch stehe ich in einem sozialen Zusammenhang und als Wissenschaftler in einem administrativen und einem technologischen; nicht zuletzt als Philosoph in einem historischen. Und dieses weite, engmaschige Kontextnetz verknüpft mich mit anderen Personen und meine Arbeit mit anderen.

Den Mentoren meiner Promotion Prof. Dr. Jürgen Schmitt, Prof. Dr. Günter Wiedemann, Prof. Dr. Stefan Dreizler, Prof. Dr. Peter Hauschildt und Dr. Jacob Bean danke ich vielmals, mich im Forschungsbereich willkommengeheißen und in seine Zusammenhänge eingeführt zu haben. Jürgen, dir danke ich insbesondere für dein Vertrauen in meine Arbeit und deine ständige Unterstützung.

Meinem Weggefährten Dimitris Mislis schulde ich zahlreiche nervenaufreibende Diskussionen, aus denen wir beide schlauer rausgingen, als wir reinkamen, sowie Inspiration und essenzielle Beiträge zu meinen Arbeiten. Thanks Dimitris, my friend, for your objective inspiration and a cheerful time in our office!

Mariana Wagner und Katja Poppenhäger waren vor allen anderen verantwortlich für meine freundschaftliche und emotionale Lebensfreude an der Hamburger Sternwarte. Merci für 'Mutual Inspiration Sessions on Astrophysics' mit Kochen und Tee! Ihr wart in den vergangenen drei Jahren für mich ganz wichtig und ich bin sicher, dass wir uns nicht aus den Augen und Herzen verlieren werden.

Jacob Bean hat Ende 2008 meinen Kontakt zu Rory Barnes, Brian Jackson und Richard Greenberg – allesamt damals am LPL in Tucson (Arizona, USA) – hergestellt. Ohne den Zugang zu diesen wahnsinnig interessanten und schlauen Menschen würde das Buch in den Händen des Lesers völlig anders aussehen.

Jacob und Katja: danke für das Gegenlesen des Manuskripts!

Dipl.-Phys. Axel M. Quetz und der Redaktion *Sterne und Weltraum* danke ich für das Recht, meinen Artikel aus dem Heft 6/2010 hier abdrucken zu dürfen. *Astronomy and Astropyhsics* sei gedankt für das Recht, meine veröffentlichten, eingereichten und im Prozess befindlichen Artikel hier verwenden zu dürfen. In dieser Arbeit habe ich von Jean Schneiders 'Extrasolar Planets Encyclopaedia' auf `www.exoplanet.eu` und vom 'Astrophysics Data System Bibliographic Service' (ADS) der NASA auf `http://adsabs.harvard.edu` Gebrauch gemacht. "Unless otherwise noted, images and video on JPL public web sites (public sites ending with a jpl.nasa.gov address) may be used for any purpose without prior permission, subject to the special cases noted below. Publishers who wish to have authorization may print this page and retain it for their records; JPL does not issue image permissions on an image by image basis." (`www.jpl.nasa.gov/imagepolicy`).

–

Annemarie, du bist mein Kleinod. Deine Begleitung und die ganzen bunten Farben in meinem Leben sind von unschätzbarem Wert für mich.